

DINECIO DOS SANTOS FILHO

ON THE PLASMA-ASSISTED MODIFICATIONS OF PRE-TEXTURED SURFACES:
SHALLOW DEPTH NITRIDING IN CAST IRON, TOPOGRAPHY AND
INSTRUMENTED SCLEROMETRY TEST RESPONSE

SÃO PAULO

2020

DINECIO DOS SANTOS FILHO

On the plasma-assisted modifications of pre-textured surfaces: shallow depth nitriding in cast iron, topography and instrumented sclerometry test response

Thesis submitted to the Polytechnic School of the University of São Paulo, in conformity with the requirements for the degree of Doctor of Science.

São Paulo

2020

DINECIO DOS SANTOS FILHO

On the plasma-assisted modifications of pre-textured surfaces: shallow depth nitriding in cast iron, topography and instrumented sclerometry test response

Versão Corrigida

(Versão original encontra-se disponível na Escola Politécnica da USP)

Thesis submitted to the Polytechnic School of the University of São Paulo, in conformity with the requirements for the degree of Doctor of Science.

Area of concentration:

Metallurgical and Materials Engineering

Supervisor: Prof. Dr. Hélio Goldenstein

Co-Supervisor: Prof. Dr. André Paulo Tschiptschin

São Paulo

2020

Autorizo a reprodução e divulgação total ou parcial deste trabalho, por qualquer meio convencional ou eletrônico, para fins de estudo e pesquisa, desde que citada a fonte.

Este exemplar foi revisado e corrigido em relação à versão original, sob responsabilidade única do autor e com a anuência de seu orientador.

São Paulo, __06__ de _____ Janeiro _____ de 2020

Assinatura do autor: _____ Dinécio dos Santos Filho

Assinatura do orientador: _____ Hélio Goldenstein

Catálogo-na-publicação

dos Santos Filho, Dinécio

On the plasma-assisted modifications of pre-textured surfaces: shallow depth nitriding in cast iron, topography and instrumented sclerometry test response / D. dos Santos Filho. – versão corr. -- São Paulo, 2020.
218 p.

Tese (Doutorado) - Escola Politécnica da Universidade de São Paulo.
Departamento de Engenharia Metalúrgica e de Materiais.

1.Ferro fundido cinzento 2.Desgaste 3.Tratamento térmico 4.Elementos de máquinas 5. Motores de combustão interna I.Universidade de São Paulo. Escola Politécnica. Departamento de Engenharia Metalúrgica e de Materiais II.t.

DEDICATORY

*In honor of all mothers
and grandmothers,
I dedicate this work to my
dear and beloved mother.*

DEDICATÓRIA

*Em homenagem a
todas as mães e avós,
dedico este trabalho à minha
querida e amada mãe.*

ACKNOWLEDGEMENTS

God, the supreme intelligence, first cause of all things.

Jesus, manifestation of the love of God, personification of His infinite goodness.

Dear parents and ancestors, seeders.

Prof. Hélio Goldenstein and Prof. André Tschiptschin, supervisor and co-supervisor of this thesis.

University of São Paulo and General Motors, for the utilization of materials and equipment, required to conduct the research.

Everyone, each in their own way, whom contributed to the accomplishment and improvement of this work, result of the efforts of countless people.

AGRADECIMENTOS

Deus, inteligência suprema, causa primária de todas as coisas.

Jesus, manifestação do amor de Deus, personificação de Sua bondade infinita.

Queridos pais e antepassados, semeadores.

Prof. Hélio Goldenstein e Prof. André Tschitschin, orientador e co-orientador desta tese.

Universidade de São Paulo e General Motors, pelo uso de materiais e equipamentos, necessários à condução da pesquisa.

Todos, cada qual a seu modo, que contribuíram para a realização e aperfeiçoamento desta obra, resultado do esforço de incontáveis pessoas.

EPIGRAPH

“Love one another,
as I have loved you.”

Jesus

EPÍGRAFE

“Amai-vos uns aos outros,
como Eu vos amei.”

Jesus

ABSTRACT

A concept of plasma treatment for enhancing pre-textured surfaces of components made in pearlitic gray cast iron is proposed. It consists of a plasma nitriding at low temperatures and short times, in order to increase the hardness of the surface by means of a shallow depth nitride formation in the surface of the iron. As a result, the roughness pattern of a previously textured surface is preserved after the treatment. A review on the wear of internal combustion engine cylinders along with background research was conducted, which consisted in the description of cylinder bore wear features observed experimentally. The background research substantiated the significance of initiatives to enhance wear and friction response of pre-textured surfaces made of cast iron, such as the internal combustion engine cylinders. A series of plasma nitriding experiments was run on specimens extracted from engine cylinders. Flat specimens, obtained from blanks extracted from the cylinder wall of an engine cylinder block, were textured in laboratory in order to emulate the typical roughness distribution of an ordinary cylinder bore plateau honing process. Complementarily, a case-study experiment was performed in a honed sample of an internal combustion engine cylinder, whose surface in its original form (cylindrical) has been textured through industrial honing operations. Therefore, one among the potential applications of the research has been assessed. 3-D interference roughness measurements were performed before and after the plasma treatment to assess topographic stability of the textured surfaces. ϵ -Iron nitride (Fe_3N) formation was identified via X-ray diffraction analysis. In addition, nitrogen concentration profile was quantitatively evaluated using wavelength-dispersive (X-ray) spectroscopy microanalysis, substantiating the nitride formation at shallow depth. Microhardness measurements and instrumented linear sclerometry test ('scratch test') results indicated that ϵ -iron nitride formation and solid solution hardening could provide enhanced properties to the surface of general pearlitic cast iron components, such as increase of wear resistance, and decrease of apparent coefficient of friction, in the assessed conditions. The results demonstrated that the roughness texture pattern was satisfactorily preserved after the treatment, which was supported by direct observation of the surfaces via scanning electronic microscopy.

Keywords: Gray cast iron. Wear. Heat treatment. Machine elements. Internal combustion engine.

RESUMO

Um conceito de tratamento por plasma para beneficiamento de superfícies previamente texturizadas de componentes produzidos em ferro fundido cinzento perlítico é proposto. Consiste de uma nitretação a plasma a baixas temperaturas e tempos curtos, de forma a aumentar a dureza da superfície através da formação de nitretos a profundidades rasas da superfície do ferro fundido. Como resultado, o padrão de rugosidade da superfície previamente texturizada é preservado após o tratamento. Uma revisão sobre desgaste de cilindros de motor de combustão interna em conjunto com pesquisa de base foi conduzida, a qual consistiu em uma descrição de características de desgaste observadas experimentalmente. A pesquisa de base reafirmou a relevância de iniciativas para melhoramento da resposta ao desgaste e atrito de superfícies pré-texturizadas produzidas em ferro fundido, tais quais são os cilindros do motor de combustão interna. Uma série de experimentos de nitretação a plasma foi realizada em amostras extraídas de cilindros de motor de combustão interna. Amostras planas, obtidas a partir de frações de material extraídas da parede de um cilindro de bloco de motor, foram texturizadas em laboratório de forma a emular a distribuição de rugosidade típica de um processo regular de brunimento de cilindro do tipo platô (plateau honing). Complementarmente, um experimento tipo estudo de caso foi conduzido em uma amostra brunida de um cilindro de motor de combustão interna, cuja superfície em sua forma original (cilíndrica) foi previamente texturizada através de operações industriais de brunimento. Desta forma, uma entre as potenciais aplicações da pesquisa foi avaliada. Medições de rugosidade por interferometria 3-D foram conduzidas antes e após o tratamento por plasma, para avaliar a estabilidade topográfica das superfícies texturizadas. A formação de nitreto de ferro- ϵ (Fe_3N) foi identificada via análise por difração de raios-X. Adicionalmente, o perfil de concentração de nitrogênio foi avaliado quantitativamente usando microanálise por espectroscopia (raios-X) por comprimento de onda dispersivo, fundamentando a formação de nitreto em profundidade rasa. Medições de microdureza e resultados do teste de esclerometria linear instrumentada indicaram que a formação de nitreto de ferro- ϵ e endurecimento por solução sólida podem prover propriedades melhoradas à superfície de componentes gerais produzidos em ferro fundido de matriz perlítica, tais quais o aumento da resistência ao desgaste e diminuição do coeficiente de atrito aparente, nas condições avaliadas. Os resultados demonstraram que o padrão de textura de rugosidade foi satisfatoriamente preservado após o tratamento, o que foi suportado pela observação direta das superfícies via microscopia eletrônica de varredura.

Palavras-Chave: Ferro fundido cinzento. Desgaste. Tratamento térmico. Elementos de máquinas. Motores de combustão interna.

LIST OF FIGURES

Figure 1:	Progression of wear of a GCI cylinder bore surface. Adapted from [27].	37
Figure 2:	Graphite geometry and position found in the cylinder bore surface varies in thickness and size. The flake orientation will affect the graphite position in a surface of interest [55].	38
Figure 3:	Schematic of cylinder bore material microstructure and characterization specimens location. a) Optical micrograph from the cylinder block material, as polished, not etched. Flake graphite is revealed. b) Optical micrograph illustrating the matrix of pearlite. (2% Nital solution). c) Scheme of cylinder block specimen location. d) SEM analysis location scheme (see Table 2). The regions of localized wear were identified by the profilometer analysis, which guided the SEM analysis.	44
Figure 4:	Cylinder Bore localized wear in the TDC and BDC regions. At end-of-test with gasoline and ethanol. Results are based on 2-D profilometer analysis reported in [58].	45
Figure 5:	Bore surface SEM Analysis. At end-of-test with (a) gasoline and (b) ethanol.	46
Figure 6:	Scheme of nitrogen diffusion for different graphite positions [63].	51
Figure 7:	Cross-section of a nitrided (without compound layer formation) 1.00 wt% C specimen. In the surface region the cementite lamellae are converted into ϵ -nitride. According to Mittemeijer et al. [64].	51
Figure 8:	WDS measured (a) nitrogen and (b) carbon contents in steel AISI D2 as a function of distance from the surface [67].	52
Figure 9:	N distribution and microhardness of AISI410S steel nitrided at 800 oC - 6h [68].	53
Figure 10:	a) Photomicrograph of Fe ₃ N on the surface of (111) α grain after nitriding in gas (NH ₃ /H ₂) process. b) SEM micrograph showing Fe ₃ N on the surface of (111) α grain after nitriding in gas (NH ₃ /H ₂) process [69].	54
Figure 11:	a) Test method schematic. b) Critical scratch load damage features in progressive load test, where: Lc1 and Lc2 refer to first and second level of critical scratch load values, respectively [70].	55
Figure 12:	a) Wear process at 2.5 mN. When the indenter reached the graphite area, the indentation depth increased. b) Apparent COF and indentation depth as a function of sliding distance at 2.5mN [71].	56
Figure 13:	a) Wear process at 5 mN. When the indenter penetrated the graphite, matrix would have been reached. b) Apparent COF and indentation depth as a function of sliding distance at 5mN [71].	56

Figure 14: Schematic diagram of the scratch test performed by Mendas and Benayoun [72].....	57
Figure 15: Wear mechanism: matrix behavior at different graphite depths [72].....	57
Figure 16: a) William Crookes. b) Michael Faraday [79].....	59
Figure 17: Radiant Matter is deflected by the action of a magnet [77].....	61
Figure 18: Relationship between 1879 Crookes tube and modern plasma nitriding unit. a) Crookes tube [77]. b) Schematic of a plasma nitriding source [10]. c) Glow discharge ion nitriding mechanisms (Koebel's models) [10].....	63
Figure 19: Specimen preparation scheme. In-lab textured flat specimens.....	65
Figure 20: Specimen preparation scheme. Case-study: as-honed surface. Section on the right illustrates the cylinder block application in the engine, including the crankshaft (CS) and piston, whose sliding direction (SD) is indicated.	66
Figure 21: Taylor Hobson, Talysurf CCI 3-D Coherence Correlation Interferometer.	67
Figure 22: Roughness characterization scheme. In-lab textured flat specimens. On the textured surface plane, the measurements begin at x-coordinate 5 mm and y-coordinate 5 mm. The five 1.6 x 1.6 mm areal measurements (s1-s5) are 2 mm distant one from each other.	68
Figure 23: 3-D profile and the respective material ratio curve. In-lab textured flat specimens. The roughness parameters identified by Sk, Spk, Svk are extracted from the curve.....	68
Figure 24: Roughness characterization scheme. As-honed surface specimen (case-study). Comparative 3-D interference roughness results were obtained from two sampling areas: (i) 1.6 x 1.6 mm and (ii) 0.3 x 0.3 mm.	69
Figure 25: Flowchart of the specimen preparation and SPN treatments. In-lab textured flat specimens.	70
Figure 26: The plasma treatment unit of Plasma Laboratory of the Department of Metallurgical and Materials Engineering of the University of São Paulo.....	71
Figure 27: Flowchart of the specimen preparation and SPN treatment. Case-study: As-honed surface specimen.	72
Figure 28: Precision abrasive cutting machine. Detail: section location guided by laser.....	73
Figure 29: Oxford WDX600 spectrometer coupled to a Cambridge Stereoscan 440 scanning electron microscope of LCT-USP. Nitrogen was measured by using synthetic LSM60 crystal.	74
Figure 30: A wavelength-dispersive spectroscopy (WDS) energy scan overlain on an energy-dispersive (EDS) spectroscopy spectrum, both acquired from monazite ([La,Ce,Pr,Nd,Sm,Gd]PO ₄). Compared to EDS, the better resolution and peak-to-background ratios of WDS clearly reveal which elements are present in a sample [94].....	74
Figure 31: Scanning electron microscope model ZEISS-EV0-MA10.....	76

Figure 32: Microhardness tester.....	77
Figure 33: CETR-UMT Micro scratch tester.	78
Figure 34: 2-D acquisition of Sp and Ss from the 3-D interference profile.....	79
Figure 35: The coordinates of measuring points. $ FN = 1.8x+1$ (N).....	80
Figure 36: a) Typical groove showing pile up (green zone). b) Idealized representation of the groove. Adapted from Buttery and Archard [95] by Franco and Sinatora [76].....	80
Figure 37: Flowchart of methods. In-lab textured flat specimens.....	82
Figure 38: Flowchart of methods. Case-study: As-honed surface specimen.	83
Figure 39: a) 3-D profile of the textured surface plane. The color scale indicates the resulting heights from valley to peak. b) Sq and Sa parameters results calculated by TalyMap 3-D software. c) Material ratio curve and respective Sk, Spk, Svk, Sr1, Sr2 parameters (d) extracted from the curve. In-lab textured flat specimen E1 in the initial condition (before SPN treatment).....	84
Figure 40: Minitab One-Way ANOVA Summary Report. Test for Sq parameter, before experiments.....	86
Figure 41: Minitab One-Way ANOVA Summary Report. Test for Sa parameter, before experiments.....	86
Figure 42: Minitab One-Way ANOVA Diagnostic Report. Test for Sq parameter, before experiments.....	87
Figure 43: Minitab One-Way ANOVA Diagnostic Report. Test for Sa parameter, before experiments.....	87
Figure 44: Experiment E1 (400 oC 4 h). Sample 01 (s1) - coordinates x, y = 5.0, 5.0 mm, sampling area = 1.6 x 1.6 μm . 3-D surface profile and material ratio curve. Conditions before (a) and after treatment (b).	88
Figure 45: Experiment E2 (400 oC 2 h). Sample 01 (s1) - coordinates x, y = 5.0, 5.0 mm, sampling area = 1.6 x 1.6 μm . 3-D surface profile and material ratio curve. Conditions before (a) and after treatment (b).	89
Figure 46: Experiment E3 (350 oC 4 h). Sample 01 (s1) - coordinates x, y = 5.0, 5.0 mm, sampling area = 1.6 x 1.6 μm . 3-D surface profile and material ratio curve. Conditions before (a) and after treatment (b).	90
Figure 47: Experiment E4 (350 oC 2 h). Sample 01 (s1) - coordinates x, y = 5.0, 5.0 mm, sampling area = 1.6 x 1.6 μm . 3-D surface profile and material ratio curve. Conditions before (a) and after treatment (b).	91
Figure 48: Boxplot of experiment results, before and after treatment. Spk roughness.....	93
Figure 49: Boxplot of experiment results, before and after treatment. Peak material ratio component Sr1.	94
Figure 50: Boxplot of experiment results, before and after treatment. Sk roughness.....	95
Figure 51: Boxplot of experiment results, before and after treatment. Svk roughness.....	96

Figure 52: Boxplot of experiment results, before and after treatment. Sr ₂ roughness.	96
Figure 53: Before/After capability comparison. Spk roughness. Experiment E1 400C 4h. ...	97
Figure 54: Before/After capability comparison. Spk roughness. Experiment E2 400C 2h. ...	97
Figure 55: Before/After capability comparison. Spk roughness. Experiment E3 350C 4h. ...	98
Figure 56: Before/After capability comparison. Spk roughness. Experiment E4 350C 2h. ...	98
Figure 57: Summary of average (Mean) peak roughness Spk with respective standard deviation.	99
Figure 58: N-content (wt%) as a function of distance from surface (μm) measured via Wavelength-Dispersive Spectroscopy (WDS) microanalysis. Avg values +/- std dev, n = 5. In-lab textured flat surface, E1-400C-4h.	100
Figure 59: WDS spectrum, Nitrogen peaks. Quantitative analysis. In-lab textured flat surface, E1-400C-4h.	100
Figure 60: N-content (wt%) as a function of distance from surface (μm) measured via Wavelength-Dispersive Spectroscopy (WDS) microanalysis. Avg values +/- std dev, n = 5. In-lab textured flat surface, E2-400C-2h.	101
Figure 61: WDS spectrum, Nitrogen peaks. Quantitative analysis. In-lab textured flat surface, E2-400C-2h.	101
Figure 62: N-content (wt%) as a function of distance from surface (μm) measured via Wavelength-Dispersive Spectroscopy (WDS) microanalysis. Avg values +/- std dev, n = 5. In-lab textured flat surface, E3-350C-4h.	102
Figure 63: WDS spectrum, Nitrogen peaks. Quantitative analysis. In-lab textured flat surface, E3-350C-4h.	102
Figure 64: N-content (wt%) as a function of distance from surface (μm) measured via Wavelength-Dispersive Spectroscopy (WDS) microanalysis. Avg values +/- std dev, n = 5. In-lab textured flat surface, E4-350C-2h.	103
Figure 65: WDS spectrum, Nitrogen peaks. Quantitative analysis. In-lab textured flat surface, E4-350C-2h.	103
Figure 66: N-content (wt%) as a function of distance from surface (μm) measured via WDS microanalysis. Avg +/- std dev, n = 5. In-lab textured flat surface. Combined chart: E1-400C-4h, E2-400C-2h, E3-350C-4h, E4-350-2h.	104
Figure 67: N-content (wt%) at the surface (zero μm distance) measured via WDS microanalysis. Avg +/- std dev, n = 5. In-lab textured flat surface. Combined chart: E1-400C-4h, E2-400C-2h, E3-350C-4h, E4-350-2h.	104
Figure 68: XRD diffractogram of the textured surface treated in the condition E1-C400h4.	106
Figure 69: XRD diffractogram of the textured surface treated in condition E2-C400h2.	107
Figure 70: XRD diffractogram of the textured surface treated in condition E3-C350h4.	107
Figure 71: XRD diffractogram of the textured surface treated in condition E4-C350h2.	108

Figure 72: XRD diffractogram of the textured surface in condition Raw, before SPN (Baseline sample/material same as case-study).....	108
Figure 73: XRD combined 3-D diffractogram of the textured surface in the conditions E1-C400h4, E2-C400h2, E3-C350h4 and E4-C350h2 and Raw.....	109
Figure 74: XRD combined diffractogram of the textured surface in the conditions E1-C400h4, E2-C400h2, E3-C350h4, E4-C350h2, and Raw.	110
Figure 75: Experiment E1 (400 oC 4 h). Comparative Scanning Electronic Microscopy (SEM) images. Conditions (a) Before SPN, (b) After SPN - secondary electron analysis, and (c) After SPN - backscattered electron analysis.....	111
Figure 76: Experiment E2 (400 oC 2 h). Comparative Scanning Electronic Microscopy (SEM) images. Conditions (a) Before SPN, (b) After SPN - secondary electron analysis, and (c) After SPN - backscattered electron analysis.....	112
Figure 77: Experiment E3 (350 oC 4 h). Comparative Scanning Electronic Microscopy (SEM) images. Conditions (a) Before SPN, (b) After SPN - secondary electron analysis, and (c) After SPN - backscattered electron analysis.....	113
Figure 78: Experiment E4 (350 oC 2 h). Comparative Scanning Electronic Microscopy (SEM) images. Conditions (a) Before SPN, (b) After SPN - secondary electron analysis, and (c) After SPN - backscattered electron analysis.....	114
Figure 79: Microhardness (HV 0.01) on the surface (zero μm distance) measured with 10 gf. Avg values +/- std dev, n = 5. In-lab textured flat surface. Combined chart: Raw, E1-C400h4, E2-C400h2, E3-C350h4, E4-C350h2.	115
Figure 80: Examples of single indentation measured through SEM. Measurements carried out preferably on plateau regions. a) Raw, b) E1-C400h4, c) E2-C400h2, d) E3-C350h4, e) E4-C350h2. Significant hardness contrast found between raw and treated samples. SPN time has not significantly affected the range of hardness response values.	116
Figure 81: Boxplot of experiment results, before and after treatment. Microhardness (HV 0.01).	117
Figure 82: Minitab One-Way ANOVA Summary Report. Test for Microhardness, before and after treatment.	118
Figure 83: Minitab One-Way ANOVA Diagnostic Report. Test for Microhardness, before and after treatment.	118
Figure 84: Instrumented linear sclerometry test. a) Top [slightly-tilted] view of the 3-D profile of the textured surface plane. Experiment E1 (400 oC 4 h). In-lab textured flat specimen. 1N pre-load applied during 10s at initial distance. Next, indenter was linearly moved increasing load, 1N to 10N, with velocity of 0.028 mm/s, resulting in the scratch of 5 mm in length. The color scale in the side indicates the resulting heights from valley to peak. b) Front [30o tilted] view of the 3-D scratch section at 1 mm distance. c-e) Similar as 'b' images at 2 mm, 3 mm and 4 mm distances, respectively, highlighting the	

progressive evolution of the sclerometry groove. The region 0-1 mm (test stabilization zone) was not considered in data analysis.....	120
Figure 85: Instrumented linear sclerometry test. 2-D profilograms of the textured surface and resulting sclerometry groove. Experiment E1 (400 oC 4 h). In-lab textured flat specimen. Section locations corresponding to previous 3-D profile images. All the graphs: test direction towards the plane of the page. a-d) “Groove area” (Ss) - in red and “pile-up area” (Sp) - in green, at distances from beginning of test: 1 mm, 2 mm, 3 mm and 4 mm. Ss and Sp computed values reported along with each graph. In addition, punctual measurement of depth (dh) is informed.	121
Figure 86: Instrumented linear sclerometry test. a) Top [slightly-tilted] view of the 3-D profile of the textured surface plane. Experiment E2 (400 oC 2 h). In-lab textured flat specimen.....	122
Figure 87: Instrumented linear sclerometry test. 2-D profilograms of the textured surface and resulting sclerometry groove. Experiment E2 (400 oC 2 h). In-lab textured flat specimen.....	123
Figure 88: Instrumented linear sclerometry test. a) Top [slightly-tilted] view of the 3-D profile of the textured surface plane. Experiment E3 (350 oC 4 h). In-lab textured flat specimen.....	124
Figure 89: Instrumented linear sclerometry test. 2-D profilograms of the textured surface and resulting sclerometry groove. Experiment E3 (350 oC 4 h). In-lab textured flat specimen.....	125
Figure 90: Instrumented linear sclerometry test. a) Top [slightly-tilted] view of the 3-D profile of the textured surface plane. Experiment E4 (350 oC 2 h). In-lab textured flat specimen.....	126
Figure 91: Instrumented linear sclerometry test. 2-D profilograms of the textured surface and resulting sclerometry groove. Experiment E4 (350 oC 2 h). In-lab textured flat specimen.....	127
Figure 92: Instrumented linear sclerometry test. a) Top [slightly-tilted] view of the 3-D profile of the textured surface plane in the condition Raw, before SPN treatment (Baseline raw sample). In-lab textured flat specimen..	128
Figure 93: Instrumented linear sclerometry test. 2-D profilograms of the textured surface and resulting sclerometry groove, in the condition Raw, before SPN treatment (Baseline raw sample). In-lab textured flat specimen..	129
Figure 94: Sclerometry test. Resulting scratch depth (dh) of condition E1-C400h4 compared to Raw (baseline).	130
Figure 95: Sclerometry test. Resulting scratch depth (dh) of condition E2-C400h2 compared to Raw (baseline).	131
Figure 96: Sclerometry test. Resulting scratch depth (dh) of condition E3-C350h4 compared to Raw (baseline).	131

Figure 97: Sclerometry test. Resulting scratch depth (dh) of condition E4-C400h2 compared to Raw (baseline).	132
Figure 98: Sclerometry test. Combined chart of the resulting scratch depth (dh) of conditions E1-C400h4, E2-C400h2, E3-C350h4 and E4-C350h2 compared to Raw (baseline).	132
Figure 99: Sclerometry test. Resulting “groove area” (Ss) of condition E1-C400h4 compared to Raw (baseline).	133
Figure 100: Sclerometry test. Resulting “groove area” (Ss) of condition E2-C400h2 compared to Raw (baseline).	133
Figure 101: Sclerometry test. Resulting “groove area” (Ss) of condition E3-C350h4 compared to Raw (baseline).	133
Figure 102: Sclerometry test. Resulting “groove area” (Ss) of condition E4-C350h2 compared to Raw (baseline).	134
Figure 103: Sclerometry test. Combined chart of the resulting “groove area” (Ss) of conditions E1-C400h4, E2-C400h2, E3-C350h4 and E4-C350h2 compared to Raw (baseline).	134
Figure 104: Sclerometry test. Resulting “pile-up area” (Sp) of condition E1-C400h4 compared to Raw (baseline).	135
Figure 105: Sclerometry test. Resulting “pile-up area” (Sp) of condition E2-C400h2 compared to Raw (baseline).	135
Figure 106: Sclerometry test. Resulting “pile-up area” (Sp) of condition E3-C350h4 compared to Raw (baseline).	135
Figure 107: Sclerometry test. Resulting “pile-up area” (Sp) of condition E4-C350h2 compared to Raw (baseline).	136
Figure 108: Sclerometry test. Combined chart of the resulting “pile-up area” (Sp) of conditions E1-C400h4, E2-C400h2, E3-C350h4 and E4-C350h2 compared to Raw (baseline)	136
Figure 109: Instrumented linear sclerometry test. Side-by-side comparison between condition (a1-c1) Raw (before SPN) and (a2-c2) E4-C350h2. a1-2) Top [slightly-tilted] view of the 3-D profile of the textured surface plane. b1-b2) Front [30o tilted] view of the 3-D scratch section. c1-c2) Section locations corresponding to 3-D profile images. “Groove area” (Ss) - in red and “pile-up area” (Sp) - in green, at distances from beginning of test: 1 mm, 2 mm, 3 mm and 4 mm. Respective Ss, Sp, dh values are informed along with each graph. The region 0-1 mm (test stabilization zone) was not considered in data analysis. In-lab textured flat specimen.	138
Figure 110: Instrumented linear sclerometry test. Scanning Electron Microscopy view of the textured surface plane and resulting scratch track, in the condition Raw, before SPN treatment (Baseline raw sample).	140
Figure 111: Instrumented linear sclerometry test. Scanning Electron Microscopy view of the textured surface plane and resulting scratch track, in the condition Raw,	

<p>before SPN treatment (Baseline raw sample). All the images: test direction from left to right. a-e) Detailed view at different distances from beginning of test: 1 mm, 2 mm, 3 mm, 4 mm and 5 mm. f) Magnified view (arbitrary distance) showing plastic deformation in the interface region to the texturing grooves: a general aspect found along the scratch length of the non-treated specimen.</p>	141
<p>Figure 112: Instrumented linear sclerometry test. Scanning Electron Microscopy view of the textured surface plane and resulting scratch track. Experiment E1 (400 oC 4 h).</p>	142
<p>Figure 113: Instrumented linear sclerometry test. Scanning Electron Microscopy view of the textured surface plane and resulting scratch track. Experiment E1 (400 oC 4 h). All the images: test direction from left to right. a-e) Detailed view at different distances from beginning of test: 1 mm, 2 mm, 3 mm, 4 mm and 5 mm. Microcracks found preferably in graphite regions. f) Magnified view (detail 2C of Fig. b) showing tensile microcracks at distance around 2 mm, in material matrix region, i.e., out of graphite pocket surroundings.....</p>	143
<p>Figure 114: Instrumented linear sclerometry test. Scanning Electron Microscopy view of the textured surface plane and resulting scratch track. Experiment E2 (400 oC 2 h).</p>	144
<p>Figure 115: Instrumented linear sclerometry test. Scanning Electron Microscopy view of the textured surface plane and resulting scratch track. Experiment E2 (400 oC 2 h). All the images: test direction from left to right. a-e) Detailed view at different distances from beginning of test: 1 mm, 2 mm, 3 mm, 4 mm and 5 mm. Microcracks found preferably in graphite regions. f) Magnified view (detail 2C of Fig. b) showing tensile microcracks at distance around 2 mm, in material matrix region, i.e., out of graphite pocket surroundings.....</p>	145
<p>Figure 116: Instrumented linear sclerometry test. Scanning Electron Microscopy view of the textured surface plane and resulting scratch track. Experiment E3 (350 oC 4 h).</p>	146
<p>Figure 117: Instrumented linear sclerometry test. Scanning Electron Microscopy view of the textured surface plane and resulting scratch track. Experiment E3 (350 oC 4 h). All the images: test direction from left to right. a-e) Detailed view at different distances from beginning of test: 1 mm, 2 mm, 3 mm, 4 mm and 5 mm. f) Magnified view (detail 1C of Fig. a) showing tensile microcracks at distance around 1 mm, in material matrix region, i.e., out of graphite pocket surroundings.</p>	147
<p>Figure 118: Instrumented linear sclerometry test. Scanning Electron Microscopy view of the textured surface plane and resulting scratch track. Experiment E4 (350 oC 2 h).</p>	148
<p>Figure 119: Instrumented linear sclerometry test. Scanning Electron Microscopy view of the textured surface plane and resulting scratch track. Experiment E4 (350 oC 2 h). All the images: test direction from left to right. a-e) Detailed view at different distances from beginning of test: 1 mm, 2 mm, 3 mm, 4 mm and 5</p>	

mm. f) Magnified view (detail 1C of Fig. a) showing tensile microcracks at distance around 1 mm, in material matrix region, i.e., out of graphite pocket surroundings.	149
Figure 120: Condition E1-C400h4 and E2-C400h2. SEM view of the textured surface at the distance $D = 2$ mm from beginning of test. Microcracks nucleated in the matrix, at similar orientation angle. Region free from graphite flakes. Same regions as shown in the previous sequences of images of Figure 113 and Figure 115.	150
Figure 121: Condition Raw, before SPN treatment. SEM view of the textured surface at the starting distance from beginning of test, $D = 0$ mm. At this point, 1N pre-load was applied. Compared to larger distances (Figure 111), minor plastic deformation was noticed. Texturing grooves and graphite pocket are suitably preserved.	151
Figure 122: Condition Raw, before SPN treatment. SEM view of the textured surface at the middle distance from beginning of test. A graphite lamella is partially covered by plastically deformed material. It was not found any sign of micro crack nucleated from the matrix or in association to a graphite interface.	151
Figure 123: Condition E4-C350h2. SEM view of the textured surface at the ending distance $D = 5$ mm of test. Microcracks nucleated in association to a graphite pocket interface (graphite tip), which acts as a stress concentrator. On the right, microcracks nucleated in the material matrix region.	152
Figure 124: Condition E2-C400h2. SEM view of the textured surface at the distance $D = 2$ mm from beginning of test. Sequence of parallel microcracks nucleated in the matrix. Region free from graphite flakes.	153
Figure 125: Condition E3-C350h4. SEM view of the textured surface at the ending distance $D = 5$ mm of test, where the normal load achieved its maximum intensity. The image field is filled out by a cluster of microcracks. Region free from graphite flakes.	153
Figure 126: Apparent COF of the textured surface in condition Raw, before SPN treatment (Baseline sample). Avg values +/- std dev, $n = 5$. In-lab textured flat specimen. 1N pre-load applied during 10s. Next, indenter was linearly moved increasing load, 1N to 10N, with velocity of 0.028 mm/s, during 180 s, resulting in the scratch of 5 mm in length. The test stabilization was comprehended into first 40 s (dashed line) and is not considered in data analysis.	155
Figure 127: Apparent COF of the textured surface treated in condition E1-C400h4. Avg values +/- std dev, $n = 5$. In-lab textured flat specimen.	155
Figure 128: Apparent COF of the textured surface treated in condition E2-C400h2. Avg values +/- std dev, $n = 5$. In-lab textured flat specimen.	156
Figure 129: Apparent COF of the textured surface treated in condition E3-C350h4. Avg values +/- std dev, $n = 5$. In-lab textured flat specimen.	156

Figure 130: Apparent COF of the textured surface treated in the condition E4-C350h2. Avg values +/- std dev, n = 5. In-lab textured flat specimen.....	157
Figure 131: Apparent COF of the textured surface. Combined chart: Raw, E1-400C-4h, E2-400C-2h, E3-350C-4h, E4-350-2h. Avg values and respective linear regression line, n = 5. In-lab textured flat specimen.....	157
Figure 132: 3-D interference measurements. Areas of measurement are 1.6 mm x 1.6 mm. a) Before SPN. b) After SPN. a1 and b1) The primary profiles. a2 and b2) Form-removal filtered profiles. a3 and b3) Material ratio curve.....	159
Figure 133: 3-D interference measurements. Areas of measurement are 0.3mm x 0.3mm. a) Before SPN. b) After SPN. a1 and b1) Form-removal filtered profiles. a2 and b2) Material ratio curve.	160
Figure 134: Summary of roughness. Area of measurement 1.6 x 1.6 mm. Spk somewhat increased after SPN. Individual measurements (Case-study). Bar errors correspond to the estimated measurement uncertainty.....	160
Figure 135: Quantitative analysis. N-content (wt%) as a function of distance from surface (μm) measured via Wavelength-Dispersive Spectroscopy (WDS) microanalysis. Average values +/- standard deviation. n = 5. Case-study: as-honed surface, 350C-2h.....	161
Figure 136: WDS spectrum. Quantitative analysis. Case-study: as-honed surface, 350C-2h.....	162
Figure 137: (a) SEM image of the SPN case-study sample: as-honed surface, 350C-2h. The gray cast iron pearlitic matrix and a graphite flake can be seen in the cross section. Nitrided zone was interrupted by the graphite flake. (b) EDS spots 1.1, 1.2 and 1.3 are located in the SPN zone, at 1 μm depth from surface and distant 5 μm from each other. The spots 3 and 4 are located out of the SPN zone, at 3 μm and 5 μm depth from surface, respectively.	163
Figure 138: Qualitative analysis. Estimation of N-content (wt%) as a function of distance from surface (μm) measured via Energy-Dispersive Spectroscopy (EDS) microanalysis. Average value +/- standard deviation (only first point). Case-study: as-honed surface, 350C-2h. Single values at distance 2.0, 3.0 and 5.0 μm for reference only. (informative).....	164
Figure 139: Qualitative analysis. EDS spectrum at 1 μm from surface. Case-study: as-honed surface, 350C-2h. Emission peaks (counts) as a function of energy (keV). The view in detail shows the N-peak qualitatively evidencing that enrichment of nitrogen occurred at 1 μm depth from surface. (informative).....	164
Figure 140: WDS (Quantitative) and EDS (Qualitative) microanalysis of N-concentration. Combined chart: Estimation of N-content (wt%) as a function of distance from surface (μm) measured via Energy-Dispersive Spectroscopy (EDS) microanalysis. Average value +/- standard deviation (only first point) - in gray; N-content (wt%) as a function of distance from surface (μm) measured via Wavelength-Dispersive Spectroscopy (WDS) microanalysis.	

Average values +/- standard deviation. n = 5 - in blue. Case-study: as-honed surface, 350C-2h.....	165
Figure 141: XRD diffractograms of the textured surface in the condition a) before SPN treatment (CS-Raw) and b) after SPN treatment (CS-C350h2). Background filter was applied. Crystallographica Search-Match (CSM) software.....	166
Figure 142: XRD diffractograms of the textured surface in the condition a) before SPN treatment (CS-Raw) and b) after SPN treatment (CS-C350h2). ϵ -nitride (Fe ₃ N) peaks growth and reduction in Fe- α peaks intensity were evidenced through direct comparison between charts. Background filter was not applied. Origin 9.4 software.	166
Figure 143: XRD combined diffractogram of the textured surface in the conditions before SPN treatment (CS-Raw) and after SPN treatment (CS-C350h2). An overlapped view of both diffractograms in single scale.	167
Figure 144: Some ϵ -nitride (Fe ₃ N) peaks obtained from the X-Ray diffractogram LCT-USP 196-2453 of the textured surface in the condition after SPN. a) (110) ϵ -nitride peak. b) (112) ϵ -nitride peak. c) (300) ϵ -nitride peak.....	168
Figure 145: Microhardness (HV 0.01) on the surface (zero μ m distance) measured with 10 gf. Average values +/- standard deviation, n = 10. As-honed surface specimen (case-study). Combined chart: CS-Raw, CS-350-2h.....	169
Figure 146: Dark-field optical microscopy images of the textured surface in condition before (a) and after (b) SPN, with respective Vickers (HV 0.01) indentations. Honing grooves of various dimensions are visible in both images.	170
Figure 147: Micro deformations in the pearlitic matrix induced by the honing operation. As-honed surface specimen (case-study), condition CS-Raw. A graphite flake is shown along with adjacent deformed pearlite region.	171
Figure 148: Micro deformations in the pearlitic matrix induced by the honing operation. As-honed surface specimen (case-study), in the condition CS-Raw (before SPN).....	171
Figure 149: 2-D acquisition of Sp and Ss from the 3-D interference profile.	172
Figure 150: Progressive linear sclerometry test. Top [tilted] view of the 3-D profile of the surface in conditions before (CS-Raw) and after SPN treatment (CS-C350h2). Case-Study: As-honed surface specimen. Pre-load: 1 N / 10 s, linear increasing load: 1-10 N, 0.028 mm/s. Resulting scratch: 5 mm in length. Color scale indicates heights from valley to peak (primary form not filtered). Profiles at different distance ranges, highlighting the progressive evolution of the sclerometry groove. Honing texture preserved after SPN. Similar scratch appearance between the two conditions, with apparent higher level of plastic flowed (pile-up) material in condition before SPN.	173
Figure 151: Instrumented linear sclerometry test. 2-D profilograms of the textured surface and resulting sclerometry groove, in the condition before SPN treatment (CS-Raw). Case-Study: As-honed surface specimen. Section locations corresponding to previous 3-D profile images. All the graphs: test direction	

<p>towards the plane of the page. a-d) “Groove area” (Ss) - in red and “pile-up area” (Sp) - in green, at distances from beginning of test: 1 mm, 2 mm, 3 mm, and 4 mm. Ss and Sp computed values reported along with each graph. In addition, punctual measurement of depth (dh) is informed.</p>	174
<p>Figure 152: Instrumented linear sclerometry test. 2-D profilograms of the textured surface and resulting sclerometry groove, in the condition after SPN treatment (CS-C350h2). Case-Study: As-honed surface specimen. Section locations corresponding to previous 3-D profile images. All the graphs: test direction towards the plane of the page. a-d) “Groove area” (Ss) - in red and “pile-up area” (Sp) - in green, at distances from beginning of test: 1 mm, 2 mm, 3 mm, and 4 mm. Ss and Sp computed values reported along with each graph. In addition, punctual measurement of depth (dh) is informed.</p>	175
<p>Figure 153: Sclerometry test. Case-Study: As-honed surface specimen. Resulting scratch depth (dh) of condition CS-C350h2 compared to CS-Raw (baseline). n = 1, error bars corresponding to the estimated uncertainty (informative).</p>	176
<p>Figure 154: Sclerometry test. Case-Study: As-honed surface specimen. Resulting “groove area” (Ss) of condition CS-C350h2 compared to CS-Raw (baseline). n = 1, error bars corresponding to the estimated uncertainty (informative).</p>	177
<p>Figure 155: Sclerometry test. Case-Study: As-honed surface specimen. Resulting “pile-up area” (Sp) of condition CS-C350h2 compared to CS-Raw (baseline). n = 1, error bars corresponding to the estimated uncertainty (informative).</p>	177
<p>Figure 156: Instrumented linear sclerometry test. Scanning Electron Microscopy view of the textured surface plane and resulting scratch track, in the condition CS-C350h2 compared to CS-Raw (baseline).</p>	179
<p>Figure 157: SEM view of the textured surface and resulting scratch track, condition CS-C350h2 compared to CS-Raw (baseline). Test direction (t.d.) from left to right. a-e) Detailed view at different distances: 1-5 mm.</p>	180
<p>Figure 158 (cont): SEM view of the textured surface and resulting scratch track, condition CS-C350h2 compared to CS-Raw (baseline). All samples: Test direction (t.d.) from left to right. a-e) Detailed view at different distances: 1-5 mm.</p>	181
<p>Figure 159: Magnified view (detail 1C of previous figure) showing tensile microcracks at distance around 1 mm, in material matrix region. SEM image. Test direction (t.d.) from left to right. Case-study, CS-C350h2.</p>	182
<p>Figure 160: Apparent COF of the textured surface in condition Raw, before SPN treatment. Case study: As-honed surface specimen.</p>	183
<p>Figure 161: Apparent COF of the textured surface in condition CS-C350h2. Case study: As-honed surface specimen. Comparing to raw condition, the apparent COF decreased after SPN treatment.</p>	183
<p>Figure 162: Apparent COF of the textured surface. Combined chart: CS-Raw and CS-C350h2, including the respective linear regression line. As-honed surface specimen.</p>	184

Figure A1: Experiment E1 (400 oC 4 h). Sample 02 (s2) - coordinates x, y = 7.0, 5.0 mm, sampling area = 1.6 x 1.6 μ m. 3-D surface profile and material ratio curve.....	194
Figure A2: Experiment E1 (400 oC 4 h). Sample 03 (s3) - coordinates x, y = 9.0, 5.0 mm, sampling area = 1.6 x 1.6 μ m. 3-D surface profile and material ratio curve.....	195
Figure A3: Experiment E1 (400 oC 4 h). Sample 04 (s4) - coordinates x, y = 11.0, 5.0 mm, sampling area = 1.6 x 1.6 μ m. 3-D surface profile and material ratio curve.....	196
Figure A4: Experiment E1 (400 oC 4 h). Sample 05 (s5) - coordinates x, y = 13.0, 5.0 mm, sampling area = 1.6 x 1.6 μ m. 3-D surface profile and material ratio curve.....	197
Figure A5: Experiment E2 (400 oC 2 h). Sample 02 (s2) - coordinates x, y = 7.0, 5.0 mm, sampling area = 1.6 x 1.6 μ m. 3-D surface profile and material ratio curve.....	198
Figure A6: Experiment E2 (400 oC 2 h). Sample 03 (s3) - coordinates x, y = 9.0, 5.0 mm, sampling area = 1.6 x 1.6 μ m. 3-D surface profile and material ratio curve.....	199
Figure A7: Experiment E2 (400 oC 2 h). Sample 04 (s4) - coordinates x, y = 11.0, 5.0 mm, sampling area = 1.6 x 1.6 μ m. 3-D surface profile and material ratio curve.....	200
Figure A8: Experiment E2 (400 oC 2 h). Sample 05 (s5) - coordinates x, y = 13.0, 5.0 mm, sampling area = 1.6 x 1.6 μ m. 3-D surface profile and material ratio curve.....	201
Figure A9: Experiment E3 (350 oC 4 h). Sample 02 (s2) - coordinates x, y = 7.0, 5.0 mm, sampling area = 1.6 x 1.6 μ m. 3-D surface profile and material ratio curve.....	202
Figure A10: Experiment E3 (350 oC 4 h). Sample 03 (s3) - coordinates x, y = 9.0, 5.0 mm, sampling area = 1.6 x 1.6 μ m. 3-D surface profile and material ratio curve.....	203
Figure A11: Experiment E3 (350 oC 4 h). Sample 04 (s4) - coordinates x, y = 11.0, 5.0 mm, sampling area = 1.6 x 1.6 μ m. 3-D surface profile and material ratio curve.....	204
Figure A12: Experiment E3 (350 oC 4 h). Sample 05 (s5) - coordinates x, y = 13.0, 5.0 mm, sampling area = 1.6 x 1.6 μ m. 3-D surface profile and material ratio curve.....	205
Figure A13: Experiment E4 (350 oC 2 h). Sample 02 (s2) - coordinates x, y = 7.0, 5.0 mm, sampling area = 1.6 x 1.6 μ m. 3-D surface profile and material ratio curve.....	206
Figure A14: Experiment E4 (350 oC 2 h). Sample 03 (s3) - coordinates x, y = 9.0, 5.0 mm, sampling area = 1.6 x 1.6 μ m. 3-D surface profile and material ratio curve.....	207
Figure A15: Experiment E4 (350 oC 2 h). Sample 04 (s4) - coordinates x, y = 11.0, 5.0 mm, sampling area = 1.6 x 1.6 μ m. 3-D surface profile and material ratio curve.....	208
Figure A16: Experiment E4 (350 oC 2 h). Sample 05 (s5) - coordinates x, y = 13.0, 5.0 mm, sampling area = 1.6 x 1.6 μ m. 3-D surface profile and material ratio curve.....	209

LIST OF TABLES

Table 1:	Summary of the review on the wear of ICE cylinder bores.	40
Table 2:	Type of characterization analysis performed by regions of the cylinder bore.	45
Table 3:	Wear severity level.....	47
Table 4:	Surface observations category.....	48
Table 5:	Some works on the nitriding of GCI, including the basic process and respective temperature.	49
Table 6:	Surface microhardness of cast iron samples reported by [60], after gas nitriding. Avg \pm StdDev (Values originally reported in GPa were converted to HV 0.1).	50
Table 7:	Matrix of Experiments.	70
Table 8:	Identification of specimens.	71
Table 9:	Corresponding load by indenter distance.....	79
Table 10:	Sq and Sa roughness parameters of the textured samples.....	85
Table 11:	Distribution height parameters, before and after treatments. Condition E1- 400C-4h.....	92
Table 12:	Distribution height parameters, before and after treatments. Condition E2- 400C-2h.....	92
Table 13:	Distribution height parameters, before and after treatments. Condition E3- 350C-4h.....	92
Table 14:	Distribution height parameters, before and after treatments. Condition E4- 350C-2h.....	92
Table 15:	Quantitative WDS microanalysis. Data group of N-content (wt%) as a function of distance from surface (μm), 5 measurements per distance. In-lab textured flat surface. Condition E1-400C-4h.....	105
Table 16:	Quantitative WDS microanalysis. Condition E2-400C-2h.....	105
Table 17:	Quantitative WDS microanalysis. Condition E3-350C-4h.....	105
Table 18:	Quantitative WDS microanalysis. Condition E4-350C-2h.....	105
Table 19:	Data group of Microhardness (HV 0.01) on the surface (zero μm distance) measured with 10 gf, n = 5. In-lab textured flat surface. Conditions: Raw, Raw, E1-C400h4, E2-C400h2, E3-C350h4, E4-C350h2.....	117

Table 20:	Data group of “Groove area” (Ss), “pile-up area” (Sp) and depth (dh), at distances/load of: 1 mm/2.8 N, 2 mm/4.6 N, 3 mm/6.4 N and 4 mm/8.2 N, n = 3. In-lab textured flat surface. Condition E1-400C-4h.	137
Table 21:	Data group of “Groove area” (Ss), “pile-up area” (Sp) and depth (dh). Condition E2-400C-2h.	137
Table 22:	Data group of “Groove area” (Ss), “pile-up area” (Sp) and depth (dh). Condition E3-350C-4h.	137
Table 23:	Data group of “Groove area” (Ss), “pile-up area” (Sp) and depth (dh). Condition E4-350C-2h.	137
Table 24:	Data group of “Groove area” (Ss), “pile-up area” (Sp) and depth (dh). Condition Raw (baseline).	137
Table 25:	Assessment of scratch damage features (microcracks in material matrix) in increasing normal load test. Qualitative Scale levels: L0 = not observed, L1 = Low, L2 = Medium, L3 = High.	154
Table 26:	Summary of roughness results. Case-study.	158
Table 27:	N-content (wt%) as a function of distance from surface (μm) via Wavelength-Dispersive Spectroscopy (WDS) microanalysis. Quantitative analysis. Case-study: as-honed surface. Individual values.	165
Table 28:	N-content (wt%) as a function of distance from surface (μm) via Energy-Dispersive Spectroscopy (EDS) microanalysis. Qualitative analysis. Case-study: as-honed surface. Individual values. (informative)	165
Table 29:	Data group of Microhardness (HV 0.01) on the surface (zero μm distance) measured with 10 gf, n = 10. As-honed surface specimen (case-study). Conditions: CS-Raw, CS-350-2h.	170
Table 30:	Synthesis Board.	188

LIST OF ACRONYMS

2-D	two dimensions
3-D	three dimensions
AFM	atomic force microscopy
ANOVA	analysis of variance
ASTM	American Society for Testing and Materials
ATM	abrasive cutting machine
Avg	average (statistical Mean)
BDC	bottom dead center
BSD-SEM	Backscattered scanning electron microscope image
COF	coefficient of friction
CS	case study
cs	crankshaft
CSM	Crystallographica Search-Match
dh	depth
DLC	diamond-like carbon
EDS	energy-dispersive (X-ray) spectroscopy
FIB	focused ion beam
GCI	gray cast iron
GDS	glow-discharge spectroscopy
GM	General Motors
HB	Brinell hardness
HV	Vickers hardness
ICDD	International Centre for Diffraction Data
ICE	internal combustion engine
IQR	interquartile range
LW	localized wear
LxWxH	length x width x height
MS	mid stroke
OCR	oil control ring
Pp	process performance
Ppk	process performance index
Q1	first quartile

Q3	third quartile
Ra	arithmetical mean deviation [of the assessed roughness profile] (ISO 4287)
RMS	root mean square
Rq	root mean square deviation [of the assessed roughness profile] (ISO 4287)
Sa	arithmetical mean height [of the scale limited surface] (ISO 25178-2)
SD	sliding direction
SEM	scanning electronic microscopy
SI	spark ignition
Sk	core height: distance between the highest and lowest level of the core surface (ISO 25178-2); core roughness
Sp	pile-up area
Spk	reduced peak height: average height of the protruding peaks above the core surface (ISO 25178-2); peak roughness
SPN	shallow plasma nitriding
Sq	root mean square height [of the scale-limited surface] (ISO 25178-2)
Sr1	material ratio (Sr1 or Smr1): (peaks) ratio of the area of the material at the intersection line which separates the protruding hills from the core surface to the evaluation area (ISO 25178)
Sr2	material ratio (Sr2 or Smr2): (dales) ratio of the area of the material at the intersection line which separates the protruding dales from the core surface to the evaluation area (ISO 25178)
Ss	groove area
StdDev	(or stdev) standard deviation
Svk	reduced dale height: average height of the protruding dales below the core surface (ISO 25178); valley roughness
t.d.	(scratching) test direction
TDC	top dead center
TEM	transmission electron microscopy
USP	University of São Paulo
UW	unworn
Λ	film thickness ratio or lambda ration
WDS	wavelength-dispersive (X-ray) spectroscopy
WOT	wide open throttle
XRD	X-ray diffractometry
σ^*	composite RMS roughness

CONTENTS

1. Introduction	032
1.1. Motivation	032
1.2. Justification	032
1.3. Proposal	034
1.4. Objectives and approach	034
2. Literature review and research fundamentals	036
2.1. On the wear of internal combustion engine cylinders	036
2.1.1. Contextual research on the wear of ICE cylinders	044
2.2. On the nitriding of pearlitic gray cast iron	049
2.2.1. Literature review on the nitriding of pearlitic gray cast iron	050
2.2.2. Development of a nitrided zone in pearlitic matrix	051
2.2.3. On the nitrogen concentration and carbon redistribution	052
2.2.4. On the Fe ₃ N nitride formation	054
2.3. Instrumented linear sclerometry test applied in GCI	055
2.4. On radiant matter: plasmas	058
2.4.1. “A brief review on the radiant matter: plasma”	058
2.4.2. Fundamentals of plasma physics	061
3. Materials and experimental procedures	064
3.1. Specimen preparation methods	064
3.1.1. In-lab textured flat specimens	064
3.1.2. Case-study: As-honed surface specimen	065
3.2. Material	066
3.3. Roughness characterization	067
3.3.1. Roughness of the in-lab textured flat specimens	067

3.3.2.	Roughness of the as-honed surface specimen (case-study)	068
3.4.	Shallow Plasma Nitriding (SPN) treatments	069
3.4.1.	SPN treatments of the in-lab textured flat specimens	069
3.4.2.	SPN treatments of the as-honed surface specimen (case-study)	072
3.5.	X-Ray diffraction (XRD) analysis	072
3.6.	N-concentration (wt%) as a function of the distance from the surface	073
3.6.1.	Quantitative analysis of N: Wavelength-dispersive (X-ray) spectroscopy (WDS)	073
3.6.2.	Qualitative analysis of N: Energy-dispersive spectroscopy (EDS)	075
3.7.	Comparative scanning electronic microscopy (SEM) analysis of the surface	076
3.8.	Microhardness analysis	076
3.9.	Instrumented linear sclerometry test	077
3.9.1.	Sclerometry test of the in-lab textured flat specimens	077
3.9.2.	Sclerometry test of the as-honed surface specimen (case-study)	078
3.10.	Sclerometry test results analysis	078
3.10.1.	3-D surface profile, “groove area” (Ss), “pile-up area” (Sp) and depth (dh)	078
3.10.2.	SEM analysis of the scratch and critical damage load	081
3.10.3.	Friction based on sclerometry test	081
3.11.	Flowchart of methods	081
4.	Results and Discussion	084
4.1.	In-lab textured flat specimens	084
4.1.1.	Roughness results	084
4.1.1.2.	Texturing pattern between specimens before treatments	084
4.1.1.2.1.	Statistical analysis of roughness results before SPN using Minitab software	085
4.1.1.3.	Texturing pattern between specimens before and after SPN treatments	087
4.1.1.3.1.	Statistical analysis of roughness results before and after SPN using Minitab	093
4.1.2.	WDS microanalysis of N-concentration	099
4.1.3.	X-Ray diffraction (XRD) analysis	106

4.1.4.	Comparative SEM analysis of the surface	111
4.1.5.	Microhardness analysis	115
4.1.5.1.	Statistical analysis of microhardness results using Minitab	117
4.1.6.	Instrumented linear sclerometry test	119
4.1.6.1.	3-D surface profile, “groove area” (Ss), “pile-up area” (Sp) and depth (dh)	119
4.1.6.2.	SEM analysis of the scratch and critical damage load	139
4.1.6.3.	Friction based on sclerometry test	154
4.2.	Case-study: As-honed surface specimen	158
4.2.1.	Roughness results	158
4.2.2.	WDS and EDS microanalysis of N-concentration	161
4.2.3.	X-Ray diffraction (XRD) analysis	166
4.2.4.	Microhardness analysis	169
4.2.5.	Instrumented linear sclerometry test	172
4.2.5.1.	3-D surface profile, “groove area” (Ss), “pile-up area” (Sp) and depth (dh)	172
4.2.5.2.	SEM analysis of the scratch and critical load approach in case-study	178
4.2.5.3.	Friction based on sclerometry test	182
4.2.6.	Summary of the case-study	184
4.3.	Synthesis	185
4.3.1.	Synthesis board	187
5.	Conclusions	191
6.	Suggestions for future research	193
	Appendix	194
	References	210

1. Introduction

1.1. Motivation

Pearlitic gray cast iron (GCI) is a widely used material for internal combustion engine (ICE) cylinders. It has been applied in liners for Al-alloy blocks and in single-piece (monolithic) GCI blocks. Such extensive usage has been attributed to economic advantages, ease of processing and mainly, the excellent tribology qualities of the GCI.

Demands for reducing pollution gas emission and for ICE power increase imply elevating the combustion pressure. Strategies aiming to reduce the oil consumption and the leakage of gaseous combustion products “blow-by” require actions toward the sealing capacity of the cylinder. For that reason, there is a need for solutions meant to enhance the wear resistance of the system components.

During the Master’s degree research, which was accomplished in the post-graduation program of the School of Engineering of the University of São Paulo, we began to investigate the resulting wear of ICE cylinders after being subjected to a durability test. The study identified characteristics of the wear at different cylinder regions, named: Top-Dead-Center (TDC), Bottom-Dead-Center (BDC), and Mid-Stroke (MS) regions of the cylinder bore [1].

These first findings motivated further literature review on the wear of ICE cylinders along with a background research, which consisted in the coordinated description of the cylinder bore wear features observed experimentally. The product of this work is described in the next chapters and substantiates the significance of studying initiatives to enhance the wear and friction responses of pre-textured surfaces made of cast iron, such as the internal combustion engine cylinders.

1.2. Justification

Textured surfaces of mechanical components can generally be worked through special machining operations. That is the case of the Internal Combustion Engine (ICE) cylinder bores, whose surface is textured by means of an operation known as ‘honing’.

The honing operation is commonly used to obtain surfaces with good functionalities for the ring/liner contact (cross hatch pattern and fine surfaces). The honing tool is composed of a

number of honing stones pressed radially outward. The tool creates a cross hatch pattern by simultaneously rotating and stroking inside the cylinder liner to hone [2].

A number of methods to further increase the wear resistance of gray cast iron (GCI) surfaces have been studied along the past decades. These technologies include, but are not limited to: alloying elements for increasing hardness [3,4], the application of heat treatments [4], and the deposition of surface coatings [4-7].

Heat-treated surfaces (e.g., quenched and tempered; austempered; case hardened) are known to be difficult to machine [8]. Consequently, increasing the wear resistance of cylinder surfaces by means of conventional heat treatment in practice may result in non-feasible alternatives. The addition of alloying elements for increasing hardness presents similar drawback, due to the hard intermetallic phases formed and distributed in the material matrix [3,4]. (Intrinsic) Distortions caused by the required cooling rates is another concern to heat treat a pre-textured surface, such as the ICE cylinder bore case [9]. The deposition of modern coatings in pre-textured cylinder liners has been demonstrated to be a reliable alternative to reduce friction. However, the coating deposition reduces the diameter of a final machined bore, while also affecting the roughness pattern on a micrometric scale [5-7].

A widespread thermochemical treatment that increases the component surface hardness with minimum dimensional alterations is the one known as 'nitriding' process. Since it does not require a phase transformation from ferrite to austenite, nor does it require a further transformation from austenite to martensite. The dimensional change can be restricted to only slight growth due to the volumetric change on the steel surface caused by the nitrogen diffusion. First developed in the early 1900s, the process has been widely used in system components subjected to wear solicitations, with well-recognized feasibility for automotive applications [10,11], e.g., cylinder head valves and piston rings, nitriding coated.

The potential of plasma application as an energy source for hardening ferrous alloys was studied and patented by Fry [10] in the early 1920s in Germany, and by Bason in 1928 [12,13]. The so-called plasma nitriding methods were developed and patented by Wehnheldt and Berghaus [10,14], and by Egan [15] in the early 1930s. Decades later, technological advances allowed the practice of this process on an industrial scale, enabling the achievement of layers with uniform thicknesses and thinner in relation to other available nitriding techniques, besides better control over the composition of the nitrided layer. In addition, the process physics allows selective hardening to occur, i.e. only in the working region of the part [14,105].

Accordingly, shallow nitriding via plasma-assisted treatments is understood as a promising technology for applications that seek to preserve the pattern of the initial machining

texture, i.e., with reduced variations in topography after the thermochemical treatment process.

By increasing the reactivity of the medium, the plasma deposition occurs in shorter times and temperatures in relation to the gas processes [16]. In addition to increasing surface hardness and wear resistance, previous studies with steels have demonstrated that the use of plasma nitriding can improve both fatigue and corrosion resistance [10,11,16]. The possibility to revert the process can add an additional benefit, which can be obtained through a plasma treatment using only hydrogen as a continuous flow atmosphere [17].

1.3. Proposal

In the present thesis, a manner for enhancing pre-textured surfaces of components made in pearlitic gray cast iron is studied. It involves controlled enrichment of nitrogen at low temperature and short time period, increasing the hardness of the surface by means of a shallow nitride formation and nitrogen enrichment in a solid solution of iron, so that the roughness pattern obtained during the texturing process is preserved after the treatment, i.e., it does not require any further manufacturing operation. The resulting hardness is not comparable to that obtained in conventional hardening processes, but is enough to assure significant enhancements to mechanical components.

On the foregoing mentioned reasons, this treatment is scientifically defined as a shallow depth nitriding in cast iron assisted by plasma. For the sake of practicality, and of comprehensive understanding, it has been technically termed ‘shallow plasma nitriding’ (SPN)¹. In this work, SPN was studied in pearlitic matrix GCI samples produced from cylinder bores, but it could be generally used on any component made from pearlitic cast iron.

1.4. Objectives and approach

The main objective of the research is to study the application of the shallow depth plasma nitriding process ‘shallow plasma nitriding’ (SPN), for enhancing the surface of cast iron components, through experiments on specimens containing an initial texture.

¹ The technology is extensive to other materials of pearlitic matrix, such as the case of ordinary carbon steels. From this section onwards, SPN acronym will be frequently mentioned in the thesis text, always with the purpose to reflect the comprehensive technical meaning described beforehand.

The intention is thus to plasma treat a surface previously textured (e.g., ground, honed), via SPN process with consequent formation of nitride phases. In order to verify the effectiveness of the procedure, the proposal is to characterize the surface topography, phases formed and response to the instrumented linear sclerometry test ('scratch test')². Therefore, evaluating the applicability of the process to a pre-textured surface, proposing a method with potential for future applications to general components produced in cast iron, such as the ICE cylinders.

The specific objectives of this research include, but are not limited to the study of:

- plasma-assisted treatment solution to increase the wear resistance of components produced in GCI, with the treatment being performed after the texturing operation;
- phases formed, nitrogen concentration, microhardness and SEM surface characterizations, resulting from experiments at low temperature and short time;
- final topography pattern in comparison to the initial pattern by means of surface roughness profile;
- wear and friction responses of the treated surface using sclerometry;
- statistical results analysis of in-lab textured specimens;
- case-study of a honing-textured specimen, aiming to approach a potential example for extensive usage of SPN in industrial component.

² Instrumented linear sclerometry test (synonym of 'instrumented linear scratch test'): scratch resistance and friction characterized using laboratory-designed, instrumented scratch testing equipment. When the term 'sclerometry test' or simply 'sclerometry' appears herein, it refers to 'instrumented linear sclerometry test', with exactly the same meaning of 'instrumented linear scratch test'. The opposite is valid: the term 'scratch test' refers to 'instrumented linear scratch test', with the same meaning of 'instrumented linear sclerometry test'. The term 'sclerometry' is preferred and deemed comprehensive in present context. In order to keep the fidelity to the citations, one or another terminology may be applied.

2. Literature review and research fundamentals

2.1. On the wear of internal combustion engine cylinders³

Considerable efforts have been devoted to producing increasingly efficient vehicles and machines, not only for economic reasons, but also to reduce anthropogenic greenhouse gas emissions [18]. The internal combustion engine (ICE) is used worldwide in very large numbers, be it in self-propelled vehicles or stationary applications [19]. The engine and its components, e.g., the cylinder block, are designed to offer the highest performance and durability, in association to minimum levels of air pollution [20].

Indeed, cylinder bore wear may influence the chamber sealing and friction losses, therefore affecting fuel consumption and gas emissions [21]. Accordingly, it has been an important area of research, involving industries, universities and technological institutes, over the past decades [3,21-44], and until today [45-52].

Previous studies have been conducted to investigate wear-related aspects of ICE cylinders after being subjected to dynamometer durability tests [3,24,27,31,36,40,43-45,49]. The cylinder bore material was either cast iron [3,24,27,36,44] or aluminum alloy [31,40,43,45,49].

Studying cast iron liner wear using dynamometer test, Sreenath and Raman [24] inferred that metal to metal contact takes place at certain cylinder dead center locations, and the rapid wear at these positions helps to achieve quick conformance between rings and the liner during running-in. At locations where there is considerable relative velocity between ring and liner surfaces, the combined sealing effect of the surfaces and the hydrodynamic oil film reduces blowby considerably, whereas at dead center locations, sealing is mainly due to the conformity of contacting surfaces. The authors believed that, in the initial breaking-in period, the surfaces could be smoothed due to material removal from the asperities summits. However, with regard to Sreenath and Raman results, Barber and Ludema [27] discuss that the action of piston rings could develop new asperities well below the level of the hone marks. The hypothesis proposed by Barber and Ludema was based on the fact that the asperities were originally of a 0.48 μm

³ Contents from this chapter have been published in ‘D. dos Santos Filho, A.P. Tschiptschin, H. Goldenstein, Effects of ethanol content on cast iron cylinder wear in a flex-fuel internal combustion engine—A case study, *Wear* 406–407 (2018) 105-117’[58].

center-line average height whereas an average of 2.1 μm of material was worn away before the flat tops were seen.

Barber and Ludema [27] examined cylinder walls and piston rings of gasoline-fueled engines, which ran both on the road and in dynamometer tests. The cylinders were made of pearlitic gray cast iron. In the TDC region, the wear process is described as a progression of events (Figure 1) involving sliding and abrasive wear, where the moving piston ring breaks off material from honing grooves ridges, and uses it to scratch vertical grooves in the cylinder wall. With further wearing, all of the ploughed material is removed and the slower wear processes then operate to remove most of the grooves from the surface.

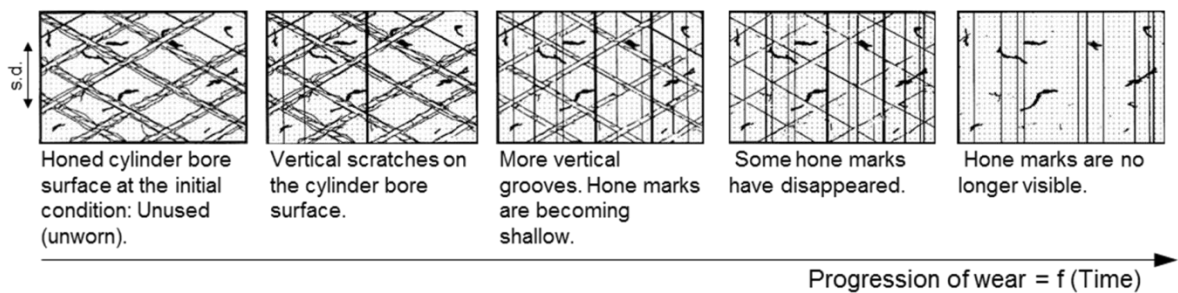


Figure 1: Progression of wear of a GCI cylinder bore surface. Adapted from [27].

Vatavuk and Demarchi [3] studied the localized wear mechanisms acting on cast iron cylinders of a diesel engine subjected to a dynamometer test. They found that the lubricant and fuel properties are important to the localized wear in the TDC, as they affect the film thickness at high temperatures near the combustion chamber and, therefore, the probability of metallic contact at the top ring reversion point. In addition to metallic contact under sliding condition, Vatavuk and Demarchi reports that a corrosive environment increases the detachment of hard particles, constituting a wear mechanism due to corrosion. The detached material will further act as abrasive particles.

Another possible wear mechanism in cast iron cylinders was described by means of cracks and the formation of large debris associated to the graphite flake morphology [25,53,54]. Riahi and Alpas [53] investigated the sliding wear of a gray cast iron after being tested against bearing steel, under an extensive range of loading and sliding speed conditions. In the mild wear regime, the graphite flakes morphology acted as weak points where the material near the contact surface would fail preferably. The large-size debris formation was described by the authors as a mechanism called “failed necks”. In this mechanism, the metallic particles did not oxidize quickly. The behavior was attributed to their large size. The particles would remain in the tribo-system as loose debris or would be entrapped in the interface. At high loading

conditions, the temperature and pressure on the particles appeared to be sufficiently high to cause after welding events [53].

Indeed, previous work demonstrated that graphite geometry and position in the cylinder bore surface varies in thickness and size due to the growth kinetics. The flake orientation with respect to the section taken will affect the graphite position, as well as the exposure area in a surface of interest (Figure 2). Graphite geometry and position will affect the stress concentration, being the flake tip a factor of influence for material matrix discontinuities [55].

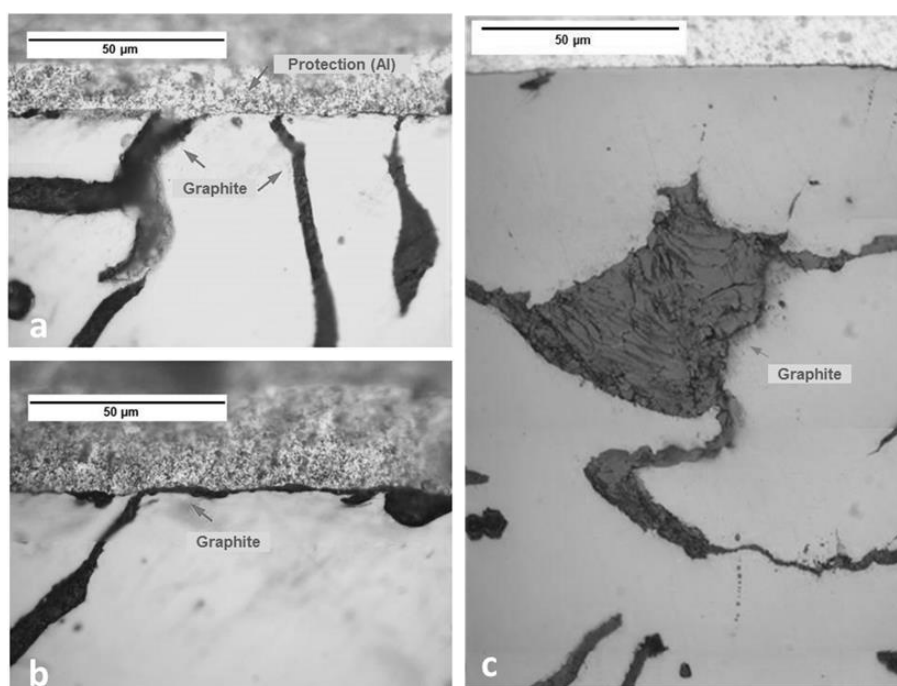


Figure 2: Graphite geometry and position found in the cylinder bore surface varies in thickness and size. The flake orientation will affect the graphite position in a surface of interest [55].

Schneider e Blossfeld [36], in 2004, reported dynamometer durability tests results of an automotive spark-ignition (SI) engine fueled with gasoline. The cylinder bore wear rate was measured using a radiotracer method. An average wear rate of 4 nm/h was reported, which occurred in the TDC, in the piston top ring position.

Gangopadhyay [33] performed wear measurements in automotive engine cylinders, from 3.0L and 4.6L displacement SI engines which had accumulated usage running in USA cab vehicles. The localized maximum wear valleys observed in several vehicles were measured and reported, after engine disassembly. An example is an engine cylinder extracted from a vehicle that ran 110 thousand km, whose localized wear valley achieved 10 µm wear.

Of the few available studies quantifying the wear occurred in the BDC, an attempt to correlate in-service wear profiles with theoretical calculations was performed by Ting and

Mayer [22,23]. In order to demonstrate and to confirm the formulated theory, an 8-cylinder diesel engine cylinder bore was analyzed, after 75690 km vehicle mileage, by wear profile measurements. The load pressure acting on the cylinder wall is composed of the gas pressure behind the ring and its natural spring tension. There is a decrease of wear at the mid-stroke due to the hydrodynamic regime granted by the higher piston speed, while the wear at the motion reversal points is increased due to the loss of oil film hydrodynamic action. The authors argue that the degree of wear at the bottom of stroke should be comparatively less than at the top of the stroke, since the gas pressures behind the rings are smaller. Indeed, most of the actual wear profiles measured by Ting and Mayer presented the maximum localized wear in the TDC. Conversely, in some cases, the localized wear in the BDC resulted in equal or higher magnitude than in the TDC [23].

Dimkovski, Baath, et al. [48] characterized wear particles embedded in the deposits inside the cylinder bore honing grooves. Among other chemical elements, the authors found iron and silicon. The iron origin was attributed to the cast iron matrix or wear debris embedded in the deposits, while the silicon would derive either from the liner material or from the charge air. Here, metallic particles were embedded into the deposits as a result of the simultaneous processes of wear and deposit accumulation. In another study, Dimkovski, Anderberg, et al. [44] discussed a potential event occurring due to the imperfection of the manufacturing process of cast iron bores, where the honing grooves, especially the deep ones, are smeared and interrupted by folds. According to Dimkovski et al., a portion of the folds would eventually detach during the running process and act as abrasive particles increasing the wear in the cylinder. Additionally, the characterization of worn cylinder liner surfaces by segmentation of honing and wear scratches demonstrated abrasive wear predominating in the TDC, whereas few scratches were found in the BDC [51].

Using TEM technics, Meng-Burany et al. [49] showed details of the oil residue layer and ultrafine grains on which an oil residue layer was formed after the wear tests. The layers incorporated debris described as nanocrystalline fragments of silicon and aluminum. The study was based on a V8 gasoline engine with monolithic Al-Si engine block.

Khorshid and Nawwar [29] reviewed the effect of sand dust and filtration on automobile engine wear, highlighting the external sources of abrasive particles. In addition, Michalski and Woś [50] performed dynamometer tests on free aspired air-cooled aircraft engines, during 10 h of fired running-in period, 21 h operation of intensified abrasive wear in the piston-cylinder assembly. The wear was forced by dosing road dust into the inlet manifold. It was reported that,

in this condition, the abrasive particles caused the equivalent wear rate as during 1500 h of durability test in real conditions.

Furthermore, the fuel type affects the carbonaceous deposits formation during engine combustion [56]. According to Kalghatgi [57], the nature of the carbonaceous residues varies from soft and oily to sticky varnish to hard and coke-like. In gasoline engines, one of the possible mechanisms described would comprise evaporation of lighter hydrocarbons, resulting in a thin film rich in heavier hydrocarbons. The film oxidizes to form a sticky varnish that can bake into a hard deposit given sufficient time. This deposit can bind particulates such as airborne dirt and solids that get into the intake manifold [57].

A number of previous works on the wear of ICE cylinder bores were reviewed and summarized in Table 1. The review summary includes: authors, cylinder material, engine fuel (when available) and the applied investigation methods.

Table 1: Summary of the review on the wear of ICE cylinder bores.

Authors	Cylinder Material	Engine Fuel	Type of test	Main type of characterization
L.L. Ting, J.E. Mayer Jr. [22]	-	-	(Theory article)	(An analytical method for determining the bore wear pattern)
L.L. Ting, J.E. Mayer Jr. [23]	Gray cast iron	Diesel	Vehicle mileage, 75690 km	2-D profilometry, Measurement of the wear profile at TDC and BDC regions
A.V. Sreenath, N. Raman [24]	Gray cast iron	Diesel	Dynamometer test: 45h running-in (break-in stage of engine wear), varying speed and load	2-D profilometry, Measurement of the wear profile at TDC and BDC regions
J. Nadel, T.S. Eyre [25]	Gray cast iron	Diesel	Vehicle mileage (mileage not reported)	SEM analysis, surface and cut-section
T.S. Sudarshan, S.B. Bhaduri [21]	-	-	(Review article)	(A review article approaching adhesion, corrosion and abrasion of ICE cylinders)
R.A. Daskivich [26]	Gray cast iron	Gasoline	700h engine normal operating (firing) time	2-D profilometry, Measurement of the wear profile

Authors	Cylinder Material	Engine Fuel	Type of test	Main type of characterization
G.C. Barber, K.C. Ludema [27]	Gray cast iron	Gasoline	Vehicle mileage, 153600 km; Dynamometer test: 20 min, 15h; Vehicle mileage, 25600 km, 115200 km	2-D profilometry, Measurement of the wear profile at TDC and BDC regions; SEM analysis, surface
T.S. Eyre, K.K. Dutta, F.A. Davis [28]	Gray cast iron	Diesel	Vehicle/Marine application, service engine (mileage not reported)	SEM analysis, surface
E.A. Khorshid, A.M. Nawwar [29]	-	-	(Review article)	(A review article approaching, abrasion of ICE cylinders)
J. Vatavuk, V. Demarchi [3]	Gray cast iron	Diesel	Dynamometer test: Global Engine Durability, 400h	2-D profilometry, Measurement of the wear profile; SEM analysis, surface
B.-G. Rosén, R. Ohlsson, T.R. Thomas [30]	Gray cast iron	(not informed)	Engine test	Atomic force microscopy (AFM) analysis, 3-D profilometry, roughness parameters, wear quantification
Y. Wang, S.C. Tung [31]	Aluminum-Silicon alloy	Gasoline	Dynamometer test: cold and hot scuffing tests: Cold scuffing tests, at 2000 rpm for 2.5 hours; Hot scuffing tests, cycled to 5200 rpm WOT, and 1200 rpm at no load	Qualitative wear scale ranking
M. Priest and C.M. Taylor [32]	Gray cast iron	Diesel	Engine long term running test (more than 628h)	2-D profilometry, Measurement of the wear profile
A. Gangopadhyay [33]	Gray cast iron	Gasoline	Vehicle mileages, 111021-247786 km (69000 – 154000 miles)	2-D profilometry, Measurement of the wear profile; development of a wear model
E. Decencièrè, D. Jeulin [34]	Gray cast iron	Gasoline	Vehicle mileage, V6 engine (mileage not reported)	2-D profilometry, Roughness parameters, wear quantification

Authors	Cylinder Material	Engine Fuel	Type of test	Main type of characterization
M.F. Jensen, J. Bottiger, H.H. Reitz, M.E. Benzon [35]	Gray cast iron	Diesel	Pin-on-disc (POD) test to simulate the wear occurring in marine engine cylinders	SEM analysis, surface; Friction and wear measurements
E.W. Schneider, D.H. Blossfeld [36]	Gray cast iron	Gasoline	Dynamometer test: cold and warm start plus steady state, with measurement of bore wear rates in real time during normal operating conditions	Measurement of the wear rates applying radiotracer technology, at break-in and steady states
A. Edrisy, T. Perry, A.T. Alpas [37]	Aluminum-Silicon alloy (with Thermal spray coating of low carbon steel plus 2.5% Al, by high velocity oxy-fuel HVOF process)	Gasoline	Race car, engine 5.7L V8, which failed by bore scuffing after four races (mileage not reported)	3-D profilometry, surface; SEM analysis, cut-section
J.J. Truhan, J. Qu, P.J. Blau [38,39]	Gray cast iron	Diesel	Reciprocating rig test to simulate the wear occurring in diesel engine cylinders	Friction and Wear measurements, comparing different oil grades
M. Dienwiebel, K. Pohlmann, M. Scherge [40]	Aluminum-Silicon alloy	Gasoline (inferred)	Dynamometer test: fired engine dynamometer test of approx. 250 h full speed and torque range of the engine	AFM analysis, surface; Focused ion beam (FIB) analysis, cut-section
J. Keller, V. Fridrici, Ph. Kapsa, S. Vidaller, J.F. Huard [41]	Gray cast iron	Diesel	Reciprocating rig test to simulate the wear occurring in diesel engine cylinders	Friction and Wear measurements; SEM analysis, surface; EDX cartography
E. Tomanik [42]	Gray cast iron	Diesel	Reciprocating rig test to simulate the wear occurring in diesel engine cylinders	Friction and Wear measurements
B.E. Slattery, T. Perry, A. Edrisy [43]	Aluminum-Silicon alloy	Gasoline	Dynamometer test: nearly 300 h of high load, high speed, and high temperature running in a dynamometer	3-D profilometry, surface; SEM analysis, surface and cut-section; FIB analysis, cut-section

Authors	Cylinder Material	Engine Fuel	Type of test	Main type of characterization
Z. Dimkovski, C. Anderberg, B.-G. Rosén, R. Ohlsson, T.R. Thomas [44]	Gray cast iron	Diesel	Engine test: seven different running periods and similar load, speed and lubrication.	3D profilometry, surface; development of an algorithm to identify and quantify cold worked material inside honing grooves
B.E. Slattery, A. Edrissy, T. Perry [45]	Aluminum-Silicon alloy	Gasoline	Dynamometer test: nearly 300 h of high load, high speed, and high temperature running in a dynamometer	3D profilometry, surface; SEM analysis, surface and cut-section; FIB analysis, cut-section
W. Grabon, P. Pawlus, J. Sep [46]	Gray cast iron	Diesel	Reciprocating rig test to simulate the wear occurring in diesel engine cylinders	Friction and Wear measurements; material ratio curve before and after the test
L. Gara, Q. Zou, B.P. Sangeorzan, G.C. Barber, H.E. McCormick, M.H. Mekari [47]	Gray cast iron	Diesel	Single cylinder test bench: steady state at 3600 rpm	3D profilometry, surface; wear quantification
Z. Dimkovski, L. Baath, S. Rosén, R. Ohlsson, B.-G. Rosén [48]	Gray cast iron	Diesel	Engine test: three different times (50h, 525h, 1100h), speed from 600 to 2100 rpm	SEM analysis, surface; FIB analysis, cut-section
X. Meng-Burany, T.A. Perry, A.K. Sachdev, A.T. Alpas [49]	Aluminum-Silicon alloy	Gasoline	Dynamometer test: Similar to Wang and Tung, 1999 [31]; Pin-on-disc (POD) test	FIB, cut-section; Transmission electron microscopy (TEM), cut-section
J. Michalski, P. Woś [50]	Cast iron	Avgas 100LL aviation fuel	Bench test, air-cooled aircraft FRANKLIN engine; dynamometer, 21 h intensified abrasive wear forced	Roughness parameters, wear quantification; ring joint gap, before and after test
Z. Dimkovski, C. Anderberg, R. Ohlsson, B.-G. Rosén [51]	Gray cast iron	Diesel	Engine test: 486 h under cyclic loading	3D profilometry, surface; wear quantification through algorithm
P.R. De Silva, M. Priest, P.M. Lee, R.C. Coy, R.I. Taylor [52]	Gray cast iron	Gasoline	Reciprocating rig test to simulate the wear occurring in gasoline engines. (PLINT TE77 tribometer)	Friction measurements, effects of ethanol and water mixed with the lubricant

2.1.1. Contextual research on the wear of ICE cylinders

In the background research presented herein, we report and discuss the results on the wear aspects in the top, middle and bottom ring reversal points, of two ICE cylinder block samples. An engine fueled with local gasoline and another one fueled with ethanol have been submitted to the engine dynamometer durability test. Selected localized wear regions have been characterized using scanning electronic microscopy (SEM) which provided the elements for the coordinated description of the cylinder bore wear features observed experimentally.

The SEM analysis, on the cylinder bore surface, was performed by an equipment model XL30-Philips, equipped with an energy dispersive X-ray spectrometer (EDS). The analysis on the surface occurred by direct observation, along three cylinder stroke heights described in Figure 3 and Table 2, after the ultrasonic cleaning. The regions of localized wear at TDC (iii) and BDC (v) had been previously identified through the 2-D profilometer analysis. The complete description of applied methods of test and analysis is found in [58].

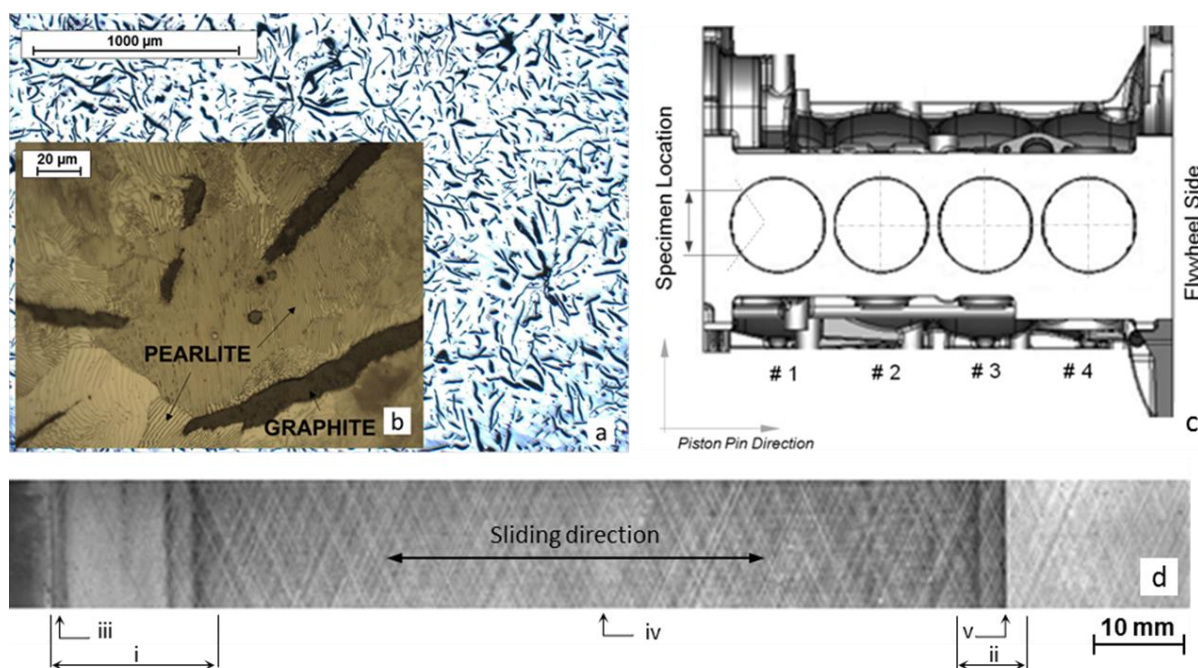


Figure 3: Schematic of cylinder bore material microstructure and characterization specimens location. a) Optical micrograph from the cylinder block material, as polished, not etched. Flake graphite is revealed. b) Optical micrograph illustrating the matrix of pearlite. (2% Nital solution). c) Scheme of cylinder block specimen location. d) SEM analysis location scheme (see Table 2). The regions of localized wear were identified by the profilometer analysis, which guided the SEM analysis.

The maximum localized wear (LW) at TDC region was of 1.7 μm for the engine tested with gasoline and of 1.5 μm for the one tested with ethanol. The LW was measured in relation to the unworn region and represents the actual extension of material radially removed in the top ring reversal point. The BDC profilograms resulted in a maximum LW of 1.8 μm for the engine tested with gasoline and of 2.7 μm for the one tested with ethanol (Figure 4).

Table 2: Type of characterization analysis performed by regions of the cylinder bore.

Analysis location	Description	Predominant lubrication regime	Characterization analysis
i	TDC region, ring reversal marks	boundary, mixed	profilometer analysis
ii	BDC region, ring reversal marks	boundary, mixed	profilometer analysis
iii	top of the ring travel	boundary	SEM surface
iv	mid stroke region	hydrodynamic	SEM surface
v	bottom of the ring travel	boundary	SEM surface

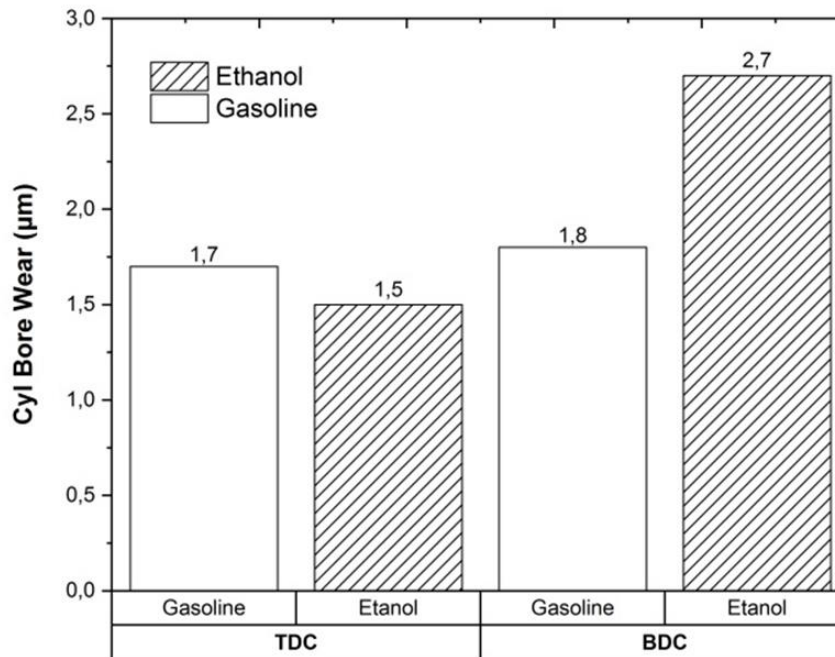


Figure 4: Cylinder Bore localized wear in the TDC and BDC regions. At end-of-test with gasoline and ethanol. Results are based on 2-D profilometer analysis reported in [58].

The bore surface appearance in different regions of the cylinder is presented in Figure 5. In order to rank the resulting wear, a criterion was proposed in Table 3. The proposed criterion consists of four levels of wear. The wear severity increases from level 0 (L0) to level 4 (L4). In addition, the surface observations were classified into four categories, as seen in Table 4. Examples of both levels and categories are indicated with arrows in Figure 5.

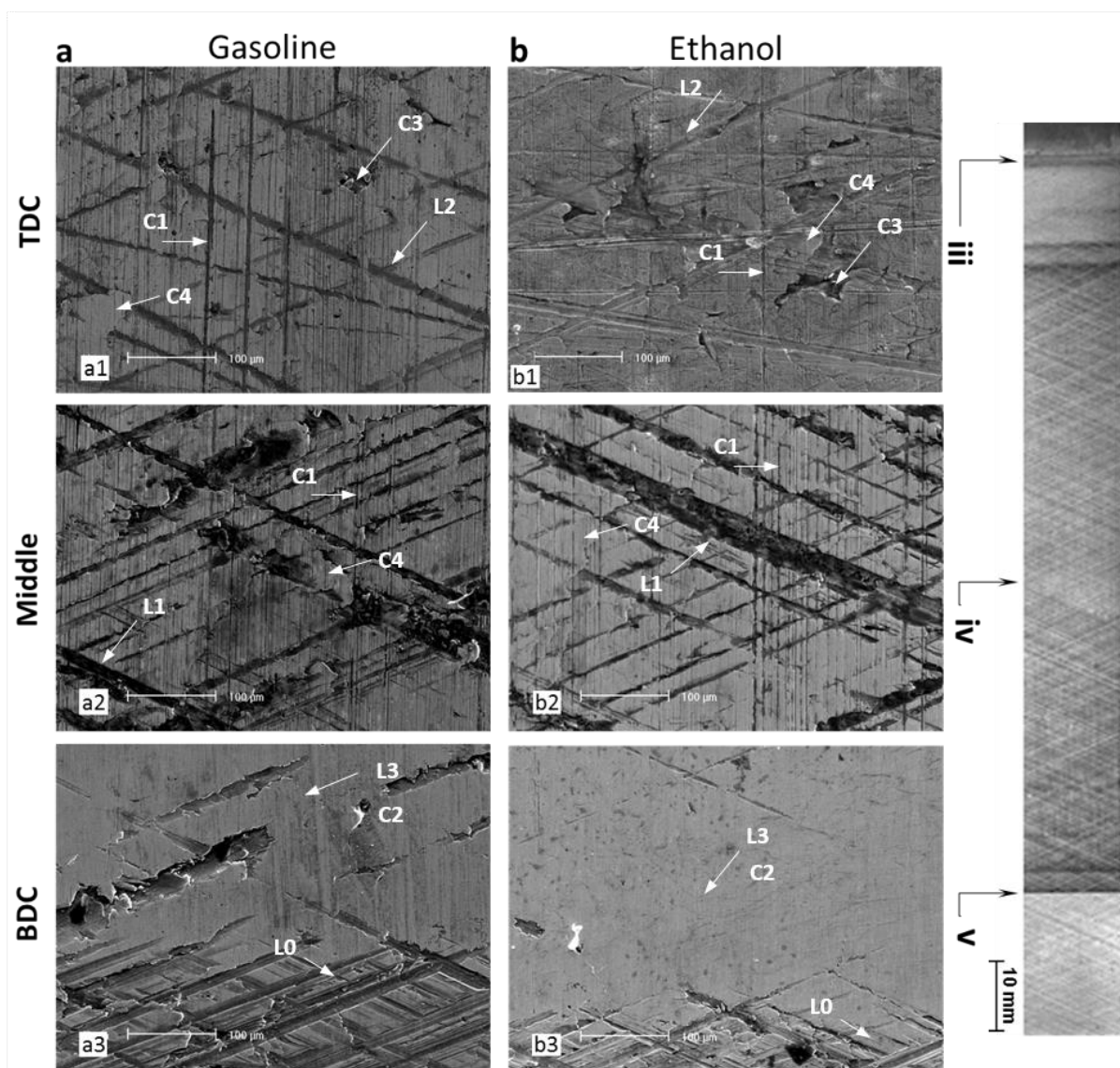


Figure 5: Bore surface SEM Analysis. At end-of-test with (a) gasoline and (b) ethanol.

Figure 5a and Figure 5b show that the honing texture was homogeneously reduced in the region of localized wear in the TDC. In that region, both the major honing grooves and intermediary grooves are partially preserved. In the mid stroke region, the major honing grooves are satisfactorily preserved, while the intermediary grooves are partially preserved, as seen in Figure 5a2 and Figure 5a3.

Table 3: Wear severity level.

	Wear severity level	Region	Gasoline	Ethanol
L0	Level 0 - unworn (UW) honed surfaces.	BDC – Below the bottom of the ring travel mark (v)	Fig. a3	Fig. b3
L1	Level 1 – Major grooves are satisfactorily preserved; intermediary grooves are partially preserved.	Mid stroke region (iv)	Fig. a2	Fig. b2
L2	Level 2 – Major grooves and intermediary grooves are partially preserved	TDC – Top of the ring travel mark (iii)	Fig. a1	Fig. b1
L3	Level 3 – Major grooves and intermediary grooves vanished, even partially or completely.	BDC – Bottom of the ring travel mark (v)	Fig. a3	Fig. b3

Therefore, the wear was less severe in the mid stroke region in comparison to the TDC region. Conversely, Figure 5a3 and Figure 5b3 show that both the major and intermediary honing grooves vanished, even partially or completely in the region of localized wear in the BDC, i.e., the bottom of the ring travel mark (v). Below this point, the unworn (UW) honed surface was observed. Vertical abrasion risks, voids, plastic deformation and micro-polishing aspect (absence of honing texture at micro level) were observed in the set of images presented in Figure 5. The observations are cylinder region dependent (Table 4).

Bore surface SEM analysis (Figure 5) revealed axial wear scratches caused by abrasive wear in the TDC and middle region, while in the BDC region there are no perceptible scratches at a corresponding scale. Several other wear mechanisms, including sliding wear/adhesion and corrosion may have led to the cylinder bore wear in the case study reported in [58], particularly in the TDC and BDC regions, where the boundary lubrication regime predominates. The characterization clearly evidenced abrasive wear occurring at TDC and mid stroke regions, at end-of-test with both gasoline and with ethanol.

Previous works described the potential sources for the abrasive particles responsible for the cylinder bore axial scratches: debris removed from the cylinder and rings during and after the engine break-in stage [27]; thin dust particles, predominantly ceramic, originated from external sources such as the air, which would not have been captured by the filtering element

due to its small size [27,29]; cold worked material detached from the TDC region [44]; particles left in the engine during manufacture and assembly [27,59]; cylinder bore material detachment due to delamination associated to a graphite pocket termination [53,54]; hard carbonaceous residues formed during engine combustion, whose content are highly influenced by the fuel type [56,57].

Table 4: Surface observations category.

	Surface observations category	General description	Region	Gasoline	Ethanol
C1	Axial wear scratches	Non-intentional abrasion.	TDC – Top of the ring travel mark (iii), Mid stroke region (iv)	Fig. a1, Fig. a2	Fig. b1, Fig. b2
C2	Micro-polishing	Smooth surface; absence of honing texture signs at micro level.	BDC – Bottom of the ring travel mark (v)	Fig. a3	Fig. b3
C3	Voids	Surface discontinuity due to lack of material.	TDC – Top of the ring travel mark (iii)	Fig. a1	Fig. b1
C4	Plastic deformation	Cold worked material due to the displacement from its original position.	TDC – Top of the ring travel mark (iii), Mid stroke region (iv)	Fig. a1, Fig. a2	Fig. b1, Fig. b2

The background research showed that the major grooves and intermediary grooves vanished, even partially (Figure 5a3) or completely (Figure 5b3) at the bottom of the ring travel mark. Figure 5a3 shows that at the end-of-displacement of the piston ring there is a transition line. Immediately above this line, the honing is worn out. This is the actuation point of the second segment of the oil control ring (OCR) assembly. The resulting surface is polished and corresponds to the reduced roughness noted in the scheme shown in Figure 1, which is based on the Barber and Ludema work on the progression of wear of a GCI cylinder bore surface [27].

The characterization results indicated that abrasion is a predominant mechanism contributing to cylinder bore wear. The contact pressure variation, which can be understood as the sum of gas pressure and the ring pressure due to its natural spring tension, associated to the resulting oil film as per predominant lubrication regime [22,23], cause the dynamic of wear

mechanisms acting separately or combined. These lead to the different observed aspects and magnitudes of cylinder bore wear with the diverse bore regions.

Comprehensive thesis research approaching the description of mechanisms of wear of ICE cylinders [107,108,109] support these contextual research results, with abrasion listed between the main mechanisms for wear. Origins and development of sclerometry test to characterize mechanical response of materials are described in [110], which also points the scratch formation as a method of controlled abrasive wear, and reasonable to use for compare abrasive wear resistance of materials, characterize aspects related to deformation and material removal. Determined by sliding a hard indenter tip across the surface of material, it also measures the response of a material to plastic deformation under sliding condition [110].

2.2. On the nitriding of pearlitic gray cast iron

2.2.1. Literature review on the nitriding of pearlitic gray cast iron

In the reviewed literature about nitriding of pearlitic GCI, Nicoletto et al. [60] performed gas nitriding in NH_3 furnace atmosphere at 520 °C. Zenker et al. [61] treated samples via plasma nitriding at 540 °C for 8 h with 4:1 $\text{N}_2:\text{H}_2$ gas composition. More recently, Salvaro et al. [6] studied duplex coating process with a plasma nitriding step at 550 °C for 1.5 h, followed by DLC deposition. The studies summarized in Table 5 approached the effects on hardness, friction, and wear.

Table 5: Some works on the nitriding of GCI, including the basic process and respective temperature.

First Author	Material	Process	Temperature (°C)
Nicoletto [60]	GCI	Gas nitriding, NH_3 atmosphere	520
Zenker [61]	GCI	Plasma nitriding, 4:1 $\text{N}_2:\text{H}_2$ gas composition	540
Salvaro [6]	GCI	Plasma nitriding followed by DLC deposition	550
Giacomelli [7]	GCI	Plasma nitriding	550
Rolinski [62]	GCI	Gas nitriding	520
Rolinski [62]	GCI	Plasma nitriding	566

It is known that, when pearlitic cast iron is nitrided, the surface treatment harden the matrix structure, but cannot improve the strength of the graphite. Contact stresses are therefore supported by the matrix with limited contribution from the graphite. In previous work [60], spheroidal cast iron resulted in average hardness somewhat higher than lamellar cast iron specimens, after being treated by gas nitriding at same time-temperature condition. In both cases, final hardness of pearlite matrix resulted superior to 700 HV 0.1 (Table 6) [60].

Table 6: Surface microhardness of cast iron samples reported by [60], after gas nitriding. Avg \pm StdDev (Values originally reported in GPa were converted to HV 0.1).

Gas nitriding, 520 °C, 9h	
Lamellar graphite cast iron	Nodular graphite cast iron
765 \pm 41 HV 0.1	806 \pm 51 HV 0.1

The method, temperature, and time of nitriding will influence the surface topographic changes [106]. Giacomelli et al. reported that intense modification on the topography of GCI was observed after 550 °C for 90 minutes of plasma nitriding [7]. Rolinski et al. [62] studied the effects of nitriding mechanisms on surface roughness of plasma and gas nitrided GCI samples. In such study, high-temperature (566 °C) gas nitrocarburizing caused a significantly rougher surface. Steps taken to minimize the problem included gas nitriding instead of nitrocarburizing, using lower processing temperature (520 °C). Furthermore, plasma processing at 566 °C for 15h resulted in lower roughness relatively to gas processing. Even so, average Ra roughness of the plasma-treated sample was about ten times higher than the initial roughness condition [62].

Studying the effects of different methods of nitriding on roughness of steel specimens, Vatauvuk et al. [106] verified similar trends as above, with plasma nitriding at 550 °C for 3h resulting in lower roughness relatively to gas processing at 570 °C for 2h, and Ra roughness of the plasma-treated sample increasing by about four times the initial Ra roughness.

In another previous study, Baranowska [63] analyzed the influence of nitriding on the surface microstructural state of cast irons. After the GCI nitriding at 575 °C for 4 h (salt bath method is assumed), a decrease in the quality of the surface was observed. The value of the measured roughness parameter increased. The dependence of roughness parameters on the shape and size of the graphite was also discussed.

Still according to Baranowska [63], if the graphite flake is parallel to the surface (Figure 6a), the graphite limits the diffusion into the sample. As a consequence, a very high concentration of nitrogen is locally obtained, with weak adhesion to the graphite flake; if the graphite flake is perpendicular to the surface, the effect on the surface quality is minimum as it is observed only as a discontinuity in the surface layer (Figure 6b) and; in the third situation the diffusion limitation decreases with the increase of the angle between the flake of the graphite and the surface (Figure 6c).

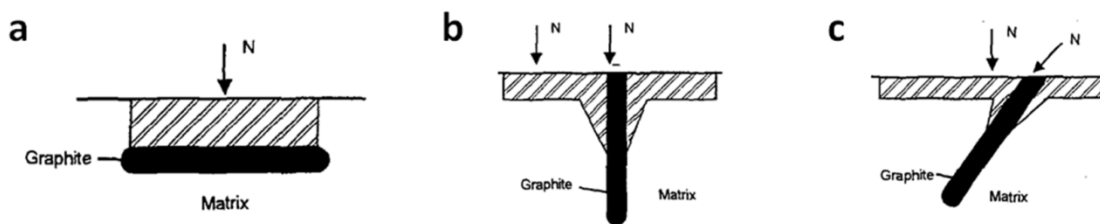


Figure 6: Scheme of nitrogen diffusion for different graphite positions [63].

2.2.2. Development of a nitrided zone in pearlitic matrix

Currently, it is well known that when nitriding iron and steels a nitrided case develops, that comprises two distinct morphological regions: an outermost compound layer, composed of brittle iron nitrides, and a diffusion zone, where small and well-distributed iron nitrides precipitate in a ferritic or a tempered martensitic matrix. Since the compound layer is brittle, it is considered undesirable, as it tends to break into small fragments [64].

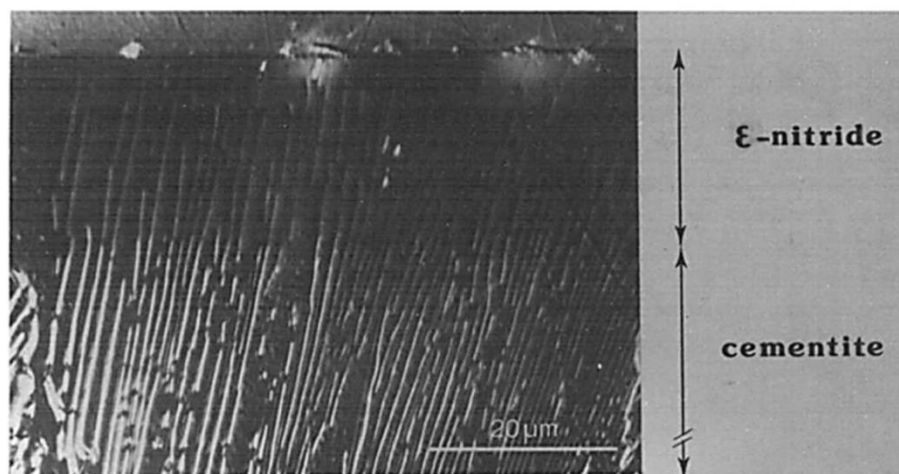


Figure 7: Cross-section of a nitrided (without compound layer formation) 1.00 wt% C specimen. In the surface region the cementite lamellae are converted into ϵ -nitride. According to Mittemeijer et al. [64].

Gas nitriding (NH_3/H_2) of a 1.00 wt% C pearlitic steel specimen has been carried out by Mittemeijer et al. [64]. The resulting structure was reported as free from compound layer formation. The formation of ϵ -nitride in the pearlitic matrix has been evidenced through combined optical microscopy (OM) and X-ray diffractometry (XRD).

In the OM image, the diffusion zone - where the ϵ -nitride is present - is clearly darker than the non-nitrided lamellar cementite region (Figure 7). Whereas the X-ray diffractograms taken from non-nitrided and nitrided specimens demonstrated that ϵ -nitride was formed in the treated specimen. According to the author, Fe_3C lamellae would also have been transformed, in situ, to ϵ -nitrides [64].

2.2.3. On the nitrogen concentration and carbon redistribution

Studying the effects of plasma nitriding in steel, Garzón, Franco e Tschiptschin [67] verified relationship between the hardened-case depth and the depth of the region where carbon diffusion occurs. According to this study, the fact that the hardened-case was higher than the nitride-case depth could be attributed to carbon diffusion against the concentration gradient (Figure 8).

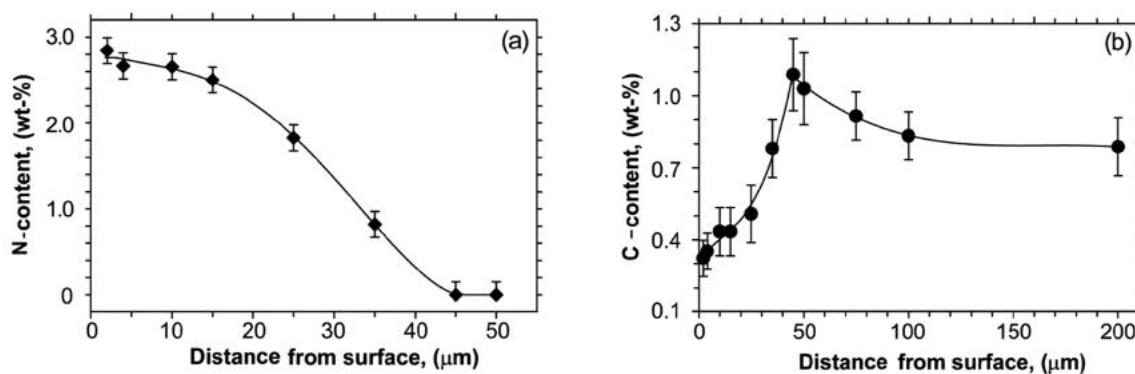


Figure 8: WDS measured (a) nitrogen and (b) carbon contents in steel AISI D2 as a function of distance from the surface [67].

Carbon diffusion from low-carbon to high-carbon content regions would occur because nitrogen absorption increases the activity of carbon atoms at the region adjacent to the steel surface, with regard to atoms at deeper regions from the surface [67].

According to Toro and Tschiptschin [68], the detection of N by EDS is usually prevented either by the reduced intensity of X-rays associated with this element, or by the overlapping

effects caused by elements such as Mo and Mn since the spatial resolution of this technique is always worse than 130–150 eV. On the other hand, the improved spatial resolution of WDS (namely 3–10 eV) can avoid overlapping problems if the operating conditions are properly chosen. The key factor in quantification is the precise balance between the probe size and the detection statistics, given that smaller probes require lower currents, and therefore the number of counts per second is strongly reduced when the volume analyzed is small.

Close correspondence between the N distribution and the hardness profile has been reported by previous works using WDS technics [68,111], as exemplified in Figure 9. When no nitride formation was observed (all N in solid solution), it has been observed that WDS measurements at the surface showed good correlation with the results from different techniques, as optical spectroscopy and glow discharge optical spectroscopy, as well as with the theoretical solid-gas equilibrium N content calculated by thermodynamic modeling [68].

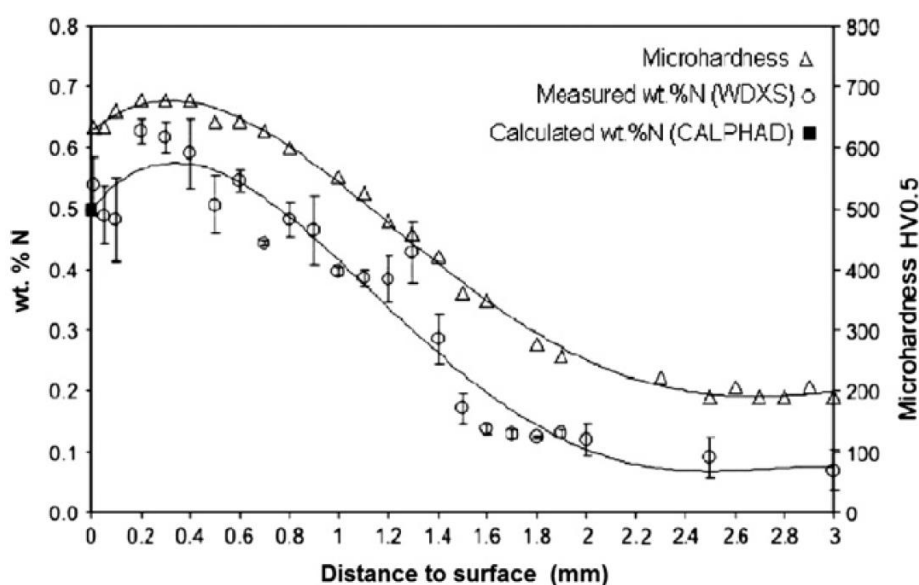


Figure 9: N distribution and microhardness of AISI410S steel nitrided at 800 °C - 6h [68].

A study on the formation of nitride layers during plasma nitriding process of a tool steel has shown that the concentration of nitrogen decreases in the nitride layer from the sample surface toward the sample core. The nitrogen concentration profile was characterized using SEM equipped with energy dispersive spectroscopy (EDS) analyzer. In order to confirm the EDS results, the authors performed additional wavelength dispersive spectrometer (WDS) as well as glow discharge spectroscopy (GDS) analysis [65].

In the same work, a corresponding carbon accumulation at the case-core transition and close to the surface, was detected by GDS. When the nitrogen content of the substrate is just

about zero, the carbon content of the substrate is relatively constant, indicating that carbon redistribution occurred [65].

Carbon redistribution is one of the phenomena's occurring in the diffusion zone, other than precipitation or nitrides and residual stress generation. Saturation of nitrogen in α -Fe and precipitation of nitrides generate these compressive residual stresses in the nitrated layer. According to Somers [66], on nitriding the carbides in pearlite are gradually transformed into ϵ -nitrides. Carbon atoms released in the in-situ transformation can either leave the steel by CH_4 development or diffuse deeper into the steel. The kinetics of diffusion of carbon ahead of the advancing nitriding front is usually faster than CH_4 formation and desorption, and enhanced carbon content accumulates [66].

2.2.4. On the Fe_3N nitride formation

The phenomenon of nitride formation on the surface of iron was described by Inokuti, Nishida, and Ohashi, using highly polished specimens of well-refined and coarsened iron grains, which have been nitrided in gas (NH_3/H_2) process [69]. In the experiment of a $(111)\text{-}\alpha$ grain surface nitride in gas (NH_3/H_2) process for 10 minutes at 500°C , precipitates having “three legs” were observed (Figure 10a and Figure 10b). The formation of Fe_3N (ϵ -nitride) was also confirmed by XRD measurements.

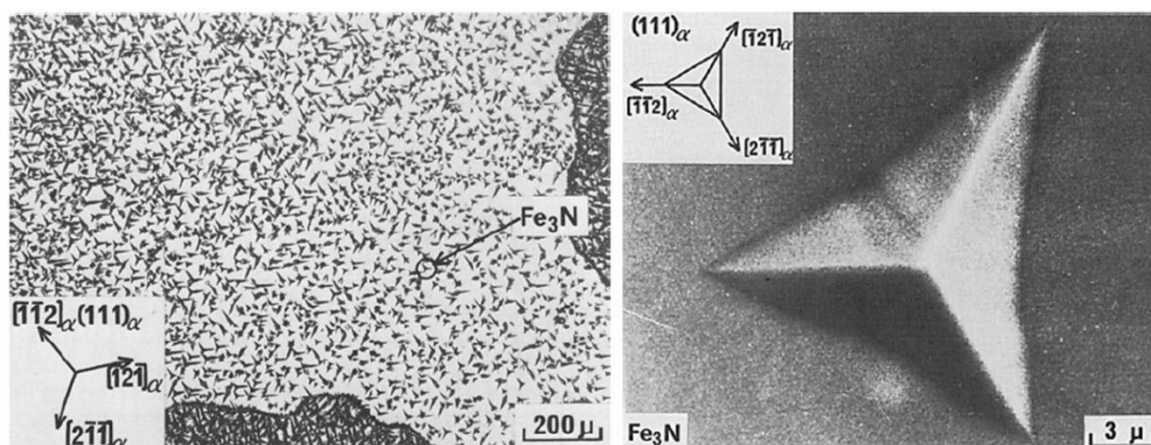


Figure 10: a) Photomicrograph of Fe_3N on the surface of $(111)\alpha$ grain after nitriding in gas (NH_3/H_2) process. b) SEM micrograph showing Fe_3N on the surface of $(111)\alpha$ grain after nitriding in gas (NH_3/H_2) process [69].

The "wedge-like" Fe_3N nitride differs from the “needle-like” Fe_4N nitride, which can grow from the tip of the Fe_3N towards the interior of the iron. In the same foregoing mentioned

previous work, the Fe_4N precipitates have been determined by the orientation relationship between these precipitates and alpha iron [69].

2.3. Instrumented linear sclerometry test applied in GCI

In the test method described in ASTM C1624-05 [70], a conical diamond indenter with an included angle of 120° and a spherical tip radius of $200\ \mu\text{m}$ is drawn across the flat surface of a test specimen at a constant speed and a defined normal force (constant or progressively increasing) for a defined distance.

The damage along the scratch track is microscopically assessed as a function of the applied force. Specific levels of progressive damage are associated with increasing normal stylus forces. The force level that produces a specific type/level of damage in the coating is defined as a critical scratch load (Figure 11) [70]. Still according to [70], the only direct and reliable method of assessing the damage remains microscopic and SEM analysis, particularly for low level damage.

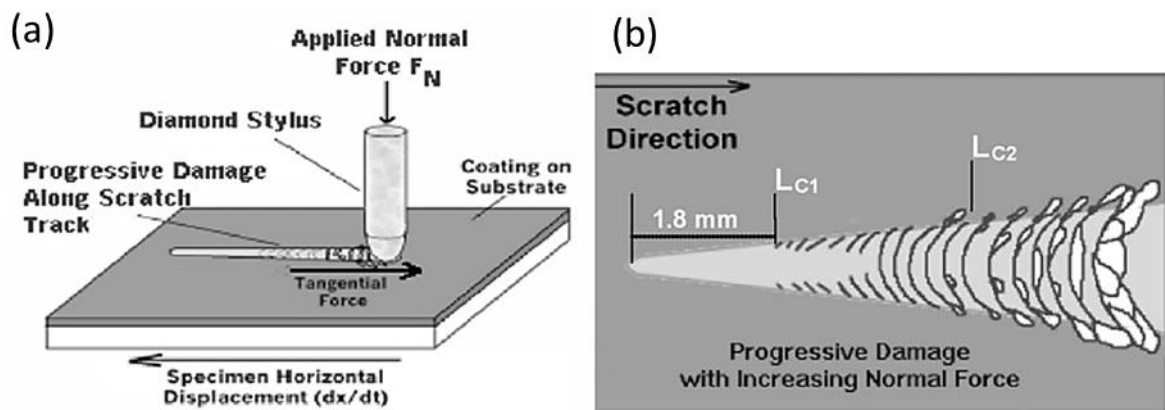


Figure 11: a) Test method schematic. b) Critical scratch load damage features in progressive load test, where: L_{c1} and L_{c2} refer to first and second level of critical scratch load values, respectively [70].

In recent works, sclerometry test has been successfully employed to study wear in gray cast irons [71-76]. In such context, Nakamura and Iwabuchi [71] studied the role of graphite in cast iron using nano-scratch wear testing. The tests were performed with constant loads of 2.5 mN and 5 mN. At 2.5 mN, when indenter reached the graphite area, indentation depth increased. This behavior was explained by the fact that graphite is soft.

Because of low load, increased indentation depth stopped in middle of graphite; and a graphite film was developed due to wedge formation (Figure 12). At 5 mN, when indenter

reached graphite area, the indenter penetrated the graphite and would have reached the matrix. This was explained as an effect of the higher indentation load. Afterwards, due to wedge formation of graphite, graphite film was formed as well. However, the formed graphite film would be broken by stick slip in end of graphite area. (Figure 13). In both cases, the apparent coefficient of friction (COF) decreased when passing through the graphite area (Figure 12 and Figure 13). From these results, Nakamura and Iwabuchi [71] indorsed that previous models applied in macro scale test of cast iron would be valid in the micro and nano scale tests.

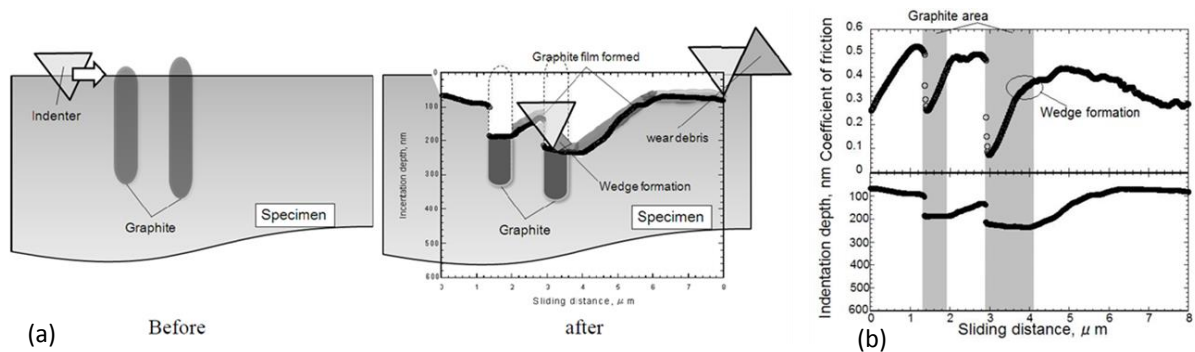


Figure 12: a) Wear process at 2.5 mN. When the indenter reached the graphite area, the indentation depth increased. b) Apparent COF and indentation depth as a function of sliding distance at 2.5mN [71].

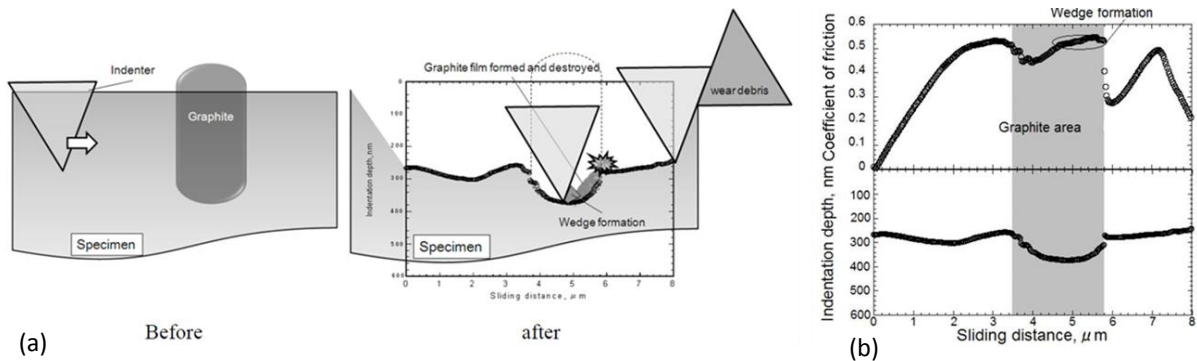


Figure 13: a) Wear process at 5 mN. When the indenter penetrated the graphite, matrix would have been reached. b) Apparent COF and indentation depth as a function of sliding distance at 5mN [71].

Mendas and Benayoun [72] investigated the effects of microstructure on the wear mechanisms in lamellar cast irons using a micro scratch test carried out using diamond conical indenters with the following apex angle and radius (2θ / tip radius R): $160^\circ / 5 \mu\text{m}$, $120^\circ / 5 \mu\text{m}$, and $90^\circ / 2 \mu\text{m}$ (Figure 14).

In [72], various applied loads (1 to 15 N) were utilized to investigate two types of lamellar cast irons: The classical lamellar GCI with a pearlitic matrix with lamellar graphite, and a micro-alloyed (with phosphorous and boron) cast iron with a pearlitic matrix with eutectic phosphorous, carbides and lamellar graphite. The results indicated that the surface damage

depends on the indenter geometry, the penetration depth, the orientation, and the depth of the graphite flakes. In addition, the study indicated that the reinforced matrix somehow improved the behavior of the GCI under scratching conditions. The authors have also proposed schemes to explain the role played by graphite in the wear process (Figure 15).

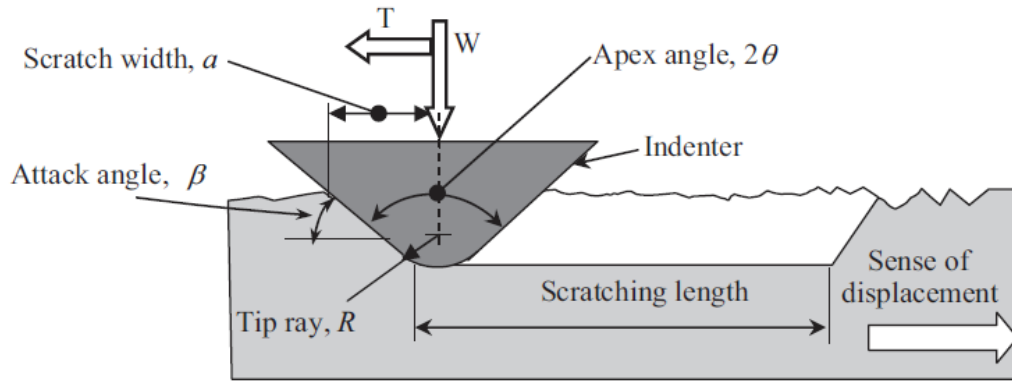


Figure 14: Schematic diagram of the scratch test performed by Mendas and Benayoun [72].

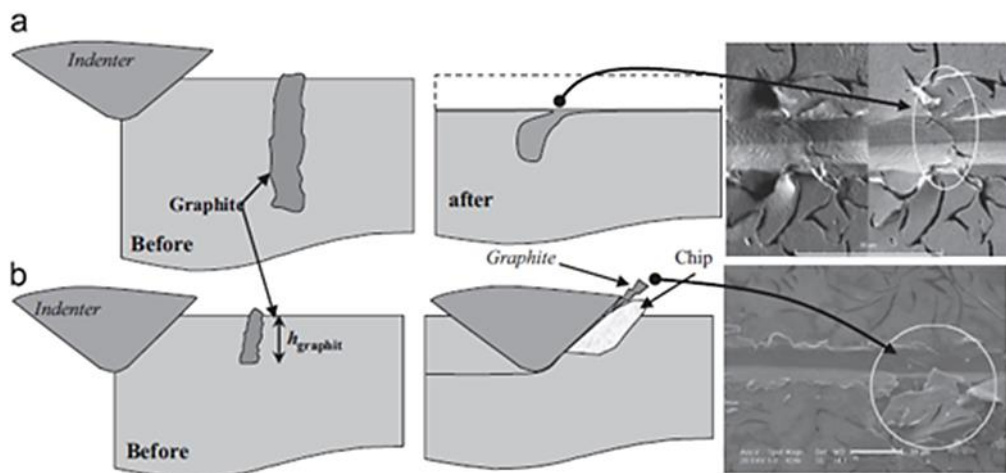


Figure 15: Wear mechanism: matrix behavior at different graphite depths [72].

The wear mode proposed by Mendas and Benayoun [72] states that spalling occurs due to the passage of the indenter through graphite area and may cause variation in the tangential force. Moreover, the depth of the graphite flakes relative to the scratch depth exerts considerable influence over the surface damage and wear mechanism. If the graphite flake depth is less than the scratch depth, the resulting damage depends on the deformation mode of the matrix. The flake deformation would be integrated into the matrix deformation within the chip. The portion of the graphite in front of the indenter is crushed and spread out into the groove leading to a weak decrease in the friction coefficient at high loads. However, depending

on the graphite depth, it can also be pushed from its cavity and runs out in front of the indenter tip [72].

Applying sclerometry in GCI, Alberto Franco, and Sinatora [76] performed a critical assessment of the role of the material removal factor “fab” in theoretical and practical approaches to abrasive wear of ductile materials, such as pearlitic GCIs. The authors measured the geometric parameters of the scratches with optical interferometry profilometer, observing correlations between scratch depth and applied load, pointing out to the presence of different mechanisms at the same scratch and the difficulties associated when measuring scratch groove and pile-up areas.

Furthermore, do Vale et al. [75] applied linear sclerometry to compare lamellar and compacted graphite irons, in order to analyze the aspects related to friction, scratch geometry, and graphite. Applying cutting tool inserts of 0.4 mm tip radius as indenters, values of apparent COF resulted lower for the lamellar graphite case. Linear sclerometry was also applied by Ghasemi and Elmquist [73,74] to study scratch wear mechanisms occurring in GCI piston rings. Their findings reinforced the role of graphite orientation, similarly to what has been previously demonstrated by Mendas and Benayoun [72,75].

The present review of linear sclerometry of GCI could be summarized: Graphite content and distribution affects the indentation depth profile and the apparent COF along the sliding distance. In general, the studies do not approach directly the effects of the matrix constituents, e.g., pearlite matrix, on either the indentation depth or COF. Instead, the models are most focused on the role played by graphite in the wear process. The models to explain the graphite effect in nano scale are deemed as analogous to the models in micro-macro scale. In the micro sclerometry, the application of conical indenters, e.g., $120^\circ/2\text{-}5\mu\text{m}$ ($2\theta/\text{tip radius } R$) is in compliance to both public standard (ASTM C1624-05 [70]) and previously published scientific work [72] approaching lamellar GCI scratch wear behavior.

2.4. On radiant matter: plasma

2.4.1. “A brief review on the radiant matter: plasma”

To throw light on the title of this doctorate research, with the fundamental basis behind the method of enhancement studied herein, we must go back more than a hundred years ago, with a brief review on the (gaseous) plasma state history.

Sir William Crookes describes in his 1879’s lecture [77] that, at 1816, Faraday, then a

mere student and ardent experimentalist, was twenty-four years old, and at this early period of his career he delivered a series of lectures on the general properties of matter, and one of them bore the remarkable title, “On Radiant Matter.”

Still according to Crookes [77], the great philosopher’s notes of this lecture are to be found in Dr. Bence Jone’s “Life and Letters of Faraday” [78], whereas the following is a passage in which Faraday first employs the expression radiant matter:

“If we conceive a change as far beyond vaporization as that is above fluidity, and then take into account also the proportional increased extent of alteration as the changes rise, we shall perhaps, if we can form any conception at all, not fall far short of radiant matter; and as in the last conversion many qualities were lost, so here also many more would disappear” [77,78].



Figure 16: a) William Crookes. b) Michael Faraday [79].

As explained by Crookes, Faraday was evidently engrossed with this so-called ‘far-reaching speculation’, for three years later 1819, when he brings evidence and argument to strengthen his hypothesis. His notes show that in the intervening three years he had thought much and deeply on this form of matter [77]. First, he points out that matter may be classed into four states: solid, liquid, gaseous, and radiant. And these modifications would depend on differences in their essential properties. In one of his letters quoted by Crookes, Faraday admits that the existence of radiant matter was yet unproved, and then proceeds, in a series of ingenious analogical arguments, to show the probability of its existence [77].

I may now notice a curious progression in physical properties accompanying changes of form, and which is perhaps sufficient to induce, in the inventive and sanguine philosopher, a considerable degree of belief in the association of the radiant form with the others in the set of changes I have mentioned.

As we ascend from the solid to the fluid and gaseous states, physical properties diminish in number and variety, each state losing some of those which belonged to the preceding state.

When solids are converted into fluids, all the varieties of hardness and softness are necessarily lost. Crystalline and other shapes are destroyed. Opacity and color frequently give way to a colorless transparency, and a general mobility of particles is conferred.

Passing onward to the gaseous state, still more of the evident characters of bodies are annihilated. The immense differences in their weight almost disappear; the remains of difference in color that were left are lost. Transparency becomes universal, and they are all elastic. They now form but one set of substances, and the varieties of density, hardness, opacity, color, elasticity, and form, which render the number of solids and fluids almost infinite, are now supplied by a few slight variations in weight, and some unimportant shades of color.

To those, therefore, who admit the radiant form of matter, no difficulty exists in the simplicity of the properties it possesses, but rather an argument in their favor. These persons show you a gradual resignation of properties in the matter we can appreciate as the matter ascends in the scale of forms, and they would be surprised if that effect were to cease at the gaseous state. They point out the greater exertions which Nature makes at each step of the change, and think that, consistently, it ought to be greatest in the passage from the gaseous to the radiant form.

(Michael Faraday) [77,78]

Crookes develops the idea of his research introduction stating: “If in the beginning of 19th century one had asked, what is a gas? The answer then would have been that it is matter, expanded and rarefied to such an extent as to be impalpable (...); invisible, incapable of assuming or of being reduced into any definite form like solids, or of forming drops like liquids; always ready to expand where no resistance is offered, and to contract on being subjected to pressure.” Sixty years before 1879 such were the attributes assigned to gases. Future research, however, has greatly enlarged and modified the views of these elastic fluids [77].

Gases were next considered to be composed of an almost infinite number of small particles or molecules, which are constantly moving in every direction without coming in contact with other molecule. But if exhaust the air or gas contained in a closed vessel, the

number of molecules become diminished, and the distance through which any one of them can move without coming in contact with another is increased, the length of the mean free path being inversely proportional to the number of molecules present [77].

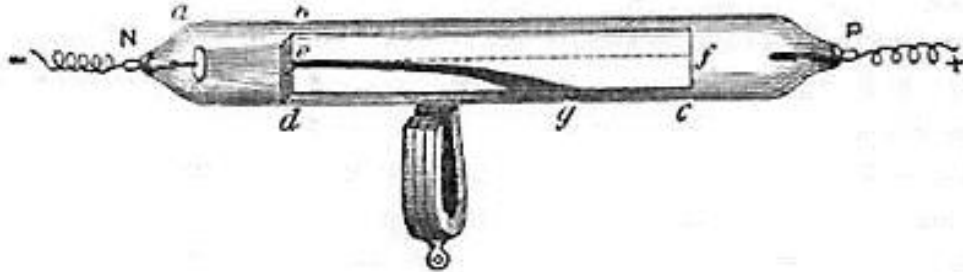


Figure 17: Radiant Matter is deflected by the action of a magnet [77].

Still according to [77], in such process, the longer the ‘molecules’ mean free path, the more the physical properties of the gas are modified. And at a certain point, on pushing the rarefaction still further, i.e., decreasing the number of molecules in a given space and lengthening their mean free path, experimental results showed that so distinct are these phenomena from anything which occurs in air or gas at the ordinary tension, that “we are led to assume that we are here brought face to face with matter in a fourth state or condition, a condition as far removed from the state of gas as a gas is from a liquid” [77].

The sequence of experiments performed as well as described with high level of details, by Sir William Crookes, characterized the existence of a fourth state of matter. One of the most prominent experiments is the cathode ray tube (Figure 17) [77] or simply, the Crookes tube.

2.4.2. Fundamentals of plasma physics

The previous chapter introduced the historical basis of the research on the fourth state of matter, so termed as “radiant matter”. The radiant state is modernly referred as “plasma” state. The approach of the physics fundamentals behind the plasma is necessary to understand the science of the phenomena, whose brief overview is provided in this section.

Radiant matter nature was further studied by Thompson, Ditmer and Langmuir [80], among other scientists. At this time, Langmuir adopted the name “plasma” to refer to radiant matter state, in 1928.

The word “plasma”, from Greek $\piλάσμα$, means "anything formed". The term was used because the glowing discharge molds itself to the shape of the Crookes tube (Figure 17) [81].

Langmuir wrote that, “Except near the electrodes, where there are sheaths⁴ containing very few electrons, the ionized gas contains ions and electrons in about equal numbers so that the resultant space charge is very small. We shall use the name ‘plasma’ to describe this region containing balanced charges of ions and electrons” [80].

According to Boulos, plasma state is frequently referred to as the fourth state of matter in the sequence: solid, liquid, gas and plasma. This classification as a state of matter is justified by the fact that more than 99% of the known Universe is in plasma state. A typical example is the sun, whose interior temperatures exceed 10^7 K. The high energy content of plasma compared to that of solids, liquids, or ordinary gases tends itself to a number of important applications [82].

Gurnett and Bhattacharjee briefly define plasma as an ionized gas consisting of positively and negatively charged particles with approximately equal charge densities [83]. Since the masses of ions and neutrals are much higher than the electron mass ($m_H/m_e = 1840$, where, m_H is the mass of the H atom, and m_e is the electron mass), neutrals and ions are classified as the heavy particles or the heavy component in a plasma. Some of these heavy particles may be in an excited state due to the high energy content of a plasma. Particles in an excited state can return to their ordinary or ground state by photon emission [82].

The latter process is at least partially responsible for the luminosity of a plasma. In addition to ions and neutral particles in the ground state, a plasma also contains excited species and photons, i.e., in general a plasma consists of electrons, ions and neutrals in the ground state, excited species, and photons. Such a mixture, however, qualifies as plasma only if the negative and positive balance each other, i.e., overall a plasma must be electrically neutral. This property is known as quasi-neutrality [82].

According to Boulos, Fauchais and Pfender [82], in contrast to an ordinary gas, plasmas are electrically conducting due to the presence of the free charge carriers. In fact, plasmas may reach electrical conductivities exceeding those of metals at room temperature. For an example, hydrogen plasma at one atmosphere heated to a temperature of 10^6 K has approximately the same electrical conductivity as copper at room temperature.

Based on laboratory experiments, Crookes [77] reported the following behavior properties of plasma, which has been the basis for the current technological application

⁴ Plasma sheath, or sometimes a positive ion sheath, is an electrically polarized region in a plasma which has a greater density of positive ions, and hence an overall excess positive charge.

feasibility: exerts powerful phosphorogenic action where it strikes; proceeds in straight lines; when intercepted by solid matter, casts a shadow; exerts strong mechanical action where it strikes; is deflected by a magnet; produces heat when its motion is arrested.

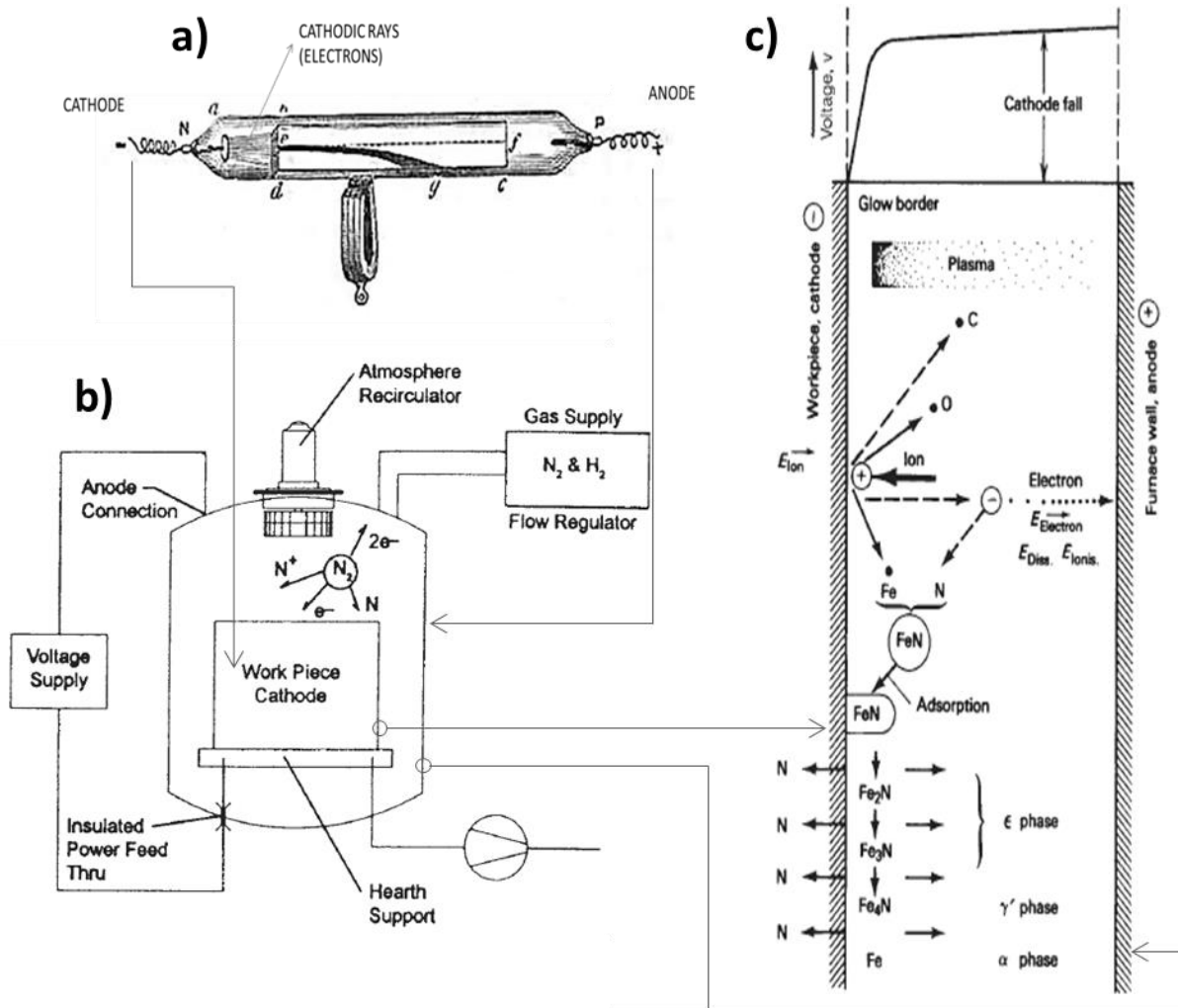


Figure 18: Relationship between 1879 Crookes tube and modern plasma nitriding unit. a) Crookes tube [77]. b) Schematic of a plasma nitriding source [10]. c) Glow discharge ion nitriding mechanisms (Koebel's models) [10].

According to George Thomson [79], in 1879 Thomas Edison invented the carbon filament lamp that required a fairly good vacuum. The need for better evacuation equipment led to improved vacuum pumps. These made discharge experiments easier and speeded up the study of cathode rays by such physicists as Eugene Goldstein in Germany, Sir William Crookes in England, and Jean Perrin in France. It was partly, at least, Crookes's work that led the German physicist Wilhelm Roentgen to discover X-rays on November 8, 1895 [79].

Finally, the work of William Crookes was definitely fundamental to the further development of plasma nitriding methods (Figure 18) in the early 1930s [10], which became significantly diffused nowadays.

3. Materials and experimental procedures

In this chapter, we describe the set of experiments and analysis performed at different time and temperature using in-lab textured flat specimens. Furthermore, we describe the case-study experiment performed in the as-honed cylindrical surface of an internal combustion engine cylinder.

The flat specimens, obtained from blanks extracted from a real engine cylinder block, were textured in laboratory in order to emulate the typical distribution of surface heights of an ordinary cylinder bore plateau honing [102] process. The flat form of the surface was particularly important to assure a repeatable methodology, and for delivering, a number of results appropriate for the statistical analysis.

The Case-study experiment and analysis were performed in the as-honed cylindrical surface of an internal combustion engine cylinder. Here, the surface has been textured through industrial honing operations. The tests and analysis were carried-out on the surface in its original form (cylindrical). Therefore, one among the potential applications of the research has been assessed.

3.1. Specimen preparation methods

The preparation method of both in-lab textured and as-honed (case study) specimens is described through the following subsections.

3.1.1. In-lab textured flat specimens

The flat specimens preparation sequence is schematically illustrated in Figure 19. Four specimens L 50 mm x W 25 mm x H 4 mm in size were obtained by milling operation. The blanks for milling were initially extracted from the wall region of a cylinder sector taken from a real engine cylinder block.

After being cubed to the foregoing mentioned dimensions, the surface corresponding to the cylinder bore side was textured, followed by the roughness characterization. The laboratory texturing method was empirically developed. A number of preliminary experiments comprehending grinding and respective 3-D roughness measurements were carried out until the

method election. The criterion established was to obtain a roughness profile whose areal surface texture parameters (e.g., S_{pk} , S_k , S_{vk}) [103], based on material ratio curve (also called Bearing Area Curve or Abbot Firestone Curve), were in similar range as those obtained in an ordinary cylinder block bore plateau honing process.

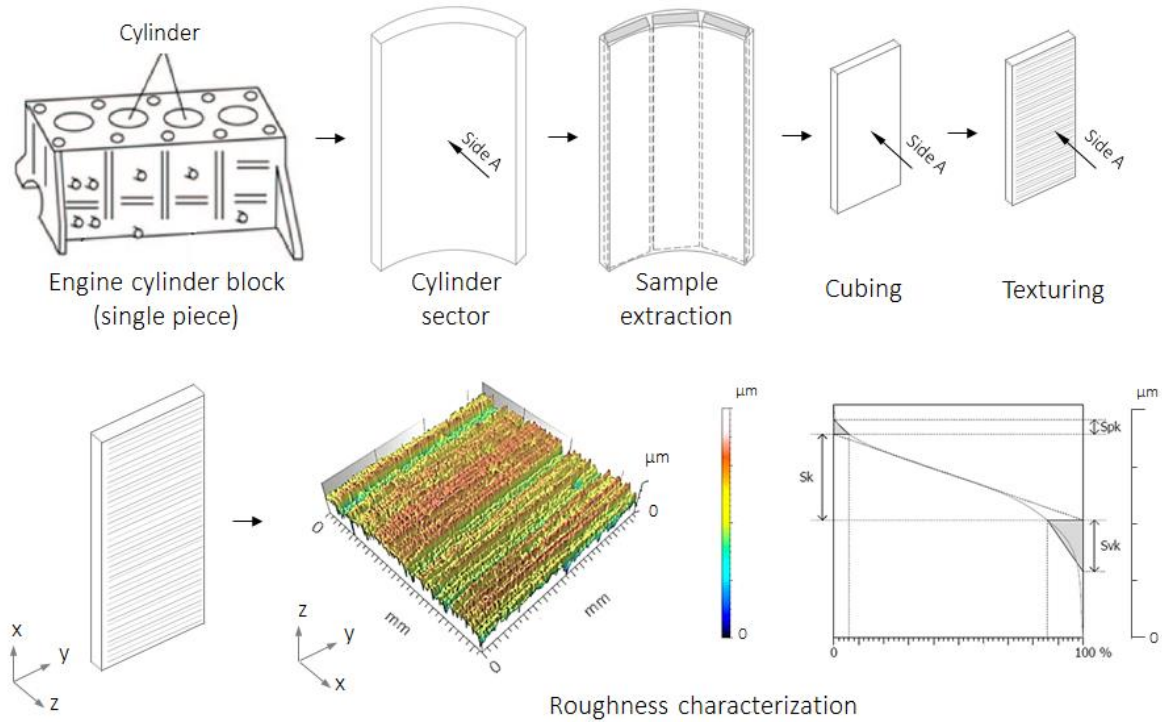


Figure 19: Specimen preparation scheme. In-lab textured flat specimens.

The texturing steps performed during the specimen preparation comprehended the following main steps (Figure 19): cutting and milling (cubing) to specified $L \times W \times H$ dimensions, manual grinding with silicon carbide (SiC) paper-220 grit, in 'y direction' during 60 seconds, followed by grinding with SiC paper-400 grit, in 'x direction' during 30 seconds, and final grinding with SiC paper-220 grit, in 'y direction' during 10 seconds.

During the laboratorial texturing process, the specimens were inspected in 3-D interferometry between grinding steps and after final grinding. As suitable, prior to characterization procedures the flat specimens were ultrasonic cleaned in isopropyl alcohol for 30 minutes.

3.1.2. Case-study: As-honed surface specimen

The case-study experiment and analysis were performed in the as-honed cylindrical surface of an internal combustion engine cylinder. The surface has been textured through industrial

plateau honing operations, three-stage, similar to the process described in previous works [102]. Tests and analysis were carried-out on the surface in its original cylindrical form.

A specimen L 10 mm x W 6 mm in size was cut from an engine cylinder block in the as-new condition. The sample location was close to the mid-stroke region [58] (piston ring-cylinder bore interface zone), as scheme shown in Figure 20. As suitable, prior to characterization procedures the case-study specimen was ultrasonic cleaned in isopropyl alcohol for 30 minutes.

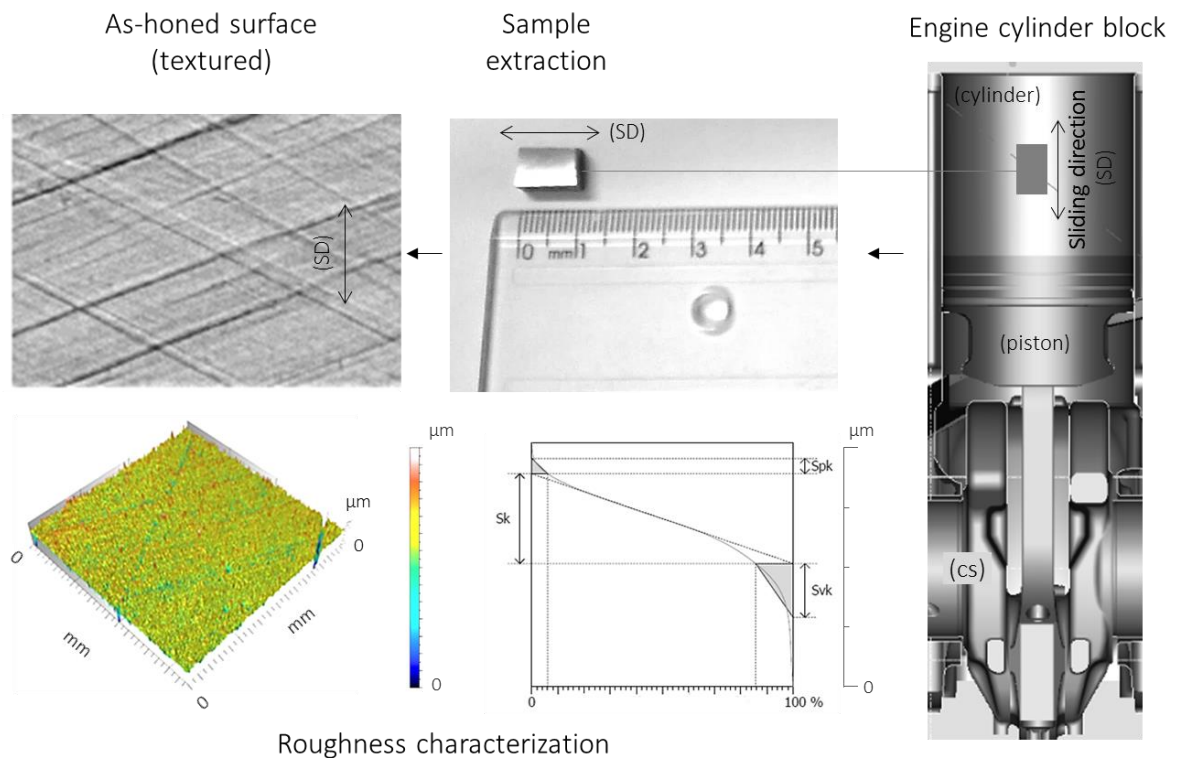


Figure 20: Specimen preparation scheme. Case-study: as-honed surface. Section on the right illustrates the cylinder block application in the engine, including the crankshaft (cs) and piston, whose sliding direction (SD) is indicated.

3.2. Material

In all of the experiments, the material microstructure consisted of flake graphite (ISO 945-1 [84]), with a minimum 70% of type A graphite, in a matrix of pearlite (minimum 95%) and with nominal hardness of 200 HB. The gray cast iron cylinder block was produced by casting and machining industrial operations, with the following nominal chemical composition in wt%: C 3.30; Si 2.20; Mn 0.70; P 0.05; S 0.08; Cr 0.40 and Cu 0.40.

Typical optical micrograph from the cylinder block material (as polished, not etched) is

shown in Figure 3a, where flake graphite is revealed. Figure 3b illustrates the typical view of the matrix of pearlite (etched, 2% Nital solution).

3.3. Roughness characterization

Roughness measurements of in-lab textured flat specimens and as-honed surface specimen were performed before and after SPN process, using a Taylor Hobson, Talysurf CCI 3-D Coherence Correlation Interferometer [85] (Figure 21).

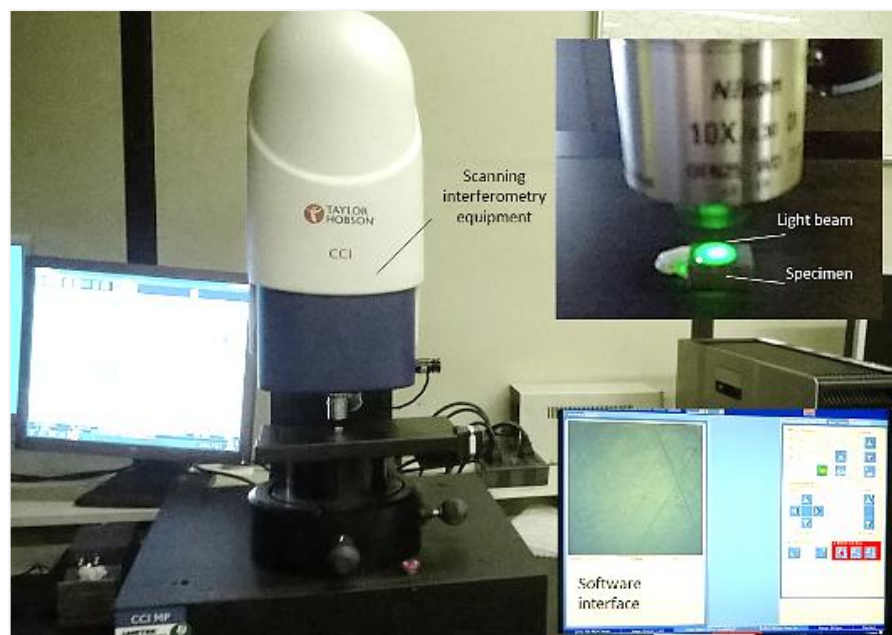


Figure 21: Taylor Hobson, Talysurf CCI 3-D Coherence Correlation Interferometer.

3.3.1. Roughness of the in-lab textured flat specimens

Roughness was measured with a group of five $1.6 \text{ mm} \times 1.6 \text{ mm}^5$ areal measurements (s1-s5) for each specimen. On the textured surface plane, the measurements location begun at x and y coordinate equal to 5 mm (s1), with the next measurements (s2-s5) in the x-direction and 2 mm distant one from each other, as shown schematically in Figure 22.

The software TalyMap 3-D was applied to calculate the standard roughness parameters after levelling of the measured data and filtering with Gaussian filter [86], similarly to previous

⁵ Common practice to assess the quality of a cylinder bore textured surface. The sampling area refers to the size of the xy plane in which an areal measurement is performed.

works [51]. Next, the roughness parameters were extracted. The roughness data analyzed in the following sections are concentrated in the most relevant parameters to this research purpose.

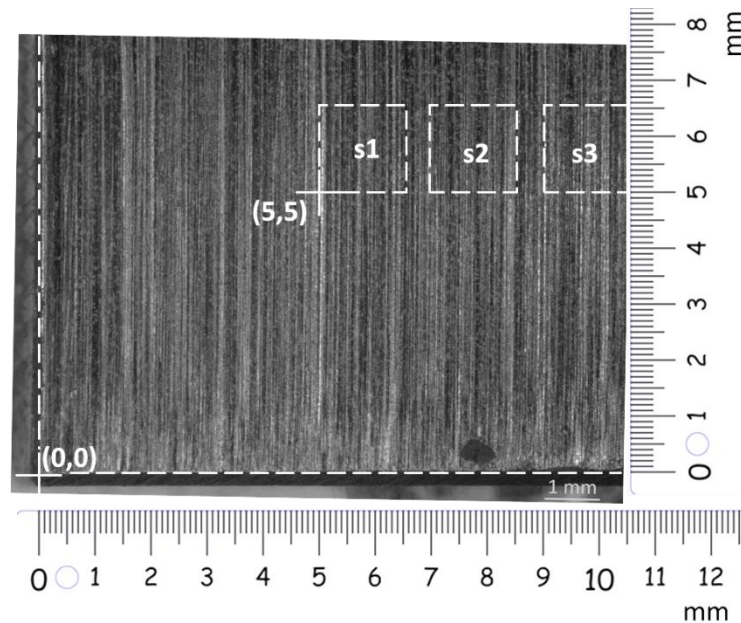


Figure 22: Roughness characterization scheme. In-lab textured flat specimens. On the textured surface plane, the measurements begin at x-coordinate 5 mm and y-coordinate 5 mm. The five 1.6 x 1.6 mm areal measurements (s1-s5) are 2 mm distant one from each other.

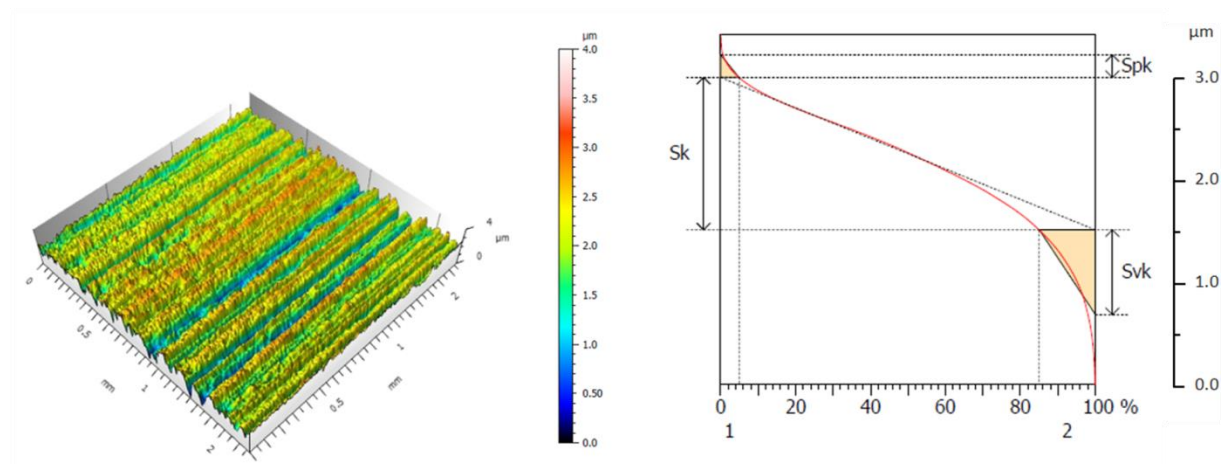


Figure 23: 3-D profile and the respective material ratio curve. In-lab textured flat specimens. The roughness parameters identified by S_k , S_{pk} , S_{vk} are extracted from the curve.

The S_q and the S_a parameters [103] were extracted and analyzed with the assistance of Minitab software [88], to confirm the texturing pattern between specimens in the condition before treatments is statistically similar. The procedure employed in the statistical analysis was One-way analysis of variance (One-way ANOVA) [89], once we wanted to compare the data of the four samples to confirm they do not differ at the 0.05 level of significance [90].

Sq and Sa [103] are the areal extension of the 2-D parameters Rq and Ra from ISO 4287 standard, mathematically defined in [87]. Ra (and Sa) is one of the most practical parameters employed to quantify mean roughness. Rq (and Sq) is specially applied in common tribology problems. In this case, Rq is commonly indicated by sigma (σ) and is used to calculate the composite RMS roughness (σ^*), applied to determine the film thickness ratio or lambda ratio, which is the relationship between minimum film thickness in a contact and the composite surface roughness [91].

3.3.2. Roughness of the as-honed surface specimen (case-study)

In the case-study, the comparative 3-D interference roughness results were obtained from two sampling areas [92]: (i) 1.6 mm x 1.6 mm and (ii) 0.3 mm x 0.3 mm (Figure 24). The first areal measurement (i) is a common practice to assess the quality of a cylinder bore textured surface. The analysis in small area (ii) is of greater interest to analyze local details of the topography with higher magnification - honed cylinder bore surfaces are inherently anisotropic and subject to a high level of grooves heterogeneity [93]. Consequently, the parameters calculation is dependent on the sampling area.

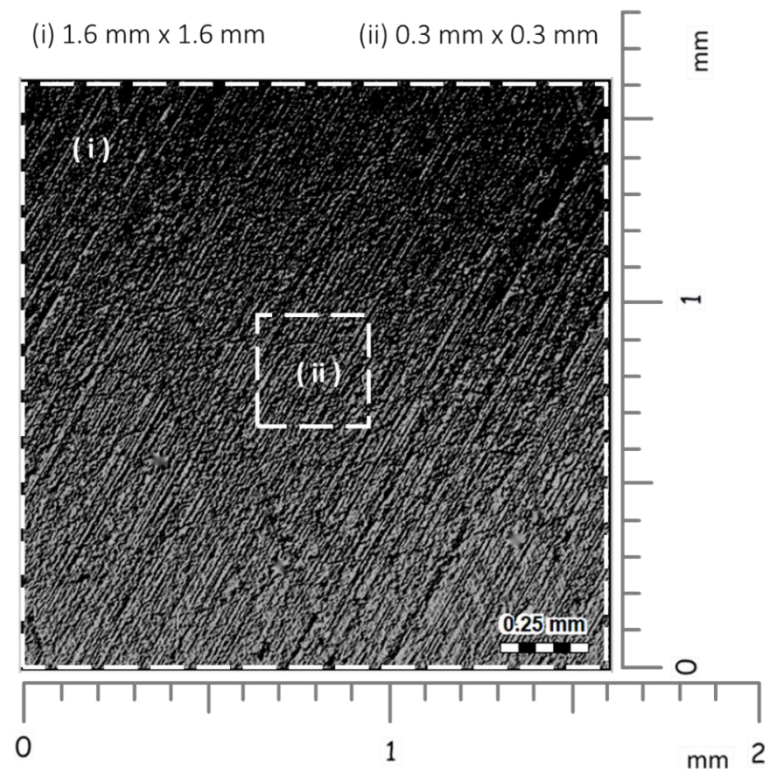


Figure 24: Roughness characterization scheme. As-honed surface specimen (case-study). Comparative 3-D interference roughness results were obtained from two sampling areas: (i) 1.6 x 1.6 mm and (ii) 0.3 x 0.3 mm.

The method applied during the roughness characterization of the as-honed surface specimen was similar to that applied for the in-lab textured specimens.

3.4. Shallow Plasma Nitriding (SPN) treatments

3.4.1. SPN treatments of the in-lab textured flat specimens

Once the One-Way ANOVA analysis confirmed that the texturing pattern between specimens was statistically similar the condition before the treatments, the plasma nitriding experiments were carried out, according to the matrix shown in Table 7. Two levels of temperature and time were considered.

Table 7: Matrix of Experiments.

Experiment	Temperature (°C)	Time (h)	Temperature (°C)	Time (h)
1	+	+	400	4
2	+	-	400	2
3	-	+	350	4
4	-	-	350	2

In all of the conditions described herein, both temperature and time were less intense compared to what has been reported in the literature about the nitriding of pearlitic gray cast irons (Table 5). The relatively low temperature and short time were defined to produce, intentionally, a shallow nitrogen implant, by means of a controlled plasma nitriding.

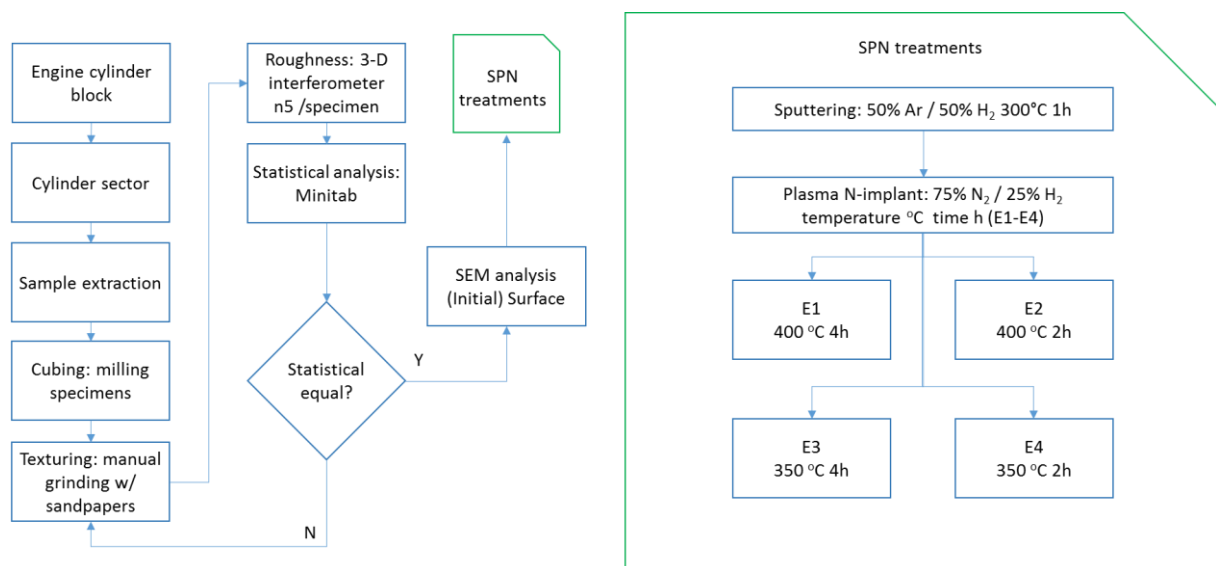


Figure 25: Flowchart of the specimen preparation and SPN treatments. In-lab textured flat specimens.

Figure 25 presents a flowchart of the specimen preparation and SPN treatments of the in-lab textured flat specimens. The identification of the specimens in association with each experimental condition was established according to Table 8. The Suffix “b” and “p” after “E#” indicates “before” and “after” treatment, respectively. Examples:

- E1b-C400h4 indicates a non-treated sample prepared for the experiment number one, i.e., in condition before being submitted to the treatment one;
- E1p-C400h4 indicates the same sample after being treated at 400 °C during four hours.

After a sputtering step of 50% Ar / 50% H₂ plasma at 300°C for one hour, each textured specimen was plasma nitrided at its temperature and time (Table 8) in a 75% N₂ / 25% H₂ atmosphere, at the Plasma Laboratory of the Department of Metallurgical and Materials Engineering of the University of São Paulo (Figure 26).



Figure 26: The plasma treatment unit of Plasma Laboratory of the Department of Metallurgical and Materials Engineering of the University of São Paulo.

Table 8: Identification of specimens.

Specimen Code	Description
E1 C400 h4	Experiment 1, 400 °C, 4 hours
E2 C400 h2	Experiment 2, 400 °C, 2 hours
E3 C350 h4	Experiment 3, 350 °C, 4 hours
E4 C350 h2	Experiment 4, 350 °C, 2 hours

3.4.2. SPN treatments of the as-honed surface specimen (case-study)

In the case study, the SPN time and temperature set-up selected was the same as that studied in the experiment number four (shortest time and lowest temperature). The treatment was performed in the as-honed cylindrical surface of an internal combustion engine cylinder, after roughness characterization.

The method applied during the SPN treatment of the as-honed surface specimen was similar to that applied for the in-lab textured specimens. Figure 27 presents a flowchart of the specimen preparation and SPN treatment of the as-honed surface specimen (case-study).

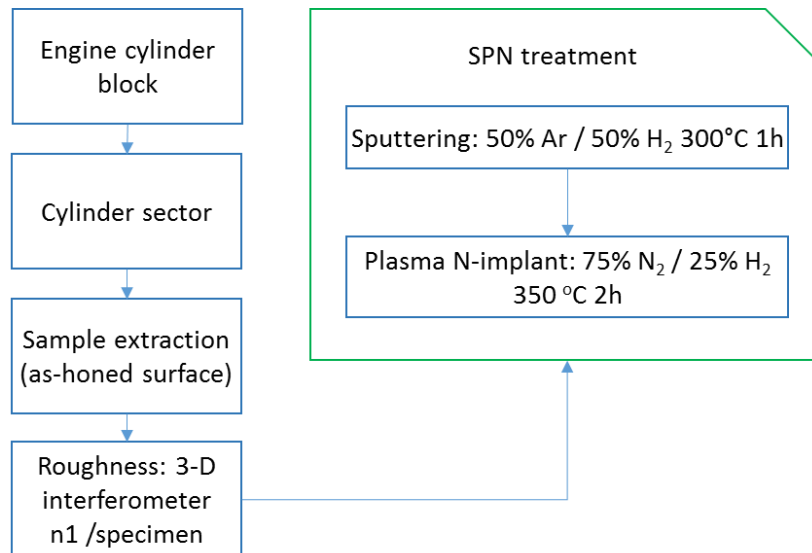


Figure 27: Flowchart of the specimen preparation and SPN treatment. Case-study: As-honed surface specimen.

3.5. X-Ray diffraction (XRD) analysis

The experimental procedure to identify the nitride phases formed during the SPN process comprised the acquisition of X-Ray diffractograms using an X'Pert Pro diffractometer, with position sensitive X'Celerator detector and Cu tube. The experimental conditions were: CuK α radiation, 45 kV, and 40 mA, 20° to 120° angle (2 θ) range, 0.02° step, and 10s time per step.

The XRD exams were performed directly on the surface of both in-lab textured flat specimens and as-honed surface specimen (case-study). The identification of the phases was carried out by comparison with ICDD (International Centre for Diffraction Data) standards, using the software Crystallographica Search-Match (CSM).

For comparison purposes, measurements were carried out in two conditions: before and after plasma nitriding treatment, following the same experimental procedure.

3.6. N-concentration (wt%) as a function of the distance from the surface

3.6.1. Quantitative analysis of N: Wavelength-dispersive X-ray spectroscopy (WDS)

A cross section of each treated sample was submitted to a wavelength-dispersive X-ray spectroscopy (WDS) microanalysis, in order to characterize, chemically, the SPN layer, measuring the nitrogen (wt%) content as a function of the distance from the surface.

Precision abrasive cutting machine model ATM Brillant 220 was used (Figure 28) to obtain cross sections perpendicular to the textured surface with high level of reproducibility. The cross sections were hot compression-mounted in phenolic resin and ground using increasingly finer silicon carbide (SiC) papers, from grit size 180 down to 1200, on an automatic polisher, and then polished using standard polishing clothes and polycrystalline diamond paste of reducing diamond particle sizes from 9 μm to 3 μm .



Figure 28: Precision abrasive cutting machine. Detail: section location guided by laser.

Similarly to previous works [67,68], the WDS analyses were carried out in an Oxford WDX600 spectrometer (Figure 29) with take-off angle of 35° , coupled to a Cambridge Stereoscan 440 scanning electron microscope equipped with a LaB_6 emission source operating at 10 or 12 kV. Nitrogen was measured by using synthetic LSM60 crystal.

Comparing WDS and EDS technics, recent literature [94] explains that the power of WDS is its energy resolution and peak-to-background ratios, which are unmatched among microanalytical techniques. This power is revealed by qualitative or quantitative analysis. Qualitative analysis identifies X-ray lines by using peak-to-background measurements or by the inspection of WDS spectra generated by scanning the spectrometer over a range of X-ray energies, revealing which elements are present in the sample.



Figure 29: Oxford WDX600 spectrometer coupled to a Cambridge Stereoscan 440 scanning electron microscope of LCT-USP. Nitrogen was measured by using synthetic LSM60 crystal.

Accordingly, Figure 30 presents an example on which a wavelength-dispersive spectroscopy (WDS) energy scan (blue) overlain on an energy-dispersive (EDS) spectroscopy spectrum (red), both acquired from monazite. Compared to EDS, the significantly better resolution and peak-to-background ratios of WDS clearly reveal which elements are present in a sample [94].

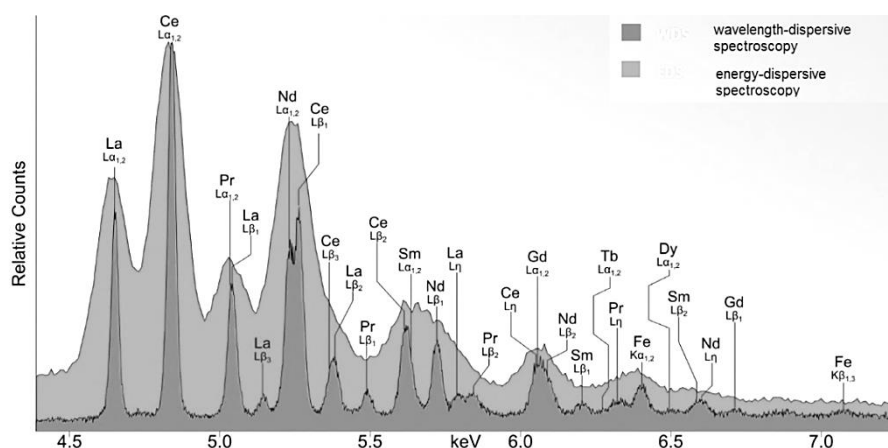


Figure 30: A wavelength-dispersive spectroscopy (WDS) energy scan overlain on an energy-dispersive (EDS) spectroscopy spectrum, both acquired from monazite ($[\text{La,Ce,Pr,Nd,Sm,Gd}]\text{PO}_4$). Compared to EDS, the better resolution and peak-to-background ratios of WDS clearly reveal which elements are present in a sample [94].

In the present study, the N-concentration of in-lab textured specimens has been quantitatively determined through WDS analysis, for the different temperature and time experiments; whereas the as-honed surface specimen (case-study) was analyzed through both

WDS and EDS, so that the presence of nitrogen could be qualitatively confirmed in a honed sample treated by virtue of same procedure with respect to one of the in-lab textured specimens. The next sub-section explores the aspects of such qualitative analysis.

3.6.2. Qualitative analysis of N: Energy-dispersive spectroscopy (EDS)

In the case-study, the cross section of the SPN treated sample was submitted to an energy-dispersive spectroscopy (EDS) analysis, in order to assess, qualitatively, the N-enrichment in the surface in contrast with the core. The cross section was directly observed in a scanning electron microscope, equipped with EDS system. Three EDS spots were performed at 1 μm depth from surface and distant 5 μm from each other. In addition, other EDS spots were performed at increasing distances from surface and towards to the sample core.

Important to mention that, in fact the application of EDS to assess N-enrichment presents limitations. According to Toro and Tschiptschin [68], the detection of N by EDS is usually prevented either by the reduced intensity of X-rays associated with this element, or by the overlapping effects caused by elements such as Mo and Mn since the spatial resolution of this technique is always worse than 130–150 eV.

The improved spatial resolution of WDS (namely 3–10 eV) can avoid overlapping problems if the operating conditions are properly chosen. The key factor in quantification is the precise balance between the probe size and the detection statistics, given that smaller probes require lower currents, and therefore the number of counts per second is strongly reduced when the volume analyzed is small [68].

Close correspondence between the N-content and the hardness profile has been reported by previous works [68]. When no nitride formation was observed (all N in solid solution), it has been observed that WDS measurements at the surface showed good correlation with the results from different techniques, as optical spectroscopy and glow discharge optical spectroscopy, as well as with the theoretical solid-gas equilibrium N-content calculated by thermodynamic modeling (CALPHAD) [68].

In spite of these facts, EDS analysis procedure is relatively simple and less expensive than WDS. Taking into consideration that in-lab textured specimens were analyzed via WDS and understanding the above-mentioned restrictions of EDS to detect N-concentration, this work will limit the usage of such technic to report a qualitative estimate of N-enrichment of the as-honed surface specimen (case-study), for practical assessment purposes.

3.7. Comparative scanning electronic microscopy (SEM) analysis of the surface

An equipment model ZEISS-EVO-MA10 (Figure 31) was used to perform the SEM analysis, on the specimen surface. Aiming to identify any eventual after-treatment surface changes, a before/after analysis has been carried out. The specimens were ultrasonic cleaned in isopropyl alcohol for 30 minutes before the surface SEM measurements.



Figure 31: Scanning electron microscope model ZEISS-EVO-MA10.

The analysis on the surface occurred by direct observation of the first 1.6 mm x 1.6 mm area measurement (s1) of each specimen, before and after the SPN treatment. These are the regions which had also been previously analyzed through the 3-D interferometer, at x, y = 5.0, 5.0 mm coordinates. In addition to the interferometer-like scale image, a greater magnification SEM image (130 μm x 130 μm area) was also captured in the same region, for side-by-side comparison purposes of details in the graphite and texturing grooves scale.

3.8. Microhardness analysis

Vickers HV0.01 surface microhardness measurements were performed using standard Vickers microhardness tester, with 10 gf of load. The hardness indentations were performed directly on

the sample surface. For comparison purposes, the measurements were carried out in two conditions: before and after plasma nitriding treatment. Average hardness values and their respective standard deviations were calculated, as well as the resulting depth of the indenter penetration.

For the sake of accuracy, each individual indentation of in-lab textured flat specimens had the diagonal values (d_1 and d_2) measured and documented through scanning electronic microscopy. Therefore, the diagonal values were used to compute Vickers hardness (HV) and indentation depth (h_{depth}).

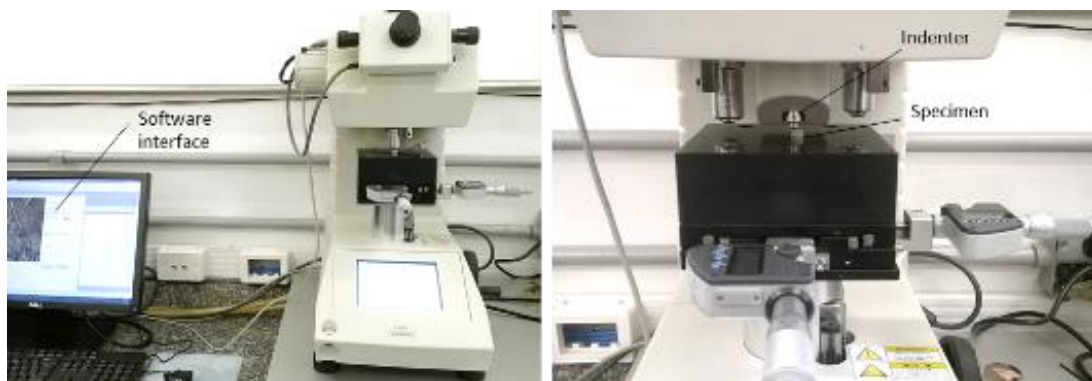


Figure 32: Microhardness tester.

3.9. Instrumented linear sclerometry test

The sclerometry test were performed based on ASTM C1624-05 [70] using a ‘Micro scratch tester CETR-UMT, Multi-specimen test system’ equipment, which is shown in Figure 33.

The scratch tester had a conical diamond indenter with an apex angle of 120° and spherical tip radius of $200\ \mu\text{m}$. A pre-load equal to 1N has been applied during 10s. Next, the indenter displacement was linearly moved increasing load with time, from 1N to 10N, with displacement velocity of $0.028\ \text{mm/s}$, resulting in a risk of 5 mm in length.

3.9.1. Sclerometry test of the in-lab textured flat specimens

On each flat in-lab textured specimen (E1-E4), a sequence of five scratches was made. In addition, a non-treated specimen has been submitted to the same procedure. Therefore, average and standard deviation could be computed in a comparative basis.

3.9.2. Sclerometry test of the as-honed surface specimen (case-study)

The as-honed textured specimen was tested in comparison to a non-treated specimen. Since the case-study experiment were performed in the as-honed cylindrical surface of an internal combustion engine cylinder, the scratch was carried-out on the surface in its original form, i.e., cylindrical.

Therefore, the diamond indenter was adjusted with respect to the specimen support so that the scratch was done in the bottom of the circular profile defined by the engine cylinder bore radius. The test was performed following the operational sliding direction in the internal combustion engine application (Figure 20).

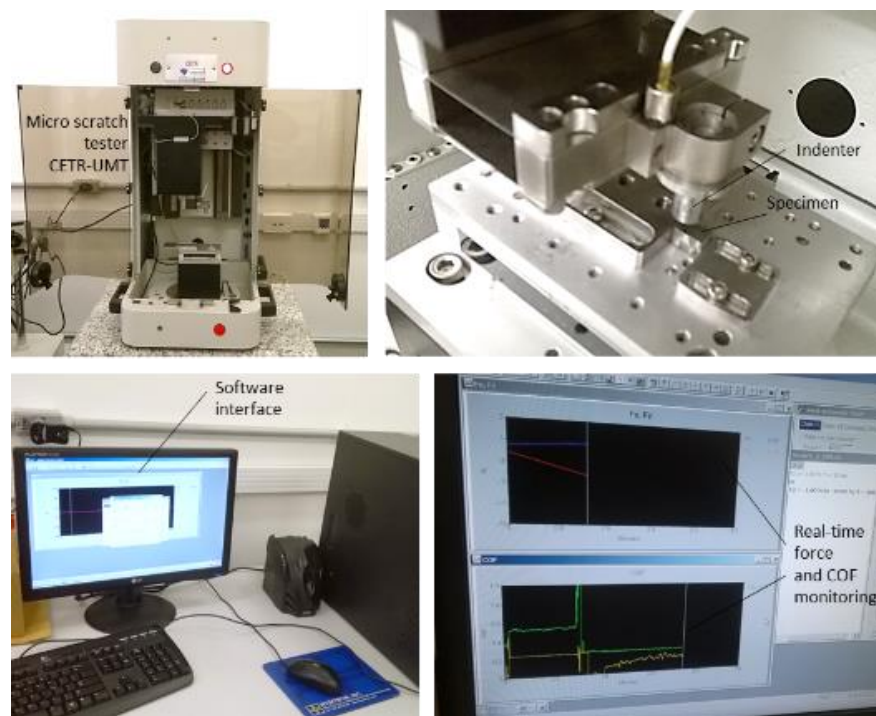


Figure 33: CETR-UMT Micro scratch tester.

3.10. Sclerometry results analysis

3.10.1. 3-D surface profile, “groove area” (S_s), “pile-up area” (S_p) and depth (dh)

The groove profile resulting from the sclerometry test was further assessed through 3-D interference measurements. Likewise roughness measurements, it was applied a Taylor Hobson, Talysurf CCI 3-D (Figure 21) for scanning the scratched region of the surface.

After the topography data acquisition and filtration, 2-D scratch cross sections were extracted using the software TalyMap 3-D, so that both “pile-up area”⁶ (S_p) and “groove area” (S_s) - could be computed (Figure 34), similarly to previous work [76]. In addition, groove depth (dh) has been computed. Table 9 shows the progressive values of load applied by the indenter as a function of the distance and time, with respective measuring points A-D (Figure 35) of the 2D cross sections.

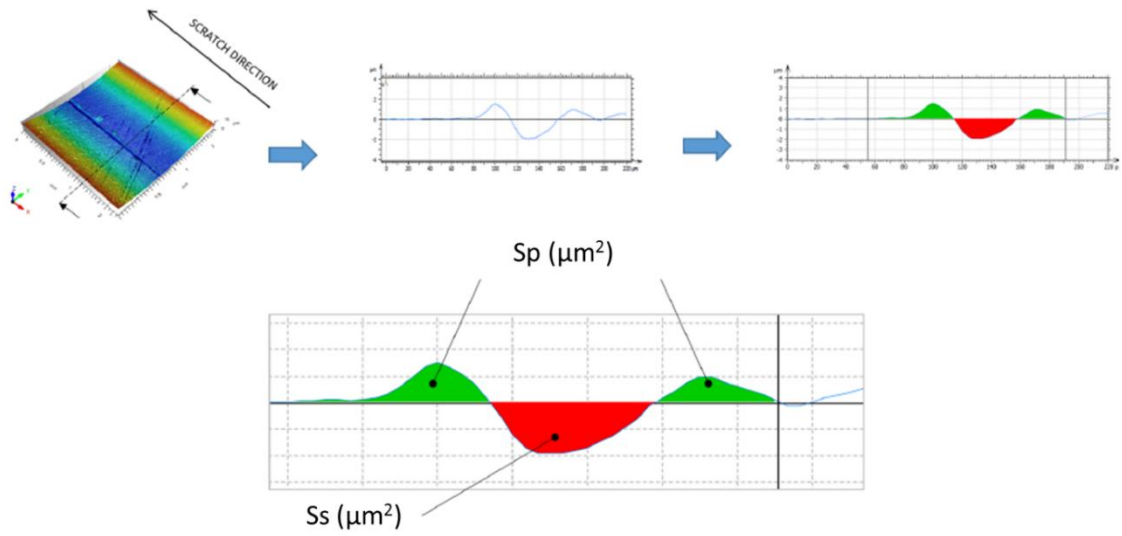


Figure 34: 2-D acquisition of S_p and S_s from the 3-D interference profile.

Table 9: Corresponding load by indenter distance.

Point	Distance (mm)	Time (s)	Load (N)
-	0	0	1.0
A	1.0	36	2.8
B	2.0	71	4.6
C	3.0	107	6.4
D	4.0	143	8.2
-	5	180	10.0

⁶ This work employs terminologies for S_p and S_s based on L.A. Franco and A. Sinatora in [76].

Synonyms of S_p : pile-up area; plastic flow area

Synonyms of S_s : groove area; groove section area; groove ditch area

The “pile-up area” S_p is defined as the total area due to the displacement of material to the sides of the groove (pile-up). Such definition is based on the idealized representation proposed by Buttery and Archard, shown in Figure 36. Comparing S_p and S_s , one could investigate whether the abrasion mechanism tends towards microplowing ($S_p=S_s$), microcutting ($S_p \ll S_s$) or other possibilities [76,95].

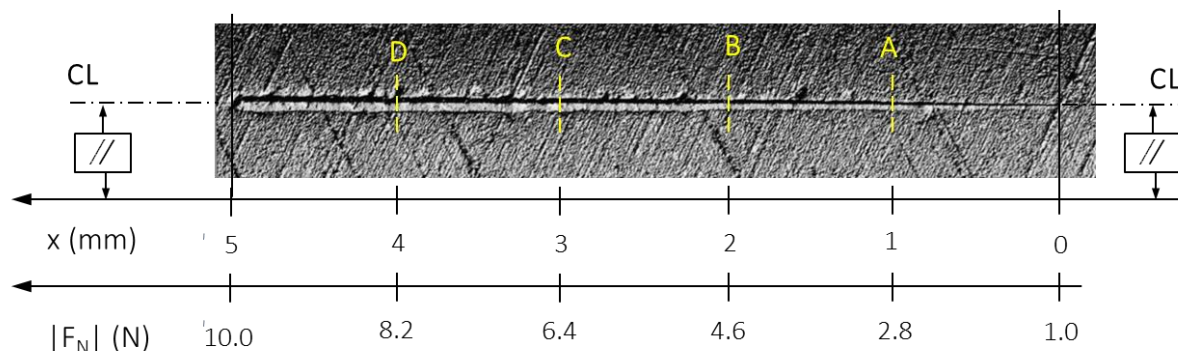


Figure 35: The coordinates of measuring points. $|F_N| = 1.8x+1$ (N)

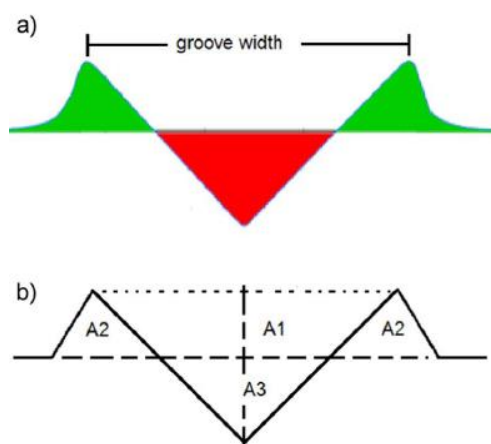


Figure 36: a) Typical groove showing pile up (green zone). b) Idealized representation of the groove. Adapted from Buttery and Archard [95] by Franco and Sinatora [76].

As highlighted by Franco and Sinatora based on previous work [76], during the analysis of results, it is important to bear in mind a known limitation, i.e., the fact that the material close the indenter is compressed plastically so that some fraction of the ‘lost’ material is not actually removed from the solid.

In the flat in-lab textured experiments, S_s and S_p were acquired from a group of three sclerometry test replications for each specimen (E1-E4). In addition, a non-treated specimen has been submitted to the same procedure. Therefore, average and standard deviation were

computed as a function of scratch distance. Similarly, the as-honed textured specimen was also analyzed in comparison to a non-treated specimen, after being submitted to sclerometry test.

3.10.2. SEM analysis of the scratch and critical damage load

Afterwards, the resulting scratch has been observed in scanning electron microscope (SEM) model Philips XL30. Test damage features were analyzed. The critical damage load [70] range was estimated, using as a criterion the occurrence of microcracks in material matrix associated with the distance and the corresponding normal force value.

Likewise previous characterizations, specimens in condition before and after SPN treatment were analyzed for comparison purpose.

3.10.3. Friction based on sclerometry test

Apparent COF as a function of time and load was measured in real-time using the CETR-UMT Multi-specimen test system coupled to the software interface (Figure 33).

Furthermore, the data resulting from specimens in condition before and after SPN treatment were plotted in charts for comparison purpose.

The apparent COF was computed and compared based on the results of five replications for each experiment E1-E4, so that reporting average associated with corresponding standard deviations.

Apparent COF chart of the as-honed textured specimen was also analyzed in comparison to a non-treated specimen. Both results were combined and presented in a single chart.

3.11. Flowchart of methods

Finally, the flowchart of methods of the in-lab textured flat and of the as-honed surface specimen (case-study), is shown in Figure 37 and Figure 38, respectively.

The charts consolidate all the analysis accomplished for each SPN experimental condition, with the summarized task flow. The main outcomes from test and characterization are indicated in flowchart bottom line.

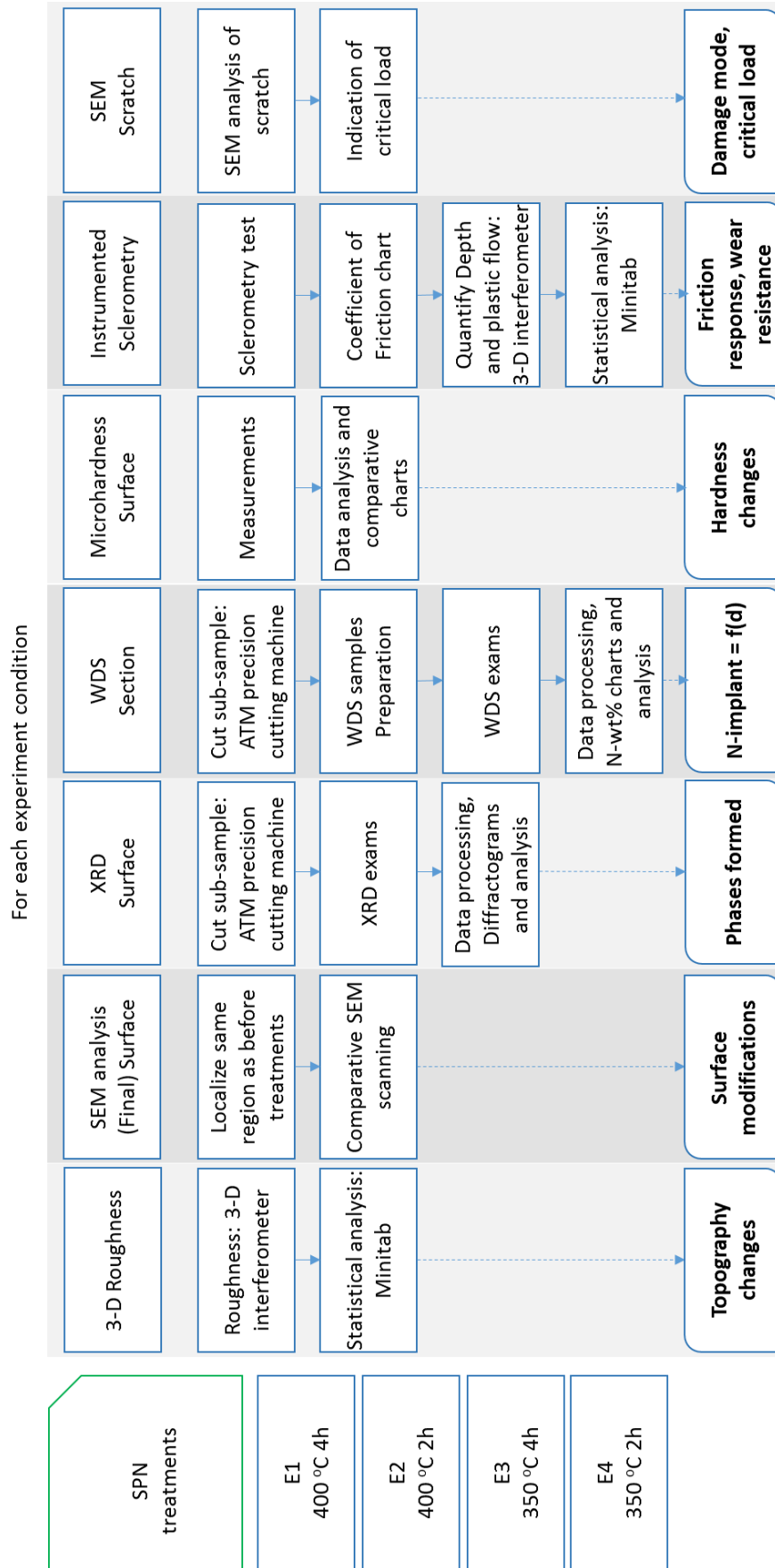


Figure 37: Flowchart of methods. In-lab textured flat specimens.



Figure 38: Flowchart of methods. Case-study: As-honed surface specimen.

4. Results and Discussion

4.1. In-lab textured flat specimens

4.1.1. Roughness results

4.1.1.2. Texturing pattern between specimens before treatments

The textured surface plane characterized through software TalyMap 3-D is shown in Figure 39a. The color scale indicates the resulting heights in μm from valley to peak. Sq and Sa parameters obtained from the 3-D profile are shown in Figure 39b. The figure shows the results of the specimen E1, areal measurement s1. Similarly, same type of data was obtained to all of the specimens, whose quantitative results were consolidated in Table 10.

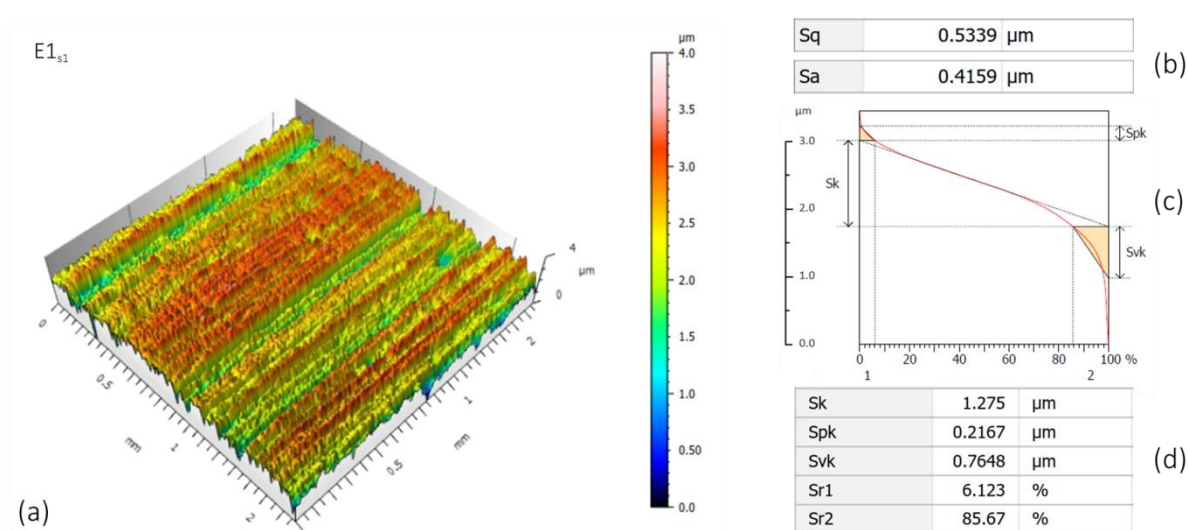


Figure 39: a) 3-D profile of the textured surface plane. The color scale indicates the resulting heights from valley to peak. b) Sq and Sa parameters results calculated by TalyMap 3-D software. c) Material ratio curve and respective Sk, Spk, Svk, Sr1, Sr2 parameters (d) extracted from the curve. In-lab textured flat specimen E1 in the initial condition (before SPN treatment).

Material ratio curve and respective Sk, Spk, Svk, Sr1, Sr2 parameters extracted from the curve are also shown in Figure 39c and Figure 39d. As described beforehand, such type of data will be applied to evaluate potential after-treatment topography changes. A detailed before/after analysis has been carried out to all of the specimens, whose results are consolidated and presented in posterior sub-section.

Sq and Sa parameters were computed to be analyzed with the assistance of Minitab

software [90] to confirm the texturing pattern between specimens is statistically similar in the condition before the treatments. Complete roughness results of the five 1.6 mm x 1.6 mm areal measurements (s1-s5) for each specimen are shown in Table 10. Average and standard deviation of each specimen in the initial condition (before SPN treatments) are reported.

Table 10: Sq and Sa roughness parameters of the textured samples.

Param (Unit)	Sq (μm)				Sa (μm)			
	E1b	E2b	E3b	E4b	E1b	E2b	E3b	E4b
Sample								
s1	0.53	0.53	0.49	0.48	0.42	0.42	0.40	0.37
s2	0.61	0.56	0.52	0.48	0.45	0.44	0.40	0.39
s3	0.69	0.53	0.56	0.45	0.53	0.43	0.44	0.36
s4	0.53	0.56	0.49	0.56	0.43	0.43	0.38	0.45
s5	0.42	0.47	0.62	0.47	0.33	0.38	0.50	0.38
Avg	0.56	0.53	0.54	0.49	0.43	0.42	0.43	0.39
StdDev	0.10	0.04	0.05	0.04	0.07	0.02	0.05	0.04

4.1.1.2.1. Statistical analysis of roughness results before SPN using Minitab software

Minitab One-Way ANOVA Summary Report of the tests for Sq and Sa parameter, in the condition before experiments, are shown in Figure 40 and Figure 41, respectively. In order to conduct the statistical analysis, a hypothesis test was created.

Hypothesis test: “All the samples in the same roughness range, i.e., texturing pattern between specimens is statistically similar the condition before the treatments.”

Based on the group of data (Table 10), calculated p-value resulted 0.349 for Sq, and 0.460 for Sa, thus the differences among the means are not significant ($p > 0.05$). In addition, ‘Means comparison chart’ (Figure 40 and Figure 41) indicated that means do not differ significantly.

Minitab One-Way ANOVA Diagnostic Report of the tests for Sq and Sa parameter, in the condition before experiments, are shown in Figure 42 and Figure 43, respectively. In this report, group of roughness data (Table 10) were plotted in ‘Distribution of data’ and ‘Data in Worksheet Order’ Minitab charts. Software analysis resulted that are consistent, i.e., data location and spread are in similar range, as well as there are no outlier or unusual data points.

As a result of the One-way analysis of variance [89], the texturing pattern between specimens was assumed statistically equal in the condition before the treatments, with 95% of confidence level (0.05 level of significance).

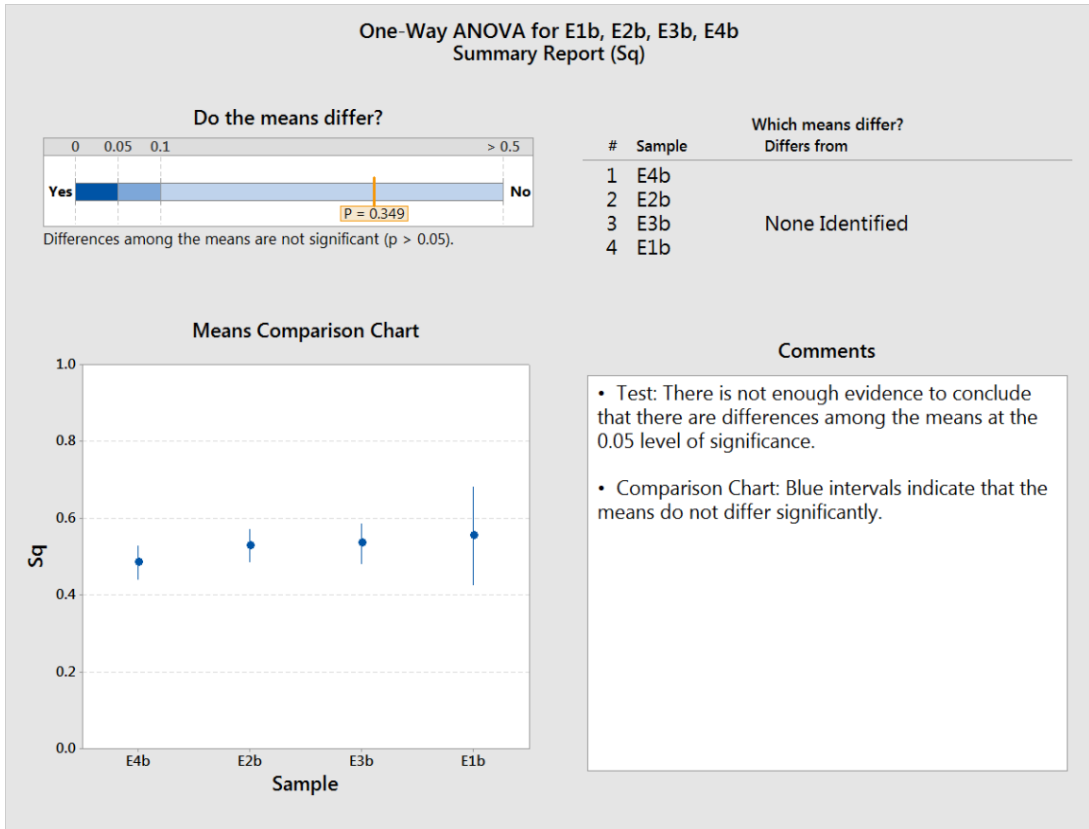


Figure 40: Minitab One-Way ANOVA Summary Report. Test for Sq parameter, before experiments.

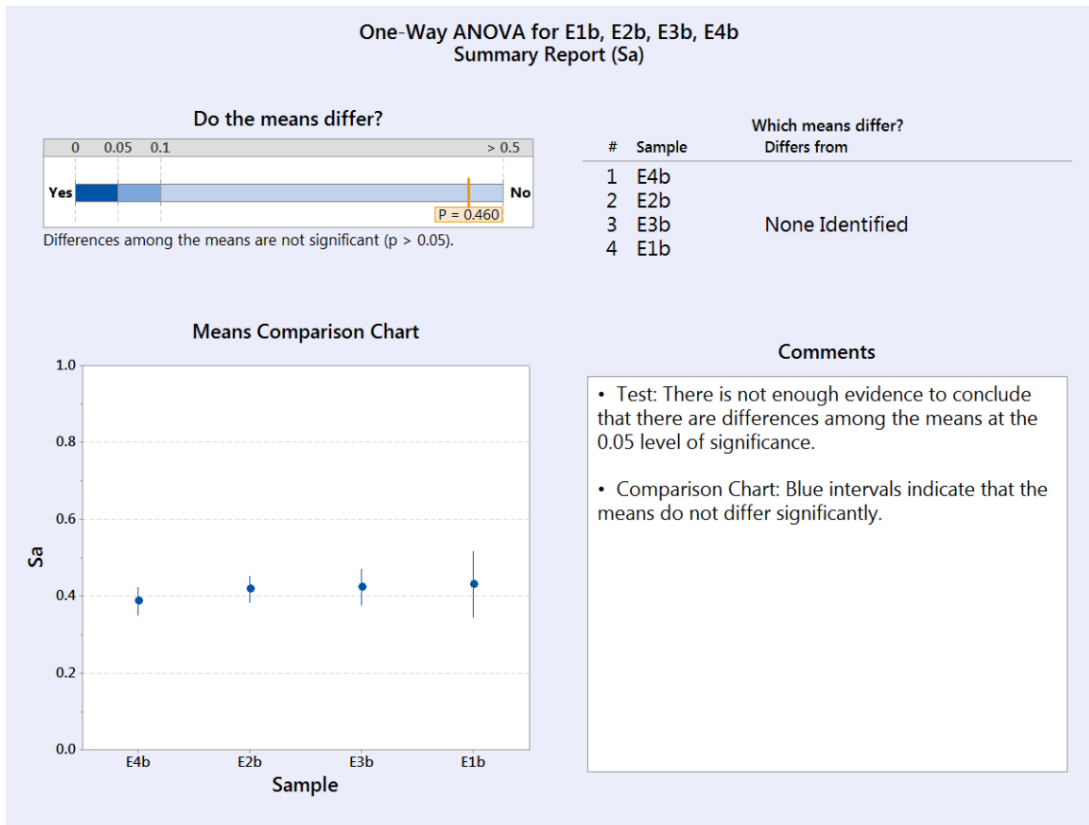


Figure 41: Minitab One-Way ANOVA Summary Report. Test for Sa parameter, before experiments.

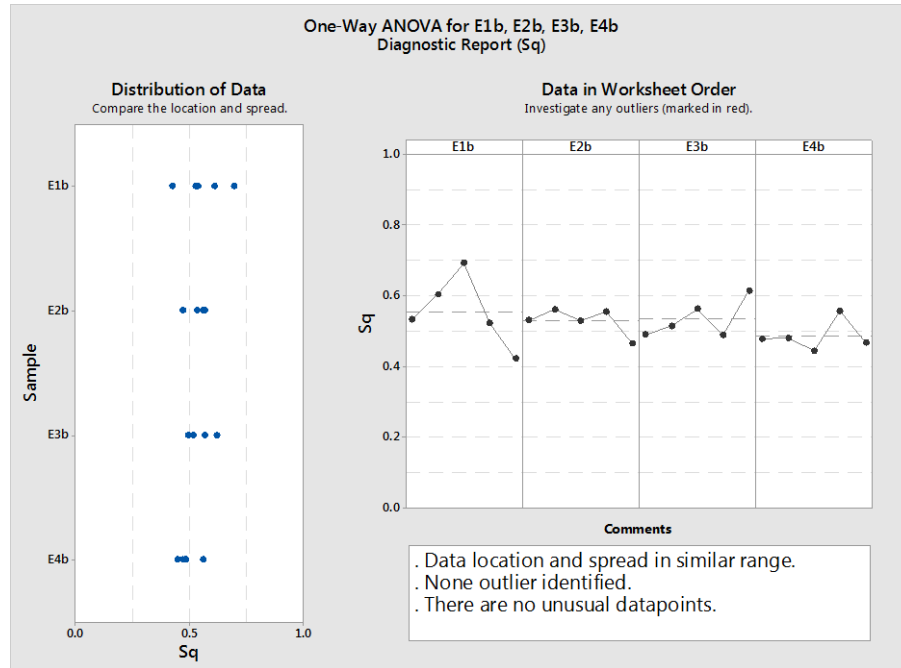


Figure 42: Minitab One-Way ANOVA Diagnostic Report. Test for Sq parameter, before experiments.

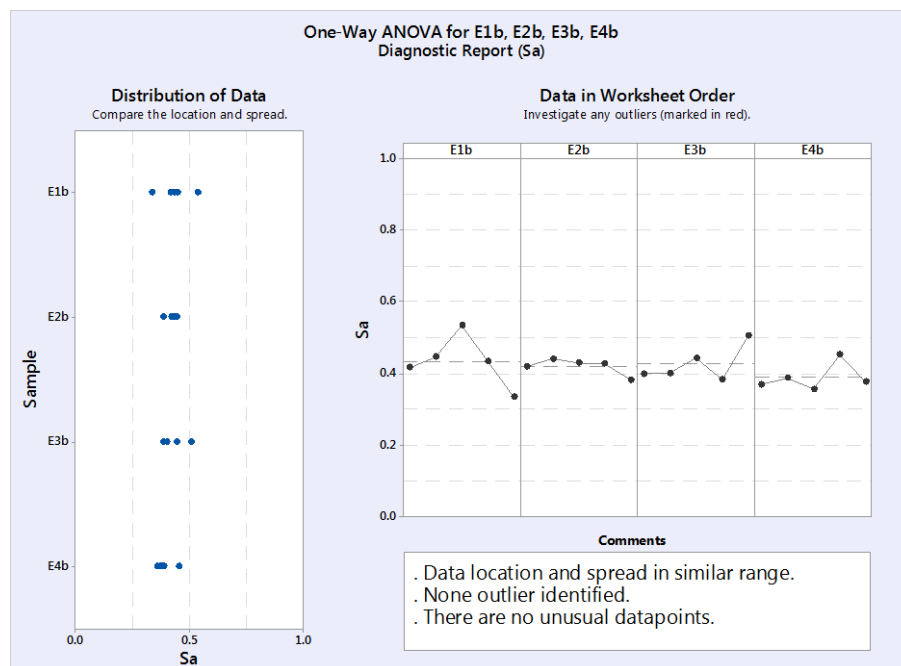


Figure 43: Minitab One-Way ANOVA Diagnostic Report. Test for Sa parameter, before experiments.

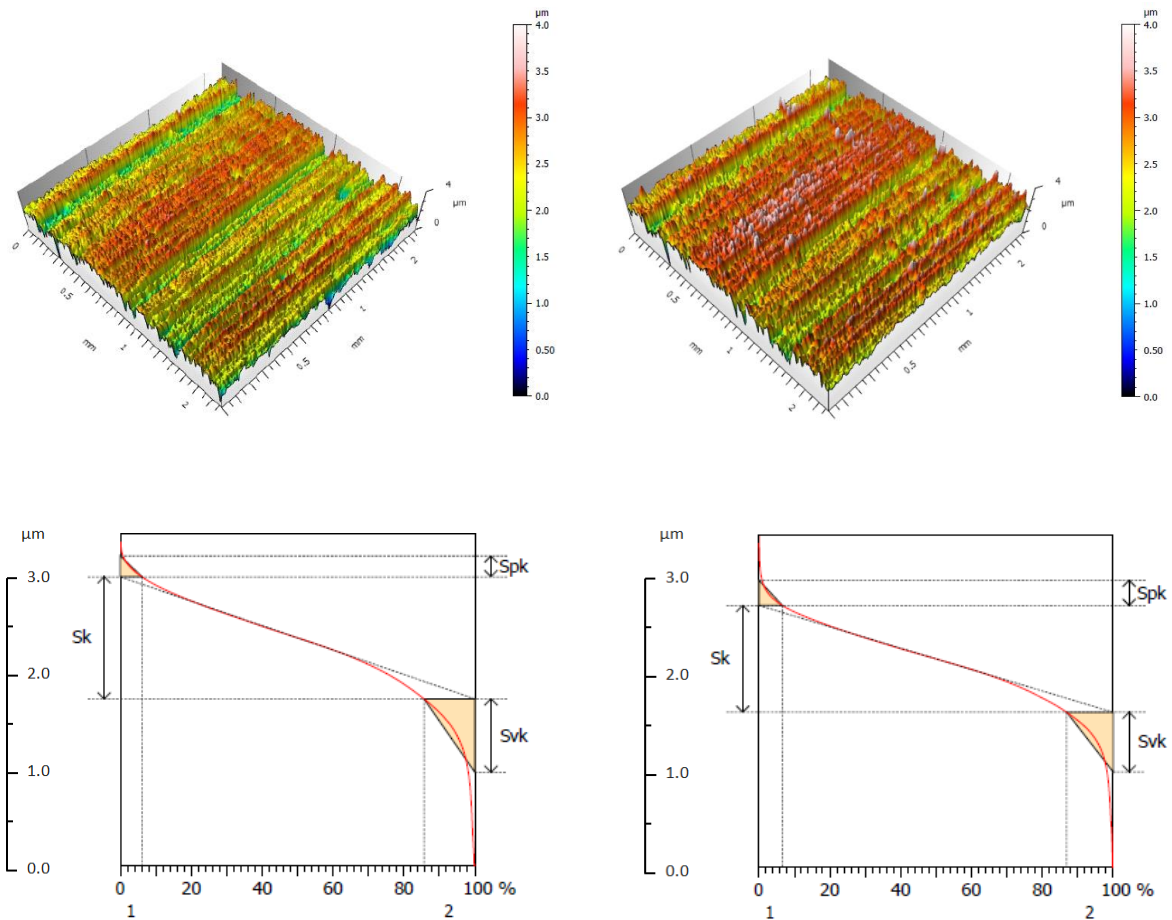
4.1.1.3. Texturing pattern between specimens before and after SPN treatments

Comparative 3-D profiles are shown in the next sequence of figures, which include the Material ratio curve and respective Sk, Spk, Svk, Sr1, Sr2 parameters results of the specimens E1-E4, areal measurement s1. Supplementary figures of areal measurements s4-s5 were included in Appendix section. Quantitative results were consolidated in Tables 12-15.

Experiment E1 (400 °C 4 h)

(a) Before SPN

(b) After SPN



Parameters	Value	Unit
Sk	1.275	μm
Spk	0.2167	μm
Svk	0.7648	μm
Sr1	6.123	%
Sr2	85.67	%

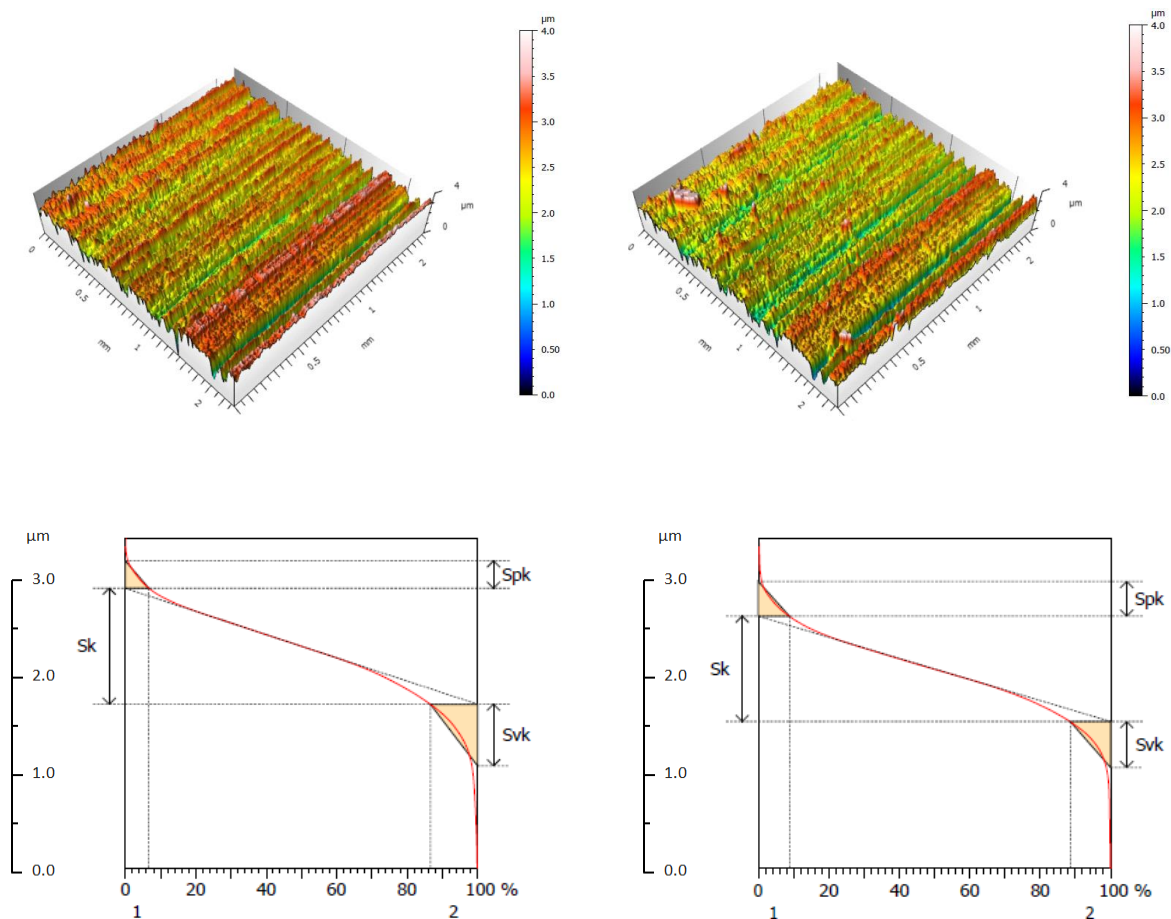
Parameters	Value	Unit
Sk	1.331	μm
Spk	0.3120	μm
Svk	0.7432	μm
Sr1	6.576	%
Sr2	86.93	%

Figure 44: Experiment E1 (400 °C 4 h). Sample 01 (s1) - coordinates x, y = 5.0, 5.0 mm, sampling area = 1.6 x 1.6 μm. 3-D surface profile and material ratio curve. Conditions before (a) and after treatment (b).

Experiment E2 (400 °C 2 h)

a) Before SPN

b) After SPN



Parameters	Value	Unit
Sk	1.308	μm
Spk	0.3086	μm
Svk	0.6955	μm
Sr1	6.697	%
Sr2	86.65	%

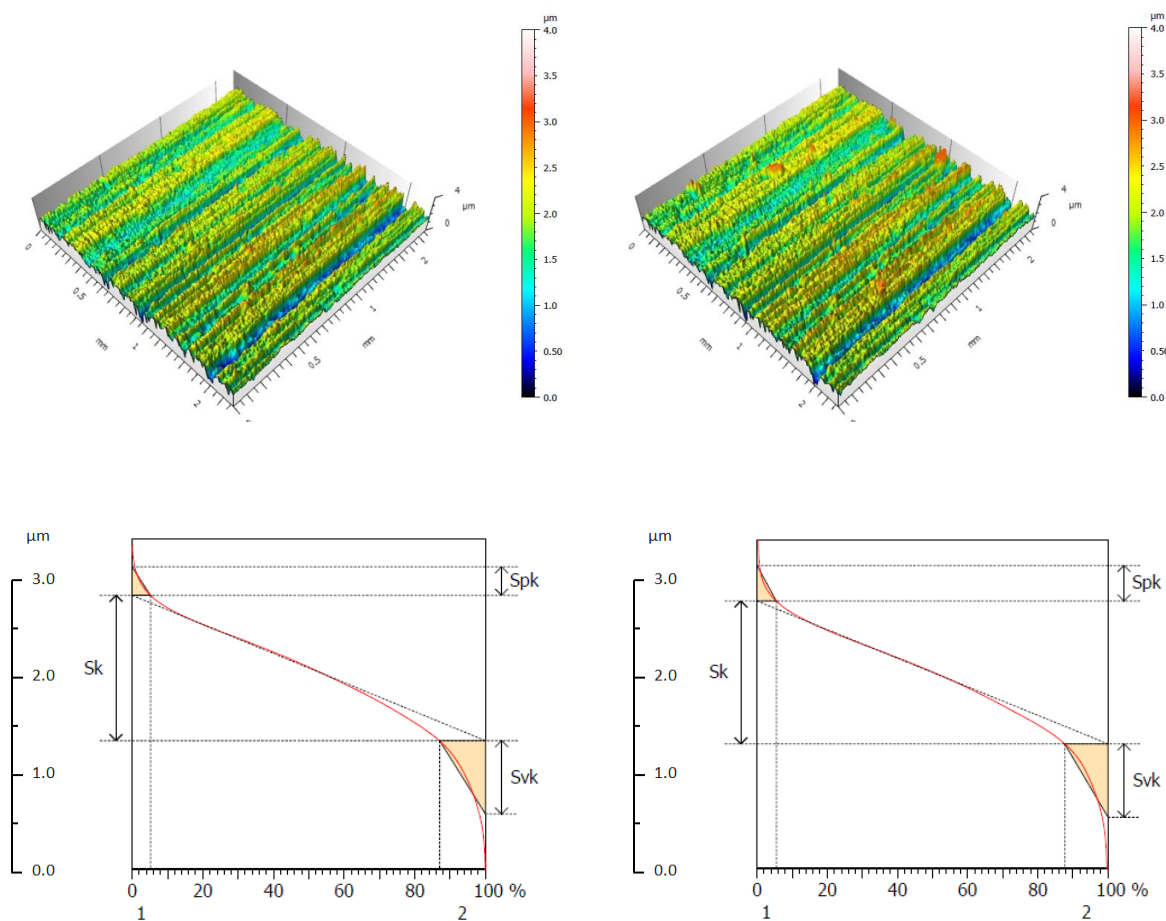
Parameters	Value	Unit
Sk	1.183	μm
Spk	0.3894	μm
Svk	0.5159	μm
Sr1	8.848	%
Sr2	88.55	%

Figure 45: Experiment E2 (400 °C 2 h). Sample 01 (s1) - coordinates x, y = 5.0, 5.0 mm, sampling area = 1.6 x 1.6 μm. 3-D surface profile and material ratio curve. Conditions before (a) and after treatment (b).

Experiment E3 (350 °C 4 h)

(a) Before SPN

(b) After SPN



Parameters	Value	Unit
Sk	1.254	μm
Spk	0.2458	μm
Svk	0.6334	μm
Sr1	5.208	%
Sr2	87.01	%

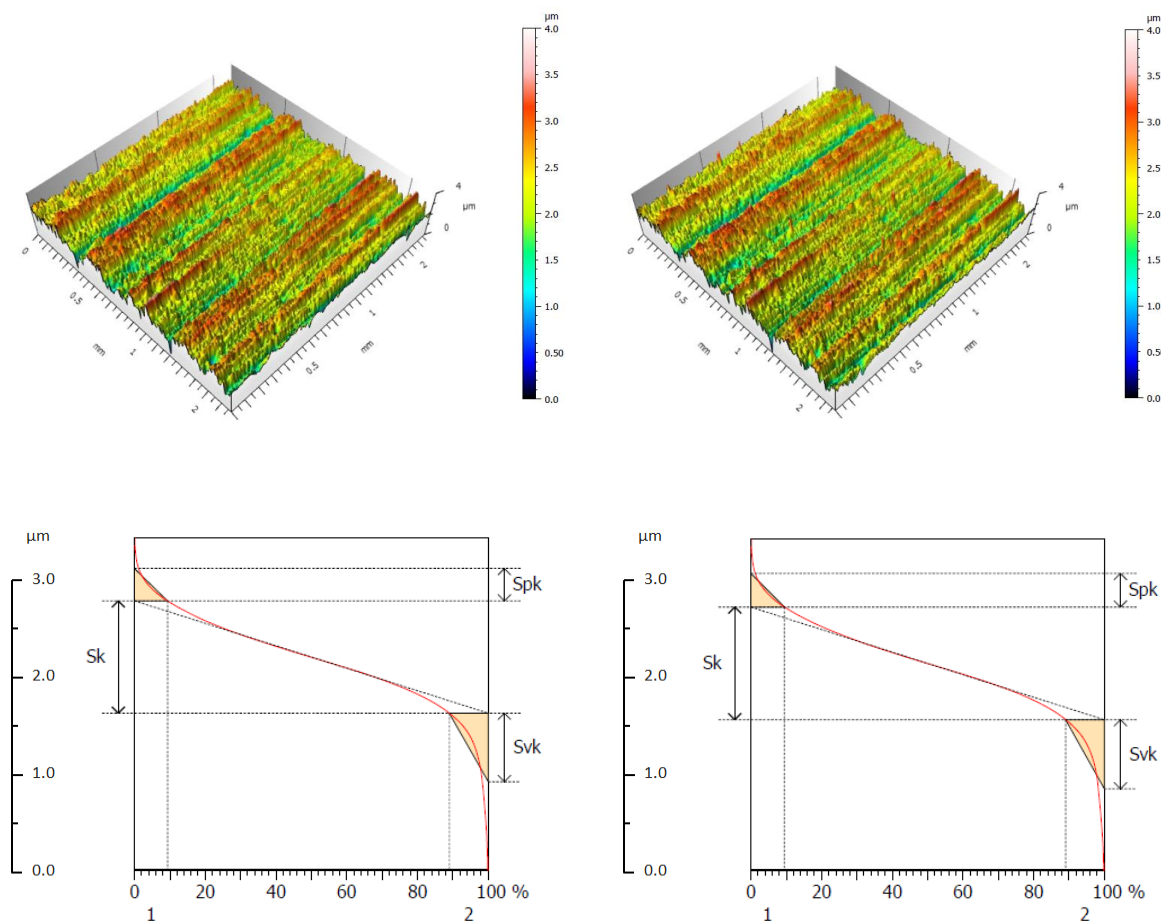
Parameters	Value	Unit
Sk	1.297	μm
Spk	0.3238	μm
Svk	0.6660	μm
Sr1	5.496	%
Sr2	87.69	%

Figure 46: Experiment E3 (350 °C 4 h). Sample 01 (s1) - coordinates x, y = 5.0, 5.0 mm, sampling area = 1.6 x 1.6 μm. 3-D surface profile and material ratio curve. Conditions before (a) and after treatment (b).

Experiment E4 (350 °C 2 h)

(a) Before SPN

(b) After SPN



Parameters	Value	Unit
S_k	1.150	μm
S_{pk}	0.3311	μm
S_{vk}	0.7024	μm
Sr_1	9.349	%
Sr_2	89.00	%

Parameters	Value	Unit
S_k	1.168	μm
S_{pk}	0.3490	μm
S_{vk}	0.7168	μm
Sr_1	9.474	%
Sr_2	89.07	%

Figure 47: Experiment E4 (350 °C 2 h). Sample 01 (s1) - coordinates x, y = 5.0, 5.0 mm, sampling area = 1.6 x 1.6 μm . 3-D surface profile and material ratio curve. Conditions before (a) and after treatment (b).

Table 11: Distribution height parameters, before and after treatments. Condition E1-400C-4h.

Experiment: E1-C400h4 (400 °C, 4 hours)										
Param (Unit)	Spk (μm)		Sk (μm)		Svk (μm)		Sr1 (%)		Sr2 (%)	
Condition	Before	After	Before	After	Before	After	Before	After	Before	After
s1	0.22	0.31	1.28	1.33	0.76	0.74	6.1	6.6	85.7	86.9
s2	0.21	0.32	1.07	1.08	1.29	1.30	4.8	5.9	81.6	81.7
s3	0.23	0.39	1.32	1.35	1.24	1.27	4.6	5.1	79.8	81.1
s4	0.16	0.36	1.47	1.51	0.57	0.57	3.3	4.4	88.8	88.4
s5	0.19	0.38	1.02	1.05	0.61	0.67	5.4	6.5	85.7	85.8
Avg	0.20	0.35	1.23	1.26	0.89	0.91	4.8	5.7	84.3	84.8
StdDev	0.03	0.04	0.19	0.19	0.35	0.35	1.1	0.9	3.6	3.2

Table 12: Distribution height parameters, before and after treatments. Condition E2-400C-2h.

Experiment: E2-C400h2 (400 °C, 2 hours)										
Param (Unit)	Spk (μm)		Sk (μm)		Svk (μm)		Sr1 (%)		Sr2 (%)	
Condition	Before	After	Before	After	Before	After	Before	After	Before	After
s1	0.31	0.39	1.31	1.18	0.70	0.52	6.7	8.8	86.7	88.6
s2	0.21	0.28	1.34	1.30	0.84	0.87	5.5	5.8	85.7	86.1
s3	0.19	0.27	1.30	1.28	0.72	0.75	4.9	5.7	85.0	84.4
s4	0.22	0.30	1.29	1.28	0.95	0.99	5.5	6.0	86.6	87.8
s5	0.17	0.23	1.10	1.18	0.62	0.59	4.5	5.4	82.4	84.7
Avg	0.22	0.29	1.27	1.25	0.77	0.74	5.4	6.3	85.3	86.3
StdDev	0.05	0.06	0.10	0.06	0.13	0.20	0.8	1.4	1.8	1.9

Table 13: Distribution height parameters, before and after treatments. Condition E3-350C-4h.

Experiment: E3-C350h4 (350 °C, 4 hours)										
Param (Unit)	Spk (μm)		Sk (μm)		Svk (μm)		Sr1 (%)		Sr2 (%)	
Condition	Before	After	Before	After	Before	After	Before	After	Before	After
s1	0.25	0.32	1.25	1.30	0.63	0.67	5.2	5.5	87.0	87.7
s2	0.26	0.29	1.23	1.24	0.82	0.93	7.1	7.2	87.3	86.1
s3	0.29	0.33	1.34	1.38	0.80	0.90	6.6	6.9	85.3	85.1
s4	0.27	0.32	1.19	1.18	0.75	0.76	7.7	8.4	88.0	87.5
s5	0.29	0.30	1.66	1.67	0.69	0.71	4.7	5.0	88.2	88.5
Avg	0.27	0.31	1.33	1.35	0.74	0.79	6.3	6.6	87.2	87.0
StdDev	0.02	0.02	0.19	0.19	0.08	0.12	1.3	1.3	1.1	1.4

Table 14: Distribution height parameters, before and after treatments. Condition E4-350C-2h.

Experiment: E4-C350h2 (350 °C, 2 hours)										
Param (Unit)	Spk (μm)		Sk (μm)		Svk (μm)		Sr1 (%)		Sr2 (%)	
Condition	Before	After	Before	After	Before	After	Before	After	Before	After
s1	0.33	0.35	1.15	1.17	0.70	0.72	9.3	9.5	89.0	89.1
s2	0.30	0.32	1.26	1.26	0.54	0.54	8.1	8.1	88.5	88.4
s3	0.33	0.36	1.15	1.17	0.47	0.46	8.7	9.2	88.8	89.9
s4	0.26	0.26	1.56	1.59	0.69	0.69	5.6	5.5	91.4	91.4
s5	0.22	0.20	1.15	1.18	0.60	0.57	5.9	5.6	85.3	86.2
Avg	0.29	0.30	1.25	1.27	0.60	0.60	7.5	7.6	88.6	89.0
StdDev	0.05	0.07	0.18	0.18	0.10	0.11	1.7	1.9	2.2	1.9

4.1.1.3.1. Statistical analysis of roughness results before and after SPN using Minitab

Minitab Boxplot graphs of peak roughness parameters Spk and Sr1, in the condition before and after experiments, are shown in Figure 48 and Figure 49, respectively. Aiming to simplify the graphs interpretation and further discussion, some definitions are recalled at this point:

- Third quartile (Q3): top of the box, 75% of the data are less than or equal this value.
- First quartile (Q1): bottom of the box: 25% of the data are less than or equal this value.
- Median: the middle of the data. Half of the observations are less than or equal to it.
- Mean: cross-in-a-circle symbol in each box graphically indicates the mean value.
- Maximum value: upper whisker line extends to the highest data value.
- Minimum value: lower whisker extends to the lowest value.

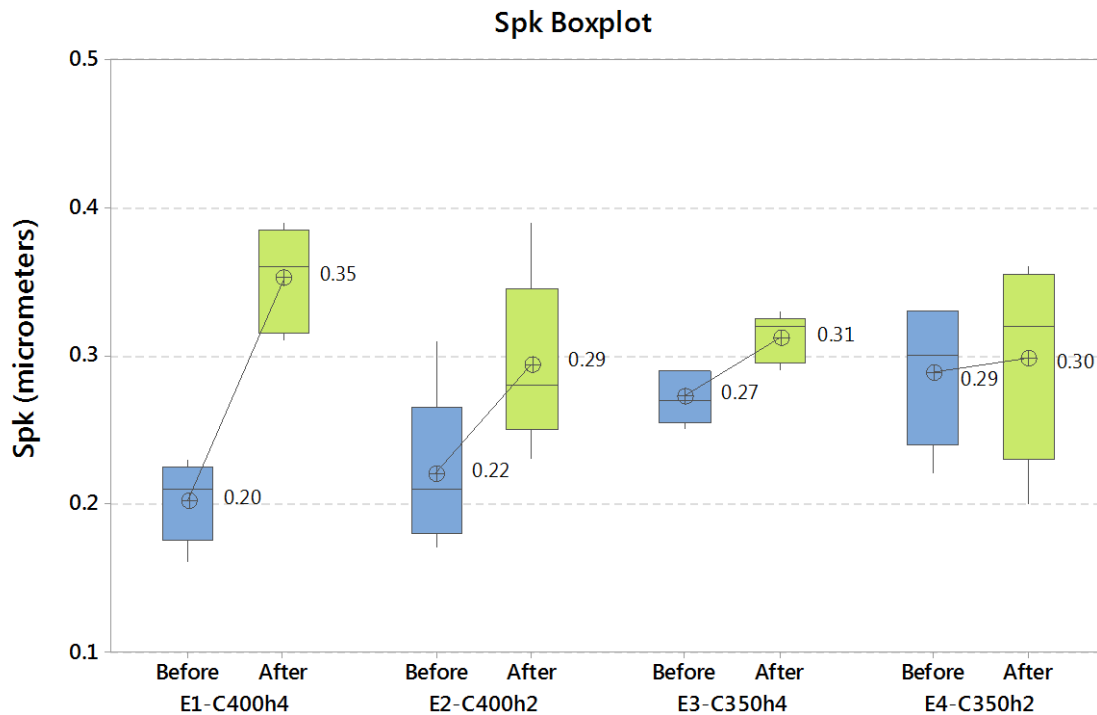


Figure 48: Boxplot of experiment results, before and after treatment. Spk roughness.

The Boxplot of experiment results, before and after treatment for Spk roughness (Figure 48) reveals some aspects related to the topography response to the shallow plasma nitriding treatment, which is commented in the following paragraphs.

In experiment E1, the After-boxplot is shifted with no overlaps with respect to Before-boxplot position. This aspect indicates that Mean statistically changed after SPN treatment. Before/After 'capability comparison analysis' presented in next pages is carried-out to quantitatively test this hypothesis. The height of the boxplot given by IQR somewhat increased

while the relative Median position appears to be stable. Therefore, variability appears to increase after SPN treatment, whereas distribution skewness did not changed - Mean position and Whisker size similar to Before-boxplot.

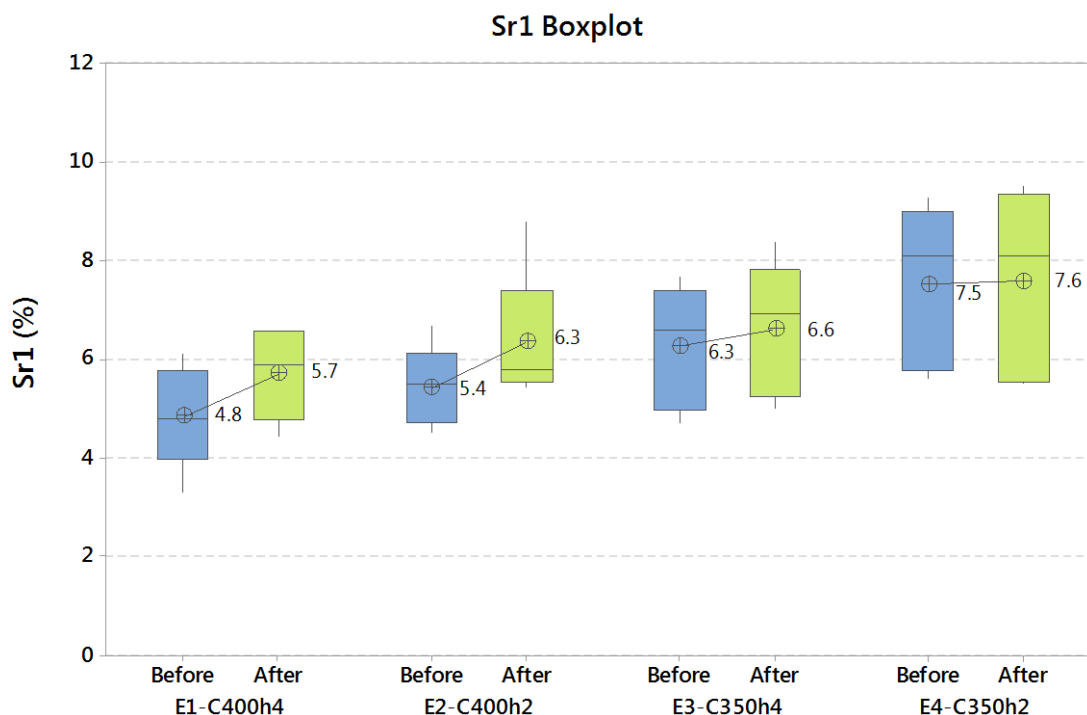


Figure 49: Boxplot of experiment results, before and after treatment. Peak material ratio component Sr1.

Similarly to E1, After-boxplot of the experiment E3 is shifted with no overlaps with respect to Before-boxplot position, indicating that Mean statistically changed after SPN treatment. However, the large box area below the Median position indicates that the data has now negative skewness - the left tail of the distribution is longer than the right tail. The IQR slightly decreased as shown by the reduced height of the boxplot. Therefore, variability appears to have changed and somewhat decreased or at least kept at similar level after SPN treatment.

In experiments E4, it does not appear that After-boxplot Mean has statistically changed after SPN. This is because there is a considerable overlap between boxplot positions, in spite of the shifts in absolute Mean (average) values. In addition, the relative Median position appears to be stable. The variability appears to increase after SPN treatment, whereas distribution skewness did not changed - Mean position and Whisker size similar to Before-boxplot.

Similarly, in experiment E2, it appears that After-boxplot Mean has statistically changed at some degree after SPN treatment. However, further test (capability comparison) must be done since there is some overlap between Before/After-boxplots. Still in experiment E2, the longer upper whisker and large box area above the median indicate that the data have a slight

positive skewness - the right tail of the distribution is longer than the left tail. Such aspect is observed in both before and after-boxplot implying that distribution skewness was preserved after SPN treatment.

The Boxplot of experiment results, before and after treatment for Sr1 parameter (Figure 49) reveals similar general tendencies as those described for the peak roughness Spk.

Considering the fact that while Spk refers to the height of peaks and component Sr1 to areal (peaks) material ratio in percent [103], the results indicate that SPN leads to the growth of pre-existent peaks whose intensity would be controlled by the temperature-time of plasma treatment. The Sr1 changes show that the development of new peaks is less frequent than the growth of existent ones, mainly in lower temperature cases (E3 and E4).

In all of the experiments, no outliers are present. The statistical analysis overall indicates possibility to perform good predictions on the topography response to the shallow plasma nitriding treatment so that production process can be designed in accordance to each Temperature-Time SPN desired circumstance.

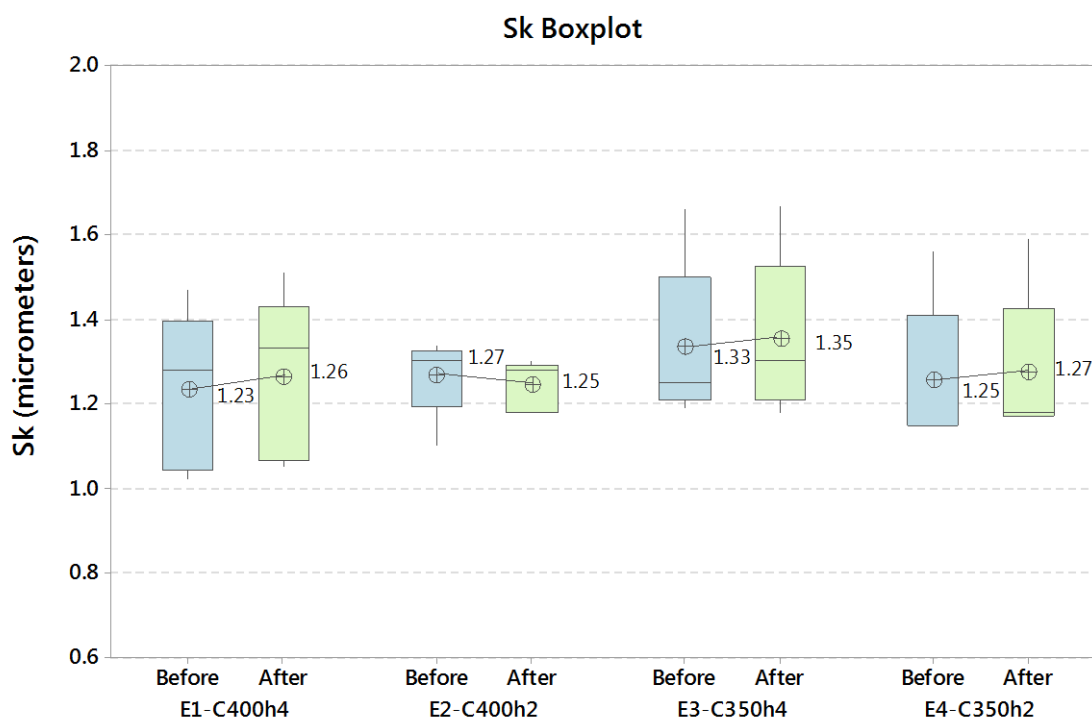


Figure 50: Boxplot of experiment results, before and after treatment. Sk roughness.

Minitab Boxplot graphs of core and valley roughness parameters Sk, Svk, and Sr2, in the condition before and after experiments, are shown in Figure 50, Figure 51, and Figure 52, respectively. The graphs revealed only slight and deemed negligible changes of core and valley parameters after SPN. Differently from peak roughness results, the summary of such roughness results reported herein will not be the primary object of further analysis and discussion.

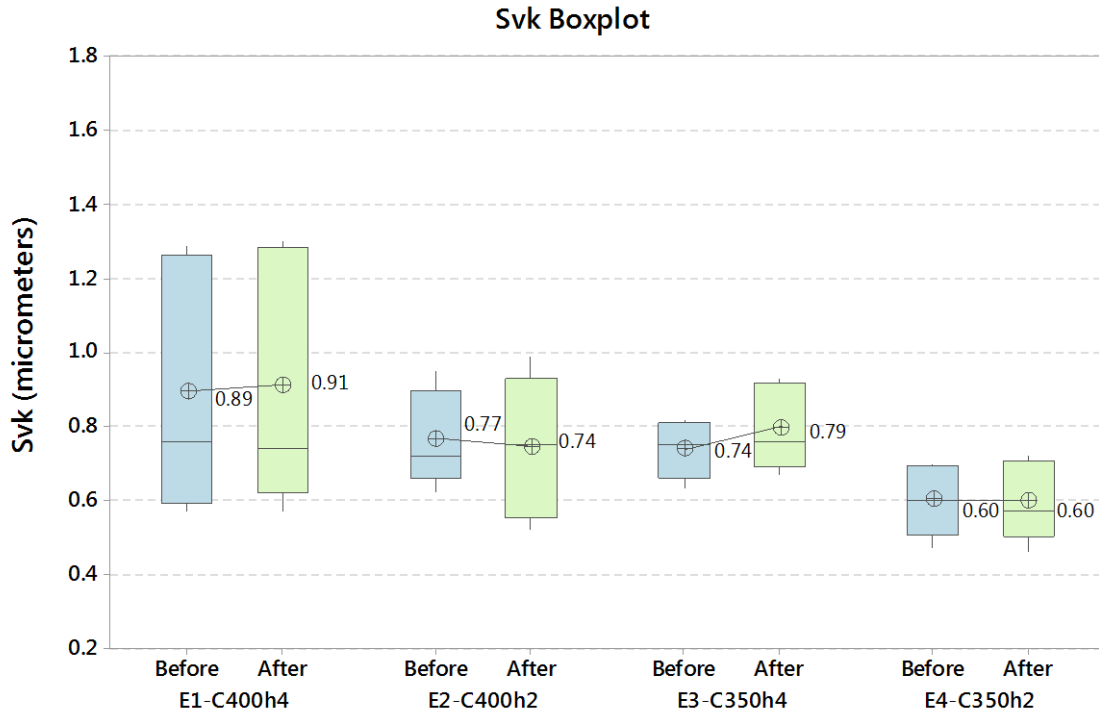


Figure 51: Boxplot of experiment results, before and after treatment. Svk roughness.

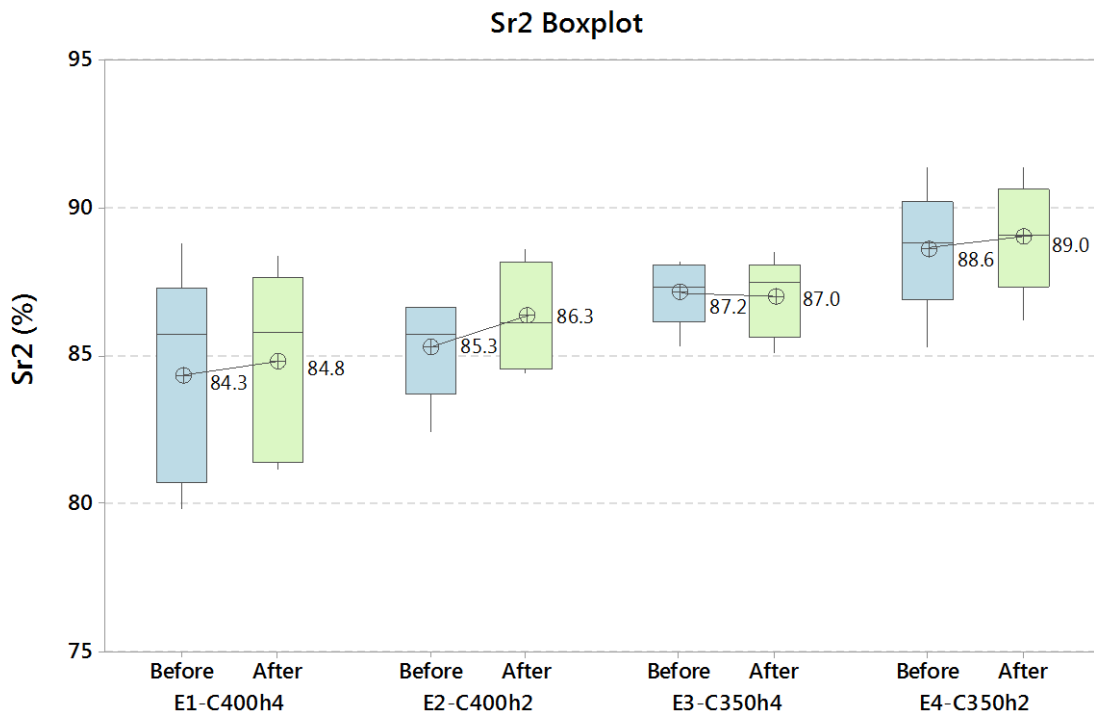


Figure 52: Boxplot of experiment results, before and after treatment. Sr2 roughness.

Before/After ‘capability comparison summary’ reports of parameter Spk are presented in Figure 53, Figure 54, Figure 55, and Figure 56. In all the cases the statistical analysis confirmed the distribution width somewhat increased as the standard deviation increased, while the process mean changed significantly in experiment cases: E1-400C-4h and E3-350-4h.

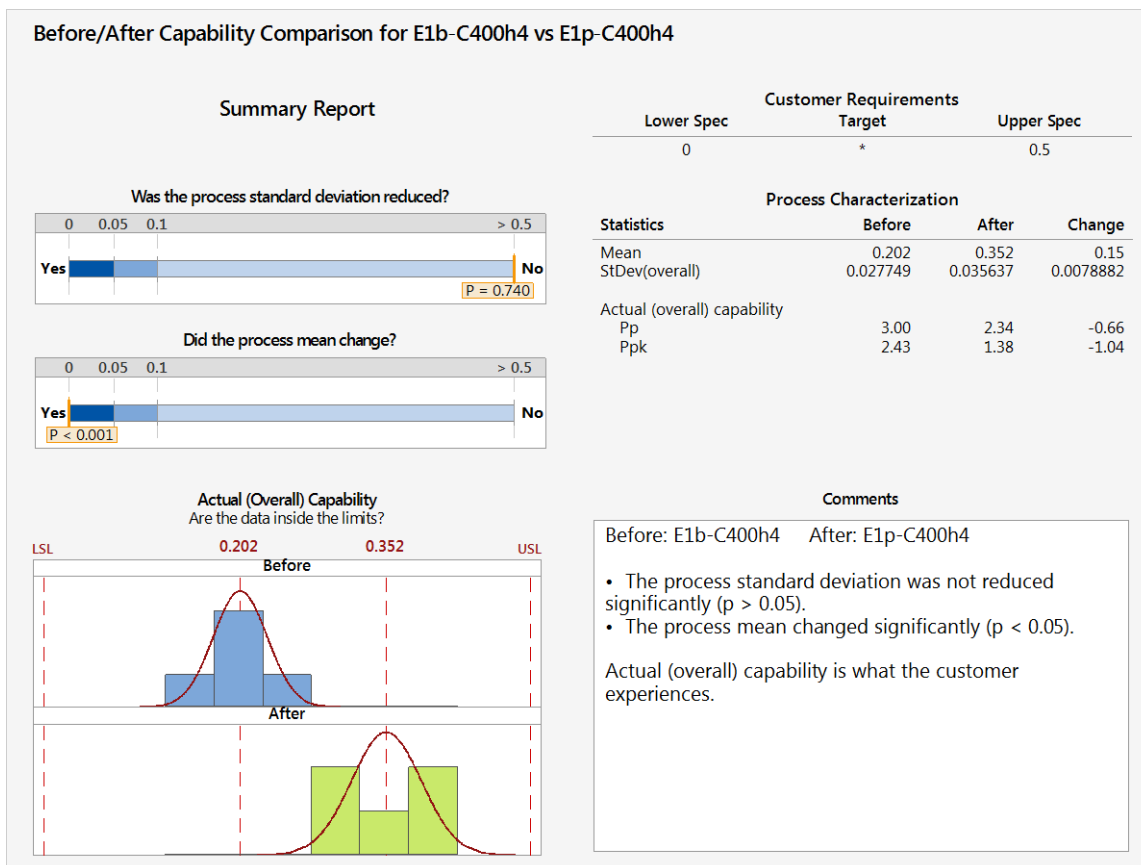


Figure 53: Before/After capability comparison. Spk roughness. Experiment E1 400C 4h.

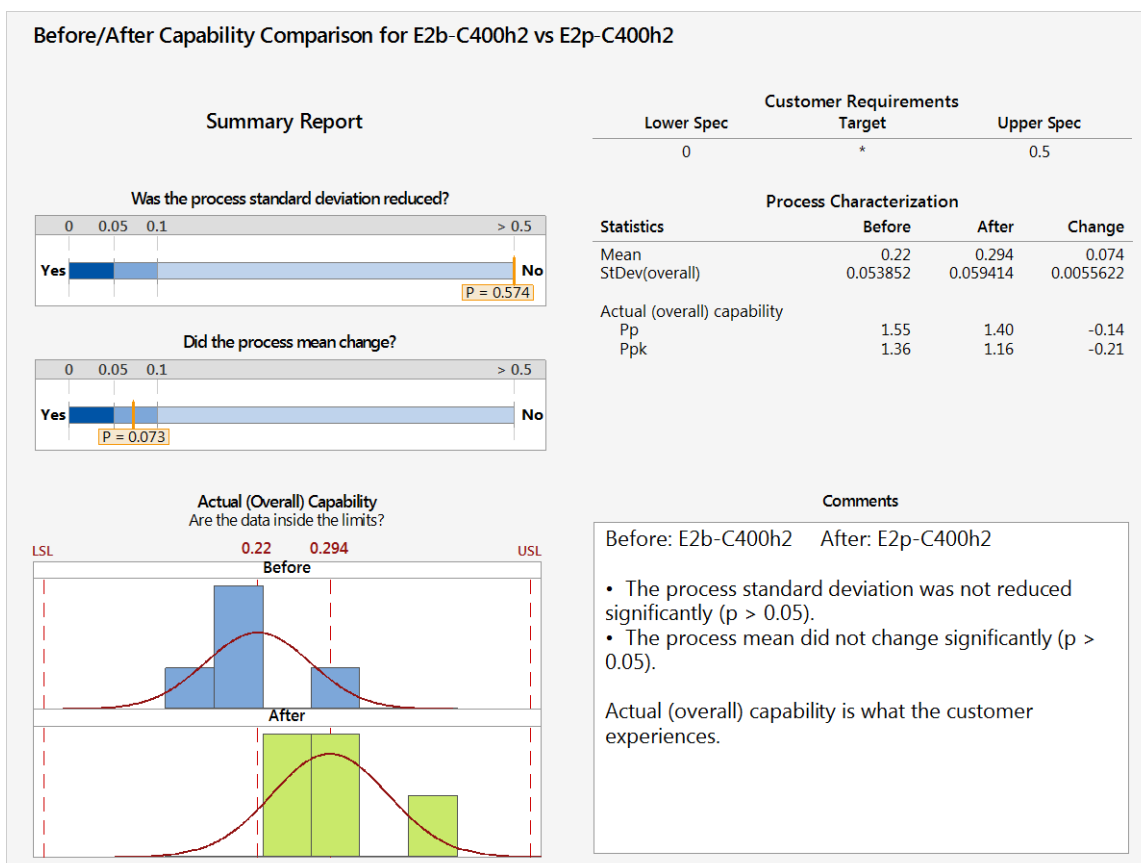


Figure 54: Before/After capability comparison. Spk roughness. Experiment E2 400C 2h.

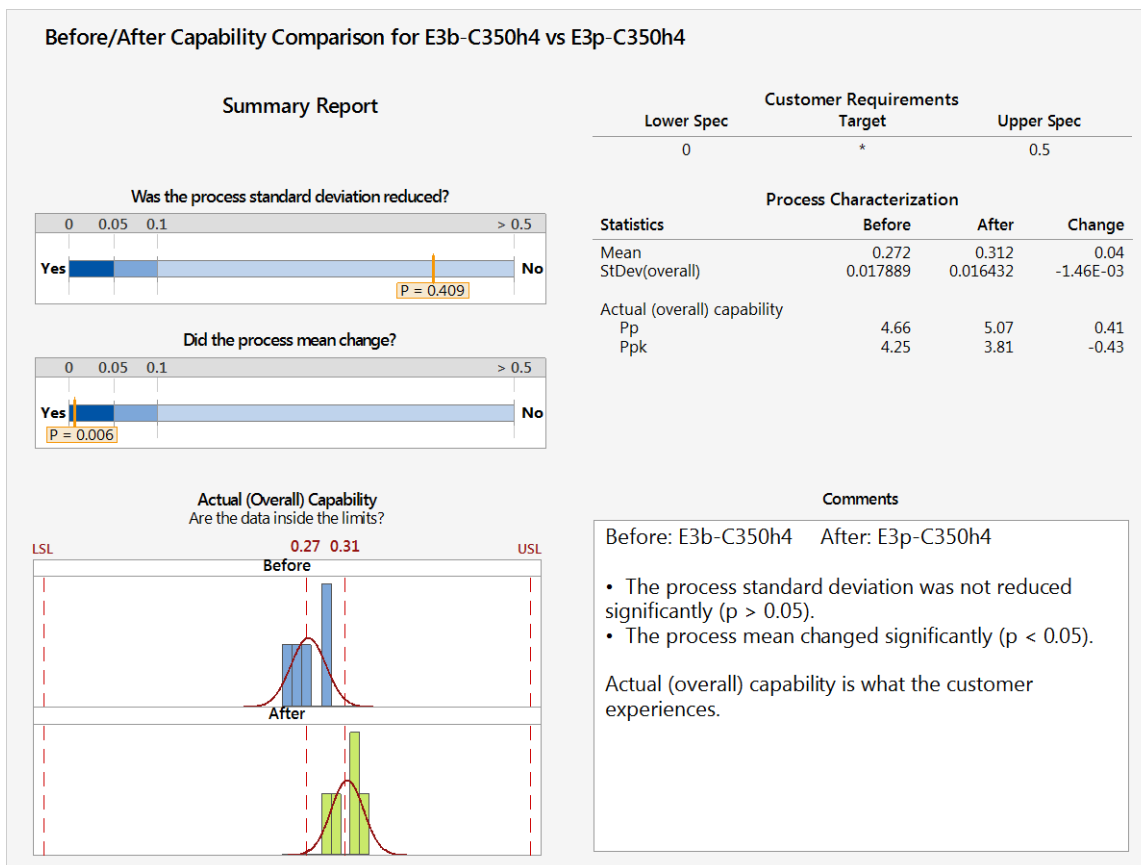


Figure 55: Before/After capability comparison. Spk roughness. Experiment E3 350C 4h.

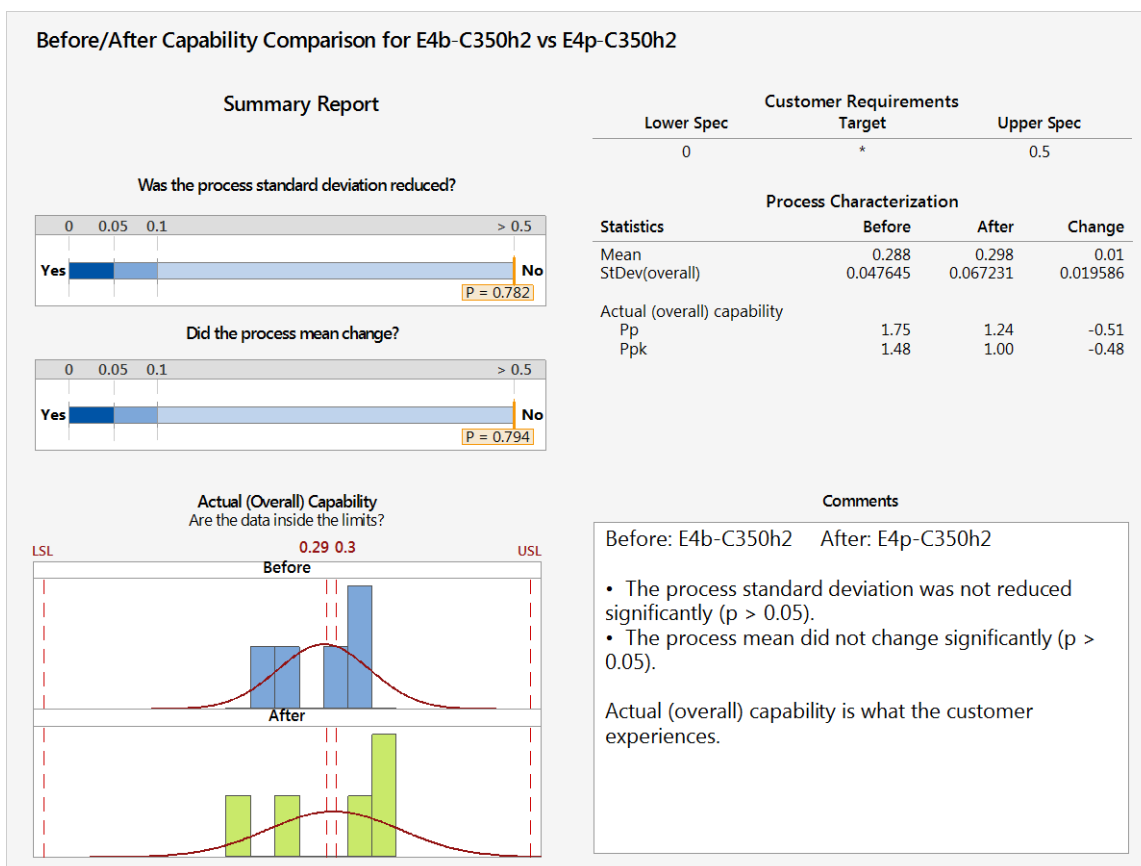


Figure 56: Before/After capability comparison. Spk roughness. Experiment E4 350C 2h.

Statistically, the before/after capability comparison results indicate that final distribution shape of peak texturing pattern is closely related to the initial distribution shape, as shown by the histograms and boxplot charts. In spite of process capability reductions pointed out by Pp and Ppk indicators, no matter the experiment condition the final data were found inside the reference engineering limits, as demonstrated by histograms.

Process capability Pp value is influenced by changes in standard deviation, i.e., by the peak roughness dispersion, whereas Ppk is influenced by both standard deviation and Mean shift. Bar chart in Figure 57 shows the summary of peak roughness results in average (Mean) with respective standard deviation values.

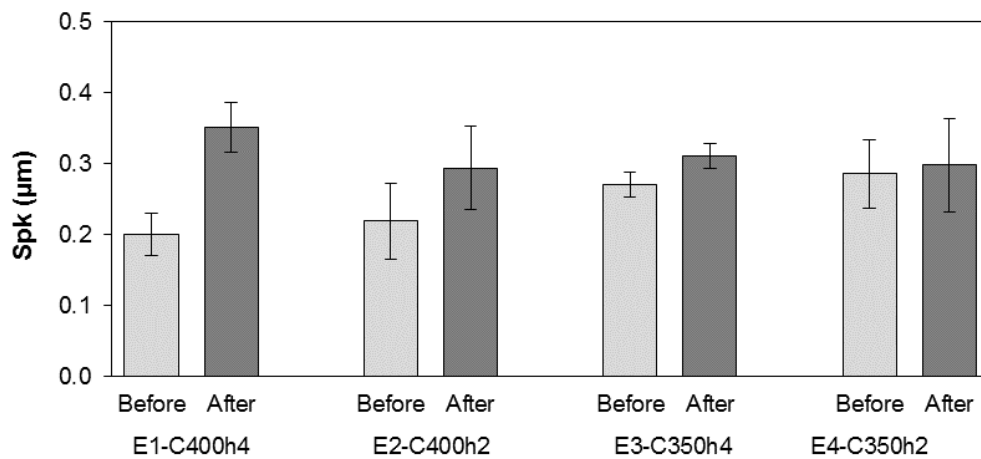


Figure 57: Summary of average (Mean) peak roughness Spk with respective standard deviation.

4.1.2. WDS microanalysis of N-concentration

Wavelength-dispersive X-ray spectroscopy (WDS) microanalysis results, of nitrogen content (wt%) as a function of the distance from the surface, are consolidated in the following sequence of Figures. Figure 58 shows the distribution of N-content in the matrix of pearlite treated at 400 °C during four hours, in a 75% N₂ / 25% H₂ atmosphere (E1), as a function of the distance. Analogously, Figure 60, Figure 62, and Figure 64 show equivalent data regarding the other three temperature-time (E2-E4) experimental conditions.

Each point in the graph corresponds to the mean value of five measurements taken in a line parallel to the best-fit line of surface. Each single measurement was distant 10 +/- 2 µm from each other. The bar error associated to each graph point corresponds to plus and minus one standard deviation resulted from the five measurements.

The first point (at zero distance) is based on five measurements taken directly on

specimen surface. Except for this point, the complete analysis was carried-out at increasing distances from surface towards to the specimen core. The measurements at the increasing distances were taken on the polished cross section, perpendicular to the textured surface.

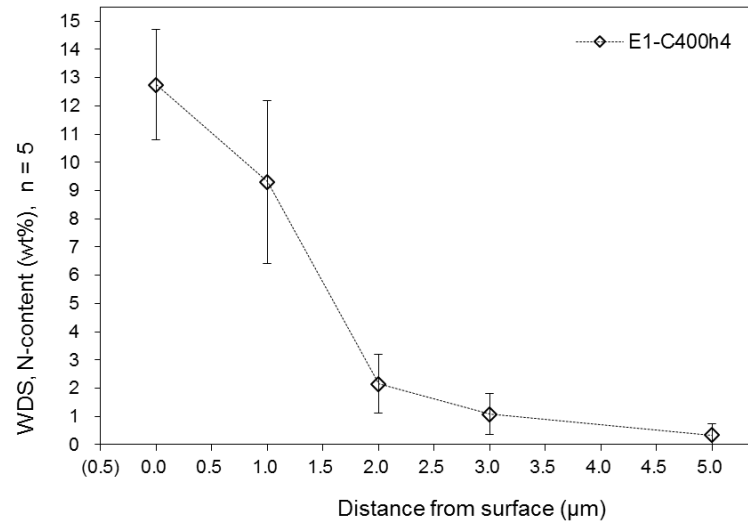


Figure 58: N-content (wt%) as a function of distance from surface (μm) measured via Wavelength-Dispersive Spectroscopy (WDS) microanalysis. Avg values +/- std dev, n = 5. In-lab textured flat surface, E1-400C-4h.

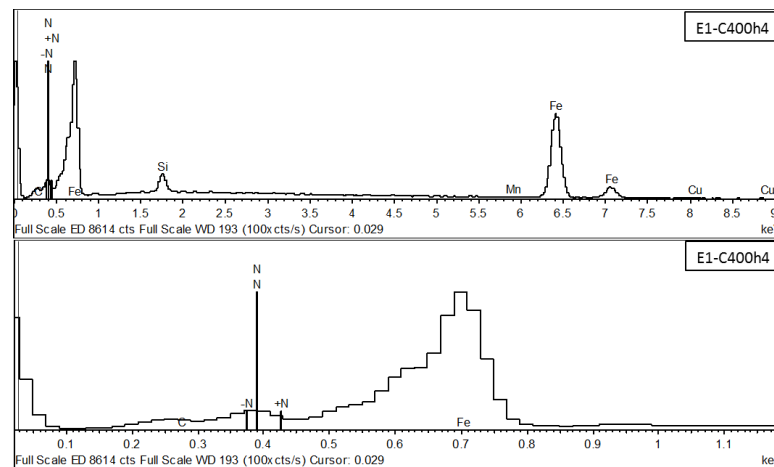


Figure 59: WDS spectrum, Nitrogen peaks. Quantitative analysis. In-lab textured flat surface, E1-400C-4h.

Figure 59 shows the WDS microanalysis spectrum taken directly on specimen surface of the gray cast iron treated at 400 °C during four hours, in a 75% N₂ / 25% H₂ atmosphere. Analogously, Figure 61, Figure 63, and Figure 65 show equivalent data regarding the other three temperature-time experimental conditions. The background correction was determined by measuring the intensity with the spectrometer offset by a suitable amount on each side of the peak (indicated by -N and +N) and interpolating linearly to the peak position [96].

The resulting peak at 0.39 keV (indicated by N) clearly evidences the surface is enriched with nitrogen. The characteristic N-peak was observed in each of the four experimental

conditions and was consistent with XRD characterization data, where ϵ -nitride was detected on the specimens' surface.

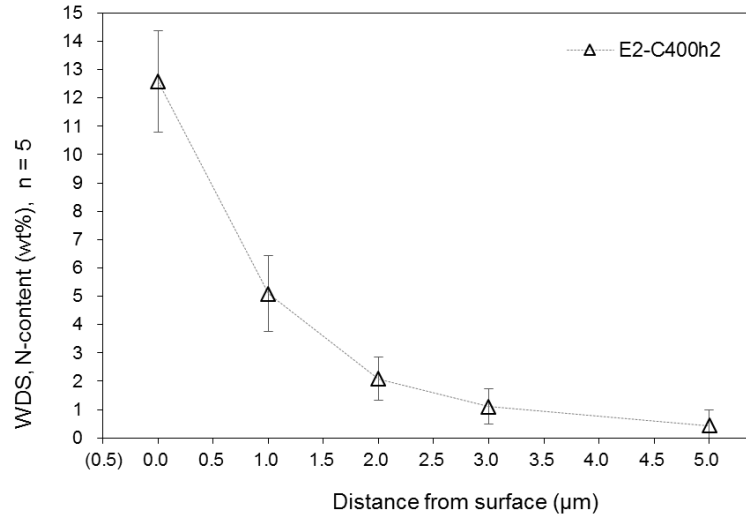


Figure 60: N-content (wt%) as a function of distance from surface (μm) measured via Wavelength-Dispersive Spectroscopy (WDS) microanalysis. Avg values \pm std dev, $n = 5$. In-lab textured flat surface, E2-400C-2h.

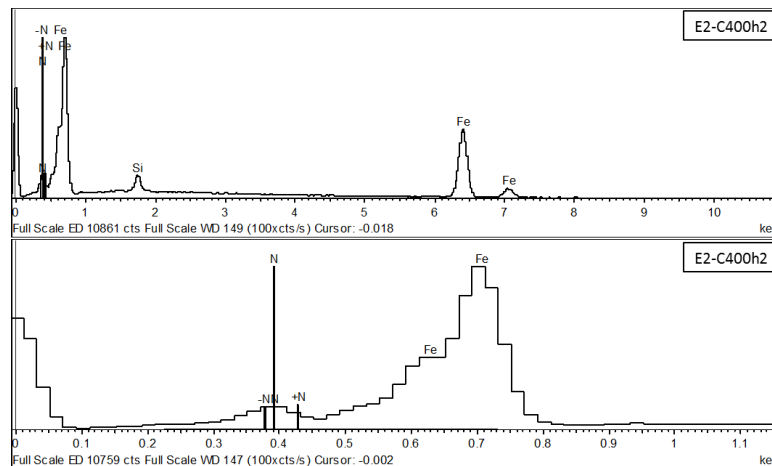


Figure 61: WDS spectrum, Nitrogen peaks. Quantitative analysis. In-lab textured flat surface, E2-400C-2h.

No matter the experiment condition, the plotted points in N-content versus distance charts yielded to curves whose nitrogen content decreases monotonically with the distance to the surface. With negative slope, the N-wt% versus distance- μm line moves down when going from left to right in x-axis.

Beyond about 3 μm of depth, the noted change of the curve slope shows that the nitrogen gradient is significantly reduced at such region, particularly for specimens treated at 350 $^{\circ}\text{C}$ as observed in Figure 66 that consolidates the four experiment charts.

At 5 μm of depth, nitrogen content tends to zero in all the experimental condition (Figure

66), indicating the proximity (or achievement) of the transition between nitrogen diffusion zone and core material. Accordingly, the use of a lower process temperature extended the cycle time for diffusion [10] so that shallow diffusion depth was successfully achieved.

After SPN treatment, the N-wt% data variability (standard deviation between measurements at each distance) did not tend to follow a pattern. Several reasons can explain such differences in error bar sizes. WDS microanalysis measured the nitrogen content of the pearlite matrix, and the pearlite chemical composition is not homogenous - WDS spots could have achieved zones of iron and/or cementite, so that the reported nitrogen results need to be understood as a local mean value. In addition, the topography of the textured surface actually may cause a variation in the exact distance between each one of the five measurements in a line and the textured surface.

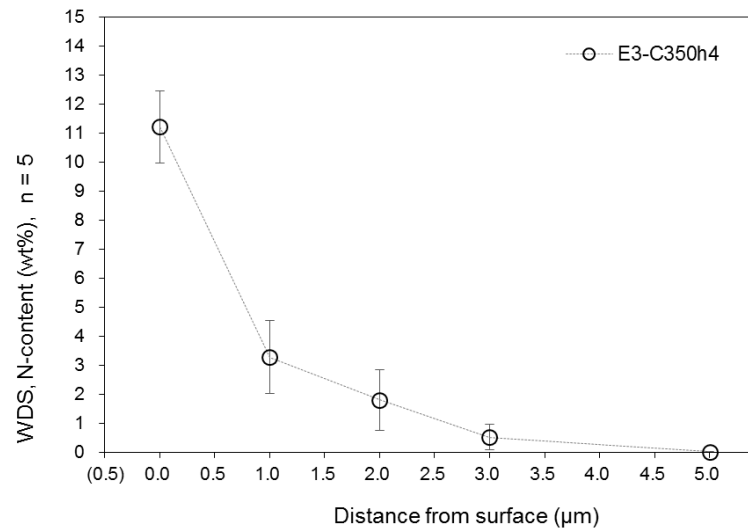


Figure 62: N-content (wt%) as a function of distance from surface (μm) measured via Wavelength-Dispersive Spectroscopy (WDS) microanalysis. Avg values \pm std dev, $n = 5$. In-lab textured flat surface, E3-350C-4h.

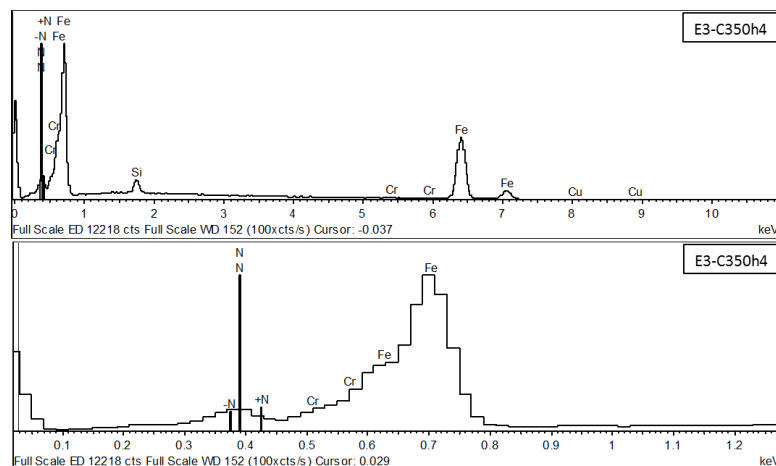


Figure 63: WDS spectrum, Nitrogen peaks. Quantitative analysis. In-lab textured flat surface, E3-350C-4h.

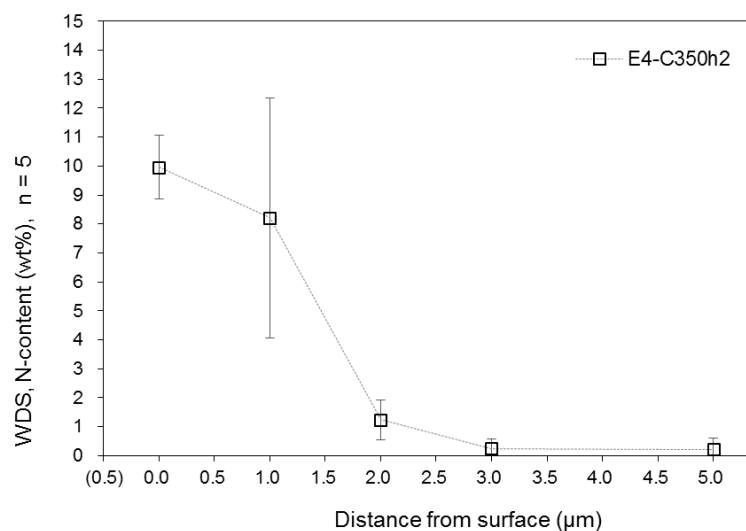


Figure 64: N-content (wt%) as a function of distance from surface (μm) measured via Wavelength-Dispersive Spectroscopy (WDS) microanalysis. Avg values \pm std dev, $n = 5$. In-lab textured flat surface, E4-350C-2h.

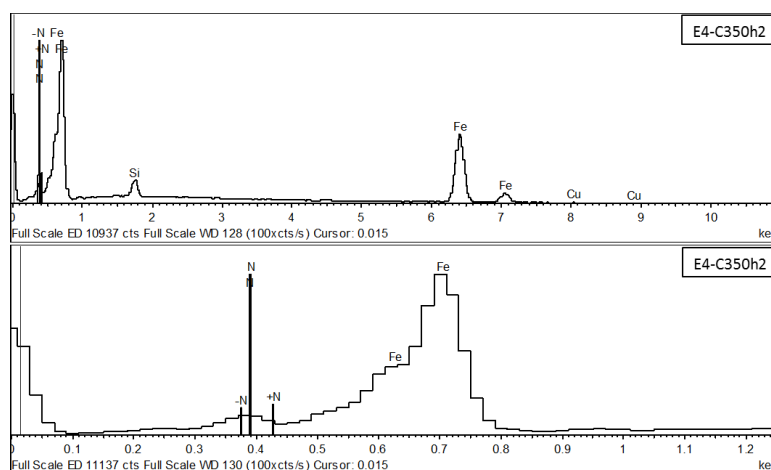


Figure 65: WDS spectrum, Nitrogen peaks. Quantitative analysis. In-lab textured flat surface, E4-350C-2h.

Direct comparison between the absolute Mean (averaged N-wt%) numbers may lead to the interpretation that final nitrogen content on the surface in general decreased from experiment E1 to E4 (Figure 67). These results are consistent with XRD patterns, where the diffractogram peak intensity increased in sequence from E4 to E1 experimental conditions, with the temperature-time increasing.

In spite of that, when analyzing experiments at 400 °C (E1 and E2) and respective bar errors, conceivably it is not possible to affirm that data statistically differed between the treatments carried out during four and two hours. On the other hand, the shift in absolute Mean (average) values on the surface was prominent between temperature conditions, notably when comparing the experiment E4 (C350h2) with E1 (C400h4) and E2 (C400h2).

In the chapter about roughness results, it was explored that textured surface is composed

by a distribution of peaks and valleys. Therefore, the line taken as reference during the WDS microanalysis as a function of distance carries some uncertainty, because it does not distinguish differences influenced by peaks. These and other facts, including sample size, might explain differences of standard deviation between points, notably near the surface, such as the case of the measurements taken at 1 μm and 2 μm , which presented the largest N-wt% variability.

One can reinforce that (even considering reported variability) the plotted points yielded to curves whose N-content decreases monotonically from surfaces with high content until it tends to zero wt% at 5 μm of depth, therefore constituting nitrogen enrichment at shallow depths.

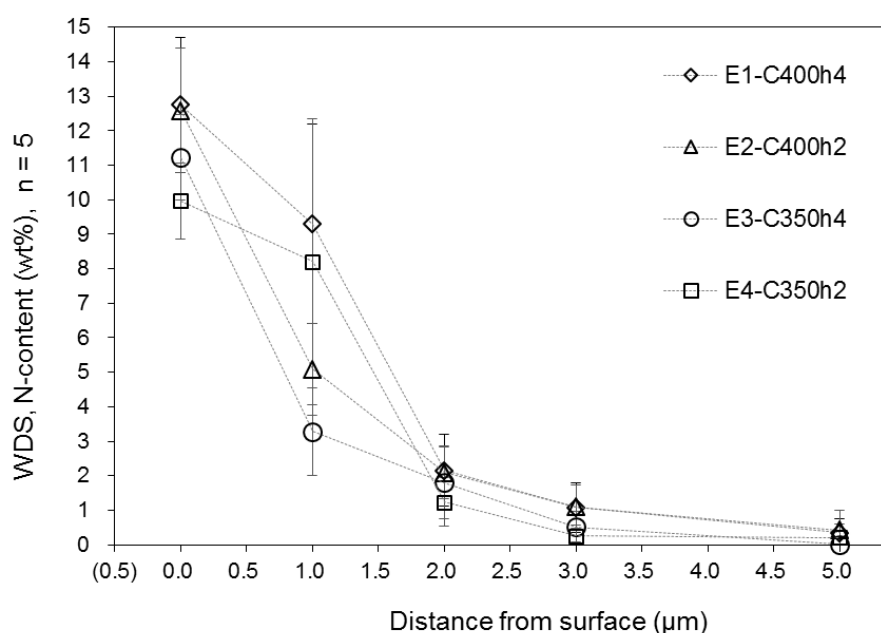


Figure 66: N-content (wt%) as a function of distance from surface (μm) measured via WDS microanalysis. Avg +/- std dev, $n = 5$. In-lab textured flat surface. Combined chart: E1-400C-4h, E2-400C-2h, E3-350C-4h, E4-350-2h.

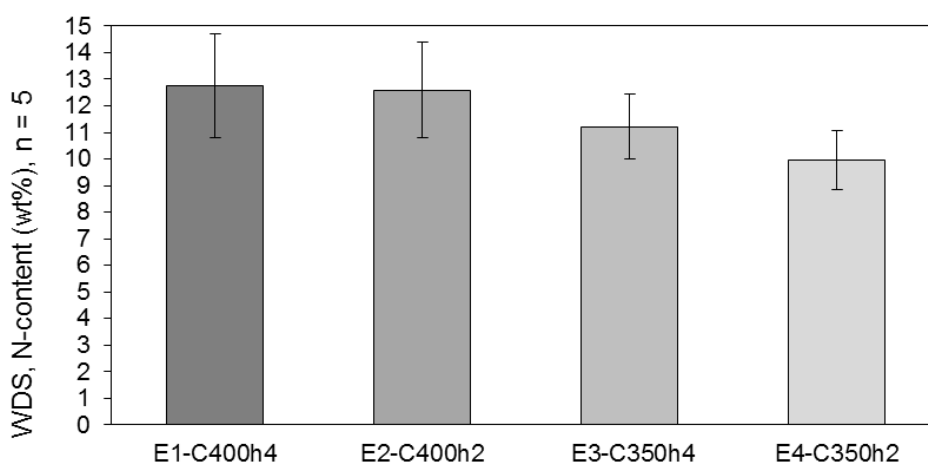


Figure 67: N-content (wt%) at the surface (zero μm distance) measured via WDS microanalysis. Avg +/- std dev, $n = 5$. In-lab textured flat surface. Combined chart: E1-400C-4h, E2-400C-2h, E3-350C-4h, E4-350-2h.

Finally, Table 15, Table 16, Table 17, Table 18, consolidate the N-content (wt%) results as a function of distance (μm) from specimen surface and lists the values of all single WDS readings in each experimental temperature-time condition.

Table 15: Quantitative WDS microanalysis. Data group of N-content (wt%) as a function of distance from surface (μm), 5 measurements per distance. In-lab textured flat surface. Condition E1-400C-4h.

Experiment: E1-C400h4 (400 °C, 4 hours)					
Distance (μm)	0.0	1.0	2.0	3.0	5.0
s1	15.83	7.39	3.44	1.14	0.03
s2	11.17	7.80	2.63	1.99	0.86
s3	13.06	12.78	1.20	0.36	0.14
s4	12.69	12.01	2.52	1.44	0.67
s5	10.98	6.44	0.97	0.32	0.00
Avg	12.75	9.28	2.15	1.05	0.34
StdDev	1.95	2.90	1.04	0.72	0.40

Table 16: Quantitative WDS microanalysis. Condition E2-400C-2h.

Experiment: E2-C400h2 (400 °C, 2 hours)					
Distance (μm)	0.0	1.0	2.0	3.0	5.0
s1	11.14	5.65	3.02	2.07	1.40
s2	11.37	7.10	0.94	0.42	0.21
s3	15.63	4.55	2.22	0.85	0.20
s4	12.43	4.52	2.25	1.29	0.33
s5	12.35	3.63	2.03	0.86	0.00
Avg	12.58	5.09	2.09	1.10	0.43
StdDev	1.80	1.33	0.75	0.62	0.56

Table 17: Quantitative WDS microanalysis. Condition E3-350C-4h.

Experiment: E3-C350h4 (350 °C, 4 hours)					
Distance (μm)	0.0	1.0	2.0	3.0	5.0
s1	10.34	1.48	0.45	0.23	0.00
s2	10.28	3.81	1.10	0.59	0.05
s3	12.44	4.92	2.16	0.14	0.00
s4	12.72	2.97	3.15	1.27	0.00
s5	10.33	3.24	2.13	0.36	0.00
Avg	11.22	3.28	1.80	0.52	0.01
StdDev	1.24	1.26	1.05	0.45	0.02

Table 18: Quantitative WDS microanalysis. Condition E4-350C-2h.

Experiment: E4-C350h2 (350 °C, 2 hours)					
Distance (μm)	0.0	1.0	2.0	3.0	5.0
s1	9.62	8.17	0.40	0.00	0.06
s2	9.99	12.43	0.90	0.78	0.00
s3	10.49	9.65	2.28	0.17	0.11
s4	10.30	9.44	1.39	0.12	0.00
s5	9.38	1.35	1.23	0.16	0.89
Avg	9.96	8.21	1.24	0.25	0.21
StdDev	0.46	4.14	0.69	0.31	0.38

4.1.3. X-Ray Diffraction (XRD) analysis

The XRD analysis identified Fe- α phase in both conditions before and after SPN process. The ϵ -nitride (Fe₃N) phase was clearly identified in the condition after nitriding process with the assistance of Crystallographica Search-Match (CSM) software.

Figure 68 shows the XRD diffractogram of the textured surface treated at 400 °C during four hours, in a 75% N₂ / 25% H₂ atmosphere (E1). Analogously, Figure 69, Figure 70, and Figure 71 show equivalent data regarding the other three temperature-time (E2-E4) experimental conditions.

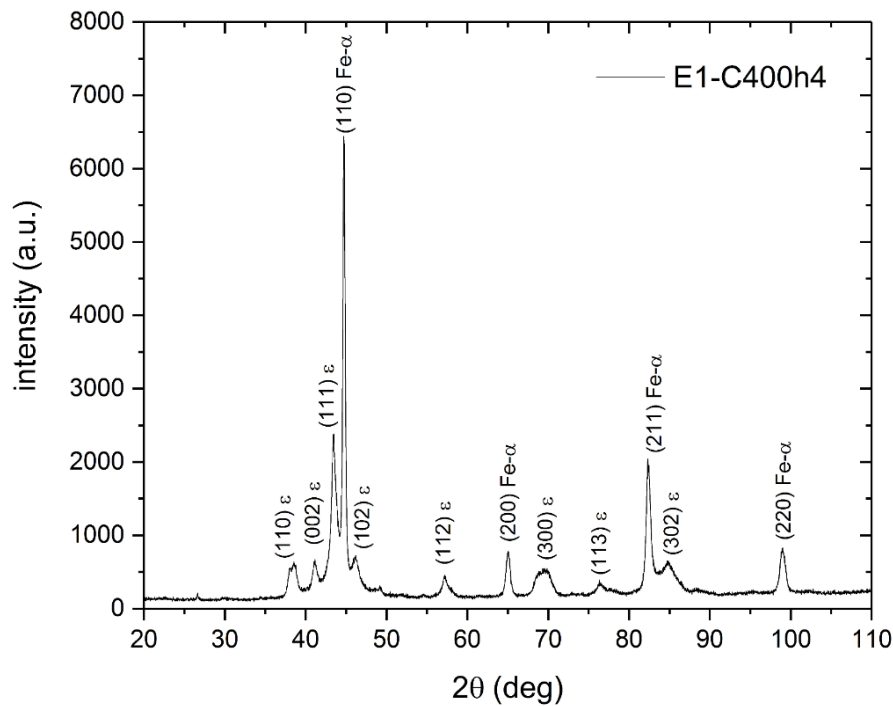


Figure 68: XRD diffractogram of the textured surface treated in the condition E1-C400h4.

The identification of the phases was carried out by comparison with ICDD (International Centre for Diffraction Data) standards loaded in CSM. The diffraction patterns (Figure 68) revealed the presence of eight ϵ -nitride peaks, being respectively, from left to right: (110)- ϵ , (002)- ϵ , (111)- ϵ , (102)- ϵ , (112)- ϵ , (300)- ϵ , (113)- ϵ , and (302)- ϵ .

For comparison purpose, the XRD diffractogram in the condition Raw, i.e., before SPN treatment, is shown in Figure 72 as a baseline of raw sample. As described beforehand, SPN was studied in pearlitic matrix GCI samples extracted from cylinder bores. Since all the specimens have similar nominal chemical composition and initial microstructure, only one

diffractogram was obtained to represent the baseline XRD pattern of all experimental conditions, so that comprehending both the 'As-honed surface specimen' (case-study) and the 'In-lab textured flat specimens'.

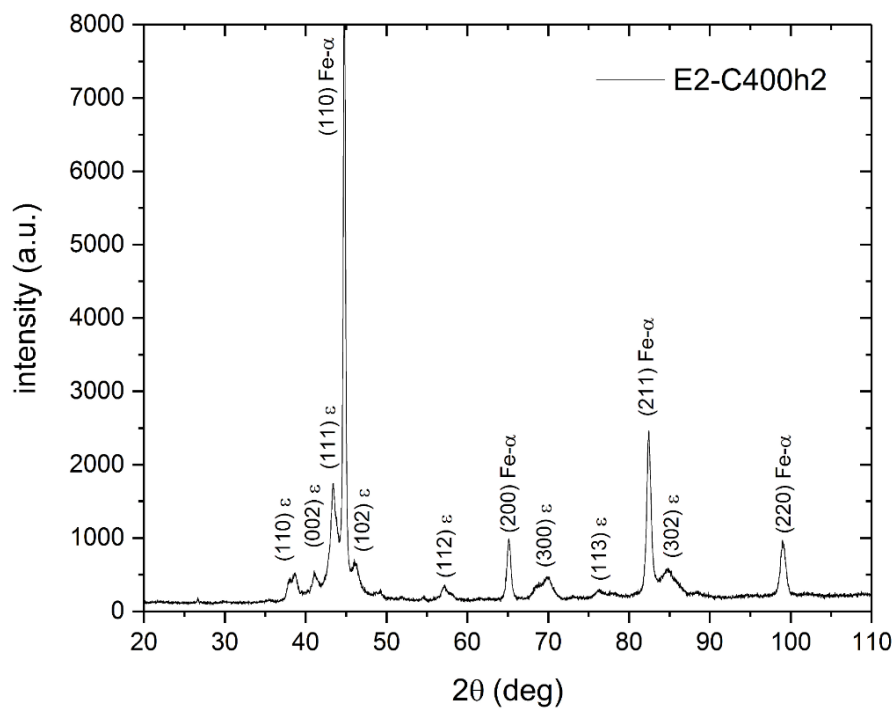


Figure 69: XRD diffractogram of the textured surface treated in condition E2-C400h2.

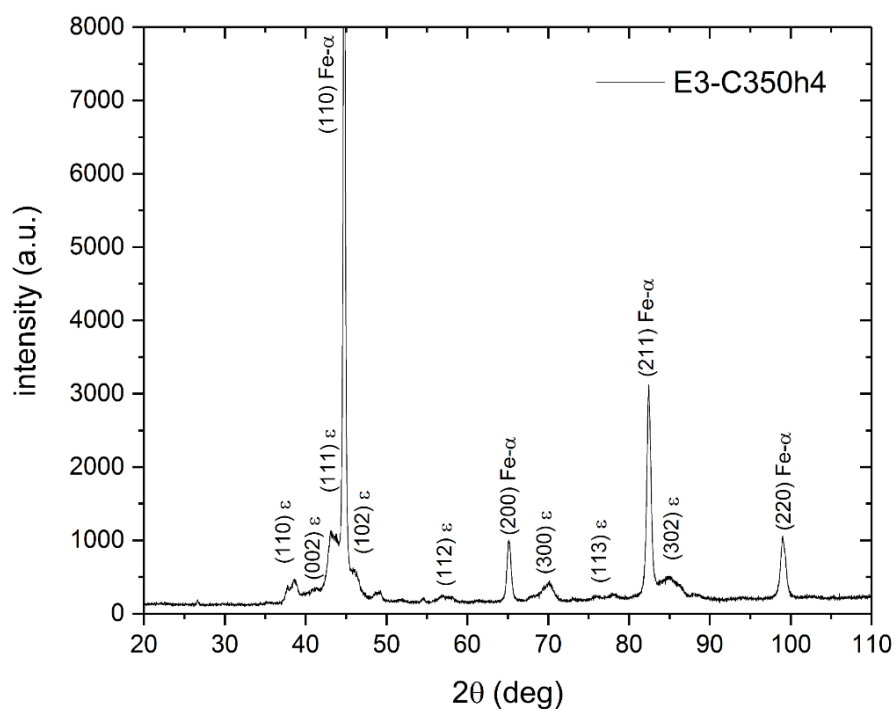


Figure 70: XRD diffractogram of the textured surface treated in condition E3-C350h4.

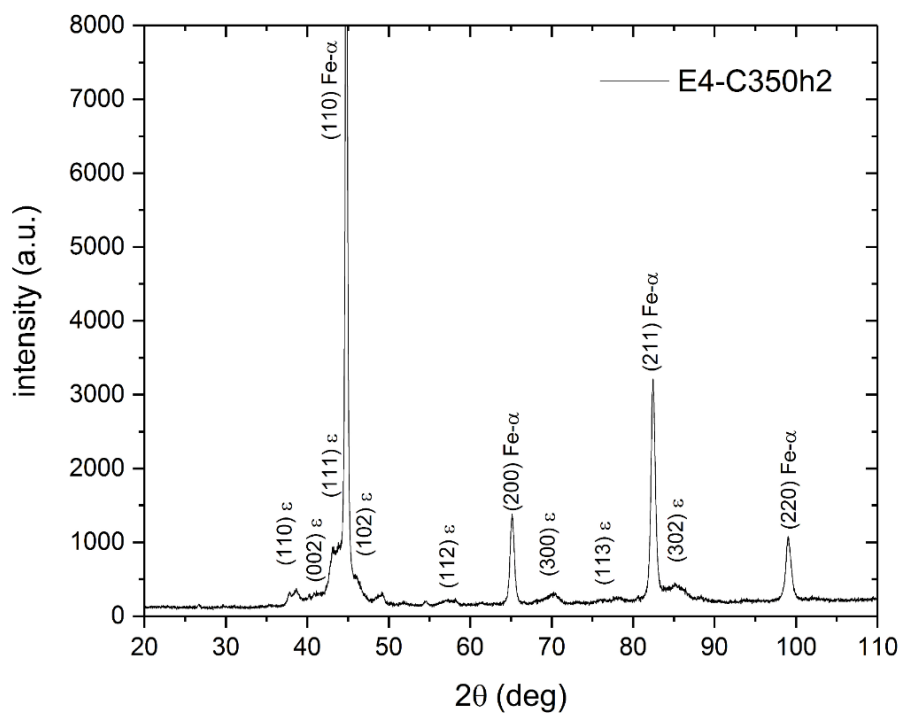


Figure 71: XRD diffractogram of the textured surface treated in condition E4-C350h2.

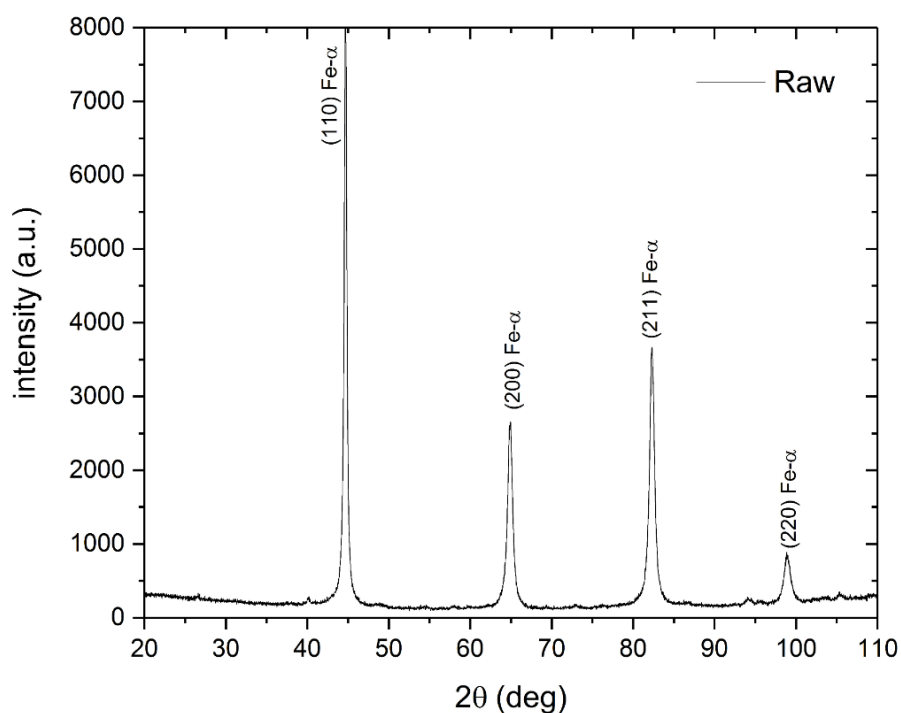


Figure 72: XRD diffractogram of the textured surface in condition Raw, before SPN (Baseline sample/material same as case-study).

XRD patterns of the textured surface in the conditions E1-C400h4, E2-C400h2, E3-C350h4, E4-C350h2, and Raw were combined in the 3-D graph view shown in Figure 73. The

progressive growth of ϵ -nitride peaks with temperature-time is visualized going from raw (represented in gray color) to E1 (represented in black color) condition, given the gradual increasing of peak intensity.

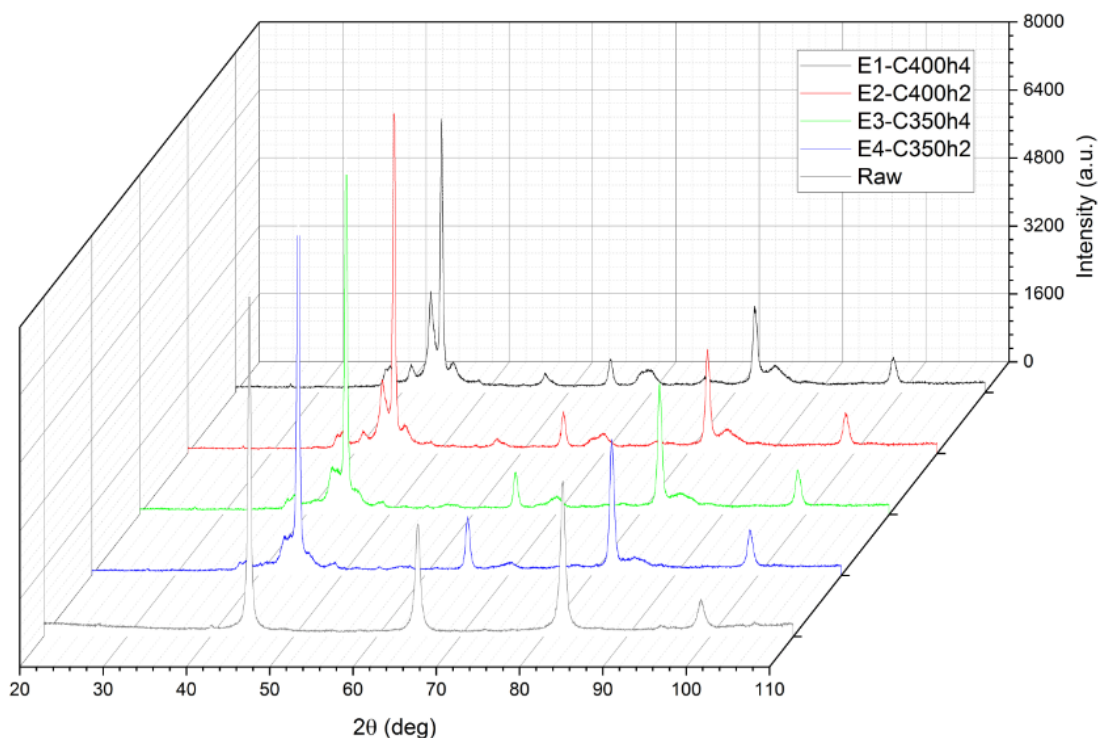


Figure 73: XRD combined 3-D diffractogram of the textured surface in the conditions E1-C400h4, E2-C400h2, E3-C350h4 and E4-C350h2 and Raw.

Figure 74 shows the five XRD patterns overlapped in a single graph, whose ϵ -nitride peaks are also shown in higher magnification. The area under the ϵ -nitride peaks relates to the amount of phase present [97], which is small relatively to Fe- α .

The graph clearly demonstrates that the area under ϵ -nitride peaks increased progressively with the temperature-time condition, and as visualized going from E4 (blue line) to E1 (black line) condition.

Therefore, XRD analysis evidenced a progressive increase of ϵ -nitride phase in the surface, in function of the experimental temperature-time condition. This result is consistent with the WDS data discussed in the previous subsection, hence confirming the modification of the pre-textured surfaces via shallow plasma nitriding, with the N-enrichment with consequent formation of ϵ -nitride (Fe_3N) phase.

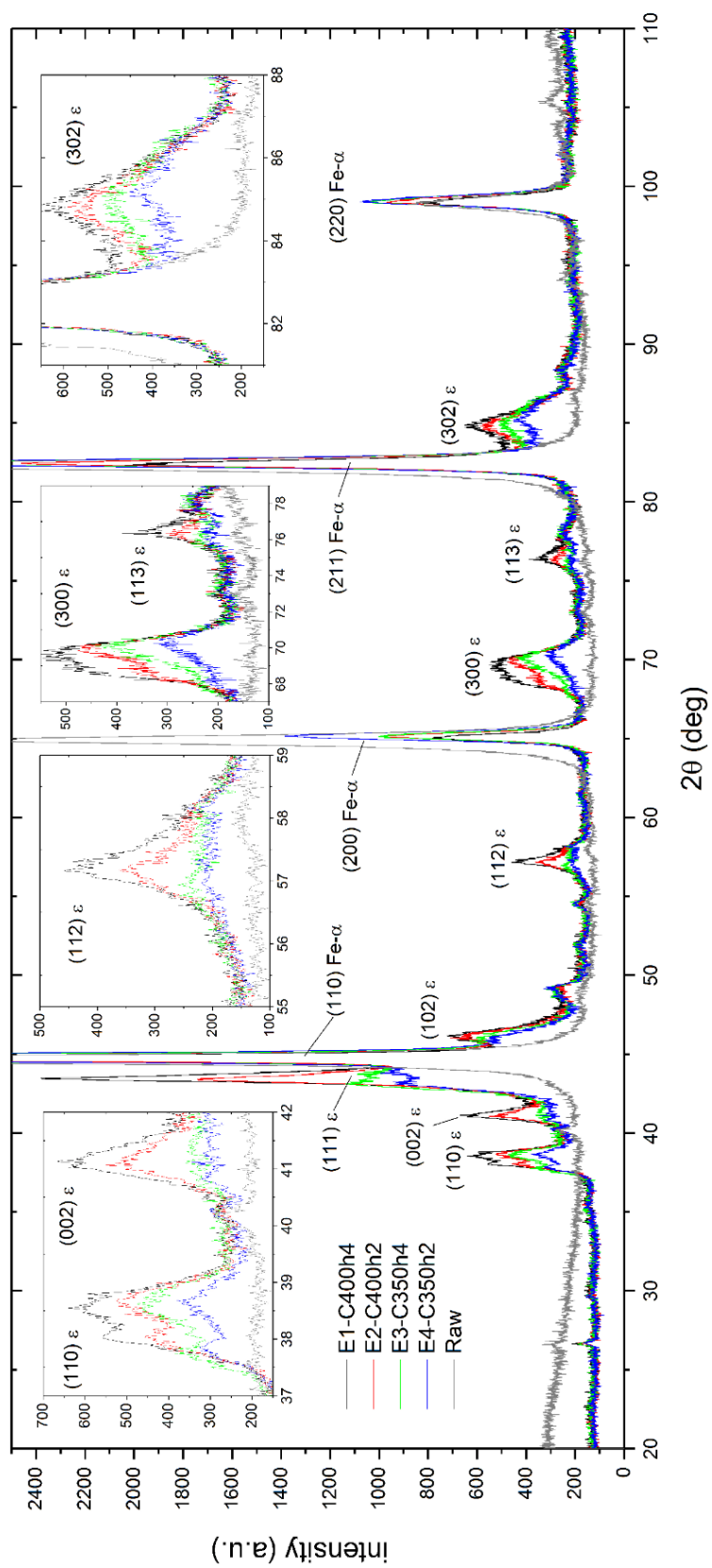


Figure 74: XRD combined diffractogram of the textured surface in the conditions E1-C400h4, E2-C400h2, E3-C350h4, E4-C350h2, and Raw.

4.1.4. Comparative SEM analysis of the surface

The textured surface appearance in a given region of the specimen treated at 400 °C during four hours, in a 75% N₂ / 25% H₂ atmosphere (E1) is presented in Figure 75, as observed through scanning electronic microscopy. The region characterized before SPN (Figure 75a), was later on localized and analyzed in condition after SPN (Figure 75b), using the same methodology.

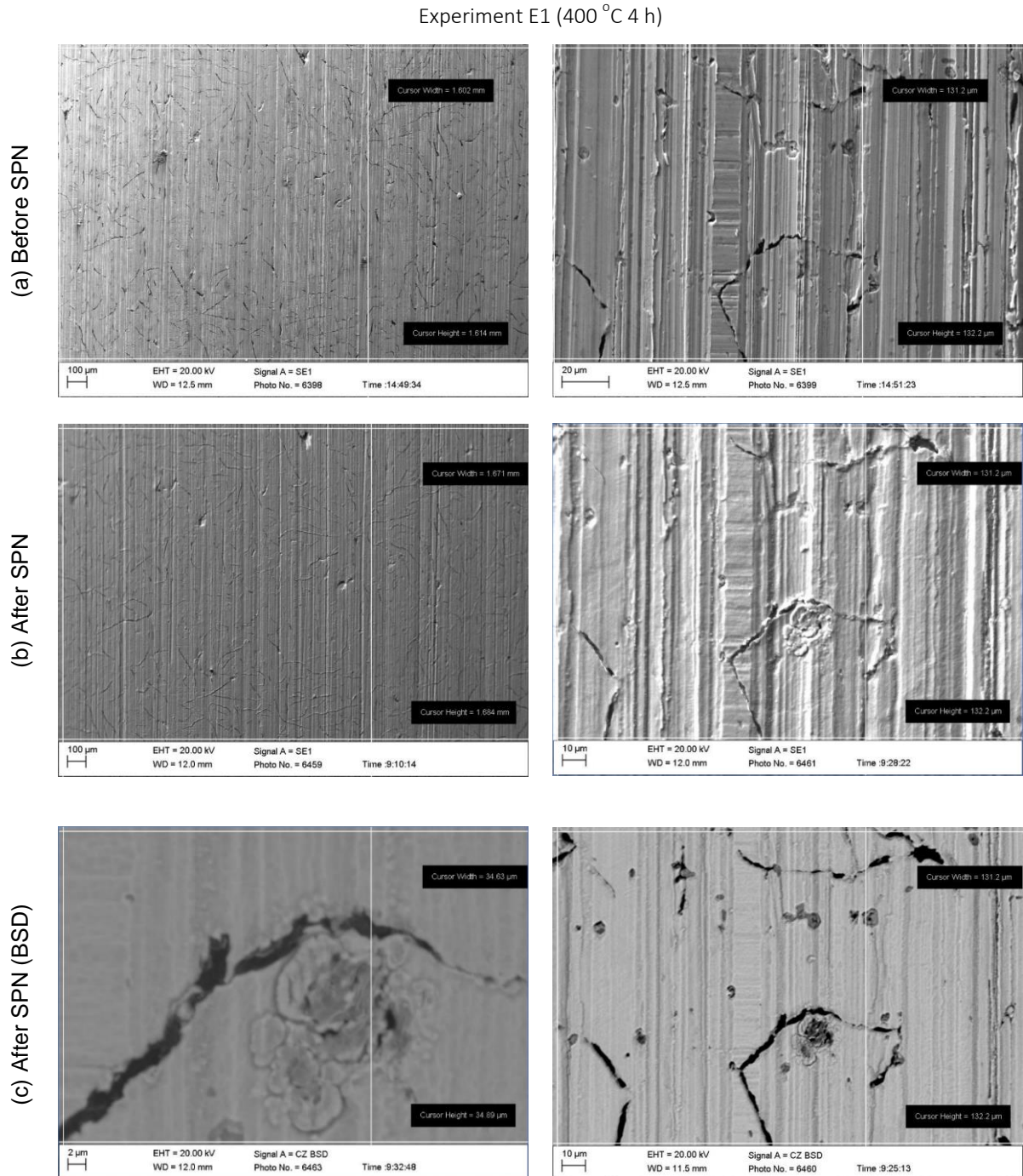


Figure 75: Experiment E1 (400 °C 4 h). Comparative Scanning Electronic Microscopy (SEM) images. Conditions (a) Before SPN, (b) After SPN - secondary electron analysis, and (c) After SPN - backscattered electron analysis.

Figure 75b, Figure 76b, Figure 77b, and Figure 78b, show that overall pattern of texturing grooves are preserved after SPN treatment. The distribution of vertical risks is still visible, reflecting the 3-D interferometry roughness results with respective parameters shown in previous sections.

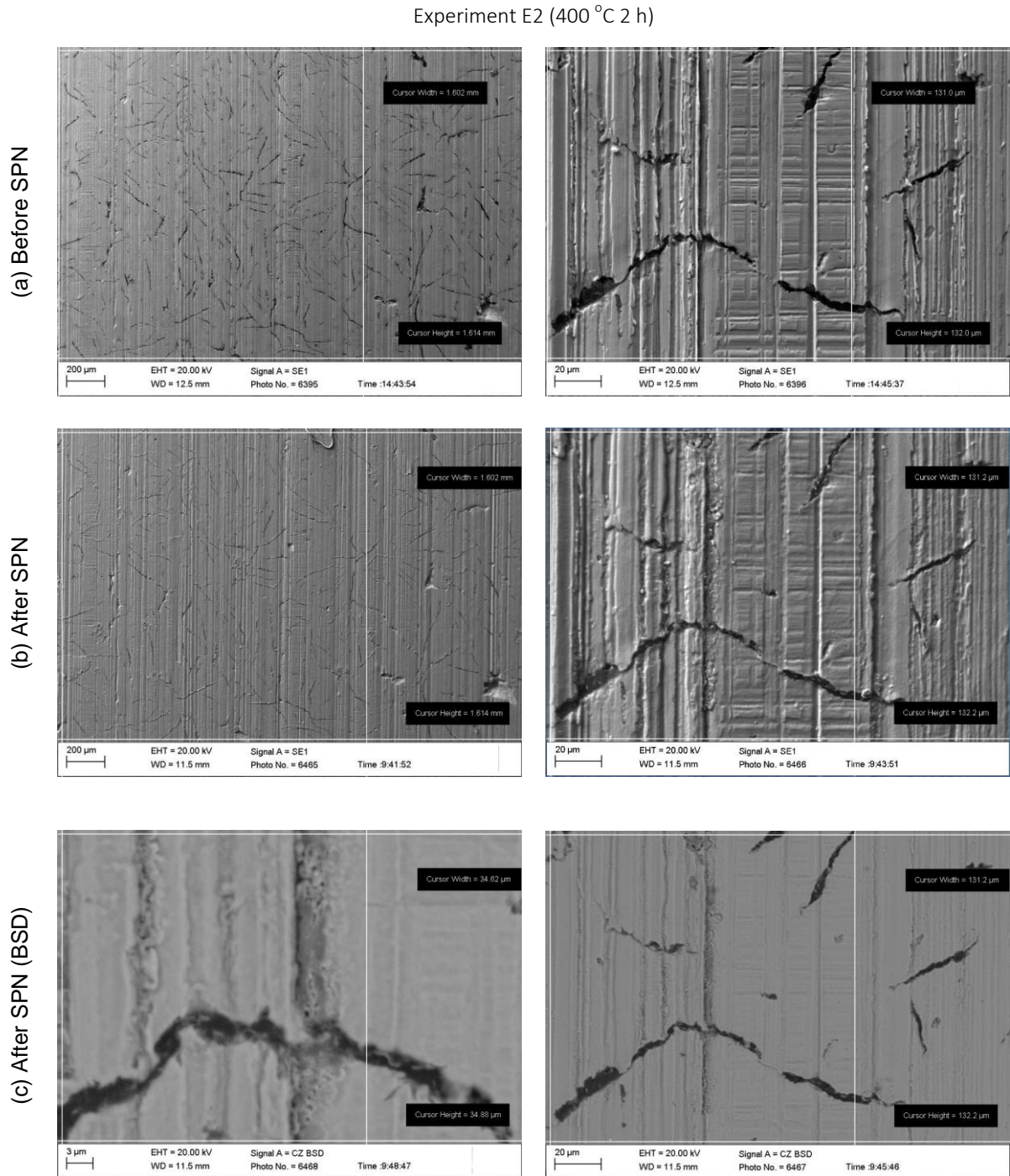


Figure 76: Experiment E2 (400 °C 2 h). Comparative Scanning Electronic Microscopy (SEM) images. Conditions (a) Before SPN, (b) After SPN - secondary electron analysis, and (c) After SPN - backscattered electron analysis.

Figure 75c, Figure 76c, Figure 77c, and Figure 78c, show the backscattered scanning electron microscope image (BSD-SEM) of same region shown in Figure 75b. Since BSD technic intensifies the contrast of the graphite rich regions, the graphite flakes appear in black or dark gray. Location, shape, and exposition of graphite flakes seem preserved after SPN.

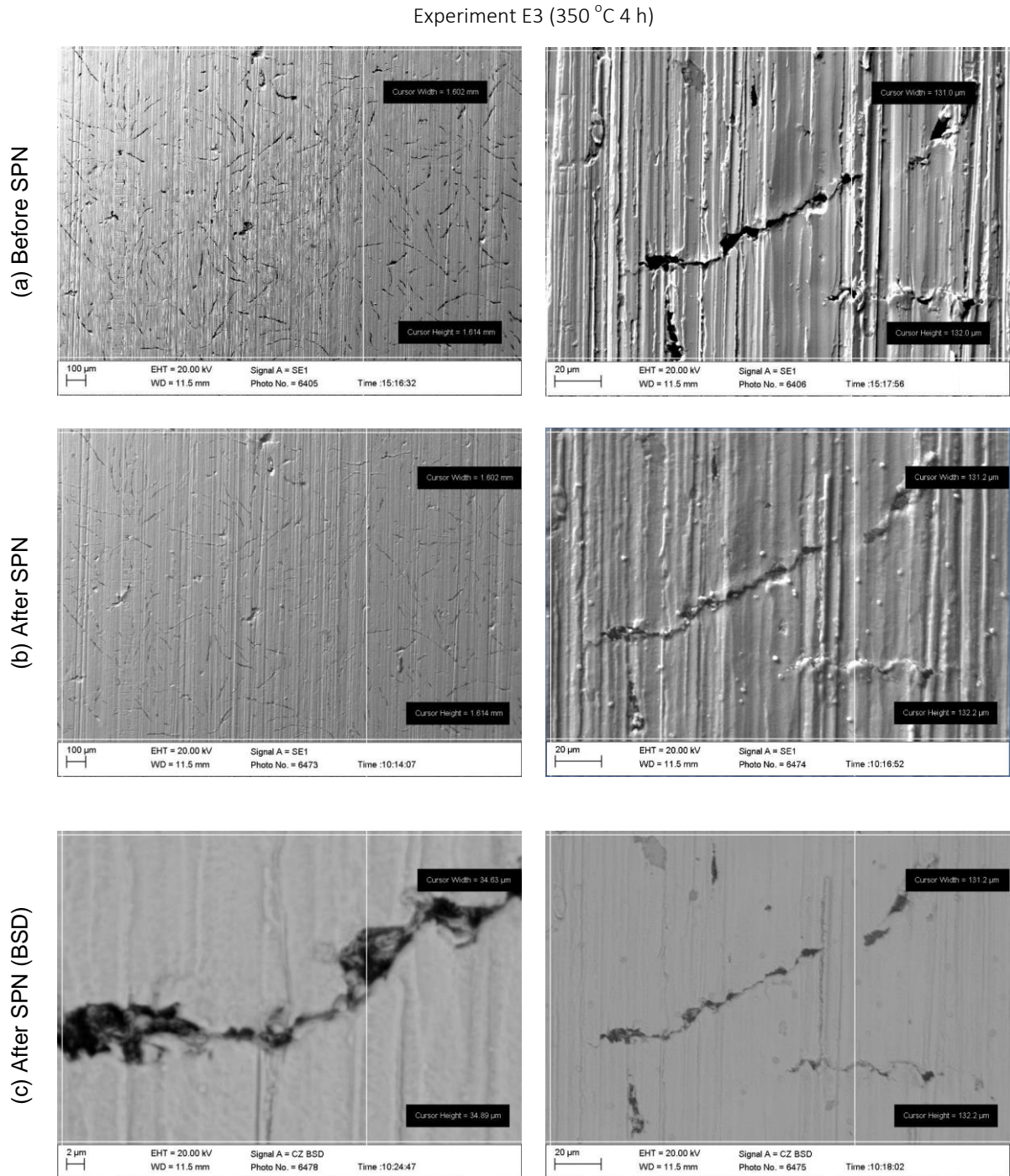


Figure 77: Experiment E3 (350 °C 4 h). Comparative Scanning Electronic Microscopy (SEM) images. Conditions (a) Before SPN, (b) After SPN - secondary electron analysis, and (c) After SPN - backscattered electron analysis.

With regard to SEM observations of surface aspect before and after SPN, no significant differences between results at different temperature-time conditions were noted, as seen in Figure 76, Figure 77, and Figure 78, which refer to the other three temperature-time (E2-E4) experimental conditions. No matter the experimental condition, the pattern of texturing grooves is satisfactorily preserved after SPN. In addition, the graphite pockets are still visible after the shallow plasma nitriding experiments.

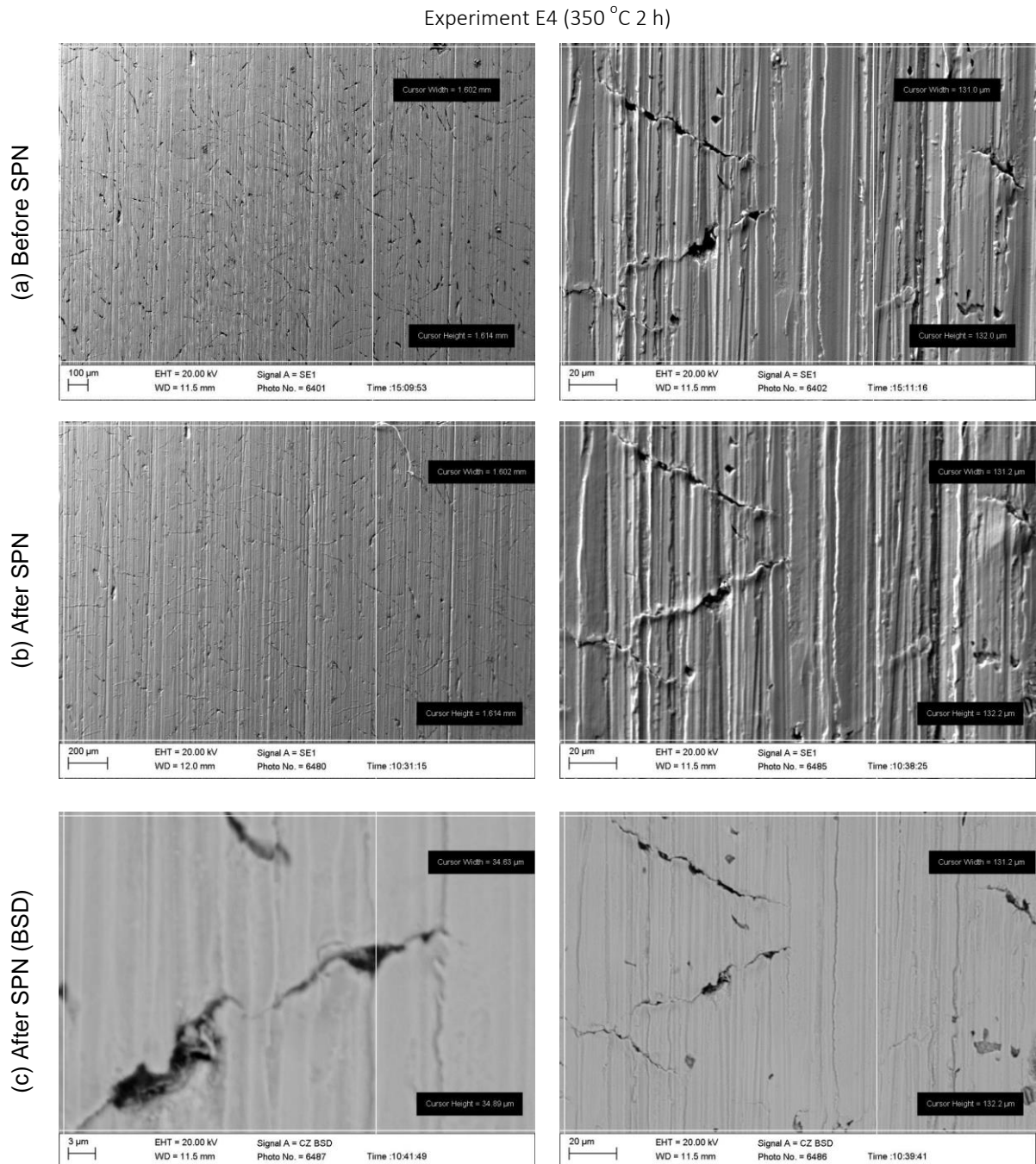


Figure 78: Experiment E4 (350 °C 2 h). Comparative Scanning Electronic Microscopy (SEM) images. Conditions (a) Before SPN, (b) After SPN - secondary electron analysis, and (c) After SPN - backscattered electron analysis.

4.1.5. Microhardness analysis

The 10 gf microhardness (HV 0.01) average and standard deviation of the samples (measured on top of the SPN zone) in the condition before and after SPN are graphically presented in Figure 79.

Higher microhardness was observed for the treated conditions at 400 °C during four and two hours, in a 75% N₂ / 25% H₂ atmosphere (E1-E2). Comparative results presented in Figure 79 indicate trends in correlation between microhardness and temperature conditions, with the average hardness increasing with the temperature.

In the initial condition, the microhardness was 428 ± 23 HV 0.01 (Table 19). The substantial hardness increase of treated conditions with respect to raw condition confirms iron nitride formation as well as indicates interstitial solid solution hardening.

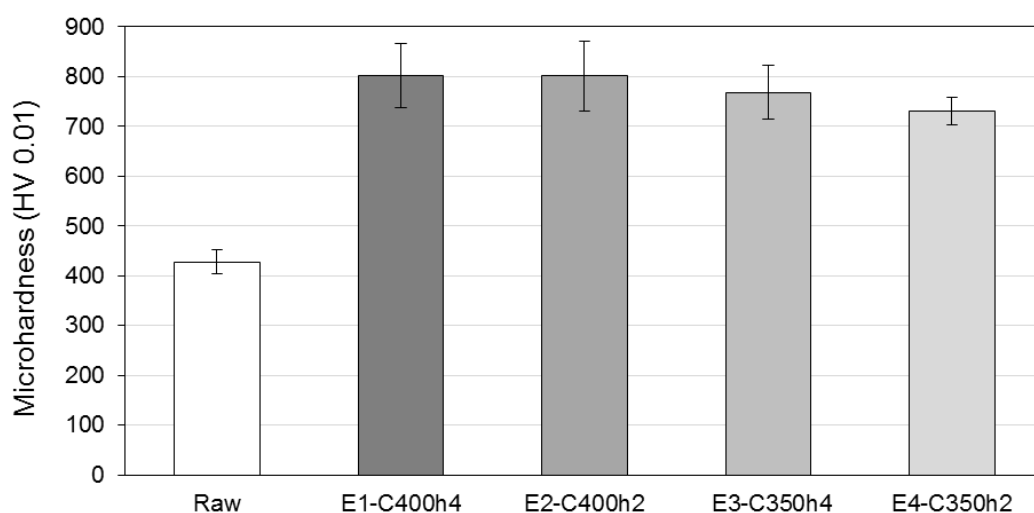


Figure 79: Microhardness (HV 0.01) on the surface (zero μm distance) measured with 10 gf. Avg values \pm std dev, $n = 5$. In-lab textured flat surface. Combined chart: Raw, E1-C400h4, E2-C400h2, E3-C350h4, E4-C350h2.

Microhardness results are consistent with both XRD patterns and WDS microanalysis results. Significant contrast in hardness was confirmed between raw and treated samples, whereas SPN time does not appear to affect significantly the range of hardness response values.

Figure 80 shows representative examples of indentations as measured through SEM. The measurements were carried out on the plateau regions of the textured surface, so that assuring appropriate quality of indentation diagonals (d_1 and d_2). Such values were reported next to each SEM image, along with the hardness value (HV) and estimative of indentation depth (h_{depth}).

The simplified calculation of depth was carried out based on average diagonal length and indenter angle (136°), and resulted in a range from $0.69 \pm 0.02 \mu\text{m}$ (E1) to $0.72 \pm 0.02 \mu\text{m}$ (E4)

in average values. Accordingly, and based on the nitrogen concentration profile, the hardness indentation depth is located within the N-enriched zone.

Statistical analysis of microhardness results using Minitab software is presented in the following subsection. The analysis considered data variation in each set of measurements.

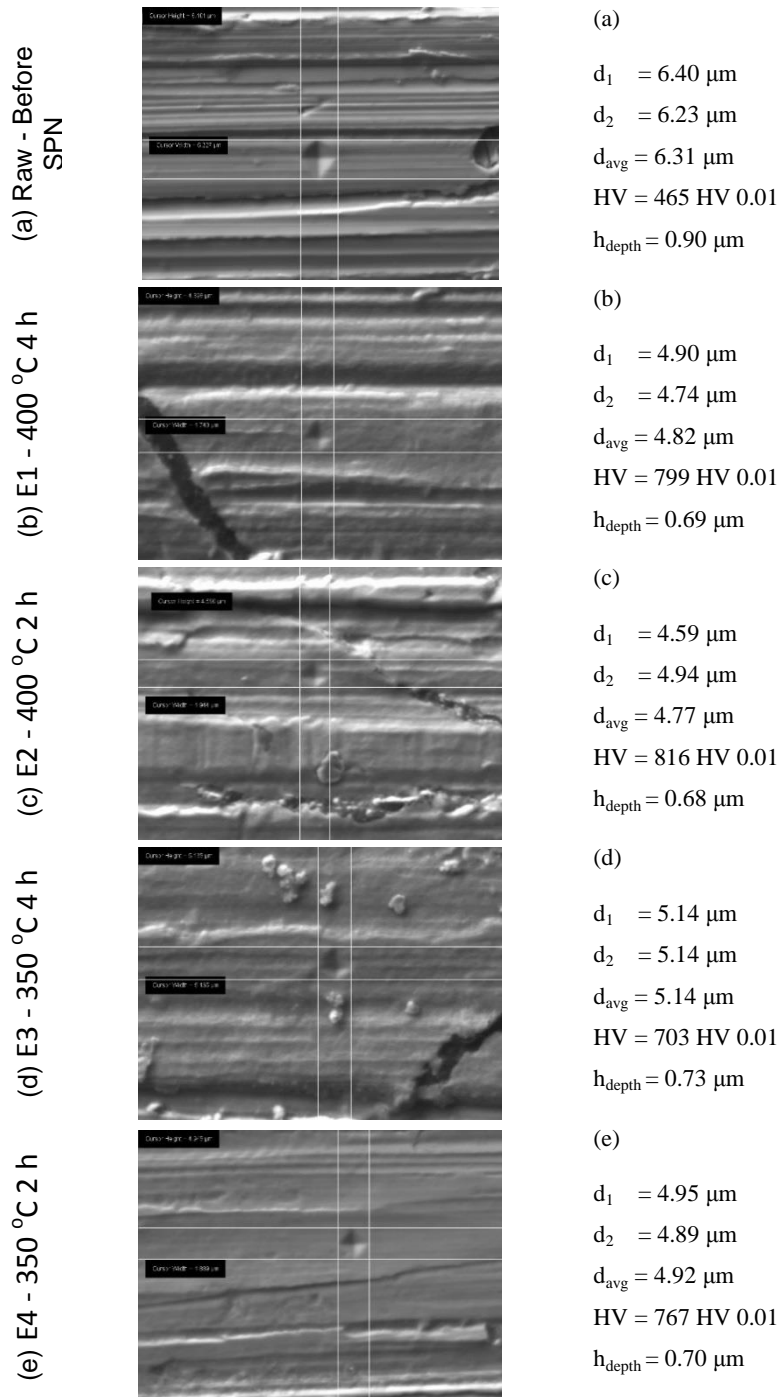


Figure 80: Examples of single indentation measured through SEM. Measurements carried out preferably on plateau regions. a) Raw, b) E1-C400h4, c) E2-C400h2, d) E3-C350h4, e) E4-C350h2. Significant hardness contrast found between raw and treated samples. SPN time has not significantly affected the range of hardness response values.

Table 19: Data group of Microhardness (HV 0.01) on the surface (zero μm distance) measured with 10 gf, $n = 5$. In-lab textured flat surface. Conditions: Raw, Raw, E1-C400h4, E2-C400h2, E3-C350h4, E4-C350h2.

Sample	Raw	E1-C400h4	E2-C400h2	E3-C350h4	E4-C350h2
s1	416	838	899	807	724
s2	465	799	753	719	748
s3	431	758	816	786	767
s4	403	725	761	703	722
s5	425	889	780	826	693
Avg	428	802	802	768	731
StdDev	23	64	70	54	28

4.1.5.1. Statistical analysis of microhardness results using Minitab

Minitab Boxplot graphs of microhardness (HV 0.01), in the condition before and after experiments, are shown in Figure 81. After-boxplots are shifted with no overlaps with respect to Before-boxplot position, regardless the temperature-time experimental condition. This aspect evidences that Mean hardness statistically changed after SPN treatment. One-Way ANOVA Before/After comparison analysis presented in Figure 82 quantitatively confirmed this result.

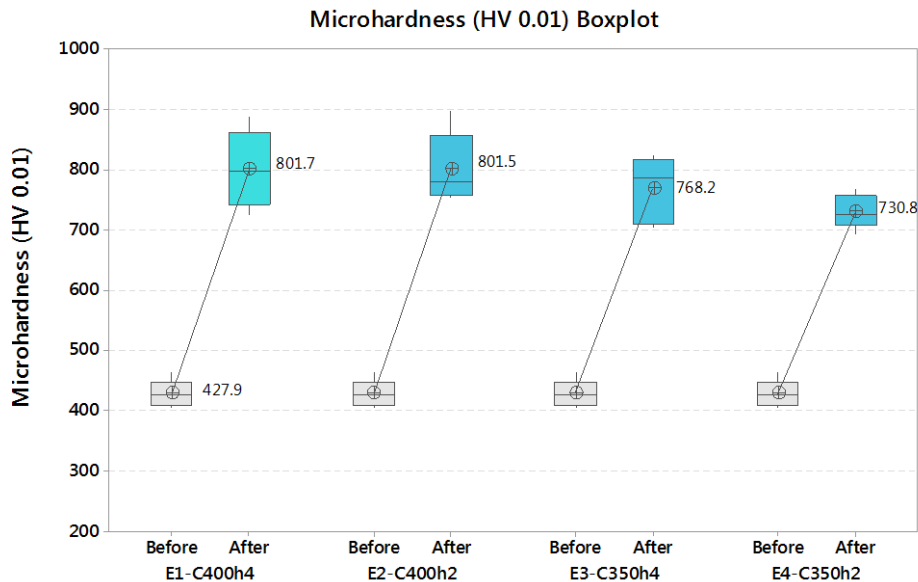


Figure 81: Boxplot of experiment results, before and after treatment. Microhardness (HV 0.01).

The height of the After-boxplots as well as the Median positions indicated that final distribution skewness varied with the experimental condition. Therefore, the hardness variability does not appear to follow a general tendency. In experiment E1, the distribution resulted nearly symmetrical. In E2, the large box area above the Median position indicates that the data has now positive skewness - the right tail of the distribution is longer than the left tail.

In E3, the data has negative skewness. In E4, the distribution is nearly symmetrical, but with reduced standard deviation with respect to other conditions. Such response was confirmed by One-Way ANOVA Diagnostic Report (Figure 83). Therefore, statistical analysis evidenced the substantial hardness increase with SPN treatments.

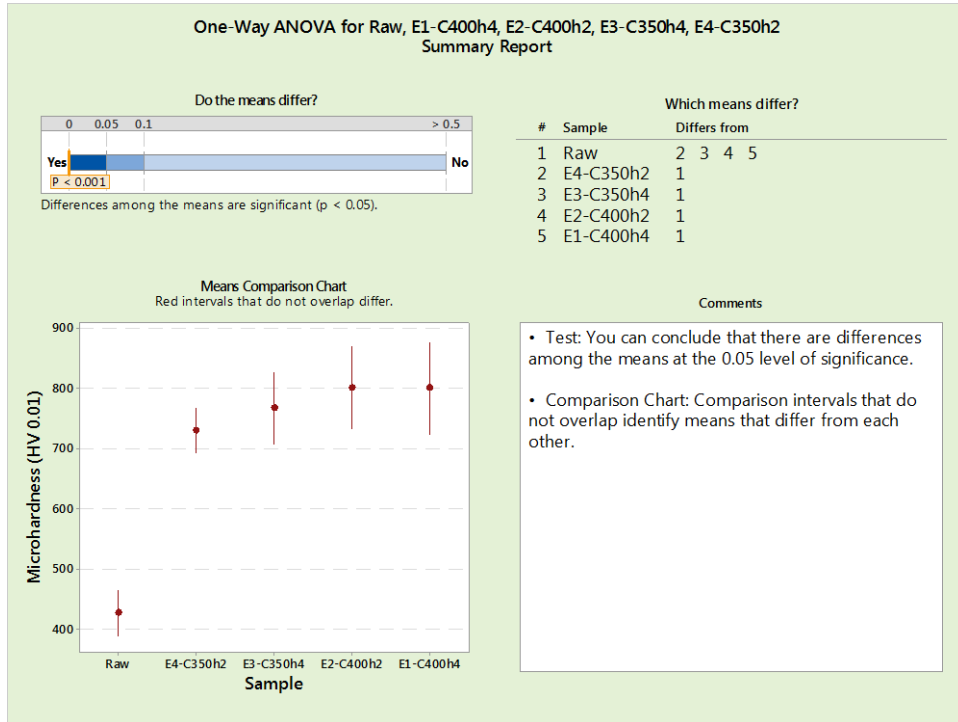


Figure 82: Minitab One-Way ANOVA Summary Report. Test for Microhardness, before and after treatment.

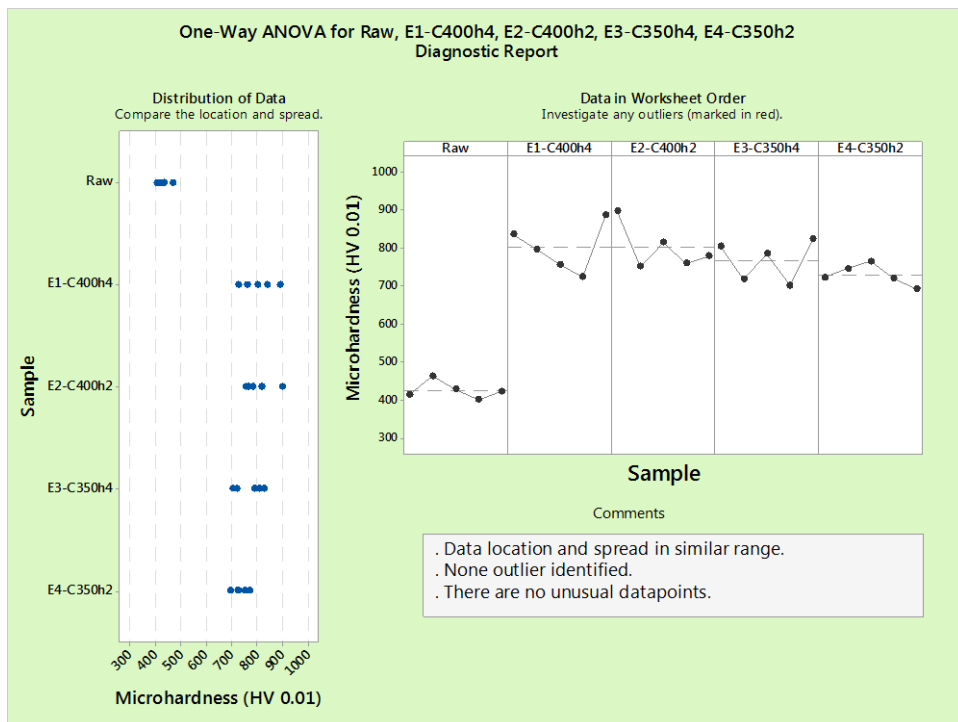


Figure 83: Minitab One-Way ANOVA Diagnostic Report. Test for Microhardness, before and after treatment.

4.1.6. Instrumented linear sclerometry test

4.1.6.1. 3-D surface profile, “groove area” (Ss), “pile-up area” (Sp) and depth (dh)

Each 3-D group of images (e.g., Figure 84) exhibited in the next sequence of figures presents the aspect of one of three scratches that were characterized for each SPN experimental condition. Corresponding 2-D profilograms of the textured surface and resulting sclerometry groove are also presented right after the interferometry 3-D profiles (e.g., Figure 85).

Vertical lines, positioned to the left and right side of the groove, have defined the limits for ‘Sp’ calculation, whereas ‘Ss’ has been limited by the profile mean line. The complete data group of computed Ss, Sp, and dh values was reported in Table format.

While groove area (Ss) and depth (dh) values were accurately defined based on the texture mean line, the definition of limits for pile-up area (Sp) includes higher inherent uncertainties from the method. This is because differently from a polished specimen situation - where the limit of piled-up material and surface topography is well demarcated - in a pre-textured specimen there is no clear point of interface between what is pile-up area and what is roughness variation. The difficulty becomes more prominent as the observer approaches smaller distances from beginning of test, which are conditions of lower indenter loads. Considering the mentioned limitations for pile-up area definition, it was deemed reasonable to reducing the pile-up calculation limits whenever the initial result was higher than groove area.

The 2-D profile analysis was done assisted by the 3-D profile images, making possible an attempt to differentiate sclerometry piled-up material from the texturing roughness peaks. Definition of such criteria was intended to avoid (or minimize) the risk of overestimating the Sp numbers, and therefore the actual ductility of a SPN surface.

In spite of the above method limitation, the characterization was considered successful, as “Ss”, “Sp” and “dh” were mapped for each single experimental condition (along with the raw condition as a baseline).

Consequently, the 3-D interferometry characterization with corresponding 2-D profiles substantiated the construction of the set of graphs further reported in the present section.

Figure 84, Figure 86, Figure 88, and Figure 90, show the Top [slightly-tilted] view of the 3-D profile of the textured surface plane in the conditions E1 (400 °C 4 h), E2 (400 °C 2 h), E3 (350 °C 4 h), and E4 (350 °C 2 h), respectively. In addition, Figure 92 shows the corresponding profile in the condition Raw, before SPN treatment (Baseline raw sample).

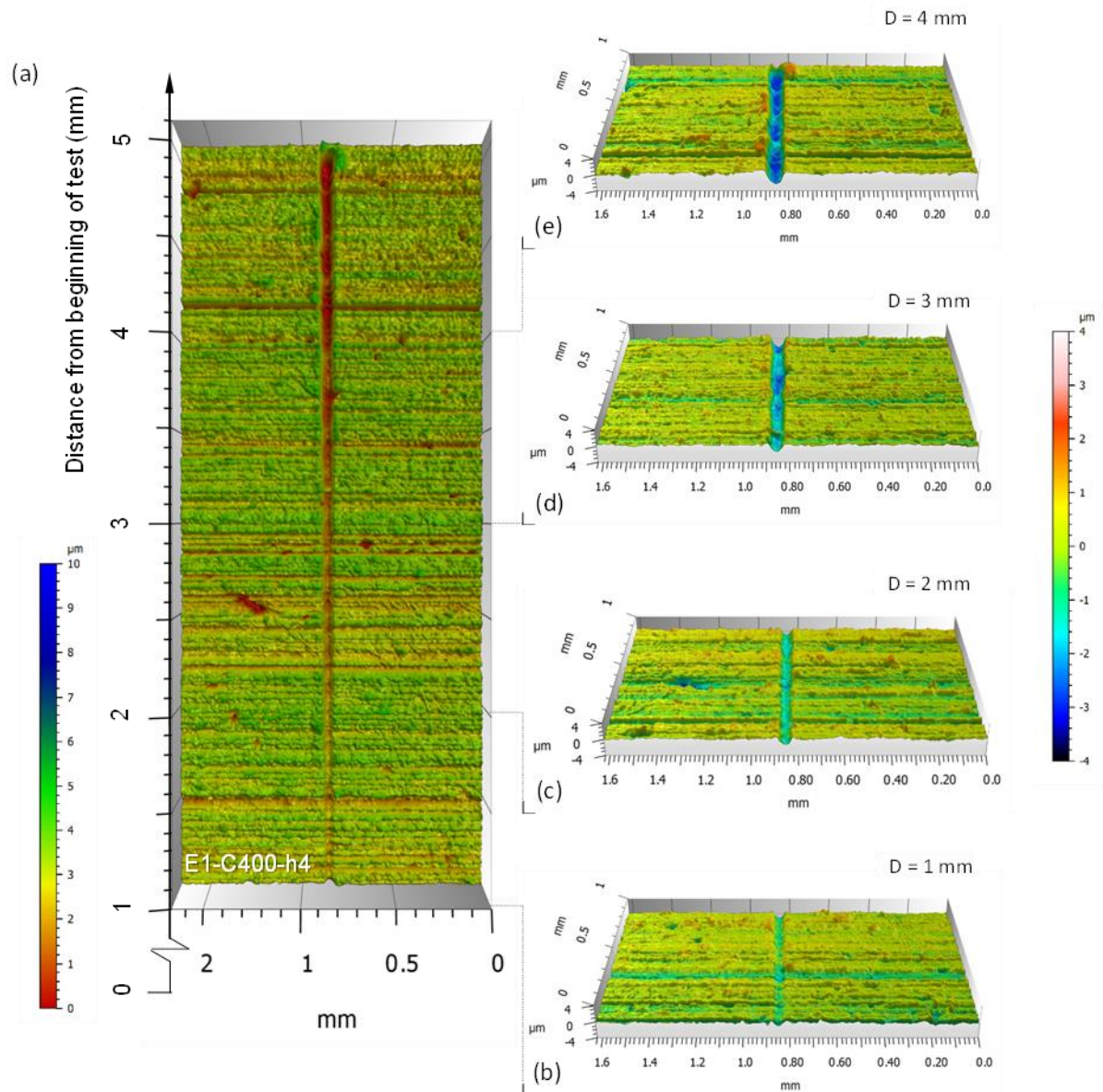


Figure 84: Instrumented linear sclerometry test. a) Top [slightly-tilted] view of the 3-D profile of the textured surface plane. Experiment E1 (400 °C 4 h). In-lab textured flat specimen. 1N pre-load applied during 10s at initial distance. Next, indenter was linearly moved increasing load, 1N to 10N, with velocity of 0.028 mm/s, resulting in the scratch of 5 mm in length. The color scale in the side indicates the resulting heights from valley to peak. b) Front [30° tilted] view of the 3-D scratch section at 1 mm distance. c-e) Similar as 'b' images at 2 mm, 3 mm and 4 mm distances, respectively, highlighting the progressive evolution of the sclerometry groove. The region 0-1 mm (test stabilization zone) was not considered in data analysis.

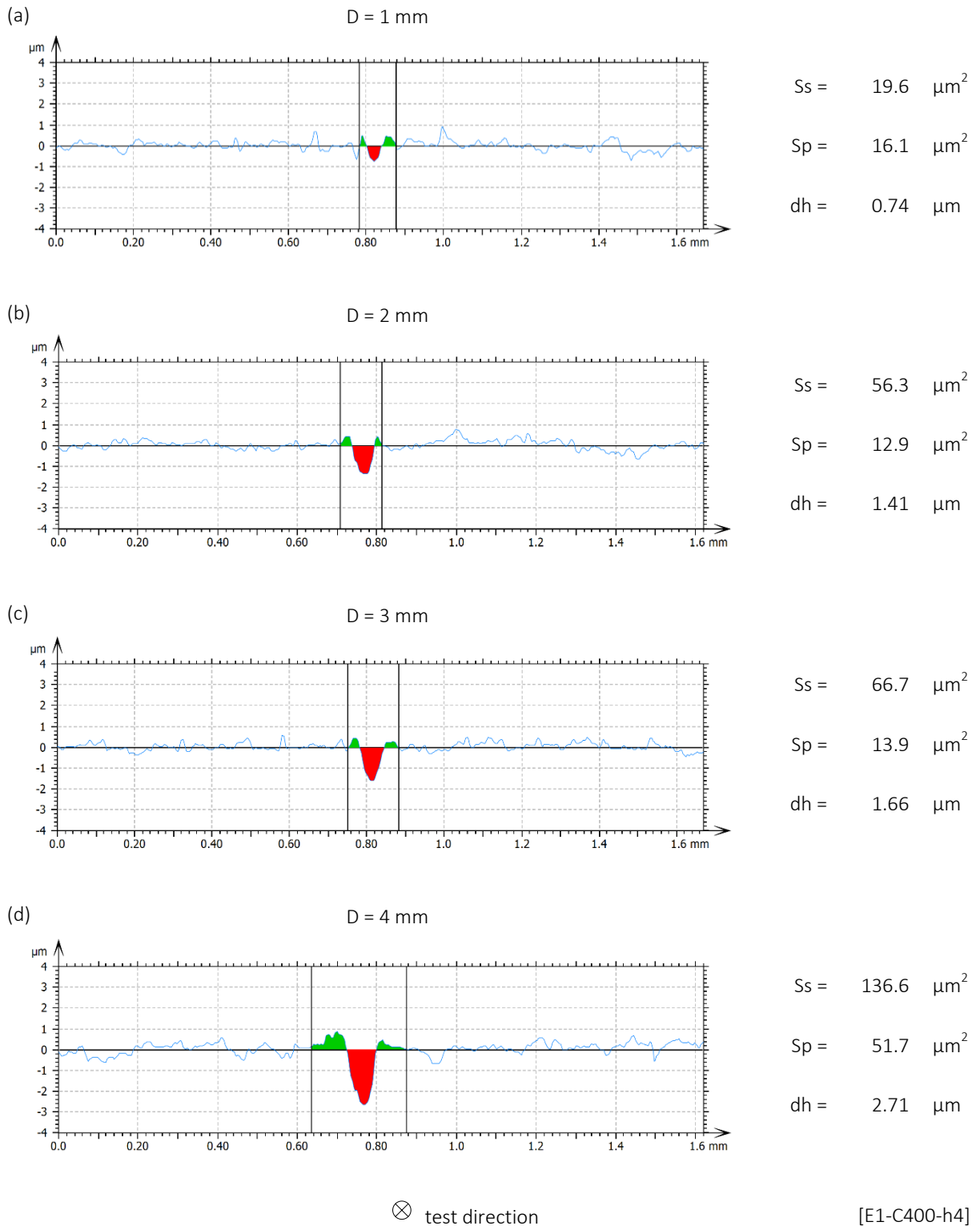


Figure 85: Instrumented linear sclerometry test. 2-D profilograms of the textured surface and resulting sclerometry groove. Experiment E1 (400 °C 4 h). In-lab textured flat specimen. Section locations corresponding to previous 3-D profile images. All the graphs: test direction towards the plane of the page. a-d) “Groove area” (S_s) - in red and “pile-up area” (S_p) - in green, at distances from beginning of test: 1 mm, 2 mm, 3 mm and 4 mm. S_s and S_p computed values reported along with each graph. In addition, punctual measurement of depth (dh) is informed.

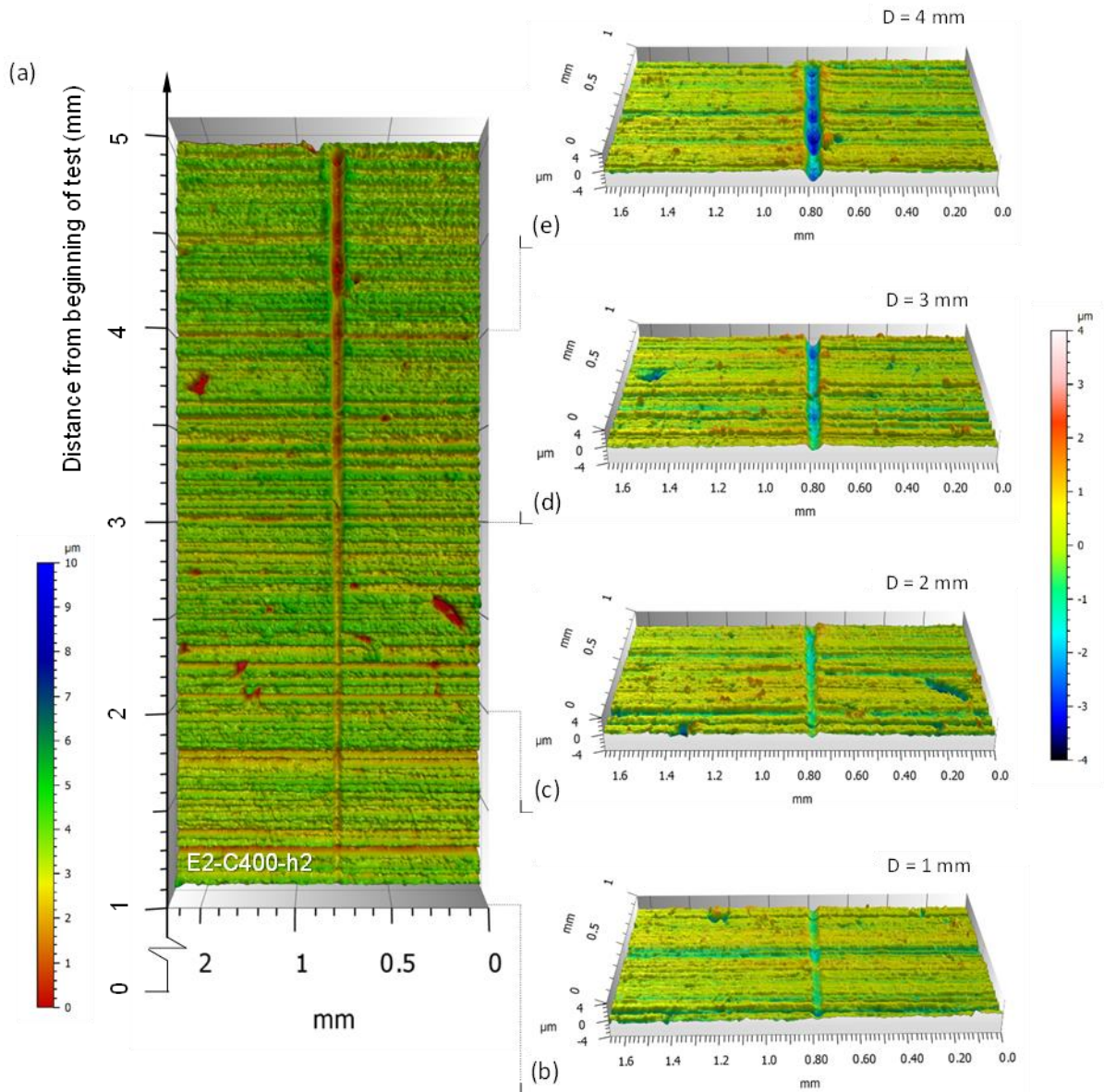


Figure 86: Instrumented linear sclerometry test. a) Top [slightly-tilted] view of the 3-D profile of the textured surface plane. Experiment E2 (400 °C 2 h). In-lab textured flat specimen. 1N pre-load applied during 10s at initial distance. Next, indenter was linearly moved increasing load, 1N to 10N, with velocity of 0.028 mm/s, resulting in the scratch of 5 mm in length. The color scale in the side indicates the resulting heights from valley to peak. b) Front [30° tilted] view of the 3-D scratch section at 1 mm distance. c-e) Similar as 'b' images at 2 mm, 3 mm and 4 mm distances, respectively, highlighting the progressive evolution of the sclerometry groove. The region 0-1 mm (test stabilization zone) was not considered in data analysis.

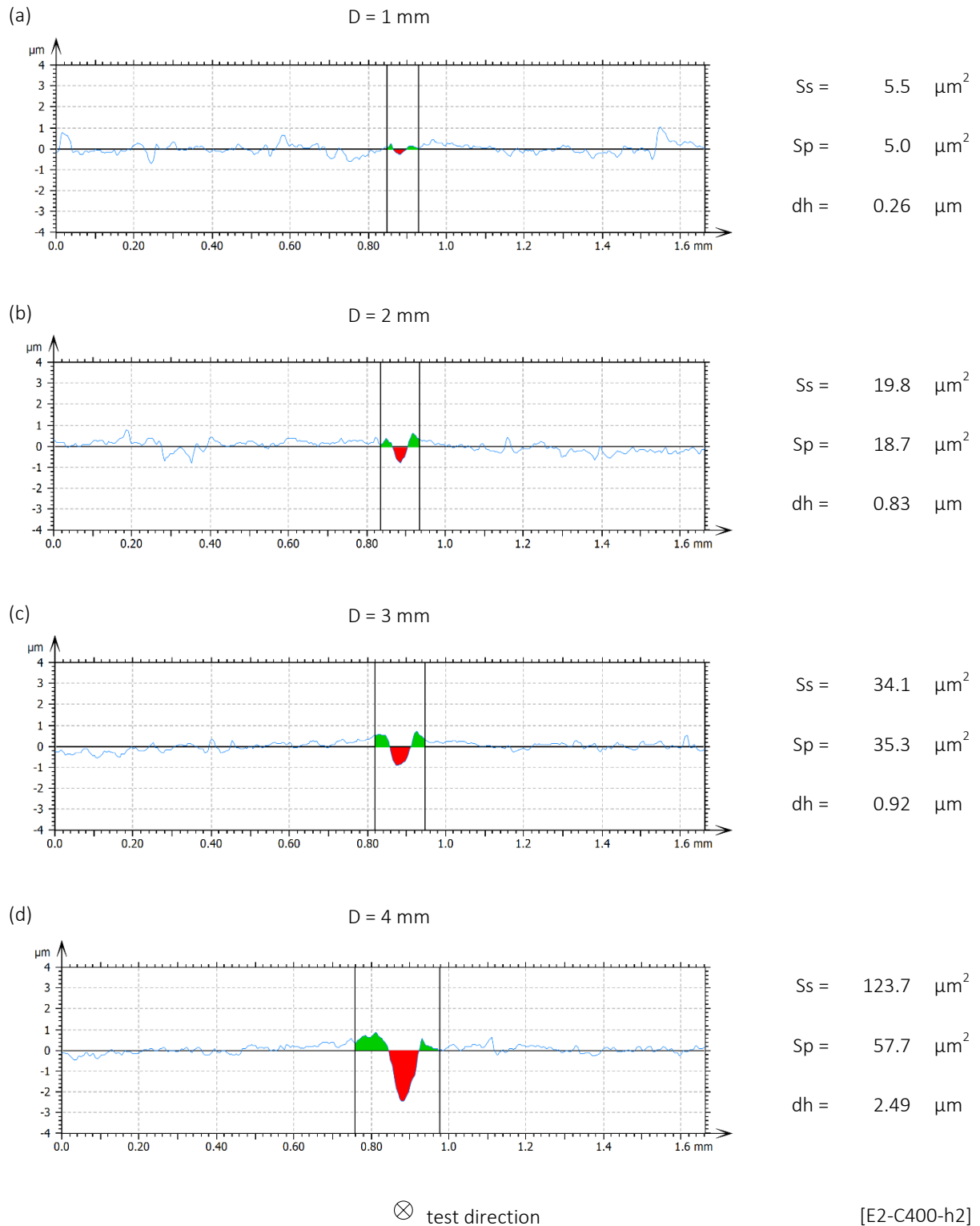


Figure 87: Instrumented linear sclerometry test. 2-D profilograms of the textured surface and resulting sclerometry groove. Experiment E2 (400 °C 2 h). In-lab textured flat specimen. Section locations corresponding to previous 3-D profile images. All the graphs: test direction towards the plane of the page. a-d) “Groove area” (S_s) - in red and “pile-up area” (S_p) - in green, at distances from beginning of test: 1 mm, 2 mm, 3 mm and 4 mm. S_s and S_p computed values reported along with each graph. In addition, punctual measurement of depth (dh) is informed.

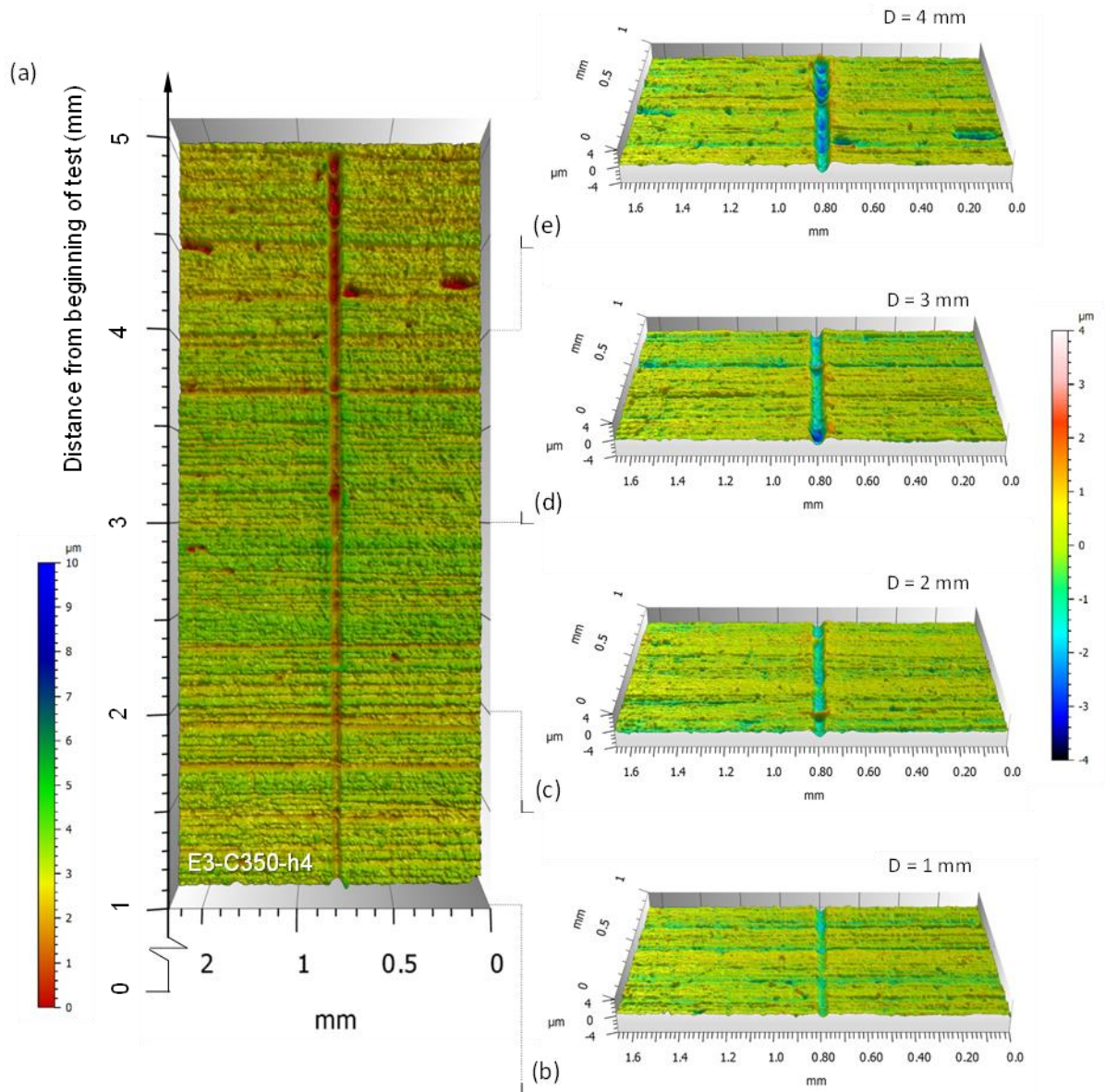


Figure 88: Instrumented linear sclerometry test. a) Top [slightly-tilted] view of the 3-D profile of the textured surface plane. Experiment E3 (350 °C 4 h). In-lab textured flat specimen. 1N pre-load applied during 10s at initial distance. Next, indenter was linearly moved increasing load, 1N to 10N, with velocity of 0.028 mm/s, resulting in the scratch of 5 mm in length. The color scale in the side indicates the resulting heights from valley to peak. b) Front [30° tilted] view of the 3-D scratch section at 1 mm distance. c-e) Similar as ‘b’ images at 2 mm, 3 mm and 4 mm distances, respectively, highlighting the progressive evolution of the sclerometry groove. The region 0-1 mm (test stabilization zone) was not considered in data analysis.

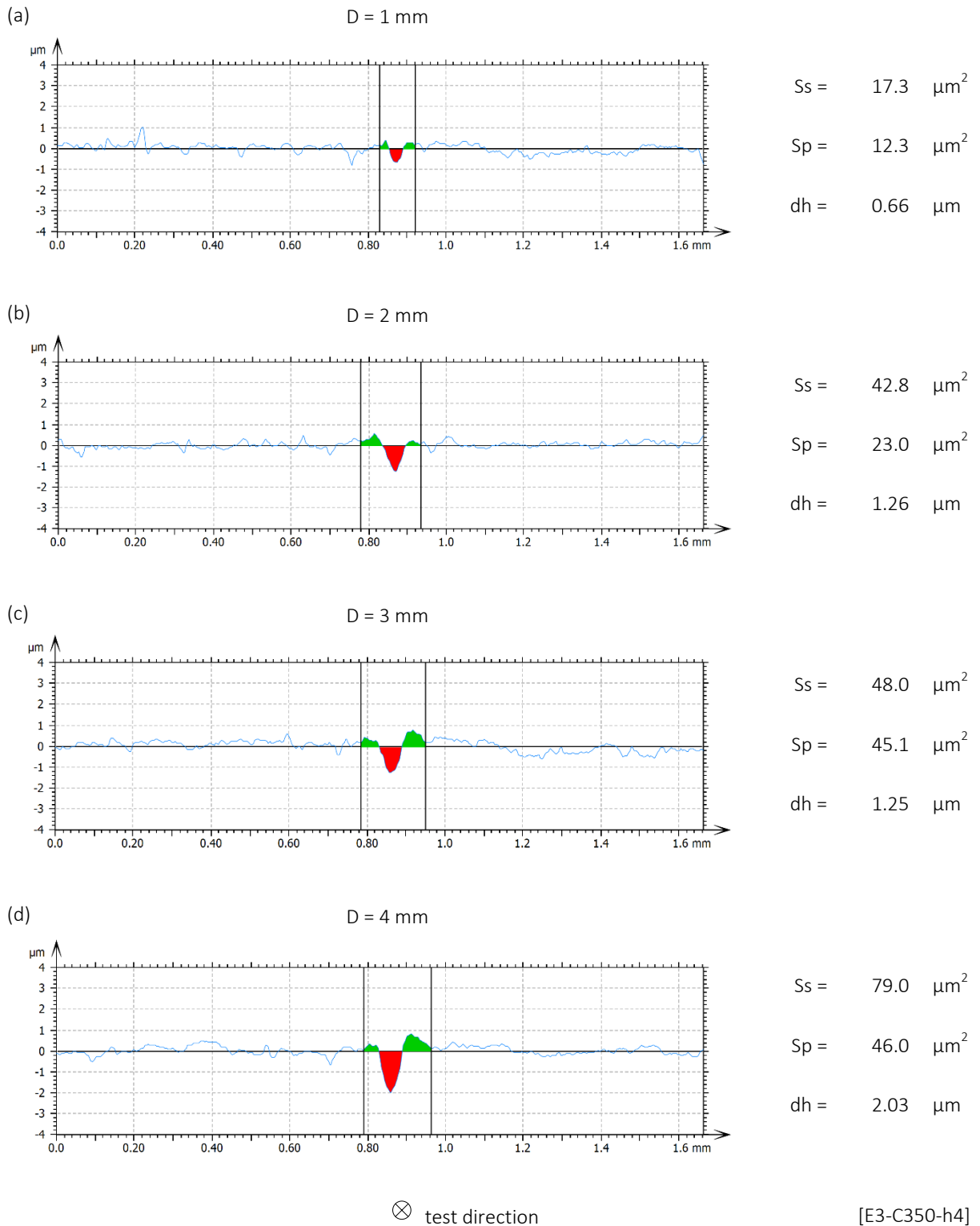


Figure 89: Instrumented linear sclerometry test. 2-D profilograms of the textured surface and resulting sclerometry groove. Experiment E3 (350 °C 4 h). In-lab textured flat specimen. Section locations corresponding to previous 3-D profile images. All the graphs: test direction towards the plane of the page. a-d) “Groove area” (S_s) - in red and “pile-up area” (S_p) - in green, at distances from beginning of test: 1 mm, 2 mm, 3 mm and 4 mm. S_s and S_p computed values reported along with each graph. In addition, punctual measurement of depth (dh) is informed.

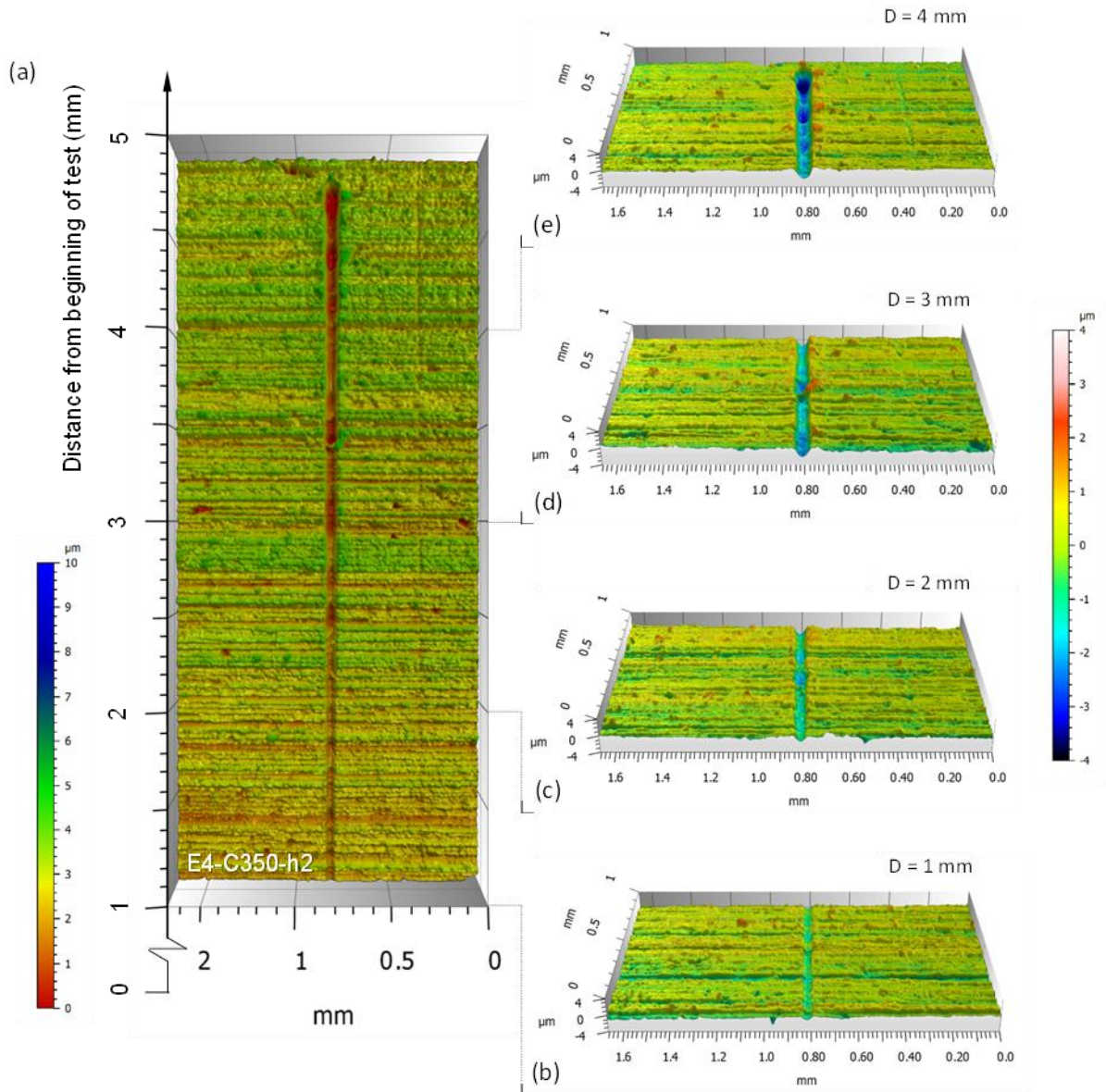


Figure 90: Instrumented linear sclerometry test. a) Top [slightly-tilted] view of the 3-D profile of the textured surface plane. Experiment E4 (350 °C 2 h). In-lab textured flat specimen. 1N pre-load applied during 10s at initial distance. Next, indenter was linearly moved increasing load, 1N to 10N, with velocity of 0.028 mm/s, resulting in the scratch of 5 mm in length. The color scale in the side indicates the resulting heights from valley to peak. b) Front [30° tilted] view of the 3-D scratch section at 1 mm distance. c-e) Similar as ‘b’ images at 2 mm, 3 mm and 4 mm distances, respectively, highlighting the progressive evolution of the sclerometry groove. The region 0-1 mm (test stabilization zone) was not considered in data analysis.

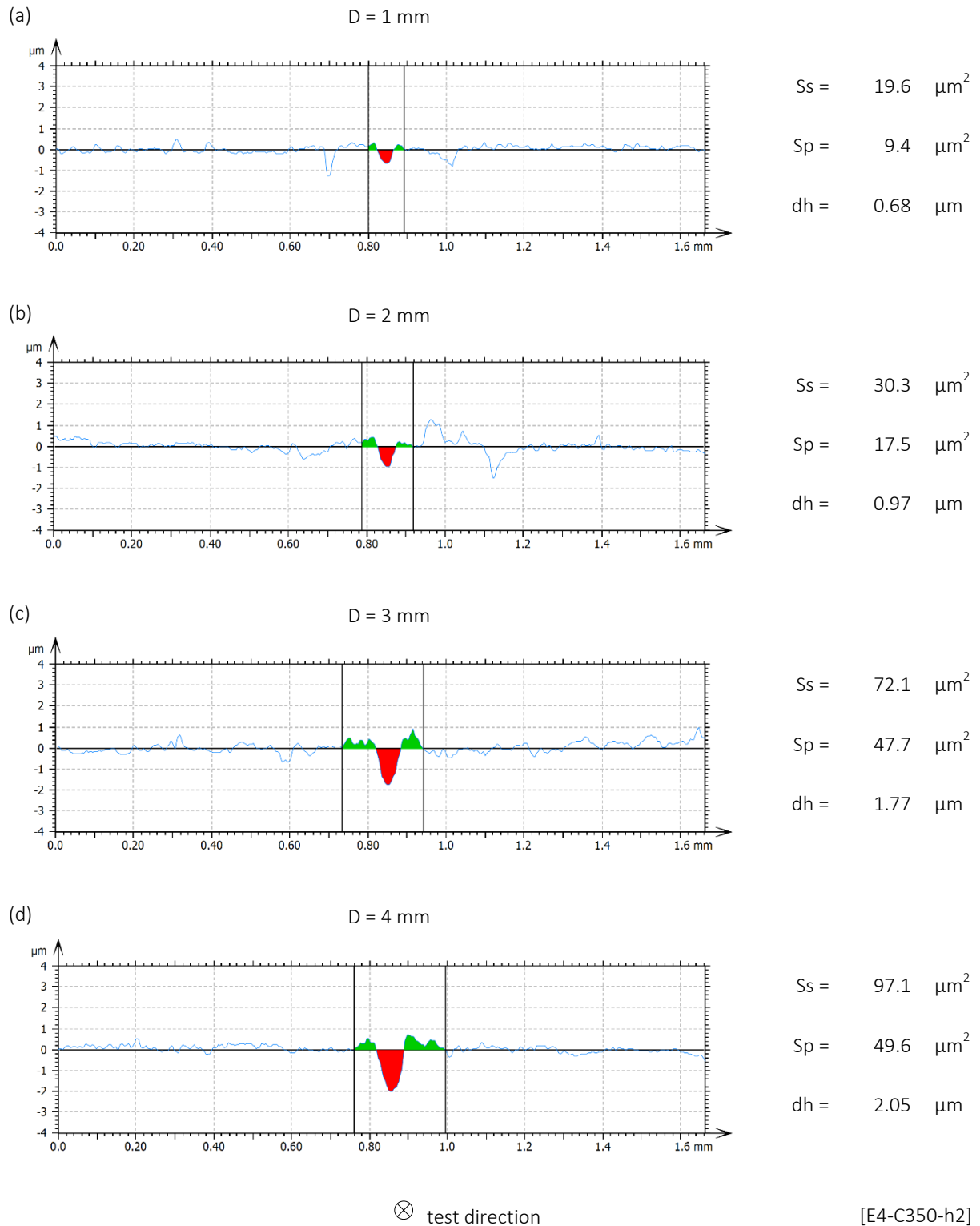


Figure 91: Instrumented linear sclerometry test. 2-D profilograms of the textured surface and resulting sclerometry groove. Experiment E4 (350 °C 2 h). In-lab textured flat specimen. Section locations corresponding to previous 3-D profile images. All the graphs: test direction towards the plane of the page. a-d) “Groove area” (S_s) - in red and “pile-up area” (S_p) - in green, at distances from beginning of test: 1 mm, 2 mm, 3 mm and 4 mm. S_s and S_p computed values reported along with each graph. In addition, punctual measurement of depth (dh) is informed.

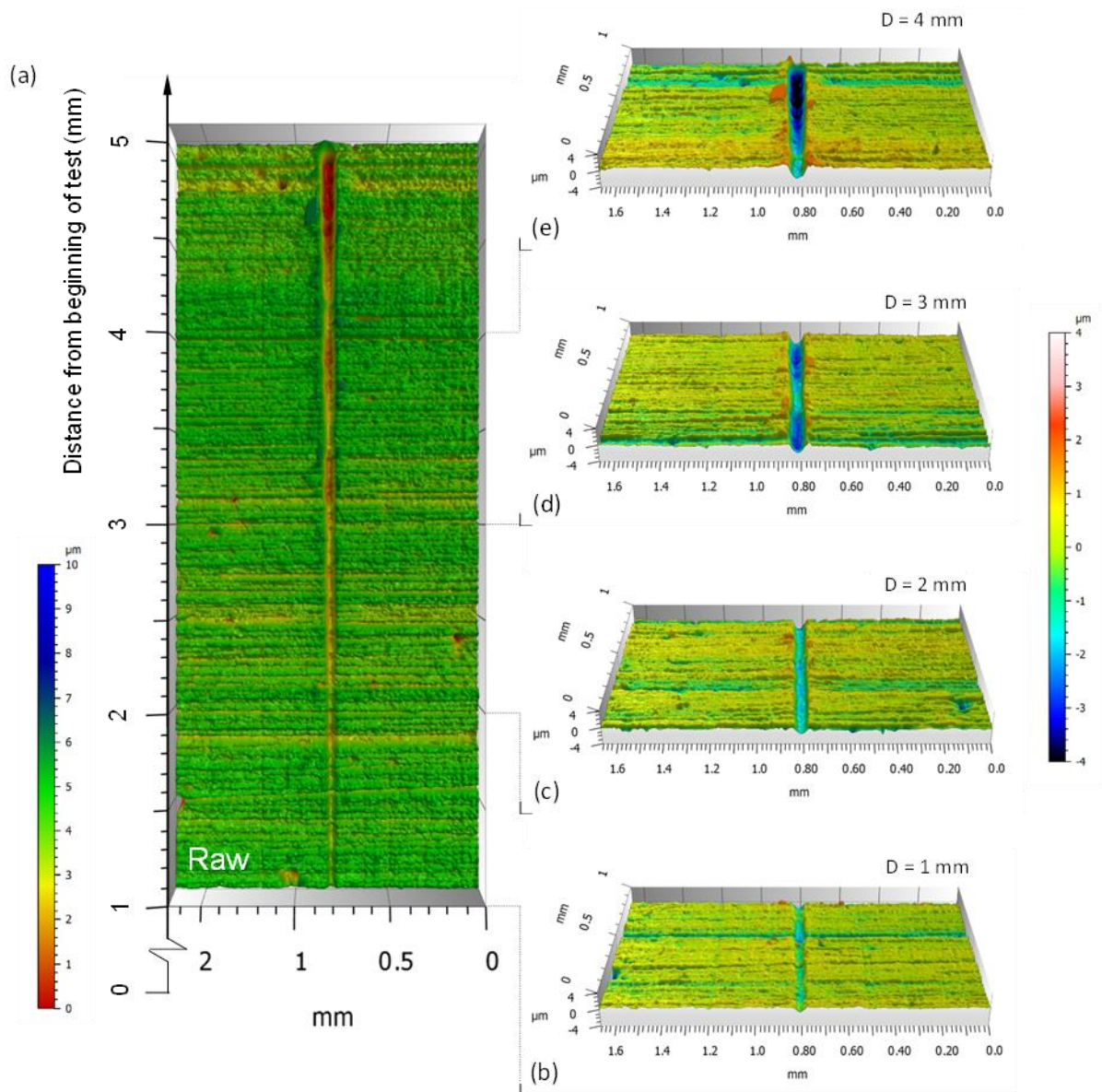


Figure 92: Instrumented linear sclerometry test. a) Top [slightly-tilted] view of the 3-D profile of the textured surface plane in the condition Raw, before SPN treatment (Baseline raw sample). In-lab textured flat specimen. 1N pre-load applied during 10s at initial distance. Next, indenter was linearly moved increasing load, 1N to 10N, with velocity of 0.028 mm/s, resulting in the scratch of 5 mm in length. The color scale in the side indicates the resulting heights from valley to peak. b) Front [30° tilted] view of the 3-D scratch section at 1 mm distance. c-e) Similar as 'b' images at 2 mm, 3 mm and 4 mm distances, respectively, highlighting the progressive evolution of the sclerometry groove. The region 0-1 mm (test stabilization zone) was not considered in data analysis.

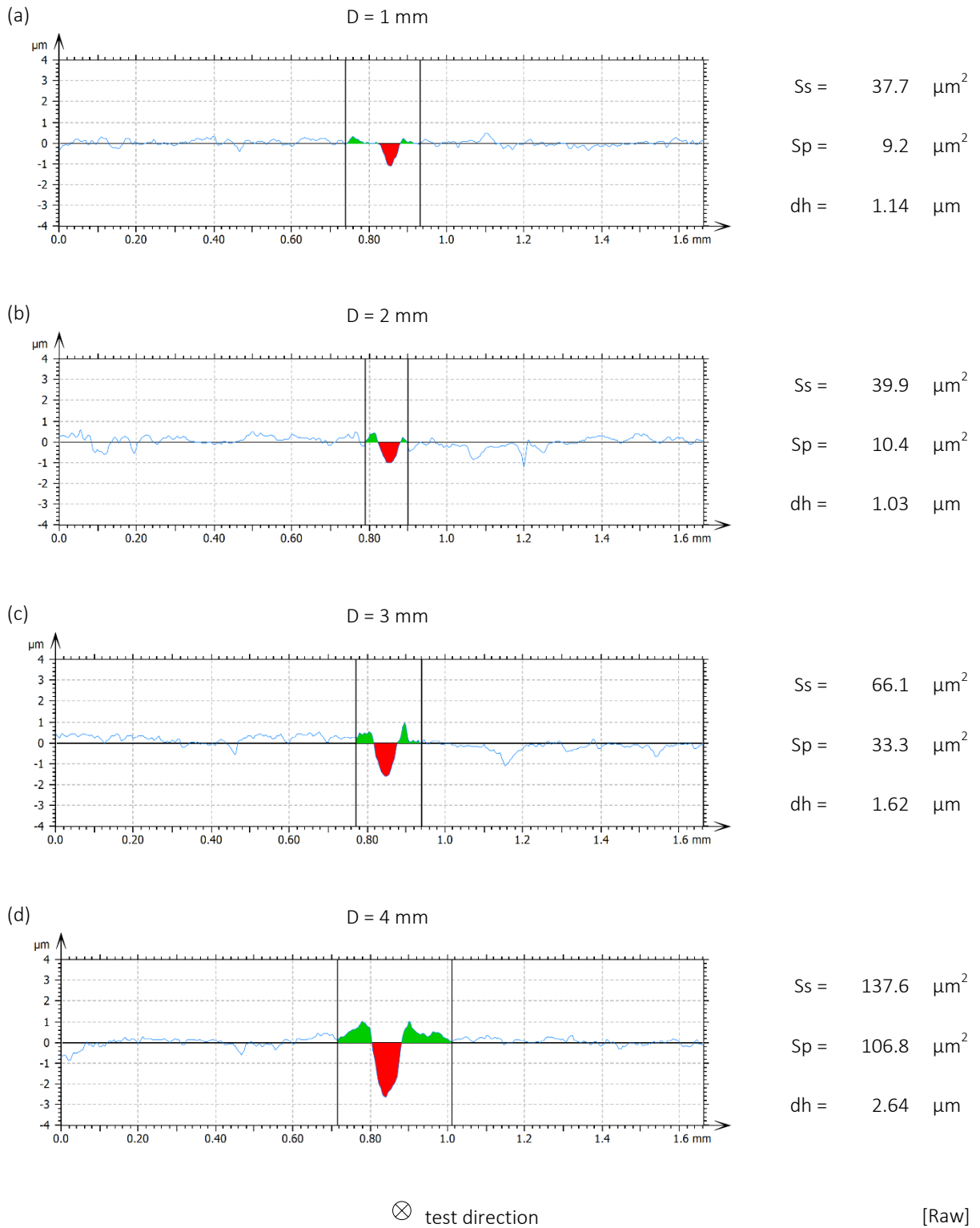


Figure 93: Instrumented linear sclerometry test. 2-D profilograms of the textured surface and resulting sclerometry groove, in the condition Raw, before SPN treatment (Baseline raw sample). In-lab textured flat specimen. Section locations corresponding to previous 3-D profile images. All the graphs: test direction towards the plane of the page. a-d) “Groove area” (Ss) - in red and “pile-up area” (Sp) - in green, at distances from beginning of test: 1 mm, 2 mm, 3 mm and 4 mm. Ss and Sp computed values reported along with each graph. In addition, punctual measurement of depth (dh) is informed.

During the sclerometry test, 1N pre-load applied during 10s at initial distance. Next, indenter was linearly moved increasing load, 1N to 10N, with velocity of 0.028 mm/s, resulting in the scratch of 5 mm in length, whose width progressively increased with distance. The test stabilization zone (see friction results in section ahead) was comprehended into first 40 s. Therefore, the region 0-1 mm was not considered in data analysis.

The color scale next to the Top view of the 3-D profile indicates the resulting heights from valley to peak. In the right side of each Figure, Front [30° tilted] views of the 3-D scratch section at 1 mm, 2 mm, 3 mm and 4 mm distances, highlight the progressive evolution of the sclerometry groove.

Figure 85, Figure 87, Figure 89, and Figure 91, show the 2-D profilograms with resulting sclerometry groove in the conditions E1 (400 °C 4 h), E2 (400 °C 2 h), E3 (350 °C 4 h), and E4 (350 °C 2 h), respectively. In addition, Figure 93 shows the corresponding profile in the condition Raw, before SPN treatment (Baseline raw sample). All the section locations correspond to previous 3-D profile images.

In all the 2-D images, the test direction is referred towards the plane of the page. The profiles show the resulting “Groove area” (Ss) - in red and “pile-up area” (Sp) - in green, at distances from beginning of test: 1 mm, 2 mm, 3 mm, and 4 mm. In addition, punctual measurement of depth (dh) is informed for each experimental condition.

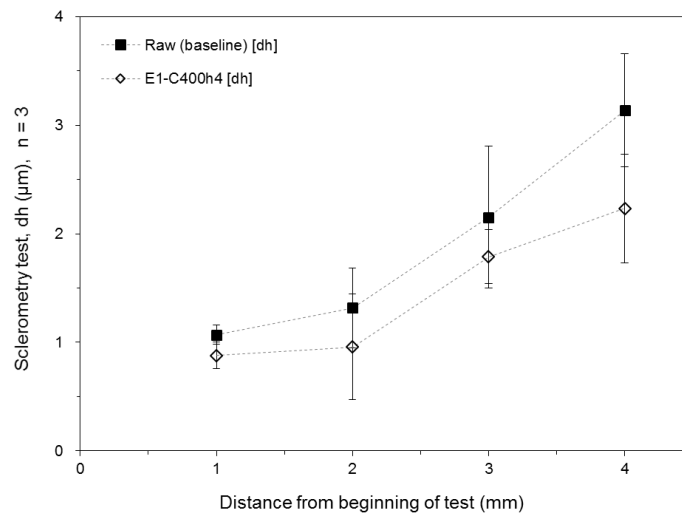


Figure 94: Sclerometry test. Resulting scratch depth (dh) of condition E1-C400h4 compared to Raw (baseline).

Similar measurements were performed for three scratches ($n = 3$) of each experimental condition. The results computed in Table 24, Table 25, Table 26, Table 27, and Table 28,

originated the series of charts to assess the instrumented sclerometry test response in terms of: resulting scratch depth (dh), “groove area” (Ss) and “pile-up area” (Sp).

Figure 94 shows the resulting scratch depth (dh) of condition E1-C400h4 compared to Raw (baseline), as a function of the distance from beginning of test. The depth overall decreased after SPN treatment, as an effect of the increase of surface strength due to plasma nitriding.

Similar behavior was noticed with regard to the other experimental conditions (Figure 95, Figure 96, Figure 97), whose results were consolidated through the combined chart shown in Figure 98.

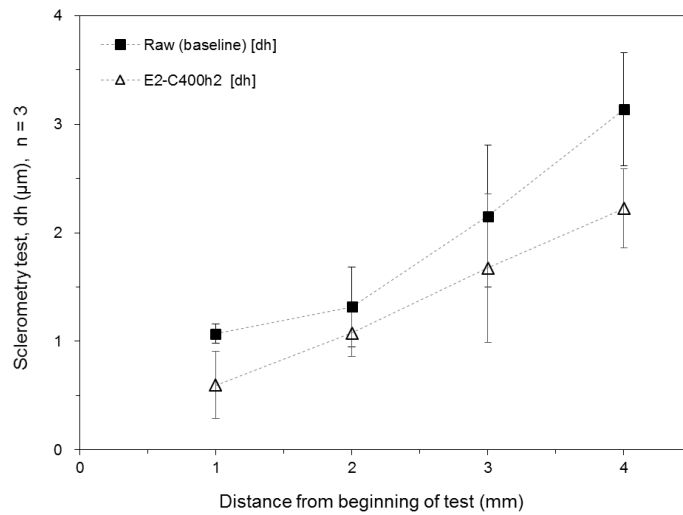


Figure 95: Sclerometry test. Resulting scratch depth (dh) of condition E2-C400h2 compared to Raw (baseline).

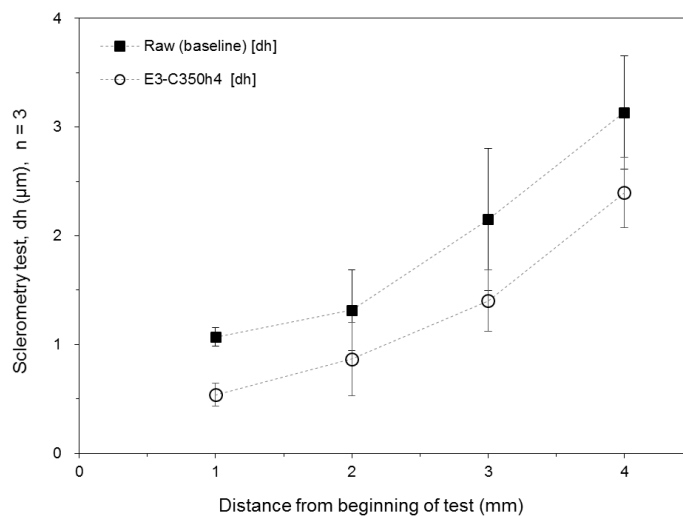


Figure 96: Sclerometry test. Resulting scratch depth (dh) of condition E3-C350h4 compared to Raw (baseline).

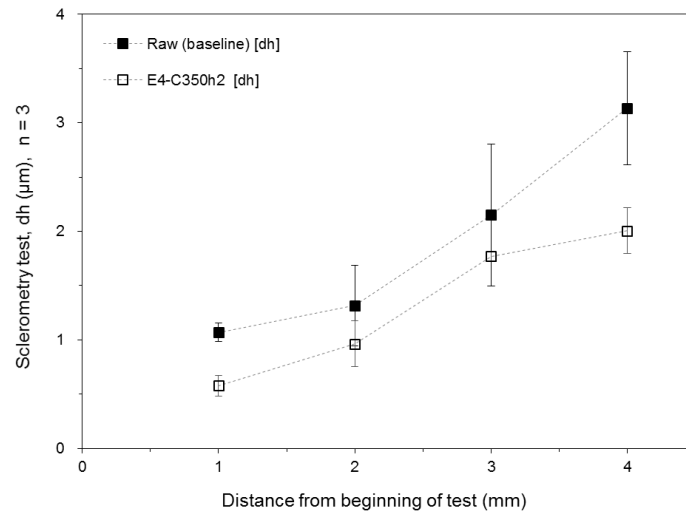


Figure 97: Sclerometry test. Resulting scratch depth (dh) of condition E4-C400h2 compared to Raw (baseline).

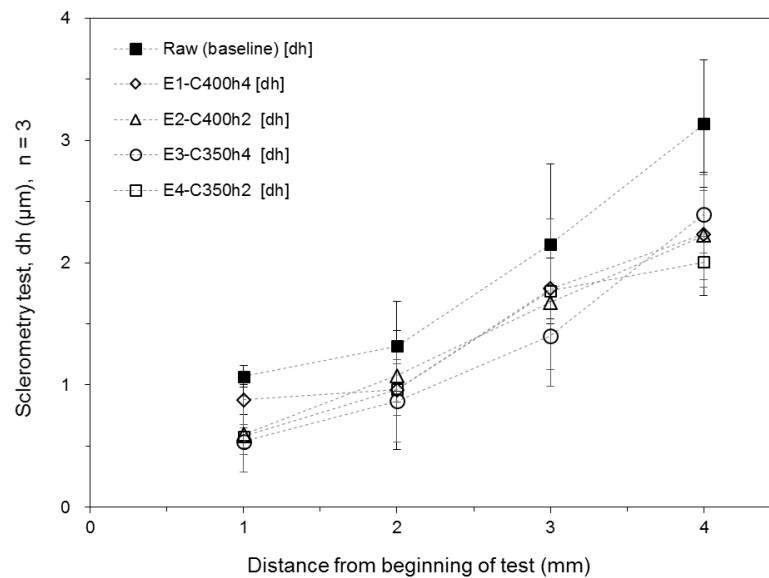


Figure 98: Sclerometry test. Combined chart of the resulting scratch depth (dh) of conditions E1-C400h4, E2-C400h2, E3-C350h4 and E4-C350h2 compared to Raw (baseline).

Figure 99 shows the resulting scratch “groove area” (S_s) of condition E1-C400h4 compared to Raw (baseline), as a function of the distance from beginning of test. As occurred with the scratch depth, the “groove area” overall decreased after SPN treatment, as an effect of the increase of surface strength due to plasma nitriding.

Similar behavior was noticed with regard to other experimental conditions (Figure 100, Figure 101, and Figure 102), whose results were consolidated through the combined chart shown in Figure 103.

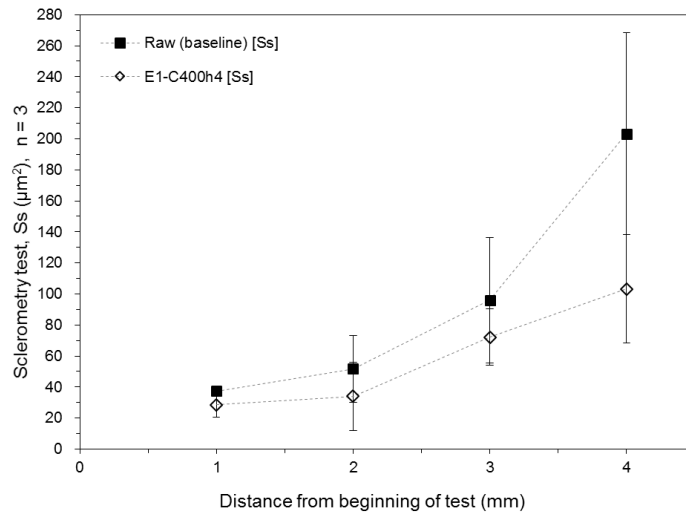


Figure 99: Sclerometry test. Resulting “groove area” (Ss) of condition E1-C400h4 compared to Raw (baseline).

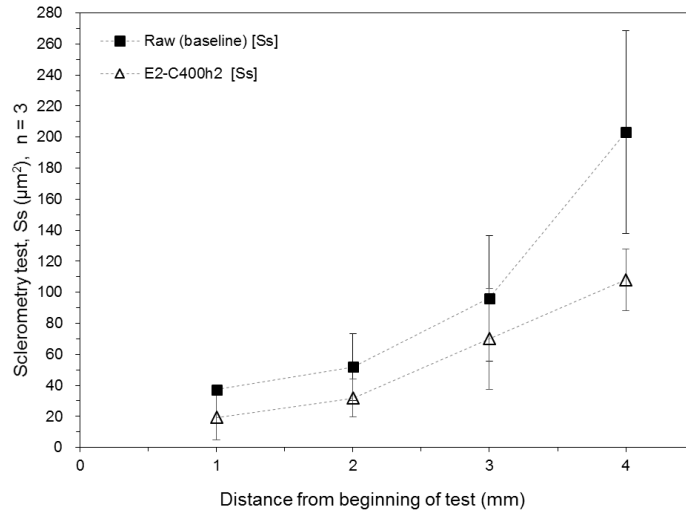


Figure 100: Sclerometry test. Resulting “groove area” (Ss) of condition E2-C400h2 compared to Raw (baseline).

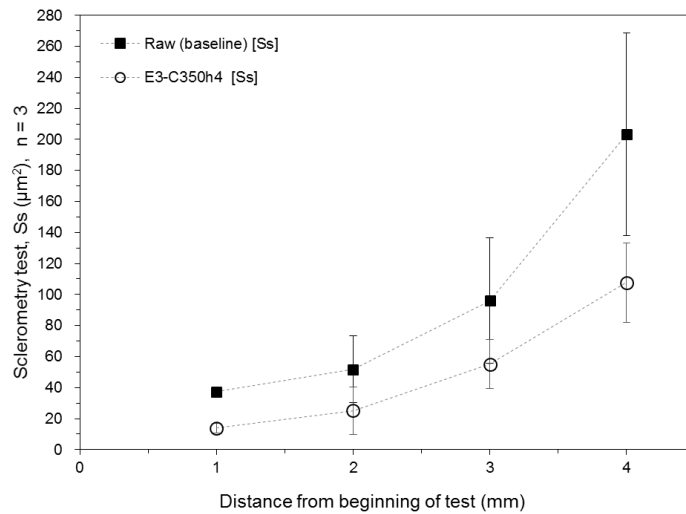


Figure 101: Sclerometry test. Resulting “groove area” (Ss) of condition E3-C350h4 compared to Raw (baseline).

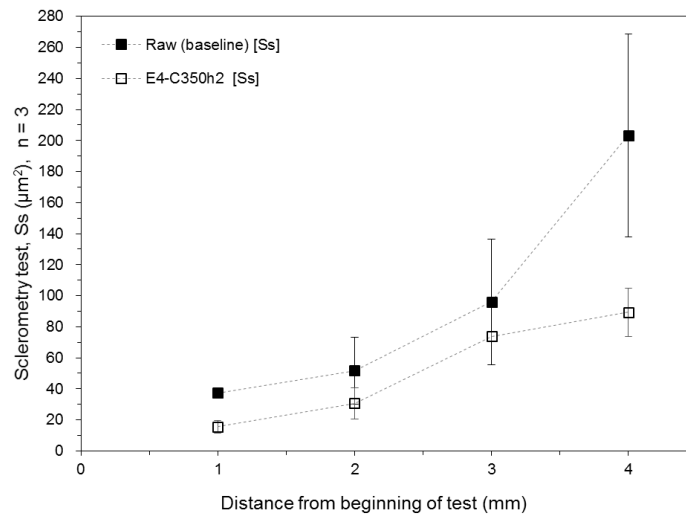


Figure 102: Sclerometry test. Resulting “groove area” (S_s) of condition E4-C350h2 compared to Raw (baseline).

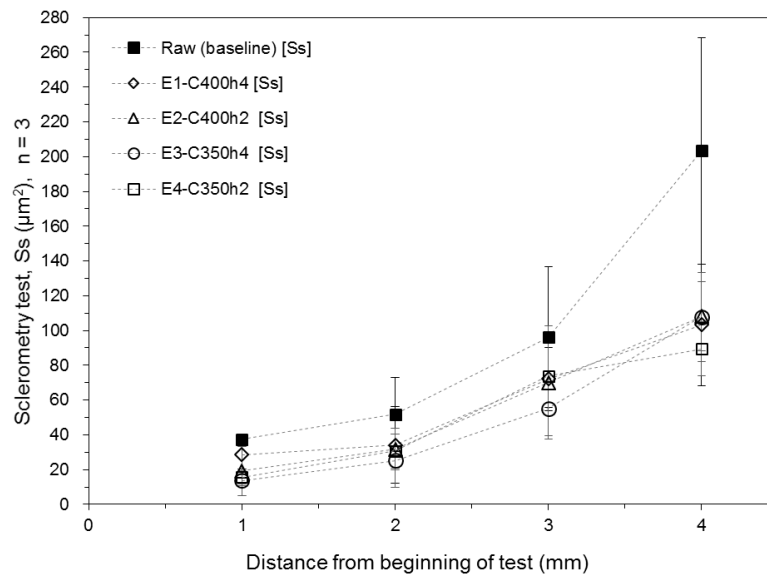


Figure 103: Sclerometry test. Combined chart of the resulting “groove area” (S_s) of conditions E1-C400h4, E2-C400h2, E3-C350h4 and E4-C350h2 compared to Raw (baseline).

Figure 104 shows the resulting scratch “pile-up area” (S_p) of condition E1-C400h4 compared to Raw (baseline), as a function of the distance from beginning of test. Similar results are reported with regard to the other experimental conditions (Figure 105, Figure 106, and Figure 107), which were consolidated through the combined chart shown in Figure 108.

It was not possible to detect any substantial contrast of S_p in relation to baseline and SPN experimental conditions within the first 2 mm of scratch distance. At 3 mm and markedly at 4 mm of scratch distance, the resulting “pile-up area” overall decreased after SPN treatment, therefore evidencing lower level of plastic deformation (micro-ploughing zone) in SPN condition with respect to Raw condition.

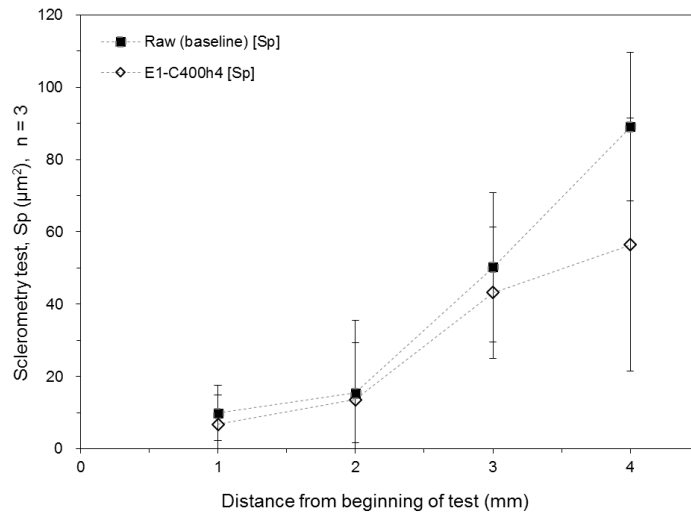


Figure 104: Sclerometry test. Resulting “pile-up area” (Sp) of condition E1-C400h4 compared to Raw (baseline).

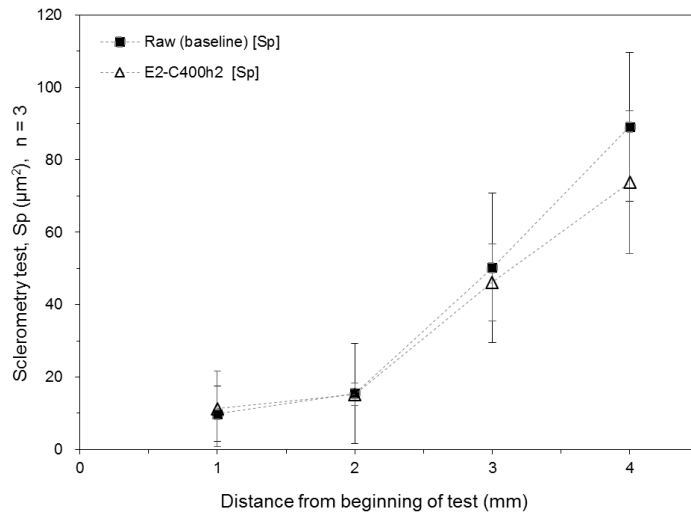


Figure 105: Sclerometry test. Resulting “pile-up area” (Sp) of condition E2-C400h2 compared to Raw (baseline).

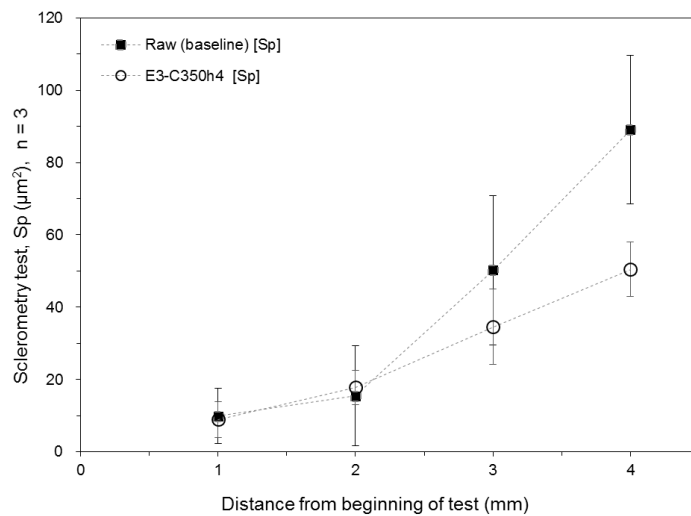


Figure 106: Sclerometry test. Resulting “pile-up area” (Sp) of condition E3-C350h4 compared to Raw (baseline).

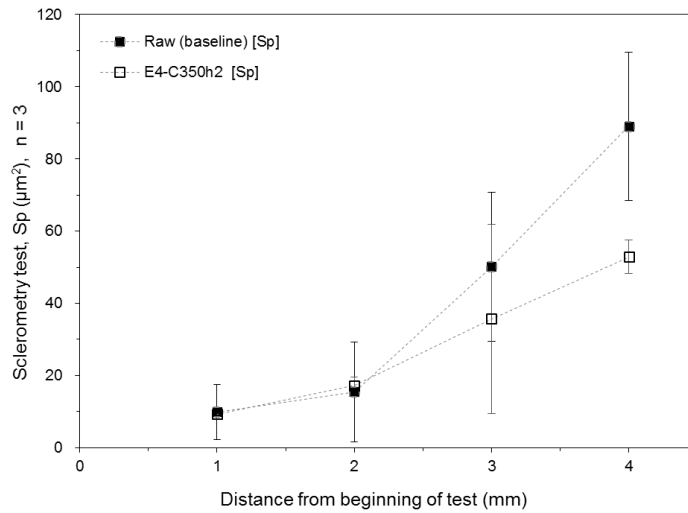


Figure 107: Sclerometry test. Resulting “pile-up area” (Sp) of condition E4-C350h2 compared to Raw (baseline).

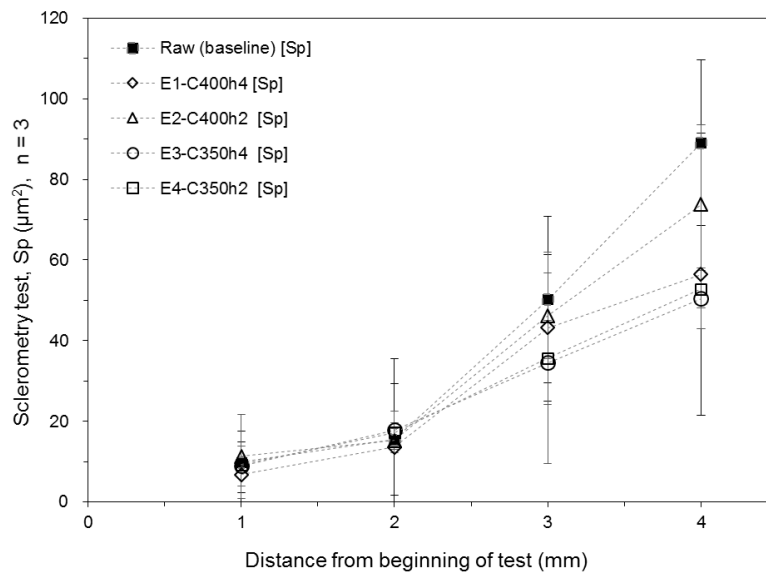


Figure 108: Sclerometry test. Combined chart of the resulting “pile-up area” (Sp) of conditions E1-C400h4, E2-C400h2, E3-C350h4 and E4-C350h2 compared to Raw (baseline)

Figure 109 shows a side-by-side comparison between condition Raw (a1-c1) and E4-C350h2 (a2-c2). The Top [slightly-tilted] view of the 3-D profile of the textured surface plane is shown along with front [30° tilted] view of the 3-D scratch section. In addition, section locations corresponding to 3-D profile images are shown with respective “Groove area” (Ss) - in red and “pile-up area” (Sp) - in green, at distances from beginning of test: 1 mm, 2 mm, 3 mm and 4 mm. Respective Ss, Sp, dh values are informed along with each graph.

Table 20: Data group of “Groove area” (Ss), “pile-up area” (Sp) and depth (dh), at distances/load of: 1 mm/2.8 N, 2 mm/4.6 N, 3 mm/6.4 N and 4 mm/8.2 N, n = 3. In-lab textured flat surface. Condition E1-400C-4h.

Experiment: E1-C400h4 (400 °C, 4 hours)												
Pos(mm)/Load(N)	1 mm / 2.8 N			2 mm / 4.6 N			3 mm / 6.4 N			4 mm / 8.2 N		
Param (Unit)	dh (μm)	Ss (μm ²)	Sp (μm ²)	dh (μm)	Ss (μm ²)	Sp (μm ²)	dh (μm)	Ss (μm ²)	Sp (μm ²)	dh (μm)	Ss (μm ²)	Sp (μm ²)
s1	0.74	19.6	16.1	1.41	56.3	12.9	1.66	66.7	13.9	2.71	136.6	51.3
s2	0.96	30.9	2.7	1.03	33.7	18.4	2.07	92.4	79.8	2.29	106.3	51.8
s3	0.94	35.3	1.6	0.44	12.2	9.3	1.64	57.3	36.1	1.71	66.8	66.3
Avg	0.88	28.6	6.8	0.96	34.1	13.6	1.79	72.1	43.3	2.23	103.2	56.5
StdDev	0.12	8.1	8.1	0.49	22.0	4.6	0.25	18.2	33.5	0.50	34.99	8.5

Table 21: Data group of “Groove area” (Ss), “pile-up area” (Sp) and depth (dh). Condition E2-400C-2h.

Experiment: E2-C400h2 (400 °C, 2 hours)												
Pos(mm)/Load(N)	1 mm / 2.8 N			2 mm / 4.6 N			3 mm / 6.4 N			4 mm / 8.2 N		
Param (Unit)	dh (μm)	Ss (μm ²)	Sp (μm ²)	dh (μm)	Ss (μm ²)	Sp (μm ²)	dh (μm)	Ss (μm ²)	Sp (μm ²)	dh (μm)	Ss (μm ²)	Sp (μm ²)
s1	0.66	18.2	5.5	1.22	31.5	13.3	1.87	78.0	46.6	2.37	114.7	67.8
s2	0.26	5.5	5.0	0.83	19.8	18.7	0.91	34.1	35.3	2.49	123.7	57.7
s3	0.87	33.9	23.4	1.18	44.1	13.7	2.25	97.9	56.6	1.81	85.8	95.7
Avg	0.60	19.2	11.3	1.08	31.8	15.2	1.67	70.0	46.2	2.22	108.1	73.8
StdDev	0.31	14.2	10.5	0.22	12.2	3.0	0.69	32.6	10.6	0.36	19.8	19.7

Table 22: Data group of “Groove area” (Ss), “pile-up area” (Sp) and depth (dh). Condition E3-350C-4h.

Experiment: E3-C350h4 (350 °C, 4 hours)												
Pos(mm)/Load(N)	1 mm / 2.8 N			2 mm / 4.6 N			3 mm / 6.4 N			4 mm / 8.2 N		
Param (Unit)	dh (μm)	Ss (μm ²)	Sp (μm ²)	dh (μm)	Ss (μm ²)	Sp (μm ²)	dh (μm)	Ss (μm ²)	Sp (μm ²)	dh (μm)	Ss (μm ²)	Sp (μm ²)
s1	0.66	17.3	12.3	1.26	42.8	23.0	1.25	48.0	45.1	2.03	79.0	46.0
s2	0.48	12.8	3.2	0.65	14.8	13.7	1.23	44.3	34.4	2.56	128.3	59.3
s3	0.48	11.5	11.3	0.70	17.8	16.7	1.73	73.1	24.2	2.60	115.9	46.2
Avg	0.54	13.8	8.9	0.87	25.2	17.8	1.40	55.1	34.6	2.40	107.7	50.5
StdDev	0.11	3.1	5.0	0.34	15.4	4.8	0.28	15.7	10.4	0.32	25.6	7.6

Table 23: Data group of “Groove area” (Ss), “pile-up area” (Sp) and depth (dh). Condition E4-350C-2h.

Experiment: E4-C350h2 (350 °C, 2 hours)												
Pos(mm)/Load(N)	1 mm / 2.8 N			2 mm / 4.6 N			3 mm / 6.4 N			4 mm / 8.2 N		
Param (Unit)	dh (μm)	Ss (μm ²)	Sp (μm ²)	dh (μm)	Ss (μm ²)	Sp (μm ²)	dh (μm)	Ss (μm ²)	Sp (μm ²)	dh (μm)	Ss (μm ²)	Sp (μm ²)
s1	0.68	19.5	9.4	0.97	30.2	17.5	1.77	72.1	47.7	2.05	97.1	49.6
s2	0.56	15.4	7.9	1.17	40.8	14.8	1.72	72.1	53.7	1.78	71.4	50.8
s3	0.50	11.8	10.6	0.75	21.0	19.4	1.82	77.5	5.7	2.19	99.7	58.2
Avg	0.58	15.6	9.3	0.96	30.7	17.3	1.77	73.9	35.7	2.01	89.4	52.8
StdDev	0.09	3.9	1.4	0.21	9.9	2.3	0.05	3.1	26.2	0.21	15.6	4.7

Table 24: Data group of “Groove area” (Ss), “pile-up area” (Sp) and depth (dh). Condition Raw (baseline).

Experiment: RAW (baseline)												
Pos(mm)/Load(N)	1 mm / 2.8 N			2 mm / 4.6 N			3 mm / 6.4 N			4 mm / 8.2 N		
Param (Unit)	dh (μm)	Ss (μm ²)	Sp (μm ²)	dh (μm)	Ss (μm ²)	Sp (μm ²)	dh (μm)	Ss (μm ²)	Sp (μm ²)	dh (μm)	Ss (μm ²)	Sp (μm ²)
s1	0.97	35.0	2.6	1.73	76.5	31.2	1.96	80.2	73.2	3.09	204.3	93.8
s2	1.10	39.4	17.8	1.19	38.9	4.9	2.88	142.1	44.1	3.68	267.9	66.7
s3	1.14	37.7	9.2	1.03	39.9	10.4	1.62	66.0	33.3	2.64	137.6	106.8
Avg	1.07	37.4	9.9	1.32	51.8	15.5	2.15	96.1	50.2	3.14	203.3	89.1
StdDev	0.09	2.2	7.6	0.37	21.4	13.9	0.65	40.5	20.6	0.52	65.2	20.5

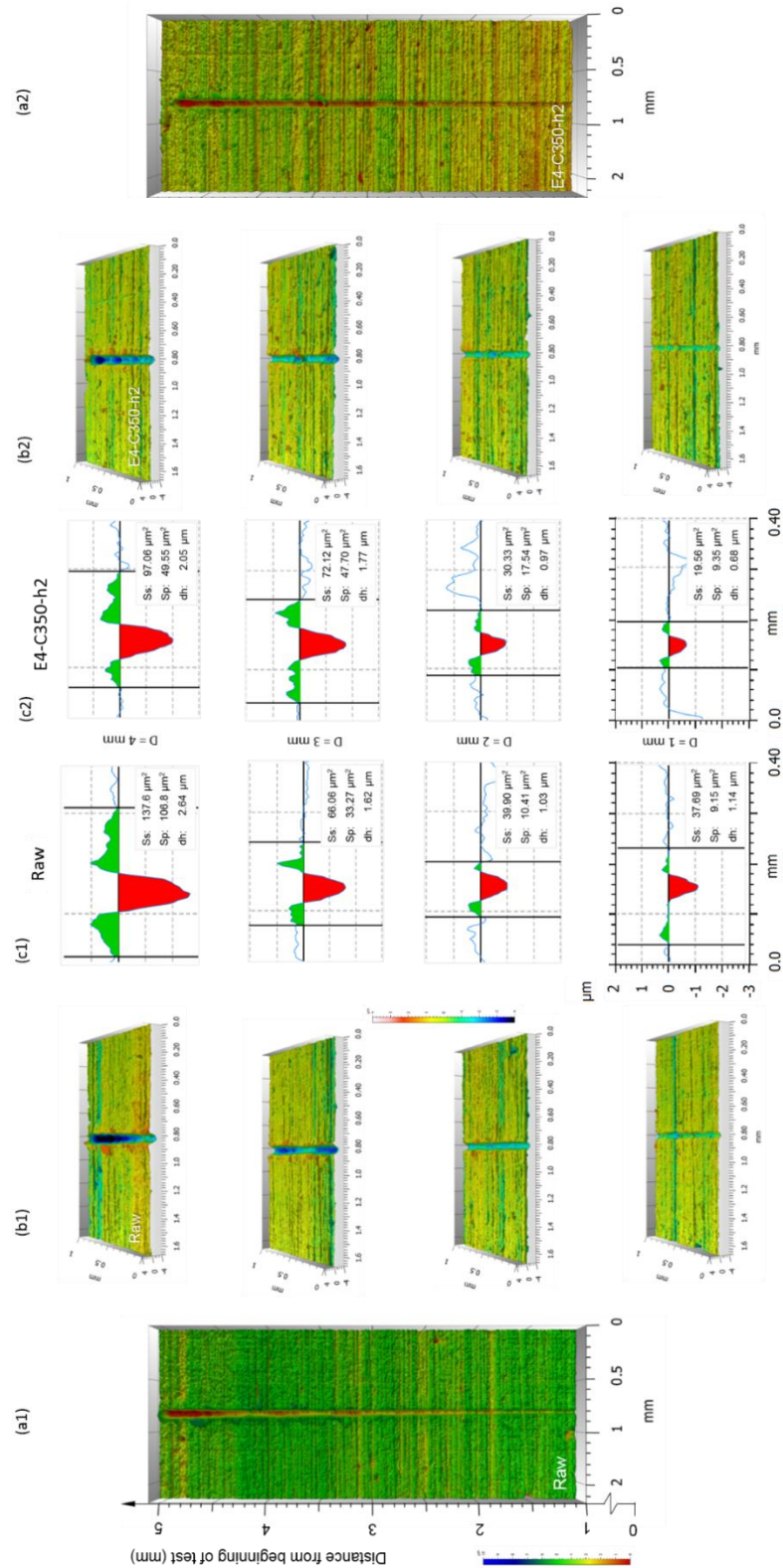


Figure 109: Instrumented linear sclerometry test. Side-by-side comparison between condition (a1-c1) Raw (before SPN) and (a2-c2) E4-C350h2. a1-2) Top [slightly-tilted] view of the 3-D profile of the textured surface plane. b1-b2) Front [30° tilted] view of the 3-D scratch section. c1-c2) Section locations corresponding to 3-D profile images. “Groove area” (Ss) - in red and “pile-up area” (Sp) - in green, at distances from beginning of test: 1 mm, 2 mm, 3 mm and 4 mm. Respective Ss, Sp, dh values are informed along with each graph. The region 0-1 mm (test stabilization zone) was not considered in data analysis. In-lab textured flat specimen.

4.1.6.2. SEM analysis of the scratch and critical damage load

Figure 110 shows the Scanning Electron Microscopy view of the textured surface plane and resulting scratch track, in the condition Raw, before SPN treatment (Baseline raw sample). Similar evaluation has been accomplished for each experimental condition after SPN treatment: E1-C400h4 (Figure 112), E2-C400h2 (Figure 114), E3-C350h4 (Figure 116) and E4-C350h2 (Figure 118).

The texturing lines are visible in all of the general view images, with the resulting scratch perpendicular to the texturing direction. The scratch width naturally increased with the distance traveled by the indenter. This is because the normal load applied was progressively increased from 1 N to 10 N.

Graphite lamellae intercepted by sclerometry scratch can still be noted in the SEM general views in conditions after SPN treatment (Figure 114, Figure 116 and Figure 118). In addition, the SEM images evidenced that texturing lines remained well preserved after SPN treatment, confirming what was seen in images of 3-D profile of the textured surface plane (e.g., Figure 84).

The dashed-line squares of Figure 110 indicate details per distance (1-5 mm) analyzed at higher magnification and shown in Figure 111. Similar procedure has also been accomplished for each SPN condition: E1-C400h4 (Figure 113), E2-C400h2 (Figure 115), E3-C350h4 (Figure 117), and E4-C350h2 (Figure 119).

Microcracks feature at different levels has been observed after shallow plasma nitriding, across the four experimental conditions (Figure 113, Figure 115, Figure 117, and Figure 119).

The density of microcracks was higher at graphite interface regions in comparison to material matrix regions, i.e., out of graphite pocket surroundings. Figure 123 shows cracks associated to the graphite tip, where the stress concentration takes place. On the right of same SEM image, microcracks nucleated in the material matrix region were noticeable.

Samples treated at 400 °C comparatively resulted in higher levels of overall quantity of microcracks nucleated in the matrix, along the entire range covered by the sclerometry indenter (distance 1 to 5 mm).

In spite of that, results indicated that first signs of nucleation occurred earlier in samples treated at 350 °C: Figure 113 and Figure 115 (400 °C) show the first tensile microcracks occurring at distance around 2 mm, whereas Figure 117 and Figure 119 (350 °C) show the first microcracks at distance around 1 mm.

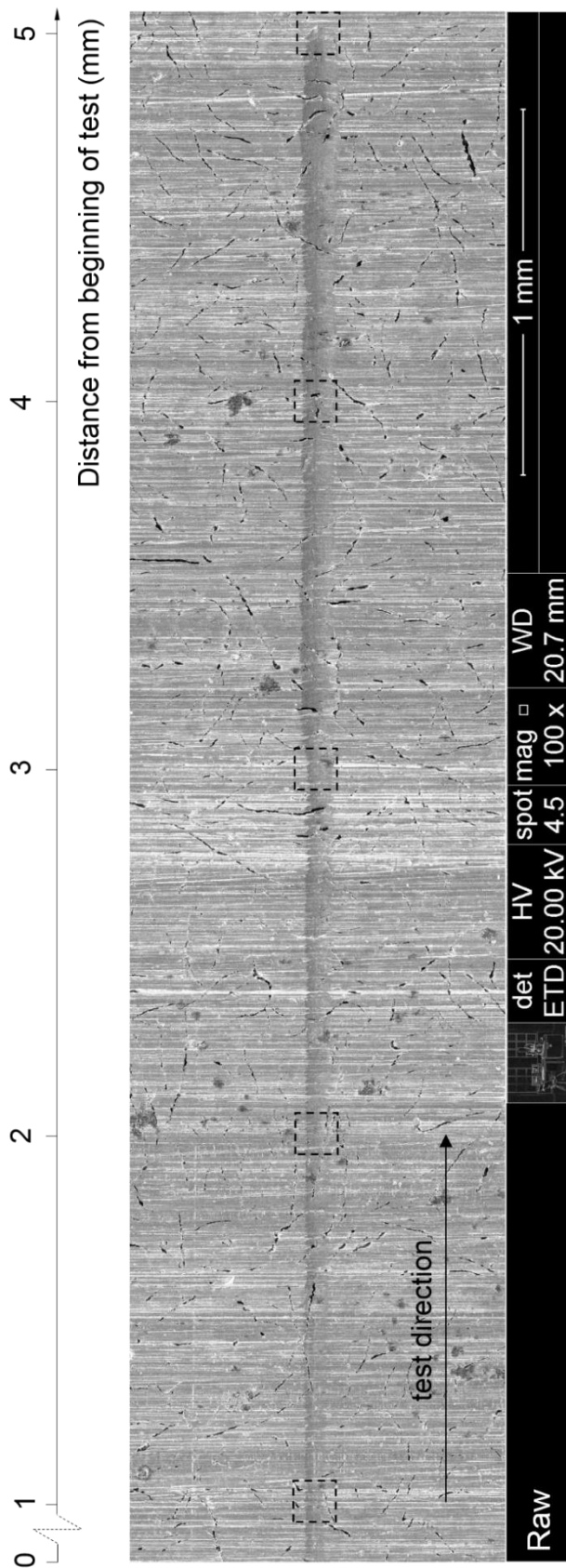


Figure 110: Instrumented linear sclerometry test. Scanning Electron Microscopy view of the textured surface plane and resulting scratch track, in the condition Raw, before SPN treatment (Baseline raw sample).

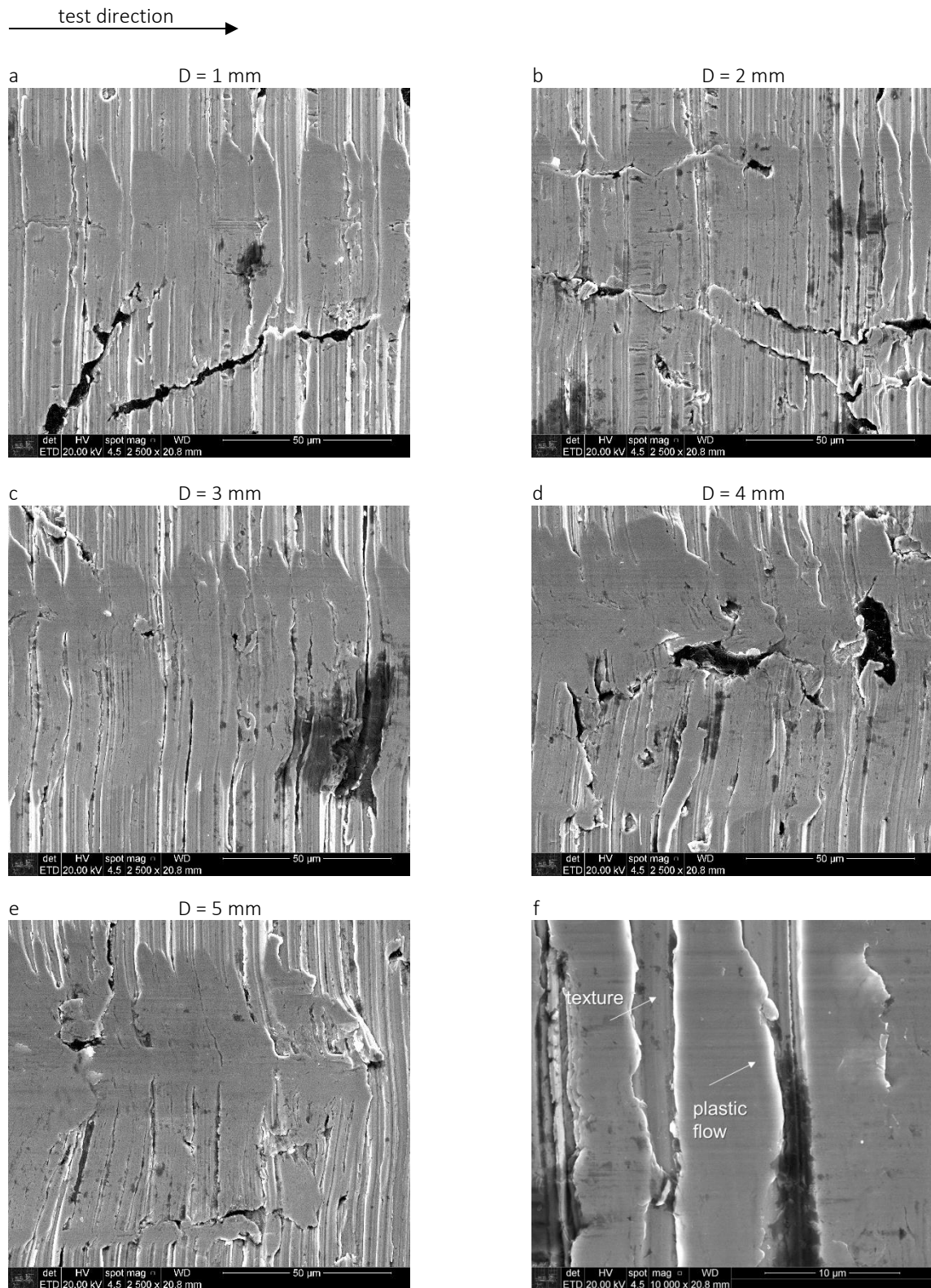


Figure 111: Instrumented linear sclerometry test. Scanning Electron Microscopy view of the textured surface plane and resulting scratch track, in the condition Raw, before SPN treatment (Baseline raw sample). All the images: test direction from left to right. a-e) Detailed view at different distances from beginning of test: 1 mm, 2 mm, 3 mm, 4 mm and 5 mm. f) Magnified view (arbitrary distance) showing plastic deformation in the interface region to the texturing grooves: a general aspect found along the scratch length of the non-treated specimen.

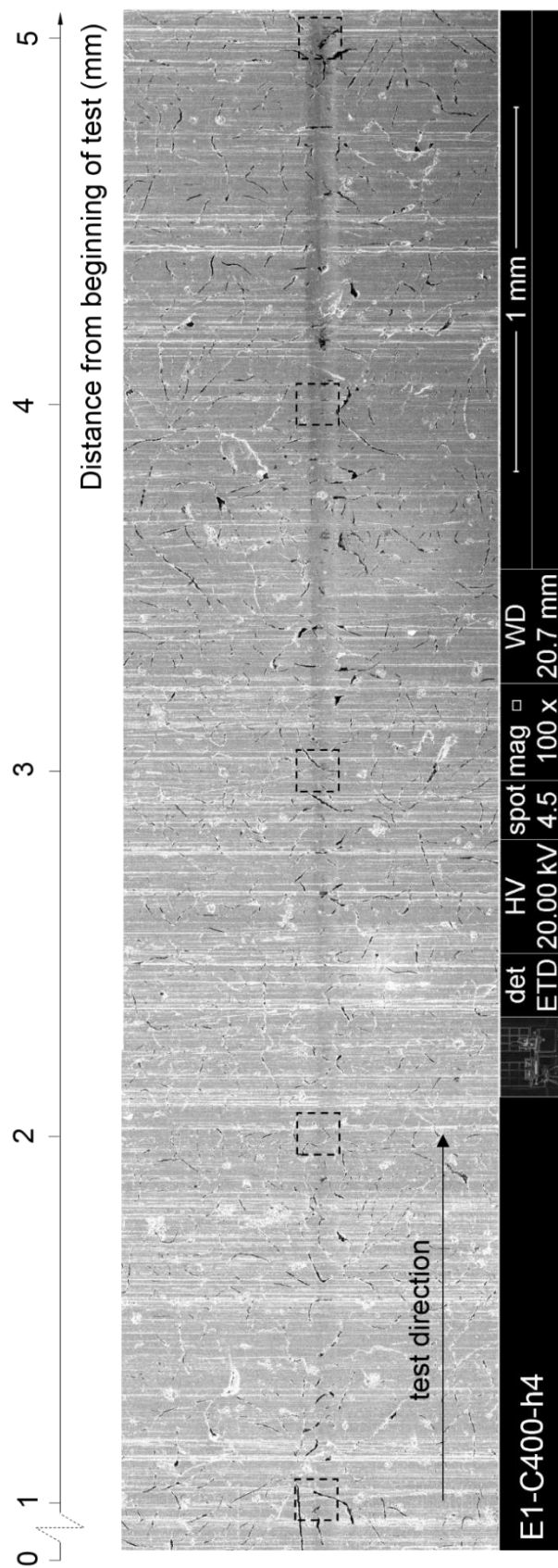


Figure 112: Instrumented linear sclerometry test. Scanning Electron Microscopy view of the textured surface plane and resulting scratch track. Experiment E1 (400 °C 4 h).

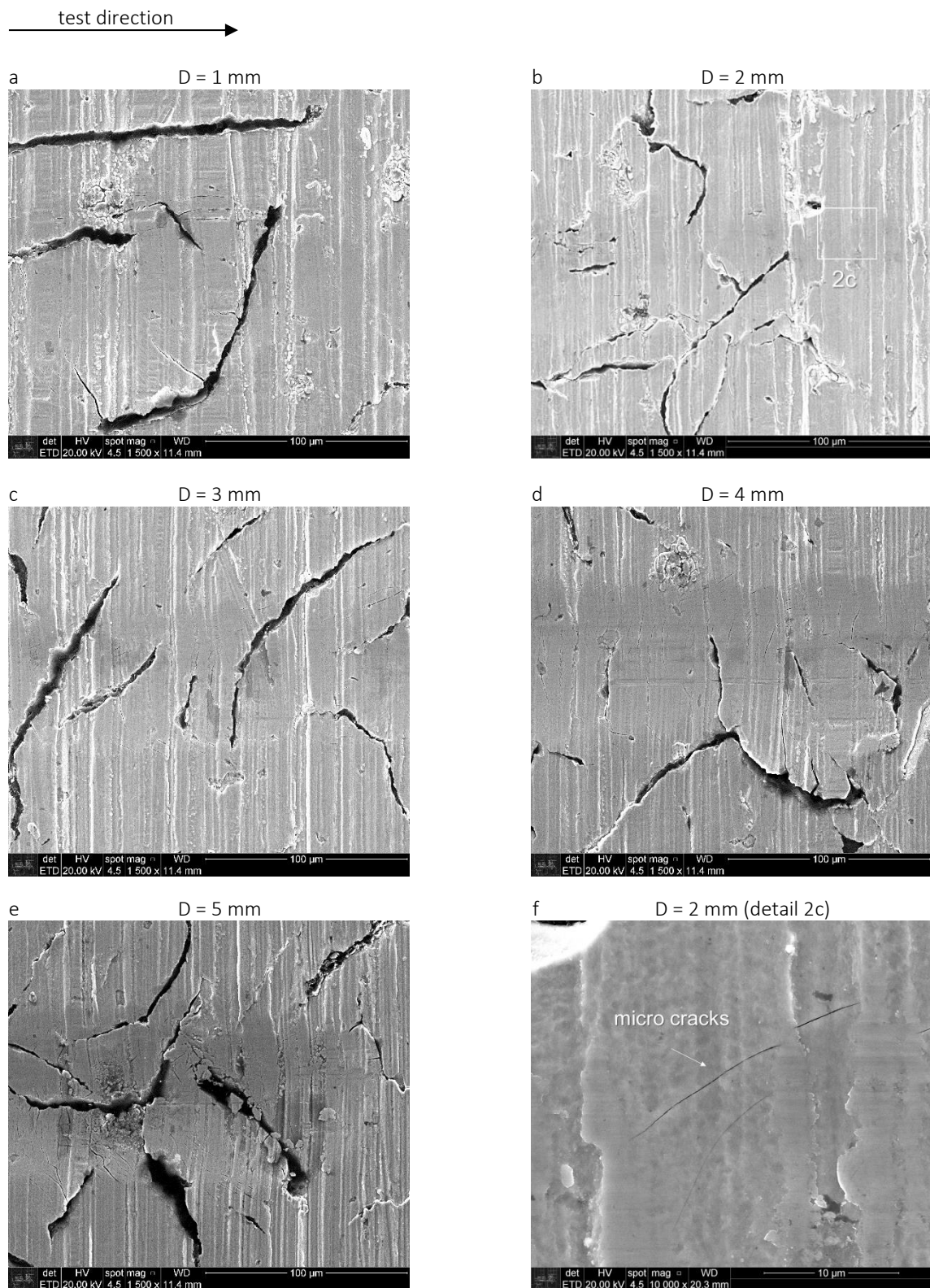


Figure 113: Instrumented linear sclerometry test. Scanning Electron Microscopy view of the textured surface plane and resulting scratch track. Experiment E1 (400 °C 4 h). All the images: test direction from left to right. a-e) Detailed view at different distances from beginning of test: 1 mm, 2 mm, 3 mm, 4 mm and 5 mm. Microcracks found preferably in graphite regions. f) Magnified view (detail 2C of Fig. b) showing tensile microcracks at distance around 2 mm, in material matrix region, i.e., out of graphite pocket surroundings.

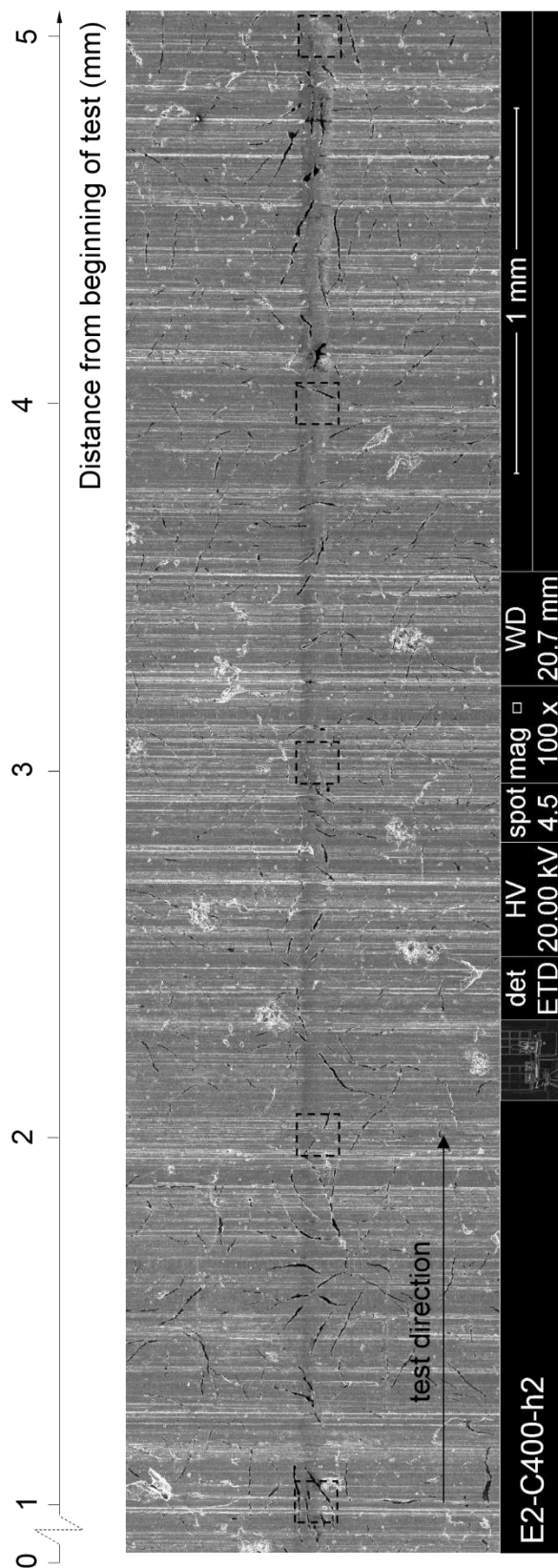


Figure 114: Instrumented linear sclerometry test. Scanning Electron Microscopy view of the textured surface plane and resulting scratch track. Experiment E2 (400 °C 2 h).

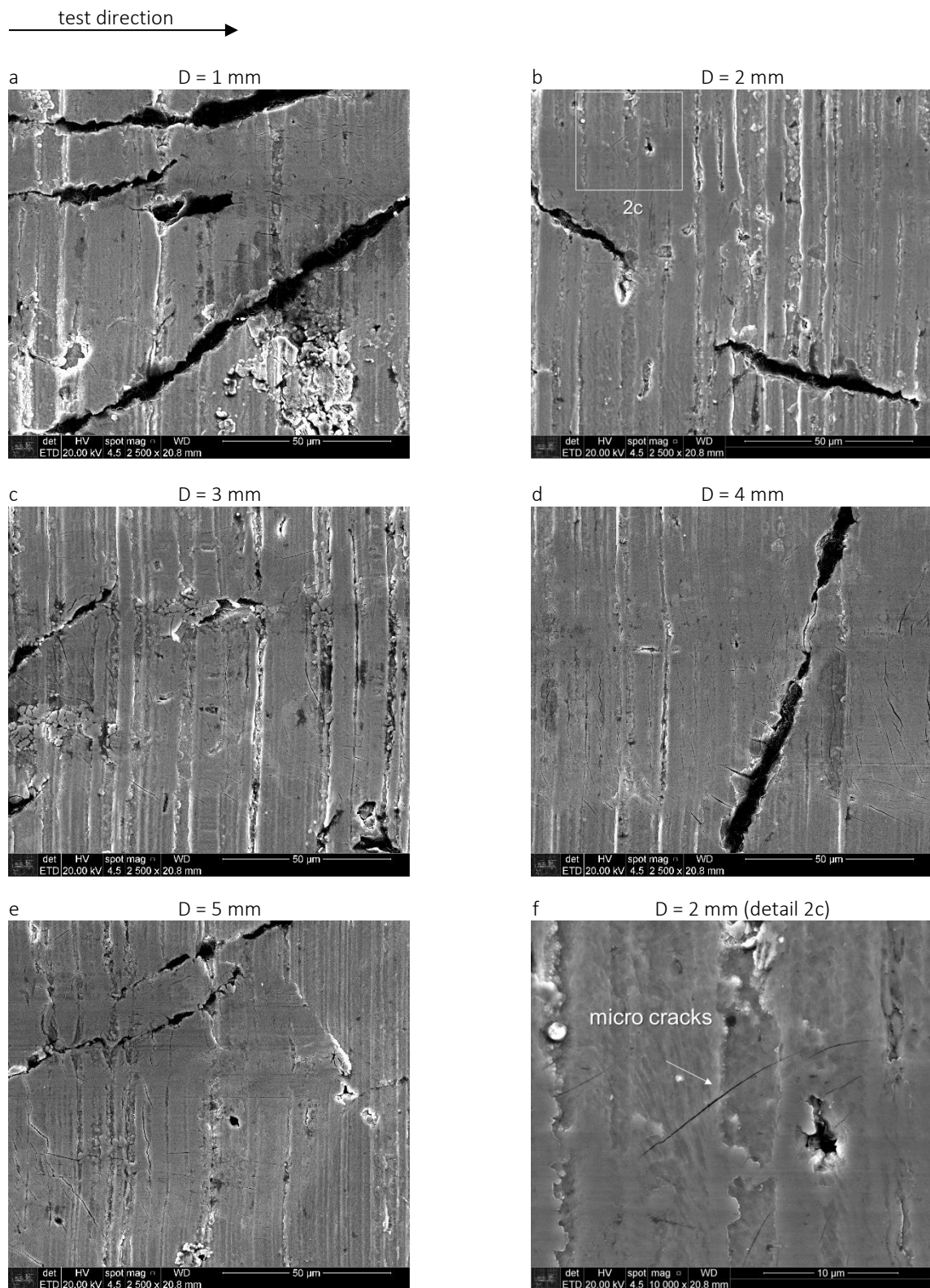


Figure 115: Instrumented linear sclerometry test. Scanning Electron Microscopy view of the textured surface plane and resulting scratch track. Experiment E2 (400 °C 2 h). All the images: test direction from left to right. a-e) Detailed view at different distances from beginning of test: 1 mm, 2 mm, 3 mm, 4 mm and 5 mm. Microcracks found preferably in graphite regions. f) Magnified view (detail 2C of Fig. b) showing tensile microcracks at distance around 2 mm, in material matrix region, i.e., out of graphite pocket surroundings.

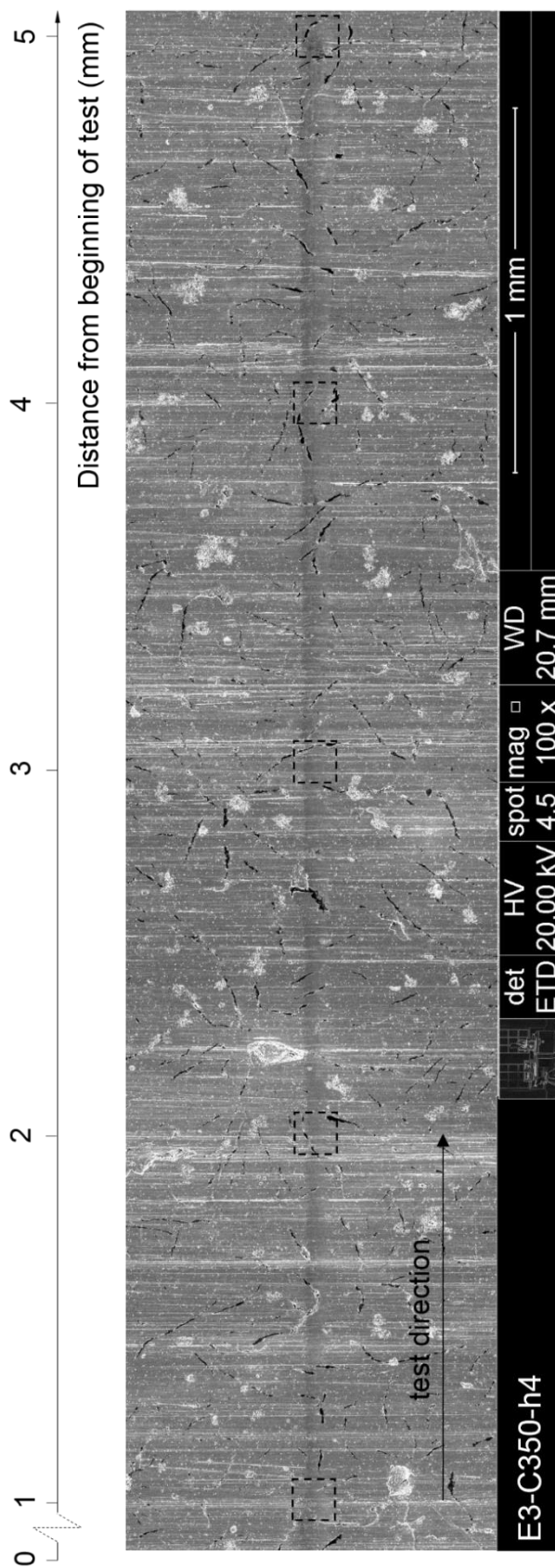


Figure 116: Instrumented linear sclerometry test. Scanning Electron Microscopy view of the textured surface plane and resulting scratch track. Experiment E3 (350 °C 4 h).

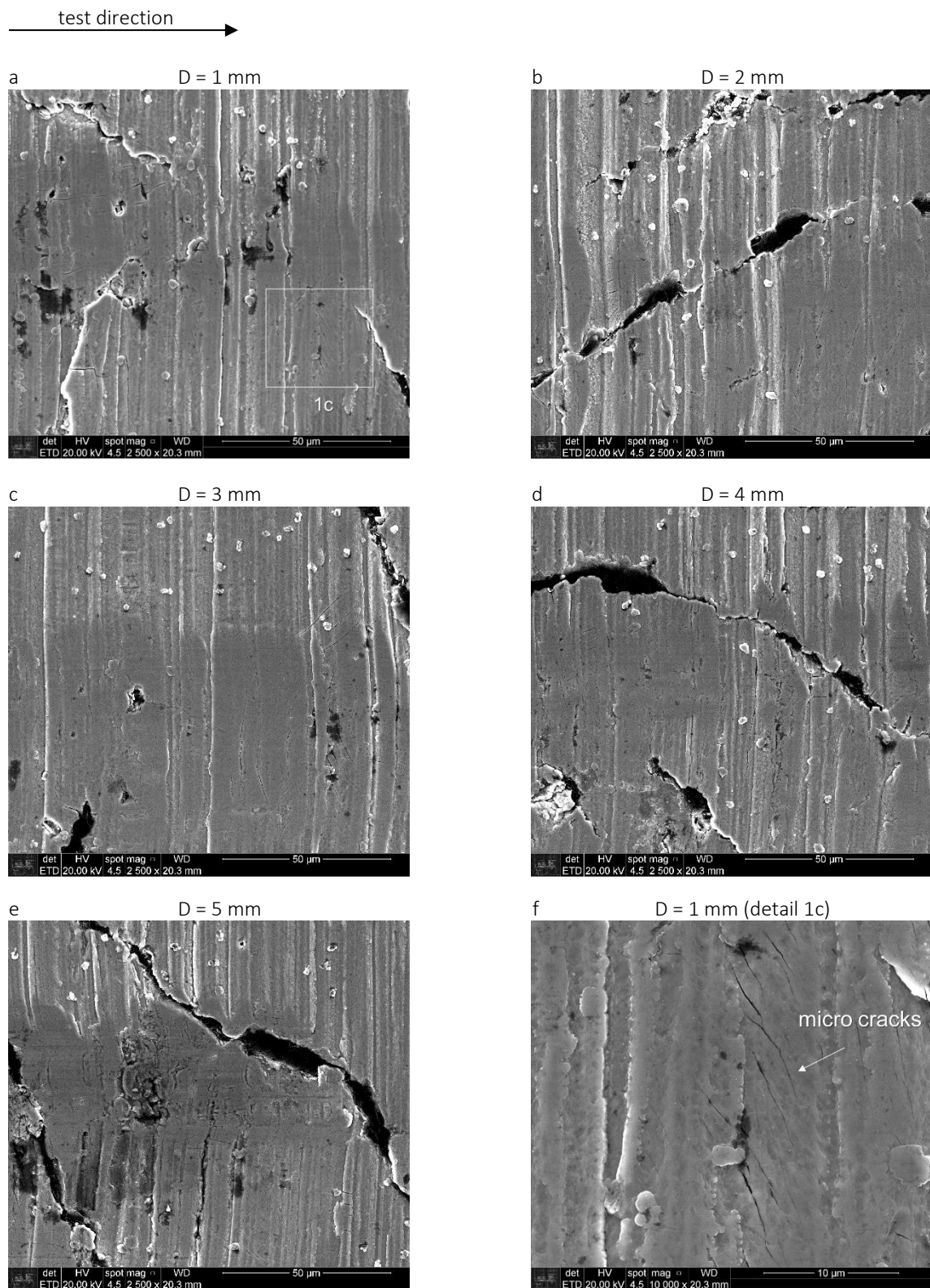


Figure 117: Instrumented linear sclerometry test. Scanning Electron Microscopy view of the textured surface plane and resulting scratch track. Experiment E3 (350 °C 4 h). All the images: test direction from left to right. a-e) Detailed view at different distances from beginning of test: 1 mm, 2 mm, 3 mm, 4 mm and 5 mm. f) Magnified view (detail 1C of Fig. a) showing tensile microcracks at distance around 1 mm, in material matrix region, i.e., out of graphite pocket surroundings.

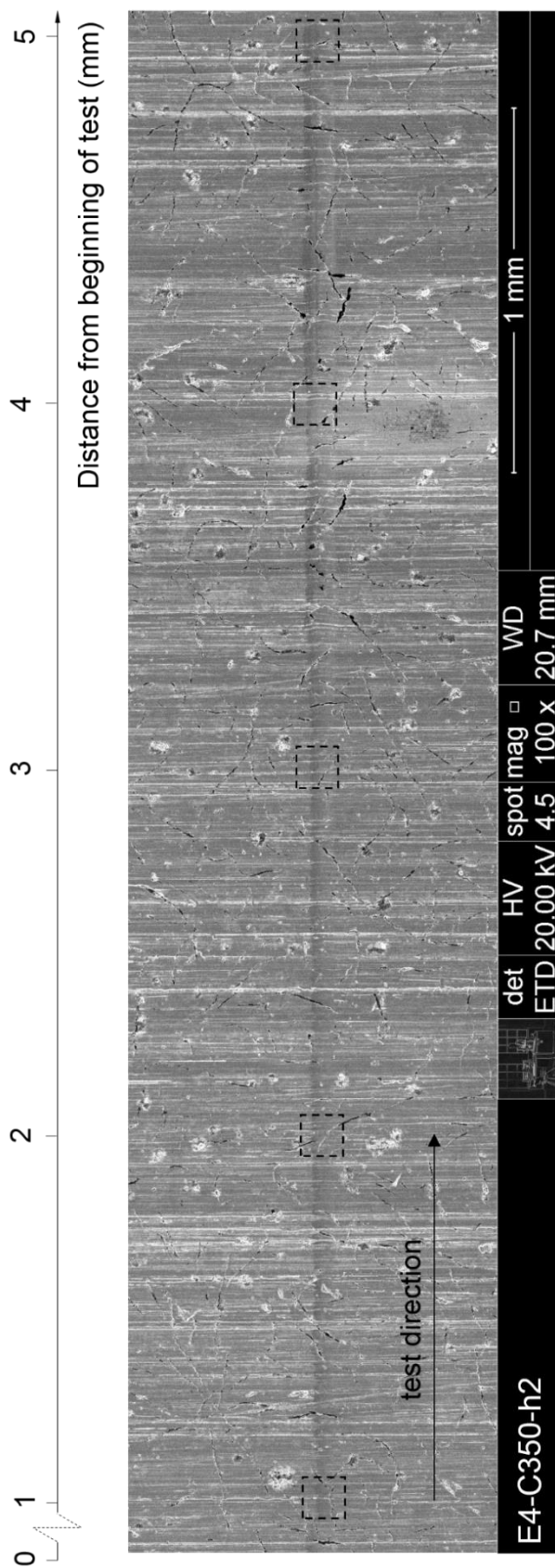


Figure 118: Instrumented linear sclerometry test. Scanning Electron Microscopy view of the textured surface plane and resulting scratch track. Experiment E4 (350 °C 2 h).

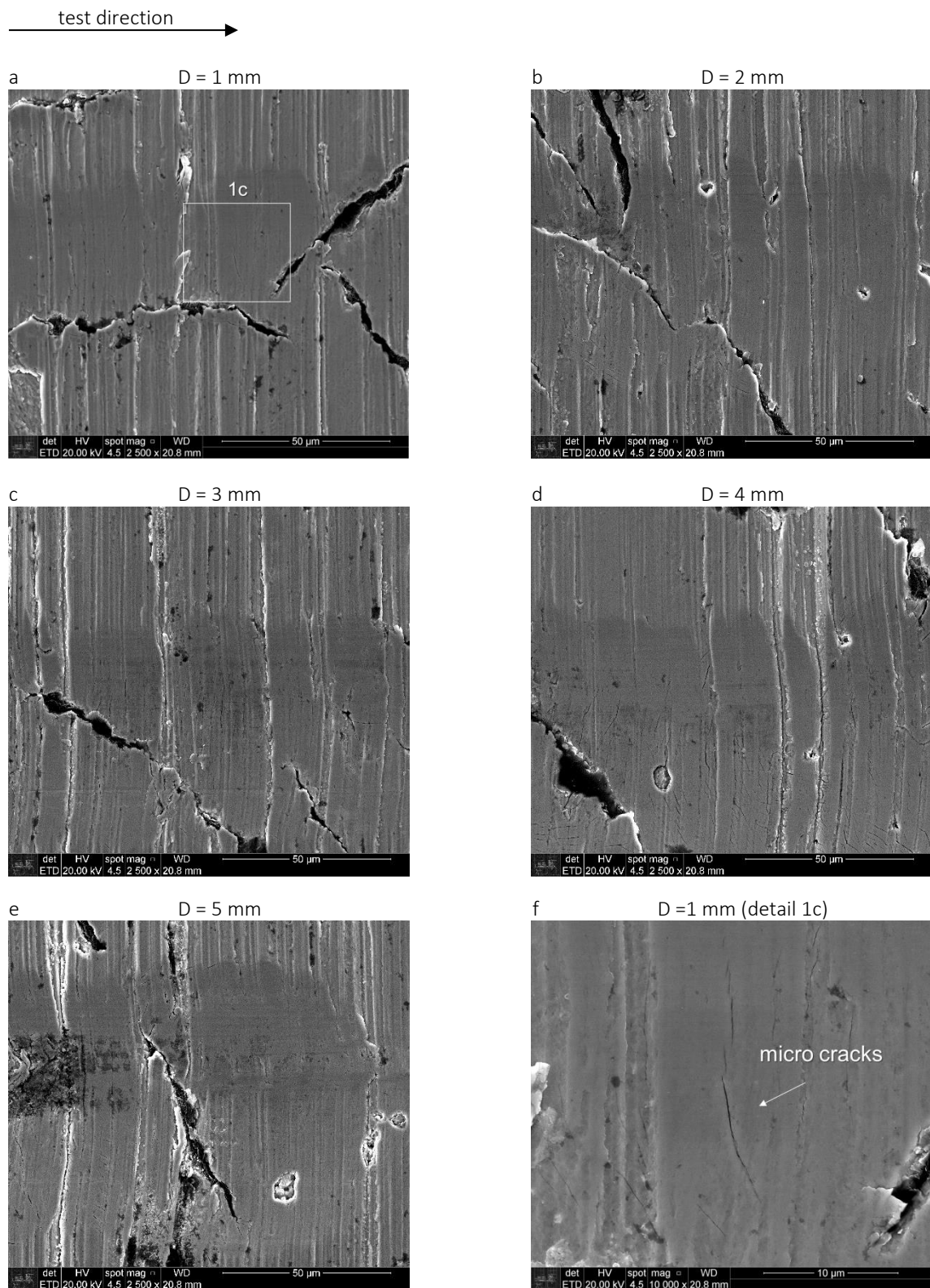


Figure 119: Instrumented linear sclerometry test. Scanning Electron Microscopy view of the textured surface plane and resulting scratch track. Experiment E4 (350 °C 2 h). All the images: test direction from left to right. a-e) Detailed view at different distances from beginning of test: 1 mm, 2 mm, 3 mm, 4 mm and 5 mm. f) Magnified view (detail 1C of Fig. a) showing tensile microcracks at distance around 1 mm, in material matrix region, i.e., out of graphite pocket surroundings.

Microcracks nucleated in the matrix, at similar orientation angle were a common feature observed in condition E1-C400h4 and E2-C400h2 (Figure 120), and was attributed to the stress state imposed by the indenter during the sclerometry test. The cracks were isolated and free from detachment of debris.

The examination of SPN treated samples via SEM has not revealed any sign of significant plastic deformation over the textured surface. Conversely, in the condition raw (before SPN treatment), plastic deformation was observed in the interface region to the texturing grooves, being a general aspect found along the scratch length of the non-treated specimen, as demonstrated in Figure 111.

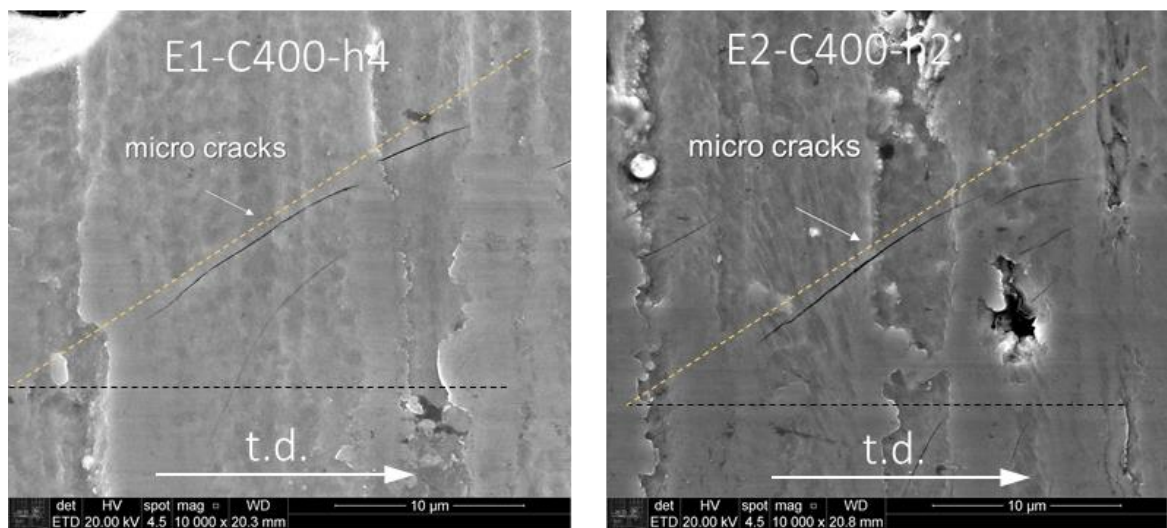


Figure 120: Condition E1-C400h4 and E2-C400h2. SEM view of the textured surface at the distance $D = 2$ mm from beginning of test. Microcracks nucleated in the matrix, at similar orientation angle. Region free from graphite flakes. Same regions as shown in the previous sequences of images of Figure 113 and Figure 115.

Furthermore, Figure 122 shows another SEM view of the textured surface in the condition raw, at the middle distance from beginning of test. Here, a graphite lamella is partially covered by plastically deformed material. It was not found any sign of micro crack nucleated from the matrix or in association to a graphite interface.

At the starting distance from beginning of test ($D = 0$ mm, 1N pre-load) minor plastic deformation was noticed. Texturing grooves and graphite pocket are suitably preserved, as shown in Figure 121. In the condition raw, the plastic deformation is intensified with indenter load and distance (Figure 111).

In the same way, after shallow plasma nitriding, the density of microcracks clearly increased with load and distance. Figure 120 shows the SEM view of the textured surface at the

distance $D = 2$ mm from beginning of test, of condition E2-C400h2. A sequence of parallel microcracks nucleated in the matrix was noticed, in a region free from graphite flakes.

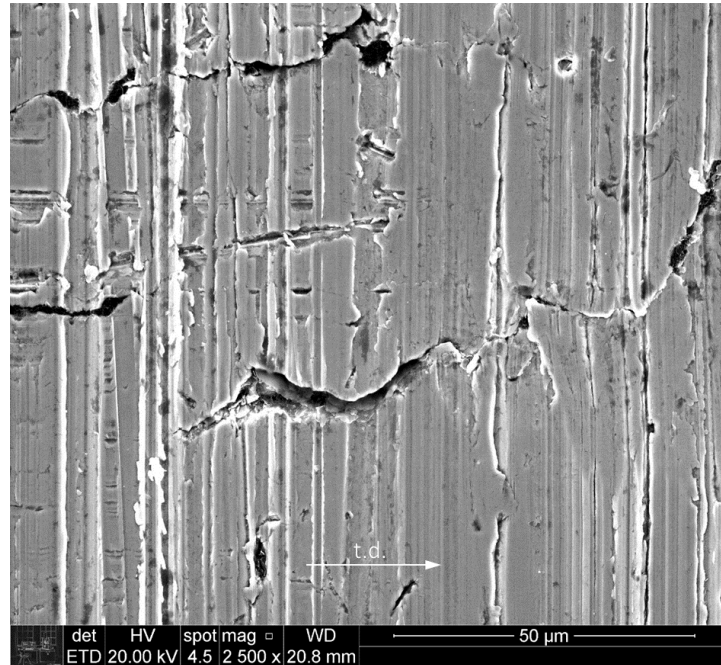


Figure 121: Condition Raw, before SPN treatment. SEM view of the textured surface at the starting distance from beginning of test, $D = 0$ mm. At this point, 1N pre-load was applied. Compared to larger distances (Figure 111), minor plastic deformation was noticed. Texturing grooves and graphite pocket are suitably preserved.

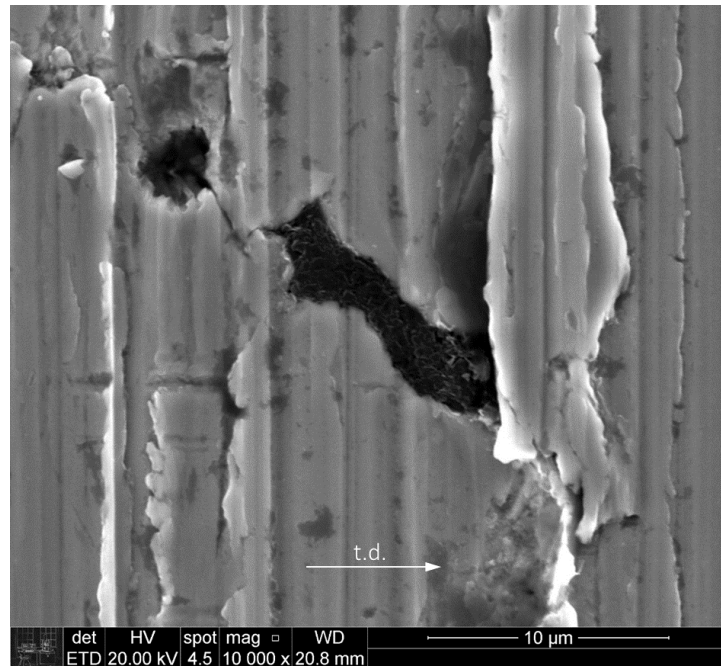


Figure 122: Condition Raw, before SPN treatment. SEM view of the textured surface at the middle distance from beginning of test. A graphite lamella is partially covered by plastically deformed material. It was not found any sign of micro crack nucleated from the matrix or in association to a graphite interface.

At the ending distance $D = 5$ mm of test, where the normal load achieved its maximum intensity, Figure 124 shows the SEM view of the textured surface of condition E3-C350h4, where the image field is filled out by a cluster of microcracks, in a region free from graphite flakes.

Table 25 consolidates the assessment of scratch damage features (microcracks) in increasing normal load test. In order to rank the resulting damage associated to each experimental condition, a criterion of qualitative scale levels were established. The proposed criterion consists of four levels of damage. The severity level increases from level 0 (L0) to level 3 (L3) for microcracks in material matrix pocket surrounding, based on the observations accomplished during the SEM analysis.

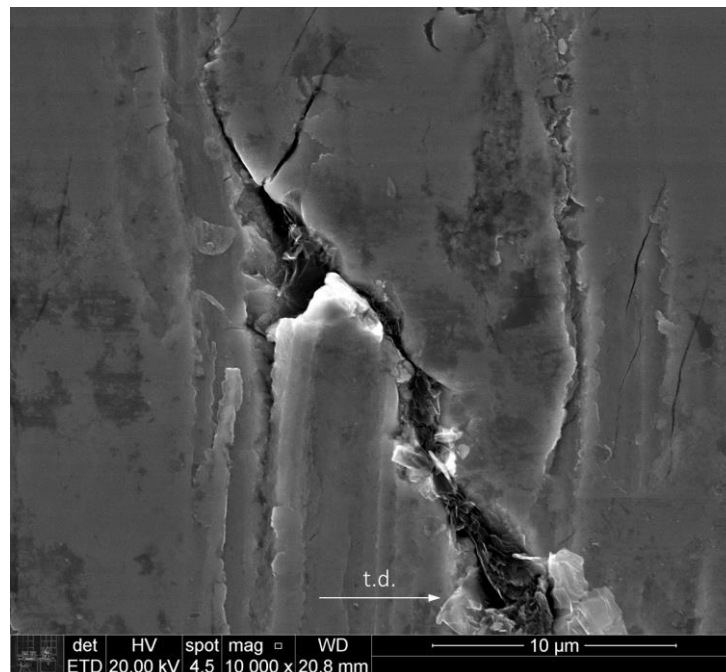


Figure 123: Condition E4-C350h2. SEM view of the textured surface at the ending distance $D = 5$ mm of test. Microcracks nucleated in association to a graphite pocket interface (graphite tip), which acts as a stress concentrator. On the right, microcracks nucleated in the material matrix region.

In fact, it is not easy to determine a critical load value by direct observation of damage features. Using Scanning Electronic Microscopy, some features that would not been detected using the magnification of ASTM reference micrographs [70] are detectable at higher magnification by using the SEM. That is the case of details 1c and 2c considered in previous images (Figure 113, Figure 115, Figure 117, Figure 119), which were considered in the present analysis.

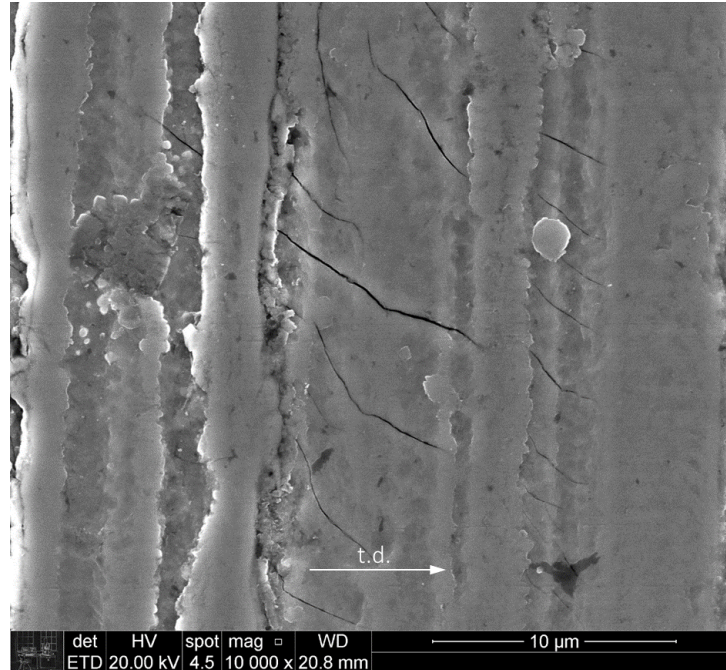


Figure 124: Condition E2-C400h2. SEM view of the textured surface at the distance $D = 2$ mm from beginning of test. Sequence of parallel microcracks nucleated in the matrix. Region free from graphite flakes.

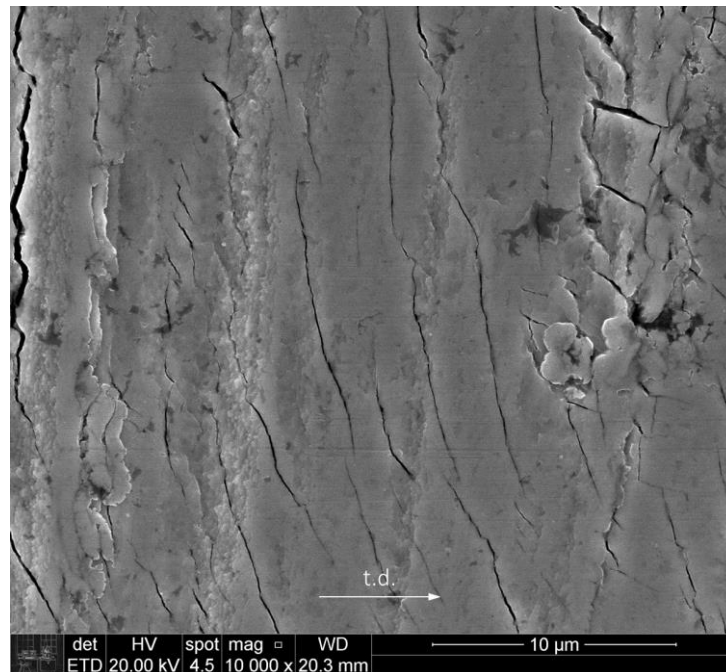


Figure 125: Condition E3-C350h4. SEM view of the textured surface at the ending distance $D = 5$ mm of test, where the normal load achieved its maximum intensity. The image field is filled out by a cluster of microcracks. Region free from graphite flakes.

Therefore, some judgement from the observer is always needed after inspecting the resulting scratch. Based on a qualitative assessment, the critical load (ASTM C1624-05) [70] for tensile microcracks feature in material matrix was deemed about 4.6 N for experiments E1-

C400h4 and E2-C400h2, and 2.8 N for experiments E3-C350h4 and E4-C350h2.

Although tensile microcracks were found in material matrix at all the experimental conditions, no spallation feature [70] was observed in any of the SPN experiments. The critical load for spallation feature was deemed no lower than 10 N, which indicates surface toughness enough to support the abusive load case of the sclerometry test applied herein with no material detachment (delamination).

Table 25: Assessment of scratch damage features (microcracks in material matrix) in increasing normal load test. Qualitative Scale levels: L0 = not observed, L1 = Low, L2 = Medium, L3 = High.

Condition	Microcracks in material matrix, out of graphite pocket surroundings, as a function of distance (D)				
	D = 1 mm	D = 2 mm	D = 3 mm	D = 4 mm	D = 5 mm
E1-C400h4	L0	L1	L2	L3	L3
E2-C400h2	L0	L1	L2	L3	L3
E3-C350h4	L1	L1	L2	L2	L3
E4-C350h2	L1	L1	L2	L2	L2

The sclerometry test applied herein subjected the sample to extreme conditions of progressive load. The load applied by the by the diamond indenter was dynamically increased, so that the local contact pressure was increased with the time and distance. Recognizably the test efforts proposedly exerted to the specimens are far more severe than the explanatory application considered above.

Indeed, the progressive load test was chosen rather than the constant load option, aiming to obtain qualitative evidences of damage features other than the quantitative assessments of scratch groove profile (S_s , S_p , dh) and friction.

4.1.6.3. Friction based on sclerometry test

In order to establish a baseline for SPN results comparison, the results in terms of apparent COF of the textured surface in condition Raw, is initially presented in Figure 126. The graph comprehends Average values +/- standard deviation, based on $n = 5$ sampling.

As described beforehand, during the sclerometry test, the in-lab textured flat specimen was submitted to 1N pre-load applied during 10s. Next, indenter was linearly moved increasing

load, 1N to 10N, with velocity of 0.028 mm/s, during 180 s, resulting in the scratch of 5 mm in length. Because of the fact the test stabilization was comprehended into first 40 s (dashed line), such graph zone was not considered in any data analysis.

Figure 127 shows the apparent COF graph of the textured surface treated in the condition E1-C400h4. Similar evaluation has been accomplished for the other three experimental conditions: E2-C400h2 (Figure 128), E3-C350h4 (Figure 129), and E4-C350h2 (Figure 130).

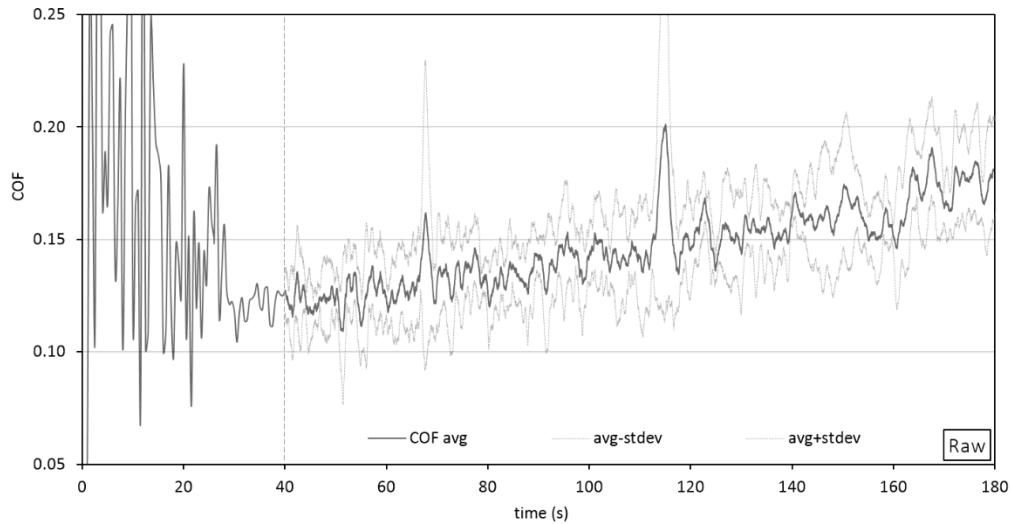


Figure 126: Apparent COF of the textured surface in condition Raw, before SPN treatment (Baseline sample). Avg values \pm std dev, $n = 5$. In-lab textured flat specimen. 1N pre-load applied during 10s. Next, indenter was linearly moved increasing load, 1N to 10N, with velocity of 0.028 mm/s, during 180 s, resulting in the scratch of 5 mm in length. The test stabilization was comprehended into first 40 s (dashed line) and is not considered in data analysis.

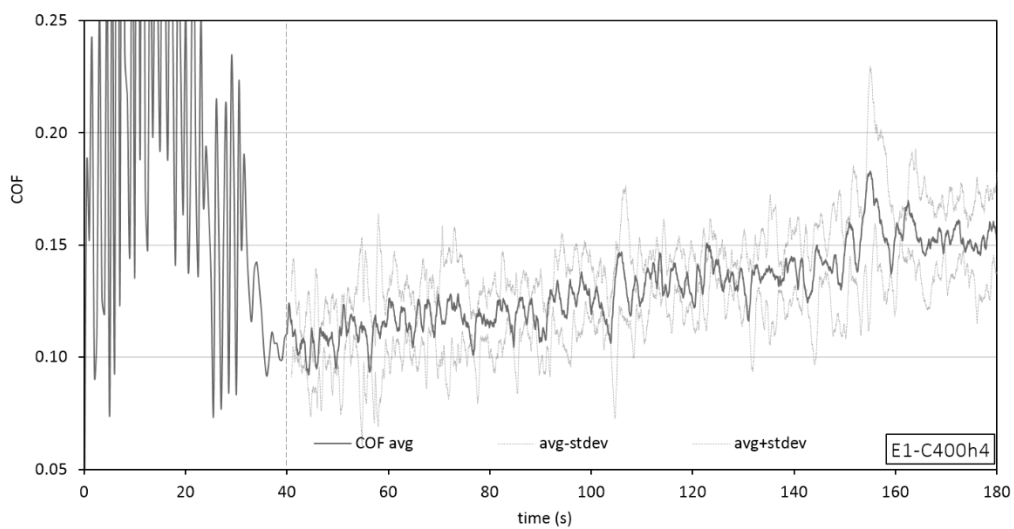


Figure 127: Apparent COF of the textured surface treated in condition E1-C400h4. Avg values \pm std dev, $n = 5$. In-lab textured flat specimen. 1N pre-load applied during 10s. Next, indenter was linearly moved increasing load, 1N to 10N, with velocity of 0.028 mm/s, during 180 s, resulting in the scratch of 5 mm in length. The test stabilization was comprehended into first 40 s (dashed line) and is not considered in data analysis.

The apparent COF measured through sclerometry somewhat decreased after shallow plasma nitriding treatment. This fact was also evidenced through the Figure 131, which shows the combined chart from experiments with respective linear regression line. Decreased friction in scratching process is an indication of lower energy consumption during the test [104].

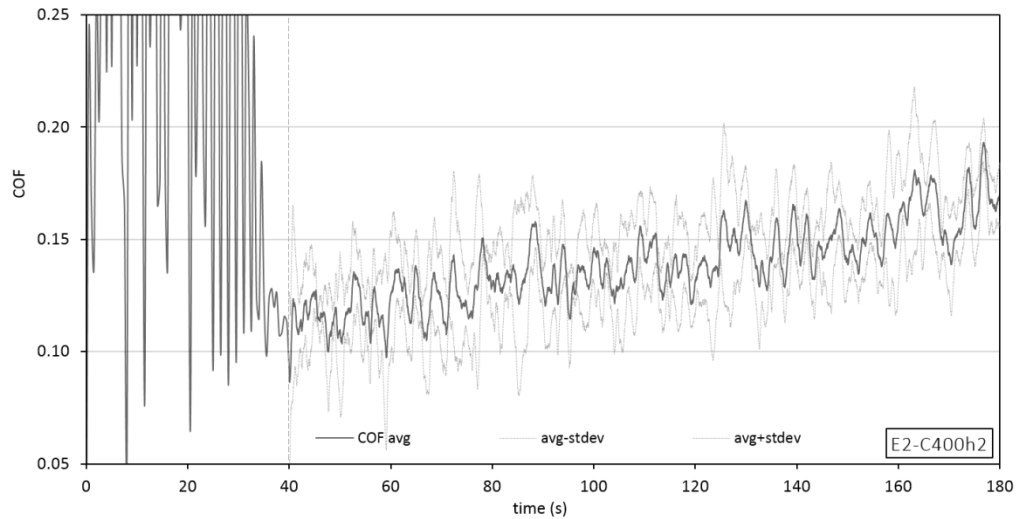


Figure 128: Apparent COF of the textured surface treated in condition E2-C400h2. Avg values \pm std dev, $n = 5$. In-lab textured flat specimen. 1N pre-load applied during 10s. Next, indenter was linearly moved increasing load, 1N to 10N, with velocity of 0.028 mm/s, during 180 s, resulting in the scratch of 5 mm in length. The test stabilization was comprehended into first 40 s (dashed line) and is not considered in data analysis.

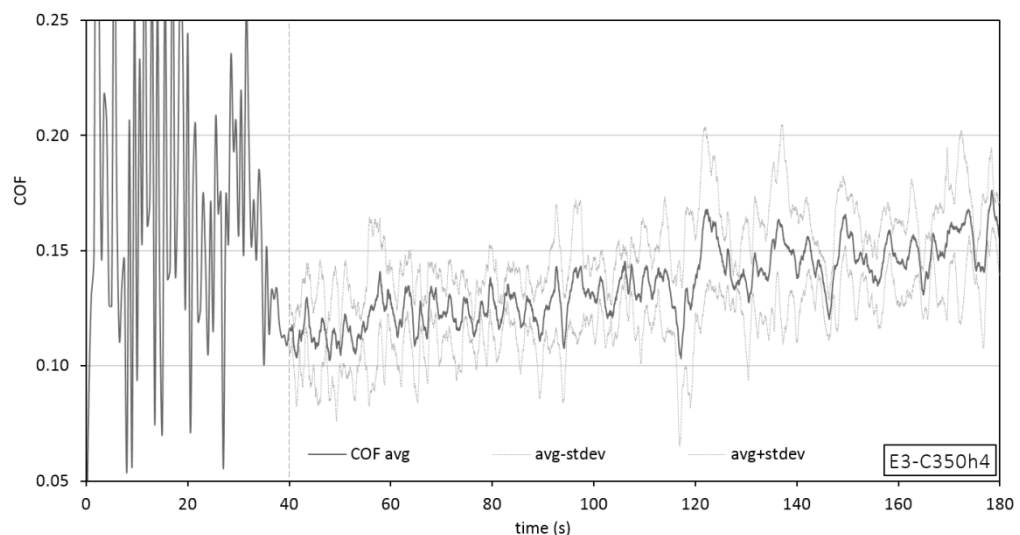


Figure 129: Apparent COF of the textured surface treated in condition E3-C350h4. Avg values \pm std dev, $n = 5$. In-lab textured flat specimen. 1N pre-load applied during 10s. Next, indenter was linearly moved increasing load, 1N to 10N, with velocity of 0.028 mm/s, during 180 s, resulting in the scratch of 5 mm in length. The test stabilization was comprehended into first 40 s (dashed line) and is not considered in data analysis.

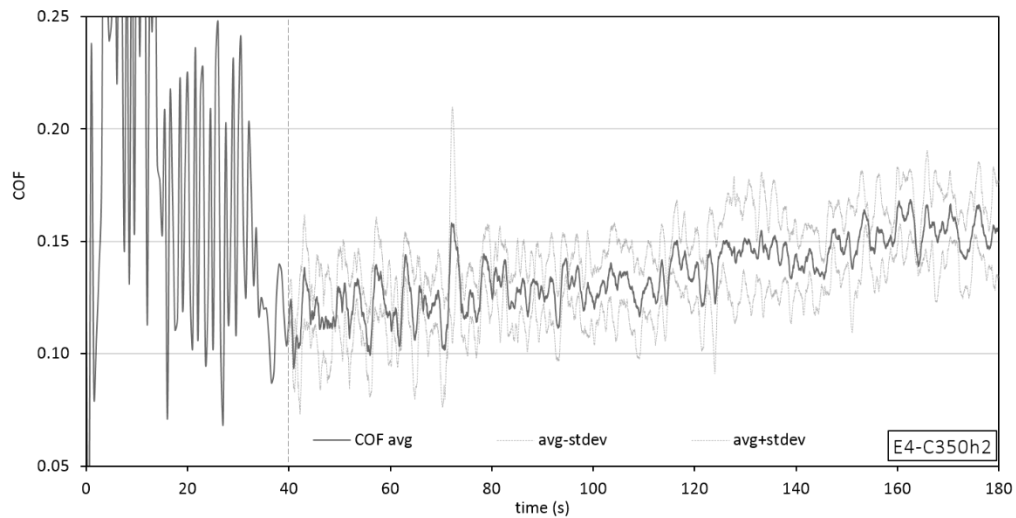


Figure 130: Apparent COF of the textured surface treated in the condition E4-C350h2. Avg values \pm std dev, $n = 5$. In-lab textured flat specimen. 1N pre-load applied during 10s. Next, indenter was linearly moved increasing load, 1N to 10N, with velocity of 0.028 mm/s, during 180 s, resulting in the scratch of 5 mm in length. The test stabilization was comprehended into first 40 s (dashed line) and is not considered in data analysis.

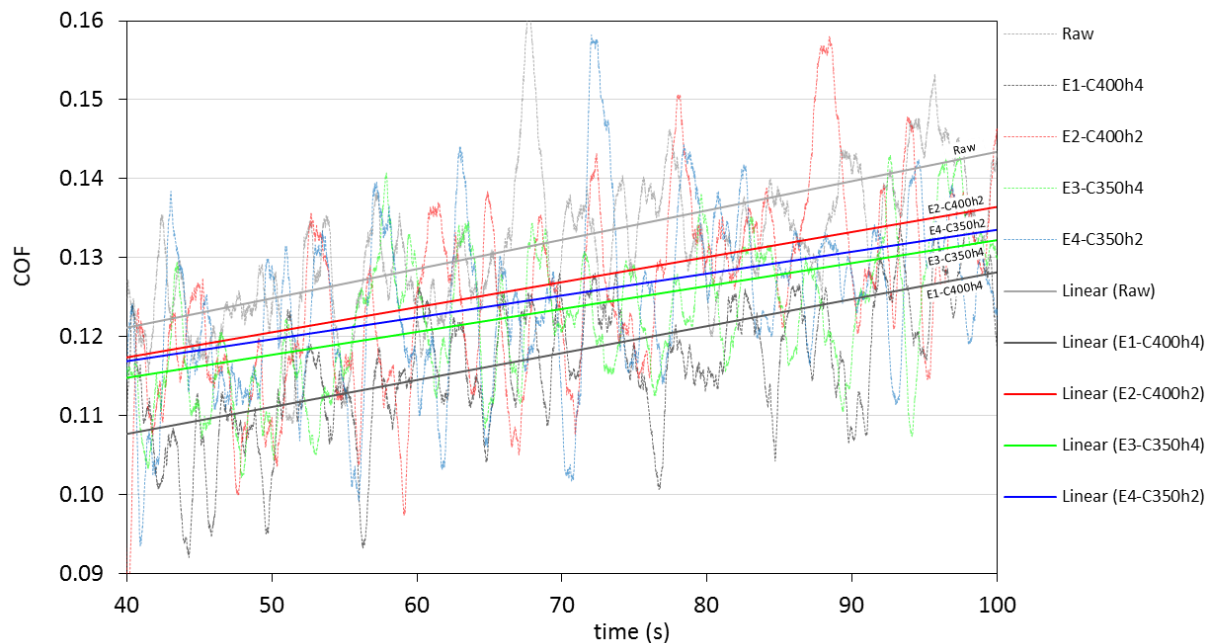


Figure 131: Apparent COF of the textured surface. Combined chart: Raw, E1-400C-4h, E2-400C-2h, E3-350C-4h, E4-350-2h. Avg values and respective linear regression line, $n = 5$. In-lab textured flat specimen.

In spite of the fact apparent COF somehow decreased after SPN treatment, it was not possible to detect a substantial contrast between experimental conditions in terms of temperature-time, within the sampling assessed in this work.

4.2. Case-study: As-honed surface specimen

4.2.1. Roughness results

The 3-D interference roughness results obtained in areas of measurement equal to 1.6 x 1.6 mm are reported in Figure 132, in the conditions before and after SPN. The crosshatch pattern of the honing grooves is visible in the primary profiles (Figure 132a1 and Figure 132b1), which corresponds to the actual cylinder bore macro form in the condition as textured.

Resulting filtered profiles, along with colored scales (valleys-to-summits), are shown in Figure 132a2 and Figure 132b2. The form-removal filter was applied via TalyMap 3-D software, in order to quantify the roughness parameters. In addition, corresponding material ratio curves are presented in Figure 132a3 and Figure 132b3, along with the calculated parameters S_k , S_{pk} , S_{vk} , S_{r1} and S_{r2} , summarized in Table 26.

Similarly, filtered profiles and material ratio curves of the 3-D interference roughness results obtained in areas of measurement are 0.3 x 0.3mm are reported in Figure 133.

Figure 134 shows the summary of results of the 1.6 x 1.6 mm areal measurements. Corresponding data is presented in Table 26. It can be noted that S_{pk} somewhat increased after SPN, which was also confirmed via the 0.3 x 0.3 mm 3-D interference measurement. Further studies including statistics and measurement uncertainty considerations would be necessary to conclude whether or not this increment can be fully attributed for the SPN treatment.

Table 26: Summary of roughness results data. Case-study.

Measured area	Parameter	(a) Before SPN	(b) After SPN
1.6 x 1.6 (mm)	S_k (μm)	0.28	0.28
	S_{pk} (μm)	0.14	0.19
	S_{vk} (μm)	0.23	0.25
	S_{r1} (%)	10.9	11.0
	S_{r2} (%)	88.0	88.2
0.3 x 0.3 (mm)	S_k (μm)	0.33	0.30
	S_{pk} (μm)	0.13	0.20
	S_{vk} (μm)	0.33	0.27
	S_{r1} (%)	9.5	10.5
	S_{r2} (%)	88.0	86.2

Considering reference values reported in literature [102] for plateau honing parameters, results indicated minimal differences of roughness texture before and after SPN treatment, for the studied sample. Therefore, one among the potential applications of the research has been assessed in terms of topography response.

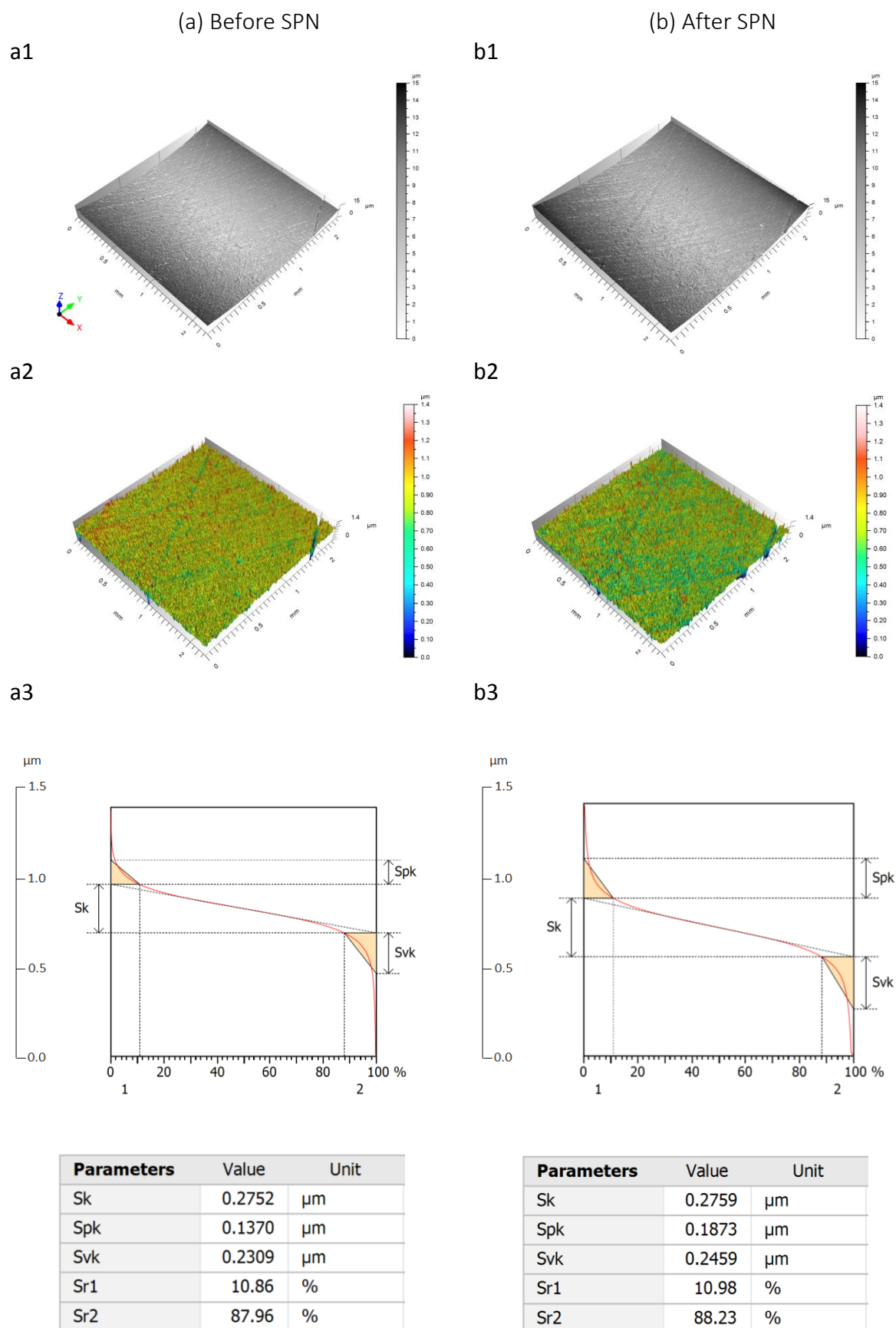


Figure 132: 3-D interference measurements. Areas of measurement are 1.6 mm x 1.6 mm. a) Before SPN. b) After SPN. a1 and b1) The primary profiles. a2 and b2) Form-removal filtered profiles. a3 and b3) Material ratio curve.

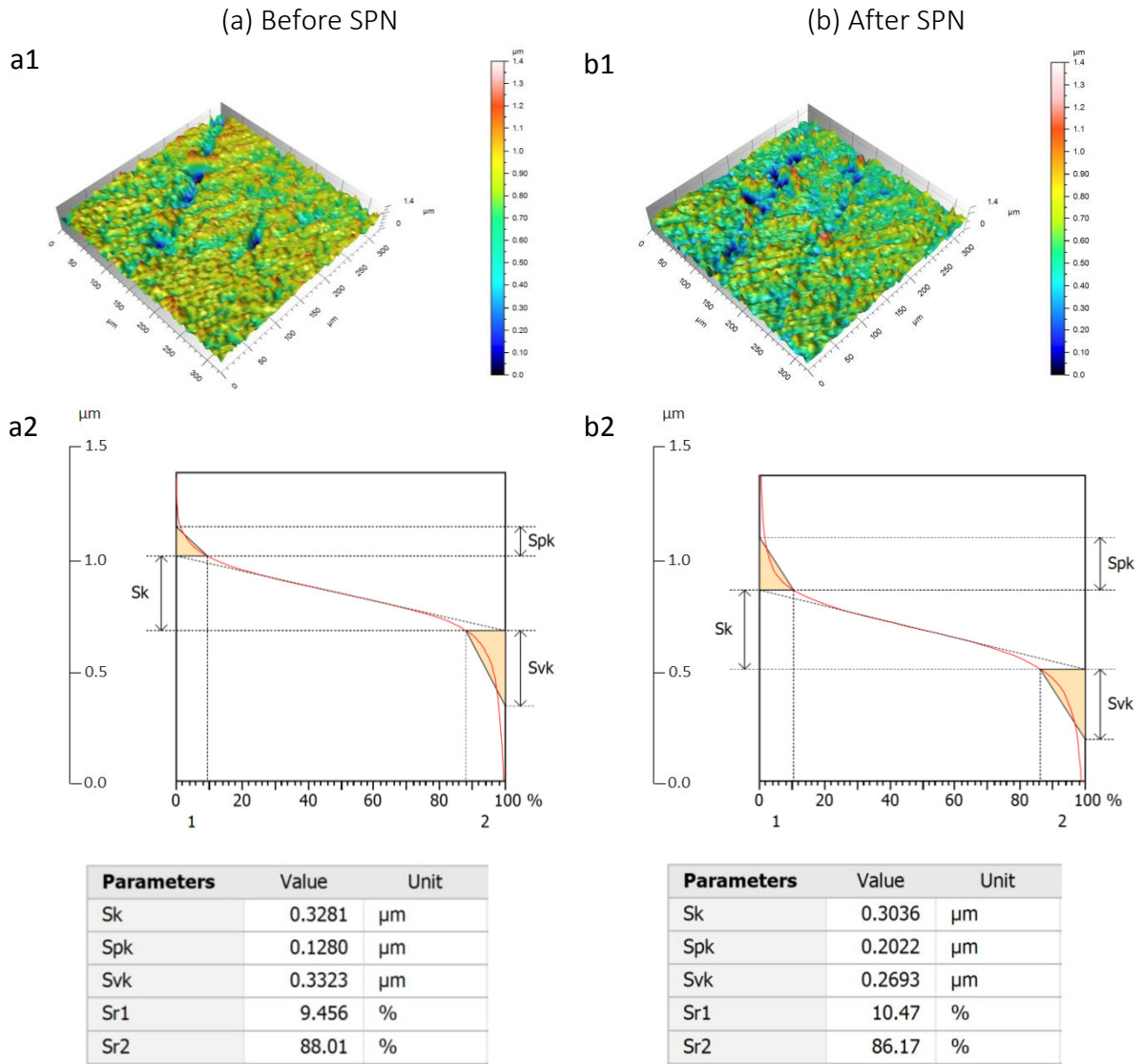


Figure 133: 3-D interference measurements. Areas of measurement are 0.3mm x 0.3mm. a) Before SPN. b) After SPN. a1 and b1) Form-removal filtered profiles. a2 and b2) Material ratio curve.

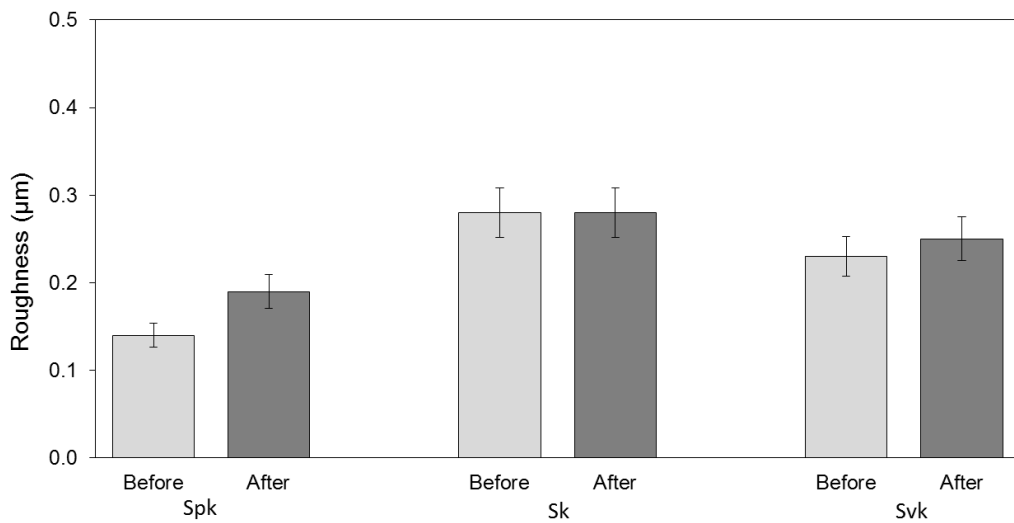


Figure 134: Summary of roughness. Area of measurement 1.6 x 1.6 mm. Spk somewhat increased after SPN. Individual measurements (Case-study). Bar errors correspond to the estimated measurement uncertainty.

4.2.2 . WDS (Quantitative) and EDS (Qualitative) microanalysis of N-concentration

Wavelength-dispersive X-ray spectroscopy (WDS) microanalysis results, of nitrogen (wt%) content as a function of the distance from the surface, are consolidated in Figure 135 and Table 27. The graph plotting average N-content versus distance yields a curve similar to previous results reported across the in-lab textured flat specimens section (Figure 66).

Figure 135 shows the distribution of N-content in the matrix of pearlite of the gray cast iron as-honed surface specimen treated at 350 °C during two hours, in a 75% N₂ / 25% H₂ atmosphere (CS-C350h2), as a function of the distance to the surface.

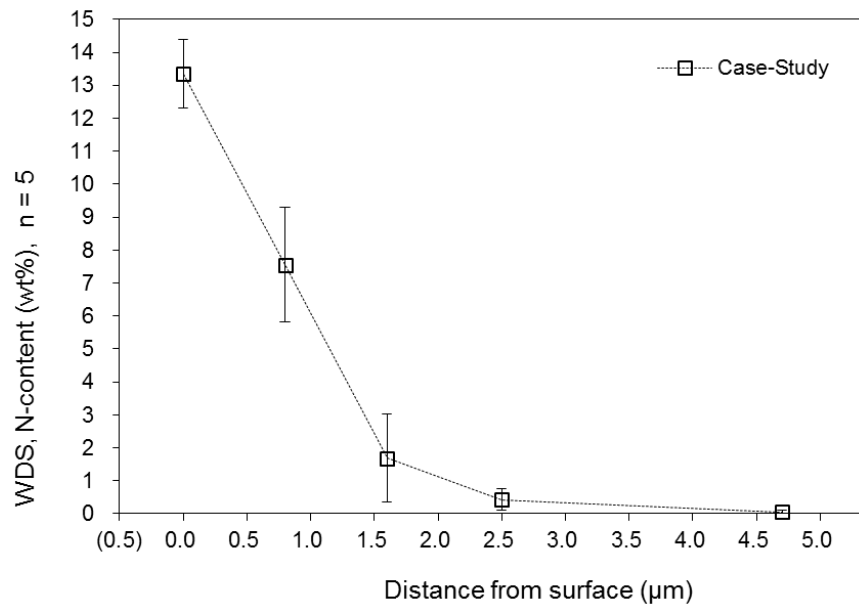


Figure 135: Quantitative analysis. N-content (wt%) as a function of distance from surface (μm) measured via Wavelength-Dispersive Spectroscopy (WDS) microanalysis. Average values +/- standard deviation. n = 5. Case-study: as-honed surface, 350C-2h.

Each point in the graph corresponds to the mean value of five measurements taken in a line parallel to the best-fit line of surface. Each single measurement was distant 10 +/- 2 μm from each other. The bar error associated to each graph point corresponds to plus and minus one standard deviation resulted from the five measurements.

The first point (at zero distance) is based on five measurements taken directly on specimen surface. Except for this point, the complete analysis was carried-out at increasing distances from surface and towards to the specimen core. The measurements at the increasing distances were taken on the polished cross section, perpendicular to the textured surface.

Figure 136 shows the WDS spectrum taken directly on specimen surface. The background

correction was determined by measuring the intensity with the spectrometer offset by a suitable amount on each side of the peak (indicated by -N and +N) and interpolating linearly to the peak position [96].

The resulting peak at 0.39 keV (indicated by N) clearly evidences the Case-Study surface is enriched with nitrogen so that reproducing the results of the in-lab textured flat specimens. The characteristic N-peak was observed in each single measurement (5 points per distance from surface), and is consistent with XRD characterization data, where ϵ -nitride was detected on the specimens' surface.

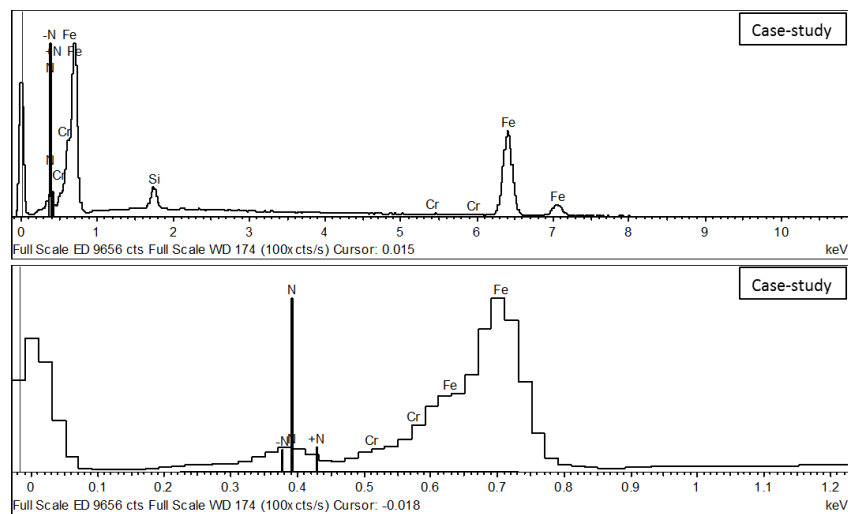


Figure 136: WDS spectrum. Quantitative analysis. Case-study: as-honed surface, 350C-2h.

The plotted points in N-content versus distance charts yielded to a curve whose nitrogen content decreases monotonically with the distance to the surface. With negative slope the N-wt% versus distance- μm line moves down when going from left to right in x-axis. Beyond about 2.5 μm of depth, the noted change of the curve slope shows that the nitrogen gradient is significantly reduced at such region (Figure 135 and data from Table 27).

At 5 μm of depth, nitrogen content tends to zero, indicating the proximity (or achievement) of the transition between nitrogen diffusion zone and core material. Accordingly, the use of a lower process temperature extended the cycle time for diffusion [10] so that shallow diffusion depth was successfully achieved.

Even considering the reported variability, the plotted points yielded to a curve that evidences nitrogen enrichment at shallow depths.

A cross section of the nitrided sample is shown in Figure 137. The gray cast iron pearlitic matrix and a graphite flake can be seen in Figure 137a. The nitrided zone was interrupted by the

graphite flake. In fact, graphite functions as a diffusion barrier for nitrogen [61,63]. In the ICE cylinder block, the size and position of the graphite particles can fluctuate across the surface, as well as their distance from the surface [55].

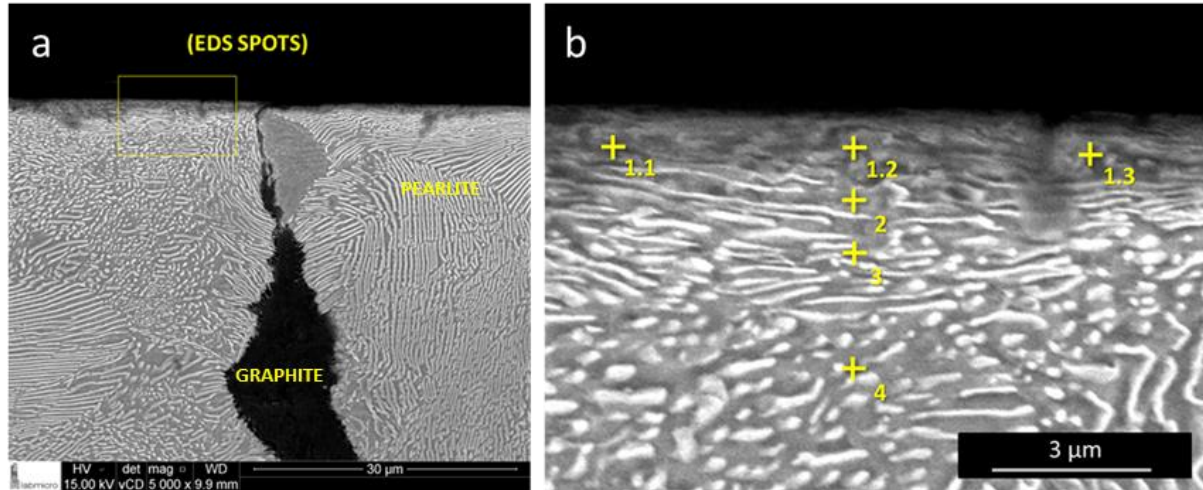


Figure 137: (a) SEM image of the SPN case-study sample: as-honed surface, 350C-2h. The gray cast iron pearlitic matrix and a graphite flake can be seen in the cross section. Nitrided zone was interrupted by the graphite flake. (b) EDS spots 1.1, 1.2 and 1.3 are located in the SPN zone, at 1 μm depth from surface and distant 5 μm from each other. The spots 3 and 4 are located out of the SPN zone, at 3 μm and 5 μm depth from surface, respectively.

Qualitative EDS spots location is schematically indicated in Figure 137b. The qualitative results obtained from such spots are graphically summarized in Figure 138, which was confirmed by the WDS quantitative data (Figure 135) presented beforehand.

In summary, nitrided zone at shallow depth (1 μm) was evidenced in both quantitative and qualitative techniques, by the substantial nitrogen concentration at distances approaching the surface (Table 27 and Table 28). According to data shown in Table 27, the average content decreased from the surface towards the core, and can be deemed herein as no further significant after 2.5 μm of depth (Figure 135).

Carbon redistribution could also have occurred in the diffusion zone, with initial carbon atoms diffusing towards the nitriding front. Resulting small peak of carbon can be detected in future analysis, also via WDS techniques [67].

Case-study WDS and EDS microanalysis results (Figure 140) trended to reproduce the overall behavior of the in-lab textured flat specimens. General pattern of the in-industry textured and the in-lab textured specimen curves showing N-content (wt%) as a function of depth (μm) is similar to each other. In all the situations, the content decreased monotonically

from the enriched surfaces until it tended to zero wt% at 5 μm of depth, therefore constituting nitrogen enrichment at shallow depths.

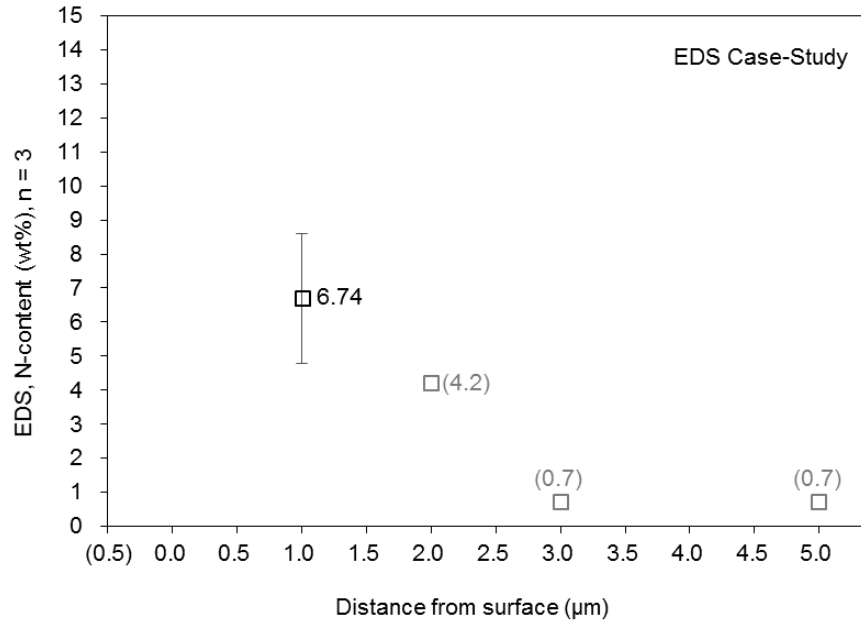


Figure 138: Qualitative analysis. Estimation of N-content (wt%) as a function of distance from surface (μm) measured via Energy-Dispersive Spectroscopy (EDS) microanalysis. Average value \pm standard deviation (only first point). Case-study: as-honed surface, 350C-2h. Single values at distance 2.0, 3.0 and 5.0 μm for reference only. (informative)

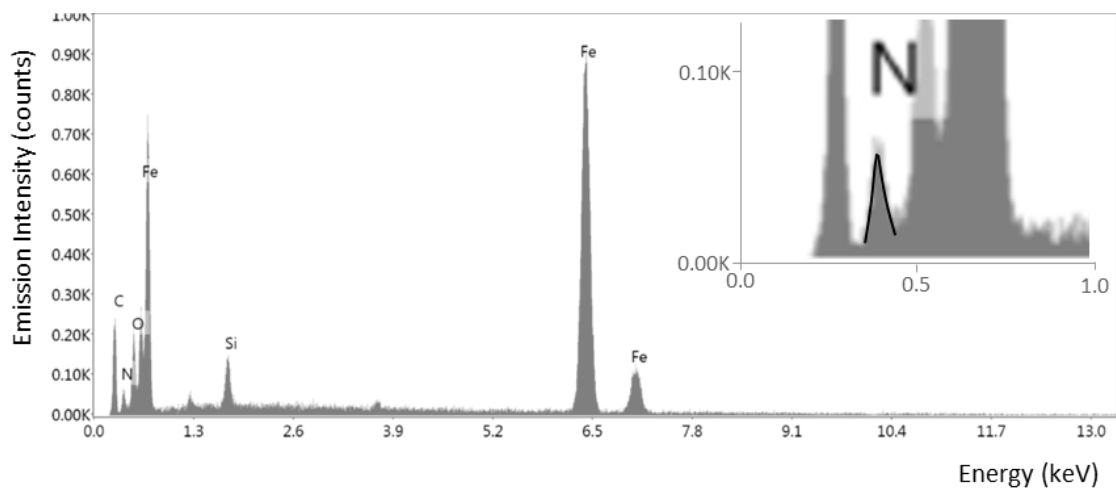


Figure 139: Qualitative analysis. EDS spectrum at 1 μm from surface. Case-study: as-honed surface, 350C-2h. Emission peaks (counts) as a function of energy (keV). The view in detail shows the N-peak qualitatively evidencing that enrichment of nitrogen occurred at 1 μm depth from surface. (informative)

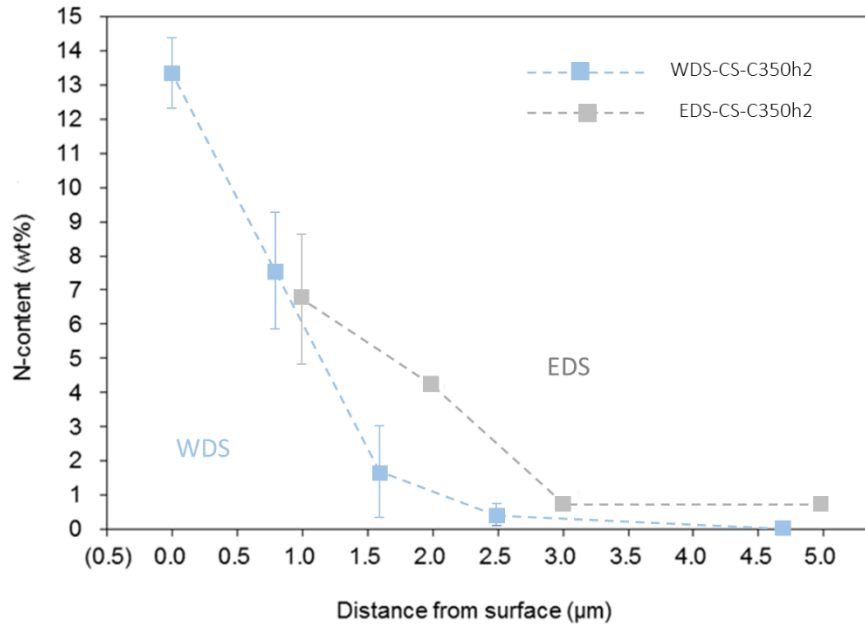


Figure 140: WDS (Quantitative) and EDS (Qualitative) microanalysis of N-concentration. Combined chart: Estimation of N-content (wt%) as a function of distance from surface (μm) measured via Energy-Dispersive Spectroscopy (EDS) microanalysis. Average value \pm standard deviation (only first point) - in gray; N-content (wt%) as a function of distance from surface (μm) measured via Wavelength-Dispersive Spectroscopy (WDS) microanalysis. Average values \pm standard deviation. $n = 5$ - in blue. Case-study: as-honed surface, 350C-2h.

Table 27: N-content (wt%) as a function of distance from surface (μm) via Wavelength-Dispersive Spectroscopy (WDS) microanalysis. Quantitative analysis. Case-study: as-honed surface. Individual values.

Individual values							
Dist (μm)	n1	n2	n3	n4	n5	Avg	StdDev
0.0	13.75	12.38	14.08	12.11	14.45	13.35	1.05
0.8	9.85	8.73	5.53	7.20	6.44	7.55	1.74
1.6	3.78	2.28	0.55	0.93	0.90	1.69	1.34
2.5	0.75	0.23	0.03	0.37	0.78	0.43	0.33
4.5	0.00	0.10	0.00	0.02	0.12	0.05	0.06

Table 28: N-content (wt%) as a function of distance from surface (μm) via Energy-Dispersive Spectroscopy (EDS) microanalysis. Qualitative analysis. Case-study: as-honed surface. Individual values. (informative)

Dist (μm)	n1	n2	n3	Avg	StdDev
0.0	-	-	-	-	-
1.0	4.61	7.96	7.64	6.74	1.85
2.0	(4.2)	-	-	(4.2)	-
3.0	(0.7)	-	-	(0.7)	-
5.0	(0.7)	-	-	(0.7)	-

4.2.3 . X-Ray diffraction (XRD) analysis

In the XRD analysis, it was possible to identify the Fe- α in both conditions before and after SPN process. The ϵ -nitride (Fe₃N) was identified in the condition after nitriding process with the assistance of both Crystallographica Search-Match (CSM) software and Origin software. The diffractograms with and without background filtering are shown in Figure 141 and Figure 142, respectively.

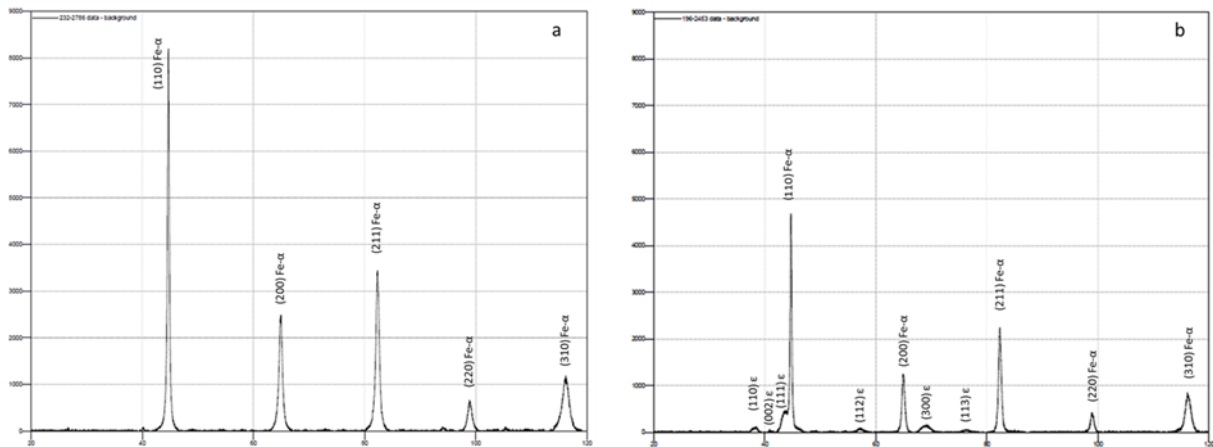


Figure 141: XRD diffractograms of the textured surface in the condition a) before SPN treatment (CS-Raw) and b) after SPN treatment (CS-C350h2). Background filter was applied. Crystallographica Search-Match (CSM) software.

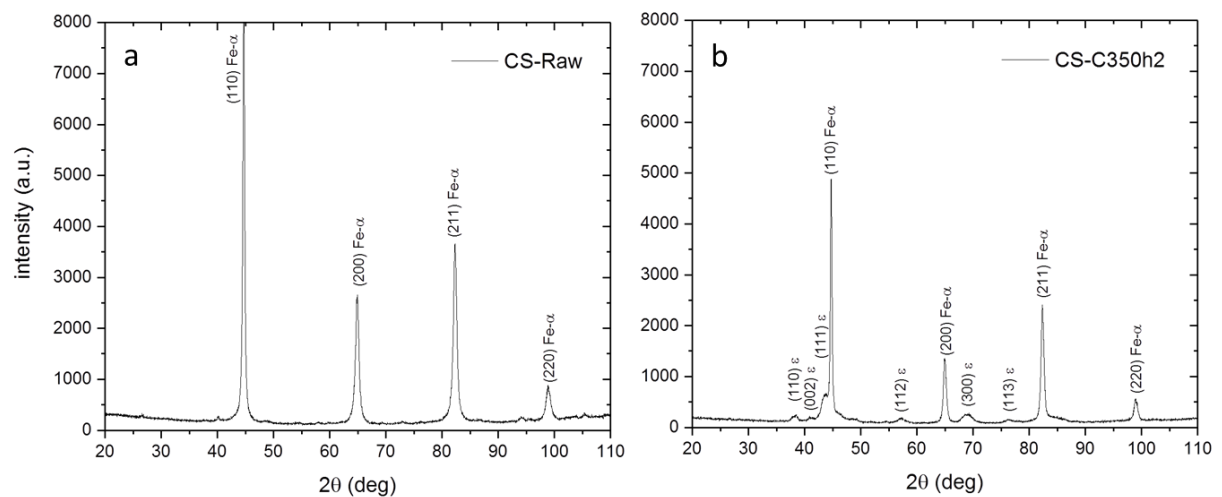


Figure 142: XRD diffractograms of the textured surface in the condition a) before SPN treatment (CS-Raw) and b) after SPN treatment (CS-C350h2). ϵ -nitride (Fe₃N) peaks growth and reduction in Fe- α peaks intensity were evidenced through direct comparison between charts. Background filter was not applied. Origin 9.4 software.

Figure 143 shows the XRD combined diffractogram of the textured surface in the conditions before SPN treatment (CS-Raw) and after SPN treatment (CS-C350h2). An overlapped view of both diffractograms in single scale evidenced the formation of ϵ -nitride, confirming the initial results of in-lab textured flat specimens discussed in previous sections.

The area under the Fe_3N peaks relates to the amount of phase present [97], which is small relatively to $\text{Fe-}\alpha$. This is due to the SPN process conducted at low temperature and short processing time. Figure 144a, Figure 144b and Figure 144c present the (110), (112) and (300) ϵ -nitride peaks in formatted scale charts. Therefore, they can be clearly registered for further considerations and future works.

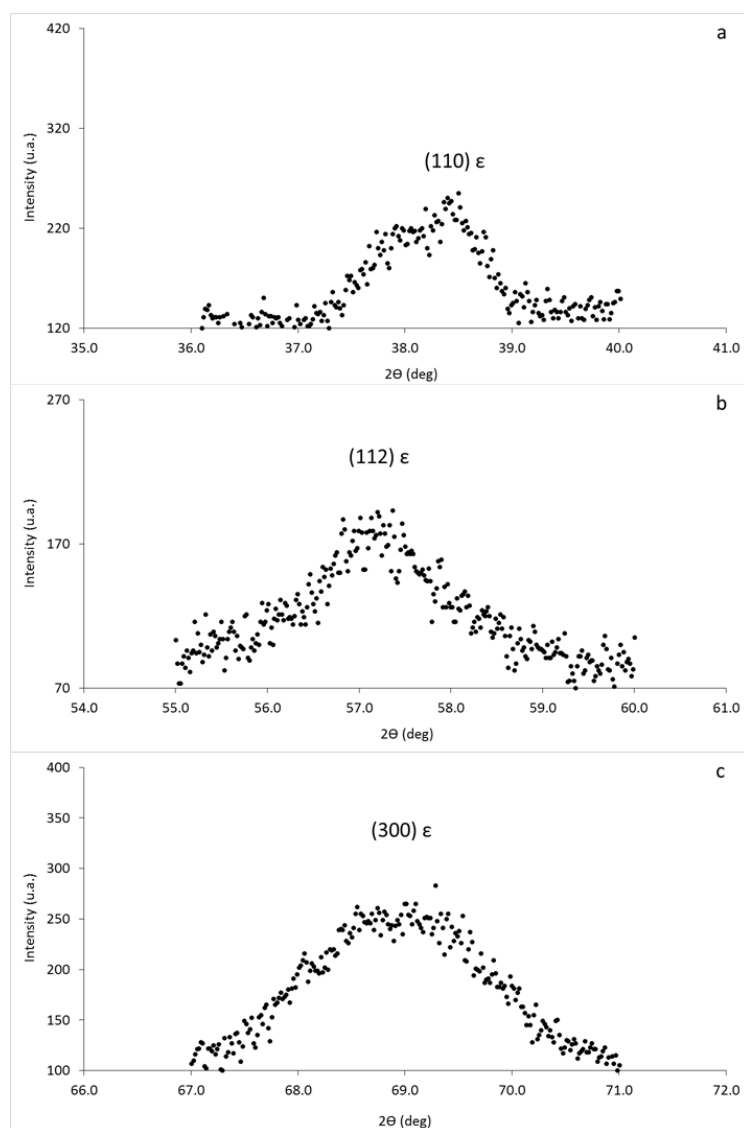


Figure 144: Some ϵ -nitride (Fe_3N) peaks obtained from the X-Ray diffractogram LCT-USP 196-2453 of the textured surface in the condition after SPN. a) (110) ϵ -nitride peak. b) (112) ϵ -nitride peak. c) (300) ϵ -nitride peak.

4.2.4 . Microhardness analysis

The microhardness (HV 0.01) average and standard deviation of the samples (measured on top of the SPN zone) in the condition before and after SPN are presented in Figure 145. Higher microhardness (749 ± 42 HV 0.01) was observed for the treated condition. In the initial condition, the microhardness was 528 ± 23 HV 0.01. The hardness increase indicates interstitial solid solution hardening as well as iron nitride formation.

The indentation depth, calculated from average diagonal length and Vickers indenter angle, resulted $0.71 \mu\text{m} \pm 0.02 \mu\text{m}$. Based on the N concentration profile described in the previous chapter, the indentation depth is located in the N-enriched zone.

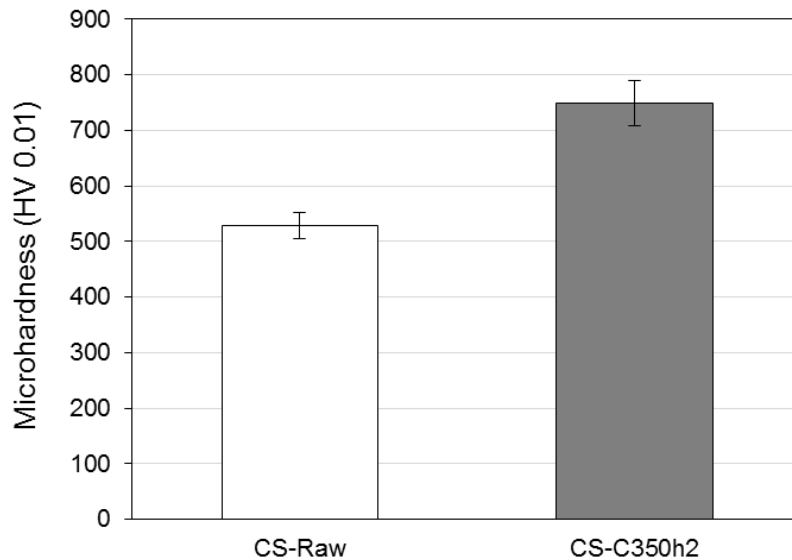


Figure 145: Microhardness (HV 0.01) on the surface (zero μm distance) measured with 10 gf. Average values \pm standard deviation, $n = 10$. As-honed surface specimen (case-study). Combined chart: CS-Raw, CS-350-2h.

Figure 146 presents dark-field optical microscopy images of the textured surface in the condition before (a) and after (b) SPN treatment, with respective Vickers microhardness (HV 0.01) indentations. It can be noted the difference in size between the Vickers indentations, as well as the honing grooves of various dimensions, which is the basis of the textured surface applied for ICE cylinder bores.

Higher hardness noted in the case-study raw specimen (528 HV) relatively to in-lab textured specimen in raw condition (428 HV) is attributed to the micro deformations in the pearlitic matrix induced by the honing operation, which reduces the pearlite interlamellar

spacing, which in turn increases strength locally [98]. Higher strength is usually explained on the basis of the reduced ferrite cells and the alignment of cementite in fibers [98-100].

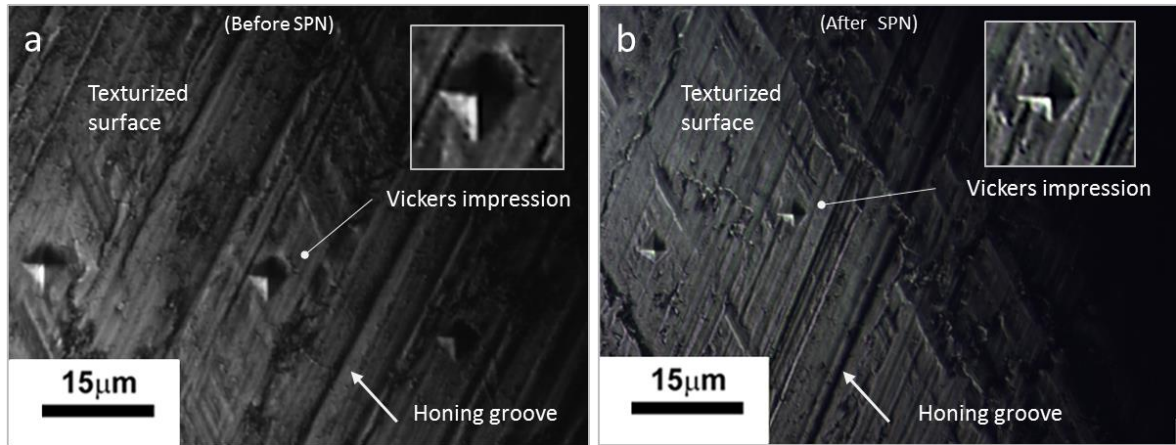


Figure 146: Dark-field optical microscopy images of the textured surface in condition before (a) and after (b) SPN, with respective Vickers (HV 0.01) indentations. Honing grooves of various dimensions are visible in both images.

Table 29: Data group of Microhardness (HV 0.01) on the surface (zero μm distance) measured with 10 gf, $n = 10$. As-honed surface specimen (case-study). Conditions: CS-Raw, CS-350-2h.

Measurement	Hardness (HV0.01)	
	Before SPN	After SPN
1	500	720
2	500	747
3	532	695
4	532	747
5	549	776
6	549	695
7	500	806
8	516	720
9	567	806
10	532	776
Avg	528	749
Std Dev	23	42

While the surface texture of flat specimens were obtained using manual grinding with sandpapers (as described in materials and methods) in lab, the case-study specimens were texturized through honing operation, in a cylinder block industrial process.

As introduced in the initial chapters of this thesis, the cross hatch pattern was created by virtue of the honing tool, which is composed of a number of honing stones, which are pressed radially outward of the cylinder bore along with simultaneous rotating and stroking movements

inside the cylinder. The micro deformations introduced in the pearlitic matrix by the honing operation were characterized in Figure 147 and Figure 148.

In spite of the reported differences of initial microhardness between case-study and in-lab textured flat specimen at raw condition, the final microhardness obtained after SPN treatment were reasonably similar between both experiments carried out at same temperature/time set-up: CS-C350h2 (industry textured) experiment resulted 749 ± 42 HV 0.01 and E4-C350h2 (in-lab textured) resulted 731 ± 28 HV 0.01.

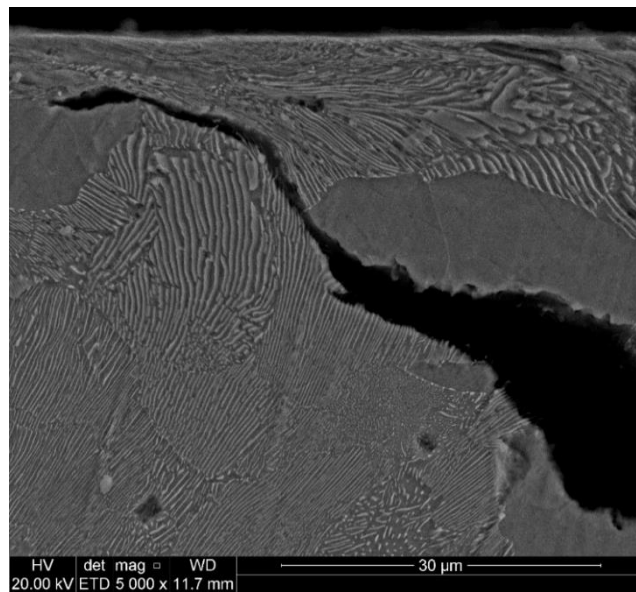


Figure 147: Micro deformations in the pearlitic matrix induced by the honing operation. As-honed surface specimen (case-study), condition CS-Raw. A graphite flake is shown along with adjacent deformed pearlite region.

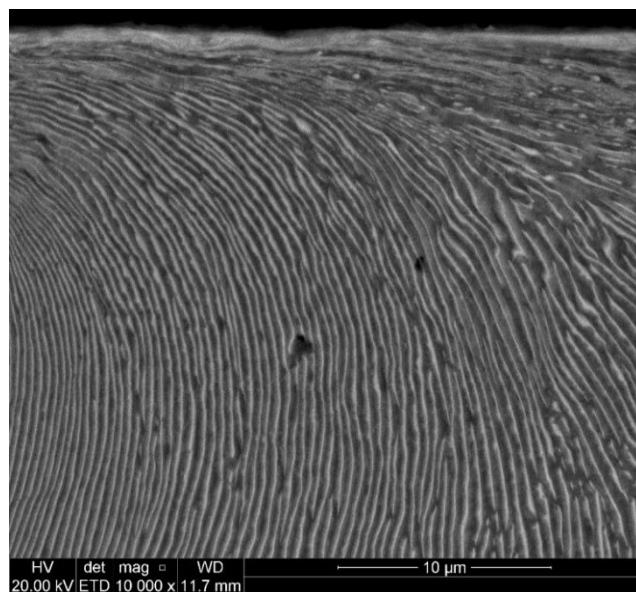


Figure 148: Micro deformations in the pearlitic matrix induced by the honing operation. As-honed surface specimen (case-study), in the condition CS-Raw (before SPN).

4.2.5. Instrumented linear sclerometry test

4.2.5.1. 3-D surface profile, “groove area” (Ss), “pile-up area” (Sp) and depth (dh)

Figure 149 shows the 2-D acquisition of Sp and Ss from the 3-D interference profile, whose results were consolidated through the Figure 151 and Figure 152. Figure 150 shows the images of the interferometry scanning of scratch grooves, before the 2-D cuts to extract Sp and Ss numbers. The images show the evolution of the scratch groove, whose width overall increased with the applied load.

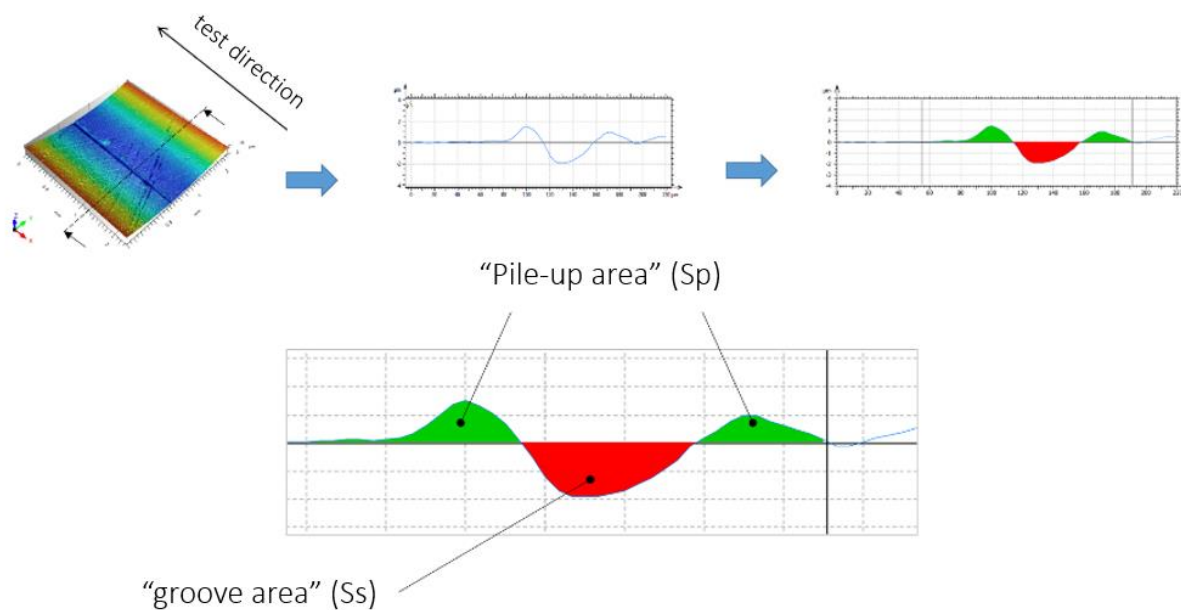


Figure 149: 2-D acquisition of Sp and Ss from the 3-D interference profile.

Accordingly, honing texture resulted preserved after SPN treatment. Similar scratch appearance between the two conditions, with apparent higher level of plastic flowed (pile-up) material in condition before SPN is shown in Figure 150.

Figure 151 shows 2-D profilograms of the textured surface and resulting sclerometry groove, in the condition before SPN treatment (CS-Raw). Similar type of result in the condition CS-C350h2 is presented in Figure 152. The section locations correspond to previous 3-D profile images, showing “Groove area” (Ss) - in red and “pile-up area” (Sp) - in green, at distances from beginning of test: 1 mm, 2 mm, 3 mm and 4 mm. Ss and Sp computed values, as well as punctual measurement of depth (dh) were summarized in the next charts.

Experiment: Case Study (CS-C350h2)

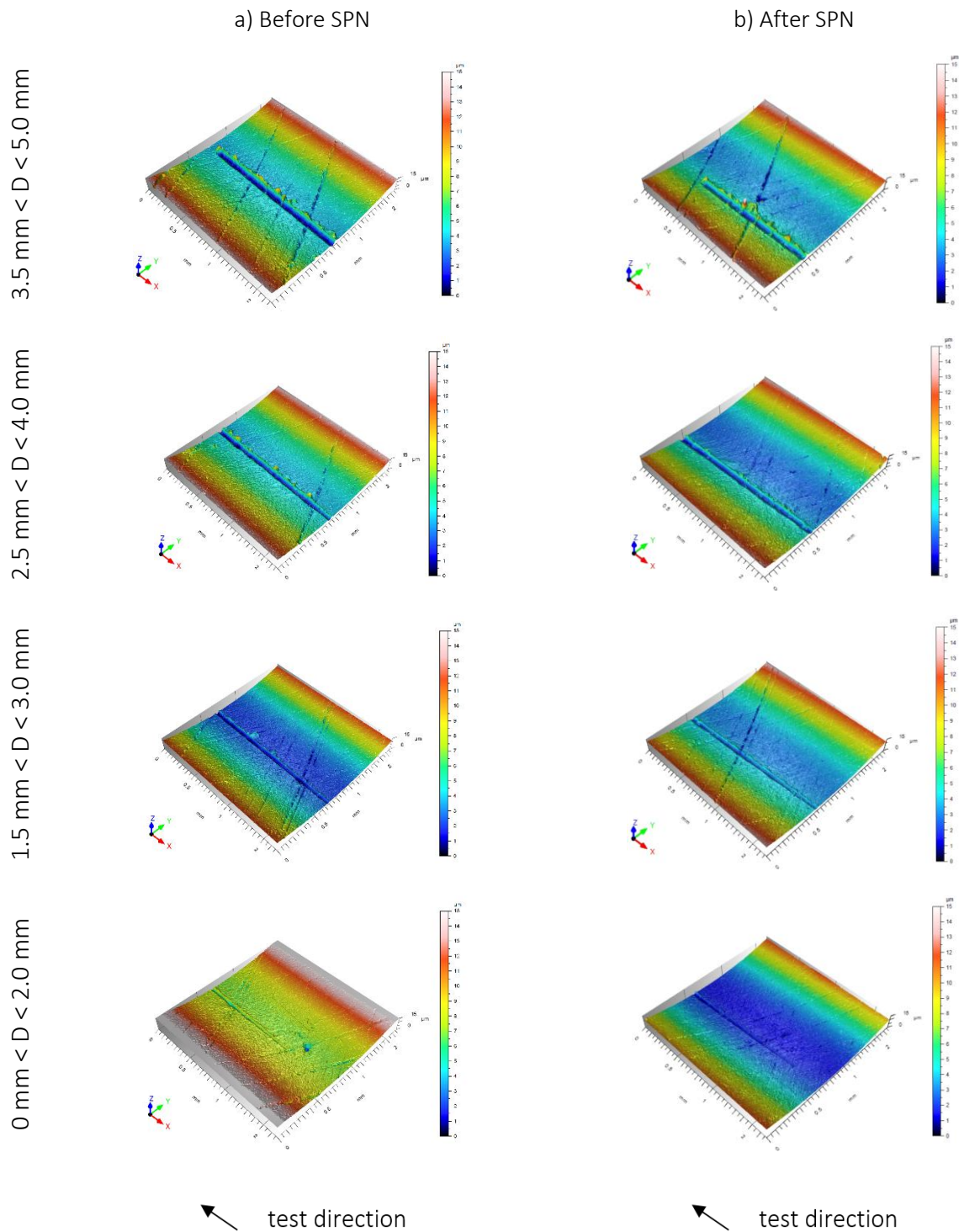


Figure 150: Progressive linear sclerometry test. Top [tilted] view of the 3-D profile of the surface in conditions before (CS-Raw) and after SPN treatment (CS-C350h2). Case-Study: As-honed surface specimen. Pre-load: 1 N / 10 s, linear increasing load: 1-10 N, 0.028 mm/s. Resulting scratch: 5 mm in length. Color scale indicates heights from valley to peak (primary form not filtered). Profiles at different distance ranges, highlighting the progressive evolution of the sclerometry groove. Honing texture preserved after SPN. Similar scratch appearance between the two conditions, with apparent higher level of plastic flowed (pile-up) material in condition before SPN.

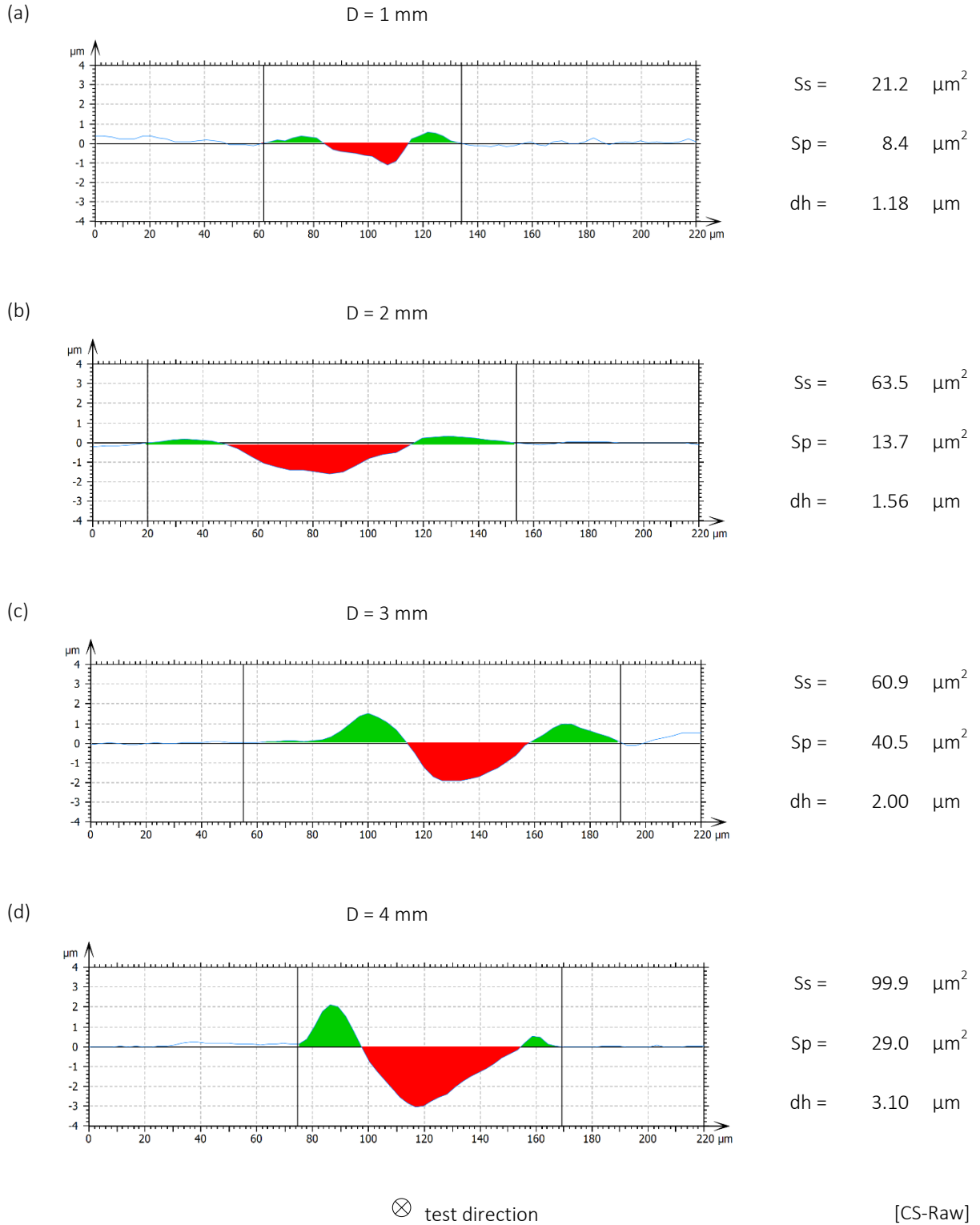


Figure 151: Instrumented linear sclerometry test. 2-D profilograms of the textured surface and resulting sclerometry groove, in the condition before SPN treatment (CS-Raw). Case-Study: As-honed surface specimen. Section locations corresponding to previous 3-D profile images. All the graphs: test direction towards the plane of the page. a-d) “Groove area” (Ss) - in red and “pile-up area” (Sp) - in green, at distances from beginning of test: 1 mm, 2 mm, 3 mm, and 4 mm. Ss and Sp computed values reported along with each graph. In addition, punctual measurement of depth (dh) is informed.

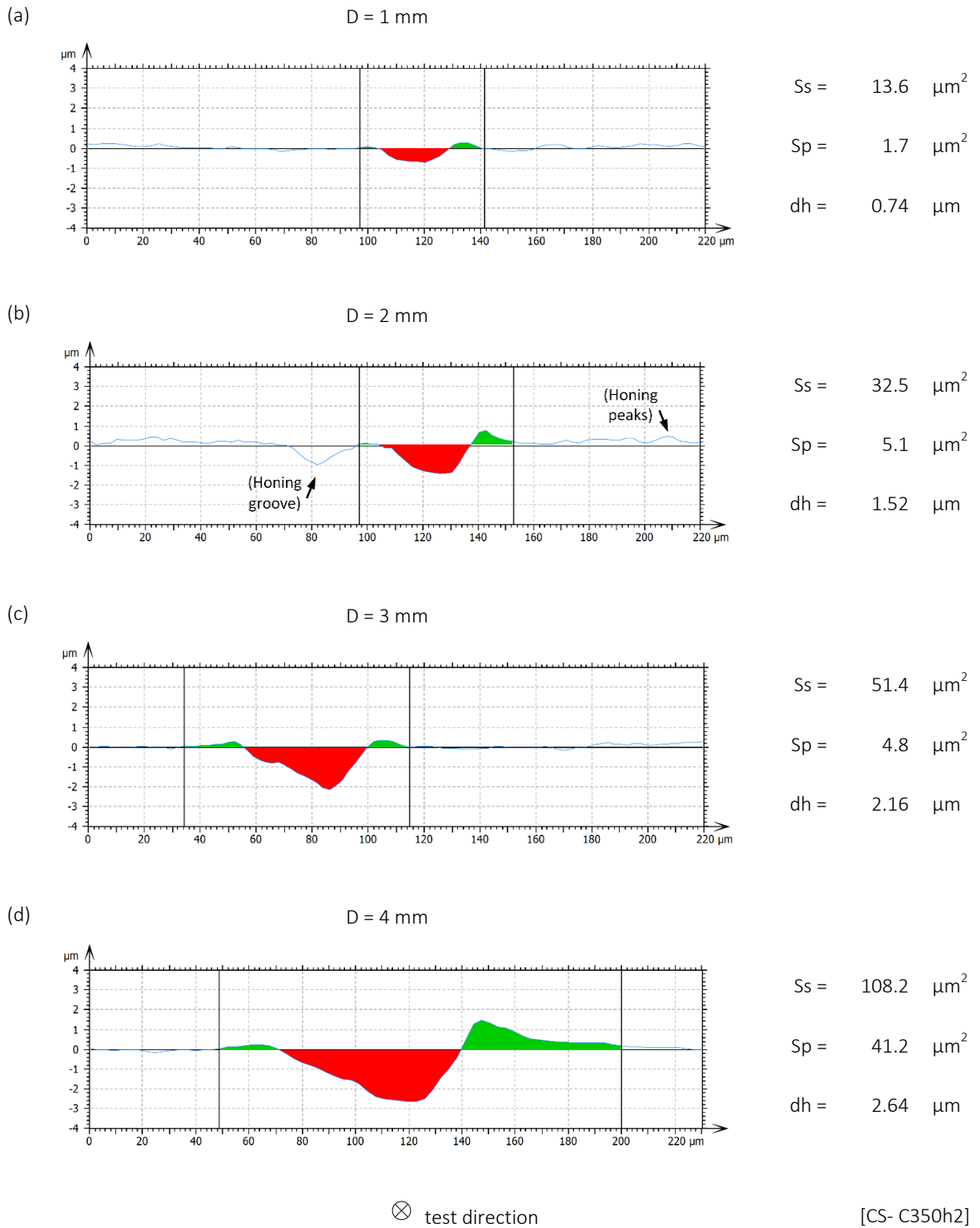


Figure 152: Instrumented linear sclerometry test. 2-D profilograms of the textured surface and resulting sclerometry groove, in the condition after SPN treatment (CS-C350h2). Case-Study: As-honed surface specimen. Section locations corresponding to previous 3-D profile images. All the graphs: test direction towards the plane of the page. a-d) “Groove area” (Ss) - in red and “pile-up area” (Sp) - in green, at distances from beginning of test: 1 mm, 2 mm, 3 mm, and 4 mm. Ss and Sp computed values reported along with each graph. In addition, punctual measurement of depth (dh) is informed.

Figure 153, Figure 154, and Figure 155 summarize the resulting scratch depth (dh), “groove area” (Ss), and “pile-up area” (Sp) area of the as-honed surface specimen before and after SPN treatment.

The resulting scratch depth (dh) of condition CS-C350h2 compared to Raw (baseline), as a function of the distance from beginning of test, indicated that depth decreased after SPN treatment at distance $D = 1$ mm, where dh of post-treated sample is lower than $1 \mu\text{m}$ (Figure 153).

Likewise previous verification through in-lab textured flat specimens, such effect was attributed to the increase of surface strength due to plasma nitriding. Beyond scratch distance $D = 2$ mm, the contrast between conditions before and after SPN in case-study sample is not clear anymore.

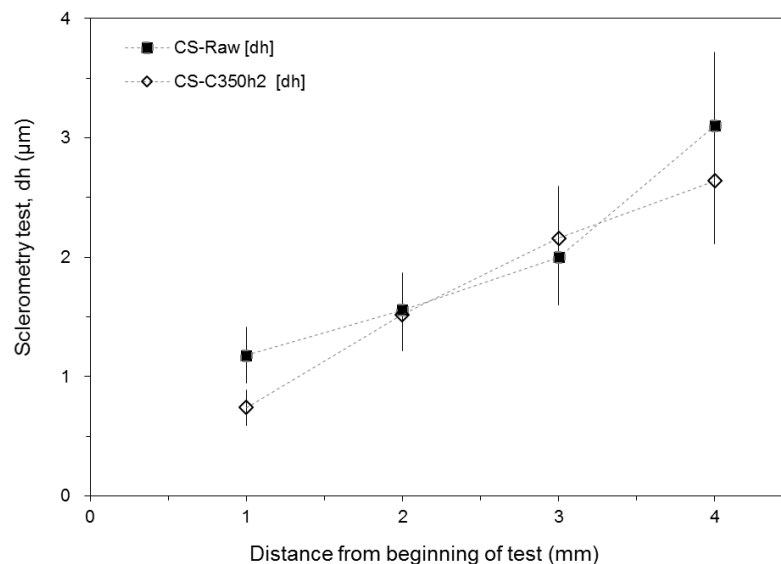


Figure 153: Sclerometry test. Case-Study: As-honed surface specimen. Resulting scratch depth (dh) of condition CS-C350h2 compared to CS-Raw (baseline). $n = 1$, error bars corresponding to the estimated uncertainty (informative).

Figure 154 shows the resulting scratch “groove area” (Ss) of condition CS-C350h2 compared to CS-Raw (baseline), as a function of the distance from beginning of test. Notably until distance $D = 2$ mm, the “groove area” decreased after SPN treatment, as an effect attributed to the increase of surface strength due to plasma nitriding.

In case-study experiment, the resulting “pile-up area” (Sp) after SPN treatment did not follow the same trending as the in-lab textured flat specimens (Figure 108). In the flat specimens, it was not possible to detect any substantial contrast of Sp in relation to baseline and

SPN experimental conditions within the first 2 mm of scratch distance. In the case-study, the resulting “pile-up area” clearly decreased after SPN treatment across the first 3 mm of scratch distance, therefore evidencing lower level of plastic deformation (micro-ploughing zone) in SPN condition with respect to Raw condition.

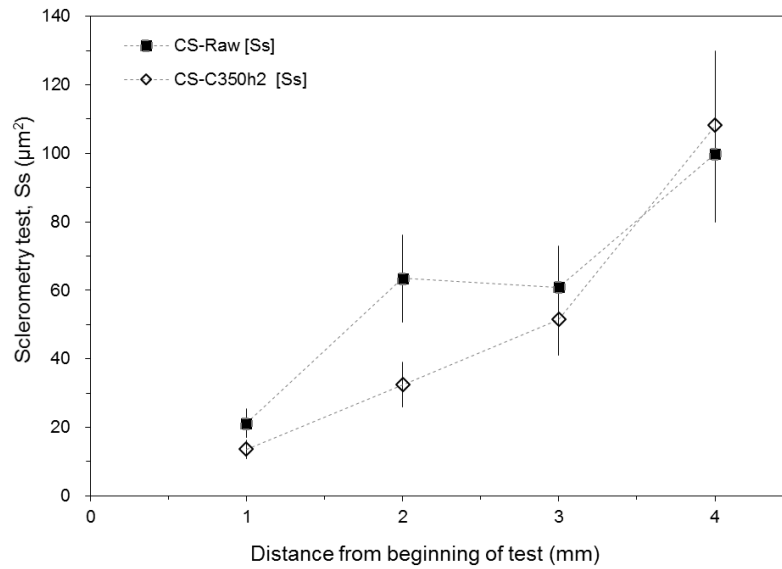


Figure 154: Sclerometry test. Case-Study: As-honed surface specimen. Resulting “groove area” (Ss) of condition CS-C350h2 compared to CS-Raw (baseline). $n = 1$, error bars corresponding to the estimated uncertainty (informative).

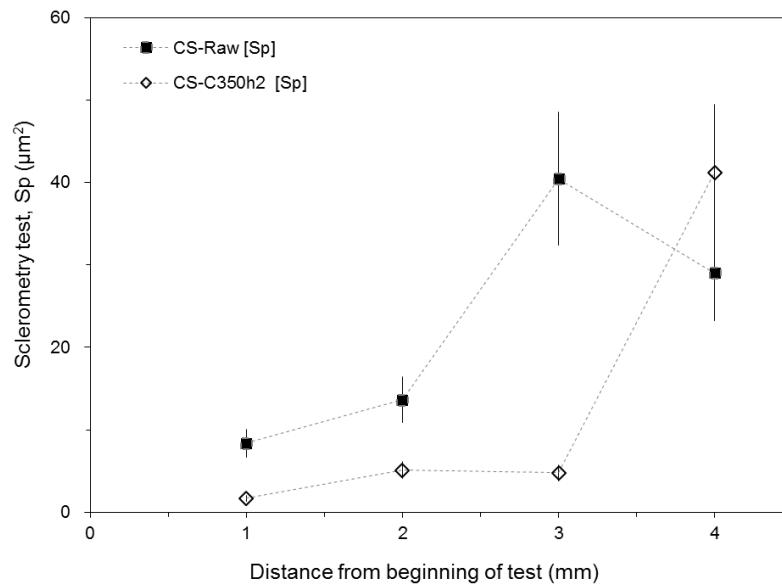


Figure 155: Sclerometry test. Case-Study: As-honed surface specimen. Resulting “pile-up area” (Sp) of condition CS-C350h2 compared to CS-Raw (baseline). $n = 1$, error bars corresponding to the estimated uncertainty (informative).

4.2.5.2. SEM analysis of the scratch and critical load approach in Case-Study

Figure 156 shows the Scanning Electron Microscopy macro view of the textured surface plane and resulting scratch track, in the condition CS-C350h2 compared to CS-Raw (baseline).

The honing texturing marks are visible in the general view images (Figure 156), with the resulting scratch crossing the honing texture along the scratch direction. The scratch width naturally increased with the distance traveled by the indenter, since the normal load applied was increased from 1 N to 10 N. The dashed-line squares of Figure 156 indicate details per distance (1-5 mm) analyzed at higher magnification and shown in Figure 157.

SEM view of the textured surface and resulting scratch track per region, in the condition CS-C350h2 compared to CS-Raw (baseline) is presented in Figure 157. With test direction (t.d.) from left to right, the combined figure shows the side-by-side detailed views at different distances: 1-5 mm, so that the final aspect of the surface after sclerometry test could be assessed in a comparative basis.

Microcracks feature has been observed after shallow plasma nitriding at 350 °C during 2 hours. Detail 1c of Figure 157 indicates the region of the first microcracks at distance around 1 mm. Magnified view of detail 1C showing such tensile microcracks is presented in Figure 159.

The parallel microcracks nucleated in the matrix of the case-study sample (Figure 159) somehow confirmed the previous results obtained with in-lab textured flat specimens (Figure 113, Figure 115, Figure 117, and Figure 119). Again, such response was attributed to the stress state imposed by the indenter during the sclerometry test and repeated the behavior found during in-lab textured specimens. In this region, the cracks found in honed specimen after SPN treatment were isolated from graphite pockets and free from detachment of debris.

The examination of case-study SPN treated sample via SEM has not revealed any sign of significant plastic deformation over the textured surface. Conversely, in the condition raw (before SPN treatment), plastic deformation was observed in the interface region to the texturing grooves, being a general aspect found along the scratch length of the non-treated specimen, as demonstrated in Figure 157a.

Based on a qualitative assessment, the critical load (ASTM C1624-05) [70] for tensile microcracks feature in material matrix was deemed about 2.8 N for experiment CS-C350h2.

Although tensile microcracks were found in material matrix, no spallation feature [70] was observed. The critical load for spallation feature was deemed no lower than 10 N, which indicates honed surface toughness enough to support the abusive load case of the sclerometry test applied herein with no material detachment (delamination).

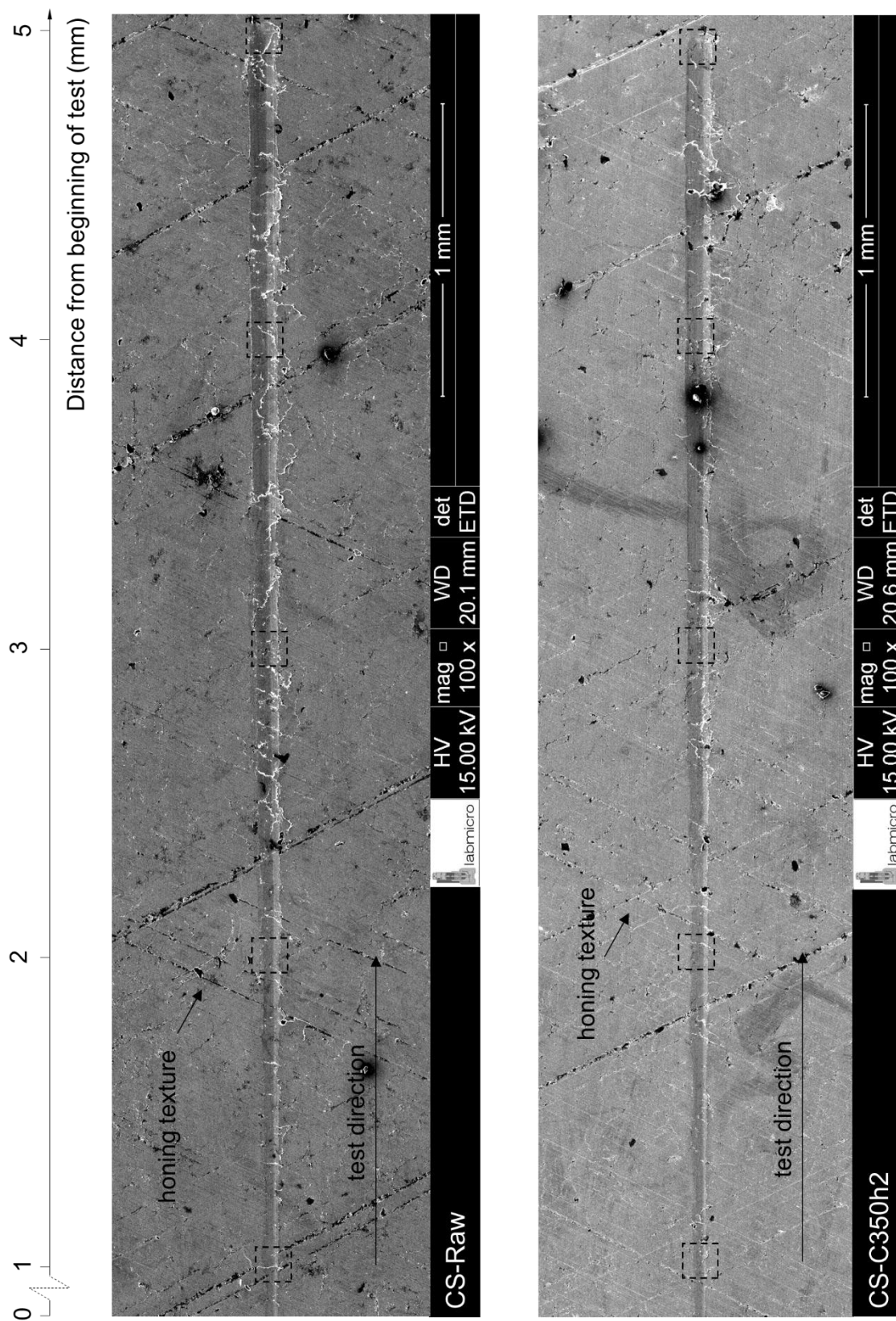


Figure 156: Instrumented linear sclerometry test. Scanning Electron Microscopy view of the textured surface plane and resulting scratch track, in the condition CS-C350h2 compared to CS-Raw (baseline).

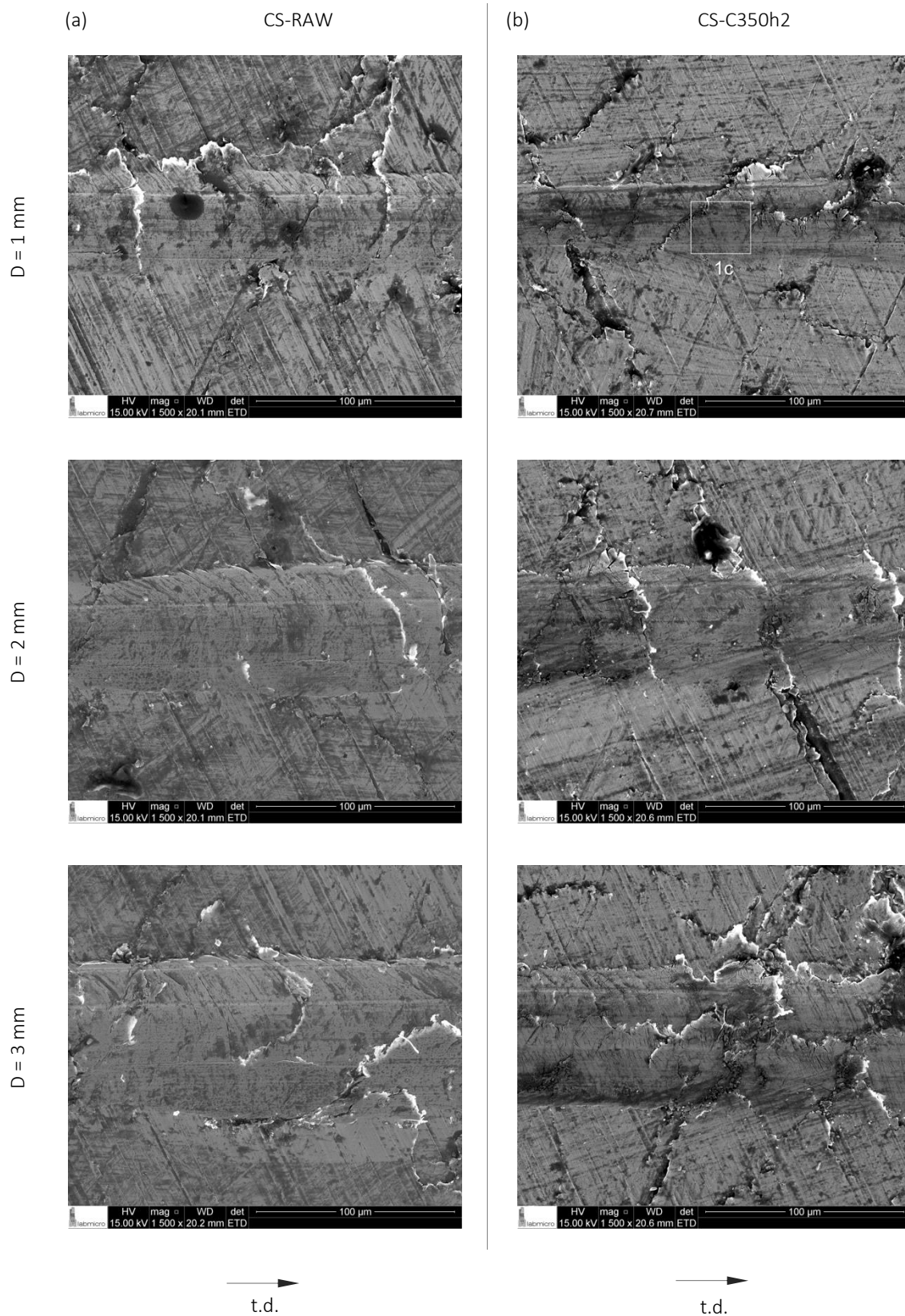


Figure 157: SEM view of the textured surface and resulting scratch track, condition CS-C350h2 compared to CS-Raw (baseline). Test direction (t.d.) from left to right. a-e) Detailed view at different distances: 1-5 mm.

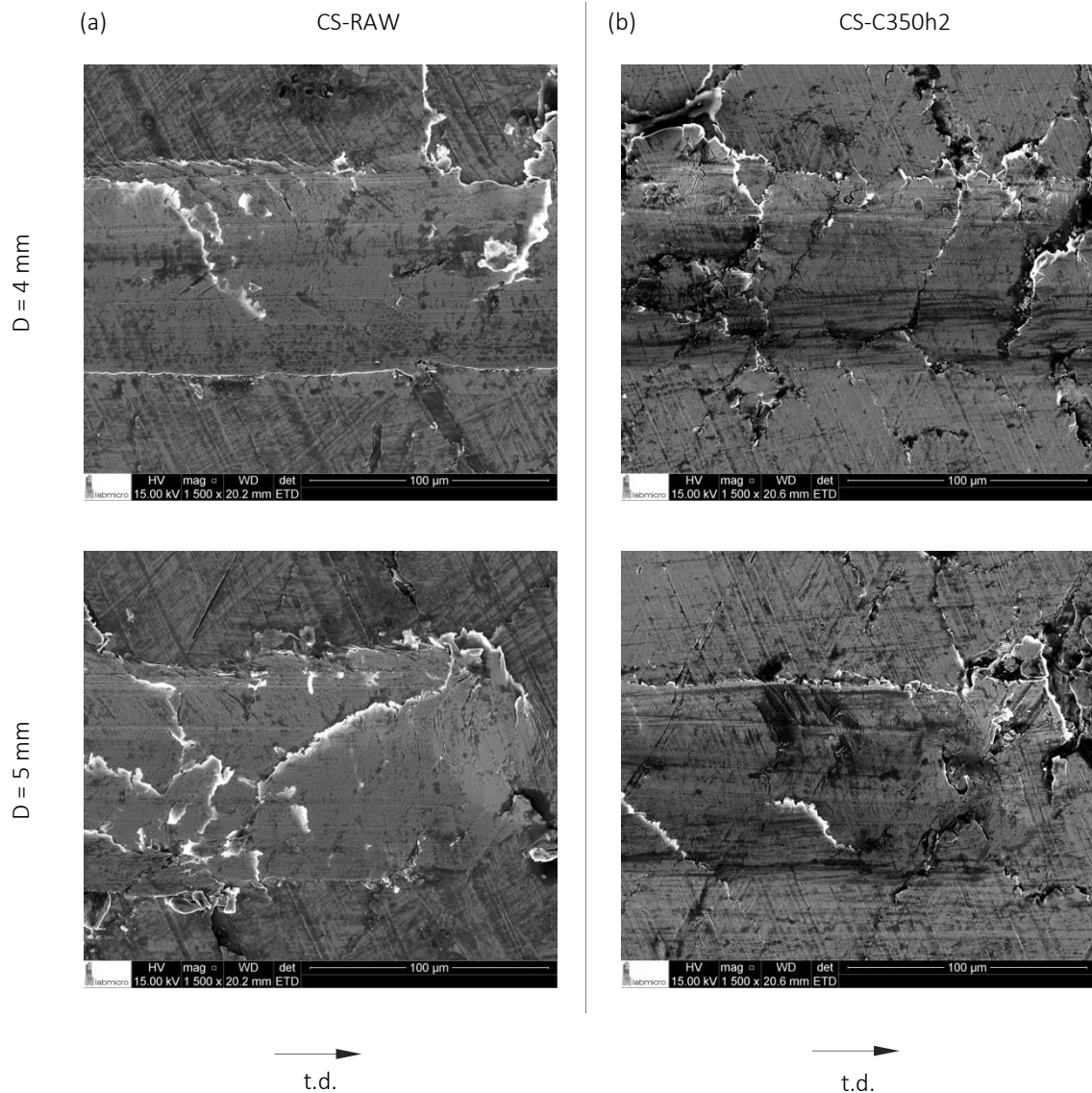


Figure 158 (cont): SEM view of the textured surface and resulting scratch track, condition CS-C350h2 compared to CS-Raw (baseline). All samples: Test direction (t.d.) from left to right. a-e) Detailed view at different distances: 1-5 mm.

Considering a real application, e.g., the cylinder of an internal combustion engine, a degree of toughness associated with the abrasion resistance to prevent spallation is desirable. This is because abrasion is a wear mechanism present in cylinder bores of ICE (Table 4), but large debris is not desirable in the piston ring-cylinder system.

Similar to experiments carried-out using in-lab textured specimens, the sclerometry test applied for as-honed specimens subjected the sample to extreme conditions of progressive load. The load applied by the diamond indenter was dynamically increased, so that local contact pressure was increased with time and distance. Recognizably, the test efforts proposedly exerted to the specimens are far more severe than the explanatory application considered above.

Applying the ASTM C1624-05 [70] terminologies, the microcracks could be classified as brittle tensile cracks of chevron/arc tensile type, straight and semi-circular, formed behind the stylus. The corresponding scratch depth at a 2.8 N L_{c1} load was around 0.7 μm . As shown by the Wavelength-Dispersive Spectroscopy (WDS) microanalysis, the surface is enriched with nitrogen (Figure 135) at this depth, therefore it is in the SPN zone.

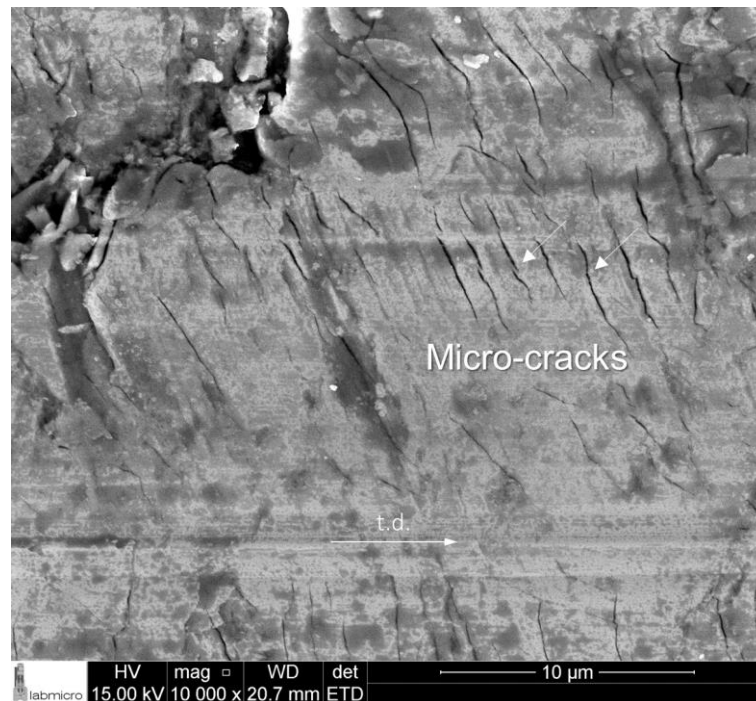


Figure 159: Magnified view (detail 1C of previous figure) showing tensile microcracks at distance around 1 mm, in material matrix region. SEM image. Test direction (t.d.) from left to right. Case-study, CS-C350h2.

4.2.5.3. Friction based on sclerometry test

In order to establish a baseline for SPN results comparison, results in terms of apparent COF from the honed surface in the condition Raw, before SPN treatment, are initially presented in Figure 160. Next, Figure 161 shows the apparent COF graph of the textured surface treated in the condition CS-C350h2.

As described beforehand, during the sclerometry test, the as-honed surface specimen was submitted to 1N pre-load applied during 10s. Next, indenter was linearly moved increasing load, 1N to 10N, with velocity of 0.028 mm/s, during 180 s, resulting in the scratch of 5 mm in length. Because of the fact the test stabilization was comprehended into first 40 s (dashed line), such graph zone was not considered in any data analysis.

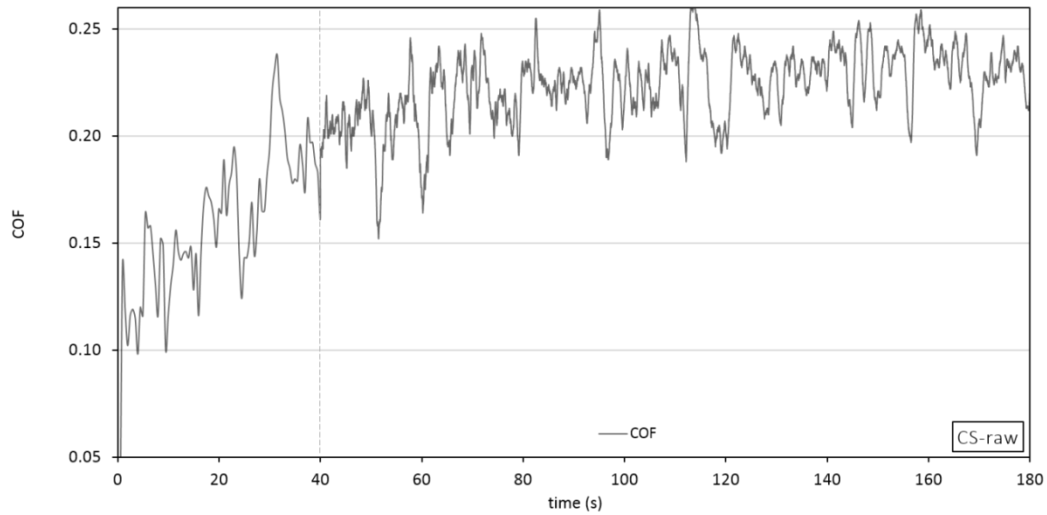


Figure 160: Apparent COF of the textured surface in condition Raw, before SPN treatment. Case study: As-honed surface specimen. 1N pre-load applied during 10s. Next, indenter was linearly moved increasing load, 1N to 10N, with velocity of 0.028 mm/s, during 180 s, resulting in the scratch of 5 mm in length. The test stabilization was comprehended into first 40 s (dashed line) and is not considered in data analysis.

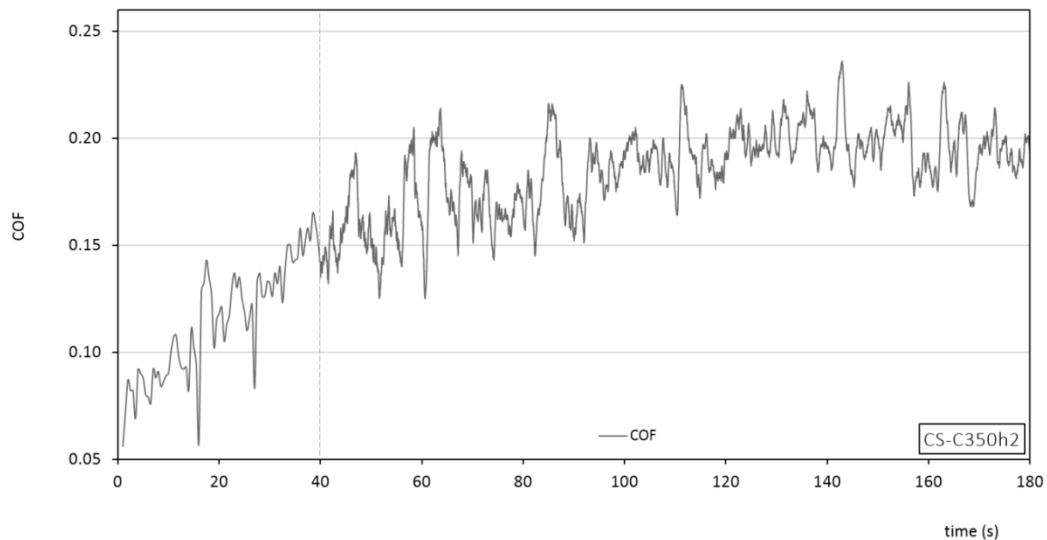


Figure 161: Apparent COF of the textured surface in condition CS-C350h2. Case study: As-honed surface specimen. 1N pre-load applied during 10s. Next, indenter was linearly moved increasing load, 1N to 10N, with velocity of 0.028 mm/s, during 180 s, resulting in the scratch of 5 mm in length. The test stabilization was comprehended into first 40 s (dashed line) and is not considered in data analysis. Comparing to raw condition, the apparent COF decreased after SPN treatment.

The apparent COF measured through sclerometry was decreased by about 25% after shallow plasma nitriding treatment. This fact was evidenced through the Figure 162, which shows the Apparent COF as a function of time and load, including the respective linear regression line.

Such behavior could be attributed to the iron nitride formation [69], whose three legs morphology [69] and superior hardness would play a role to reduce the friction of the matrix in contact with the indenter.

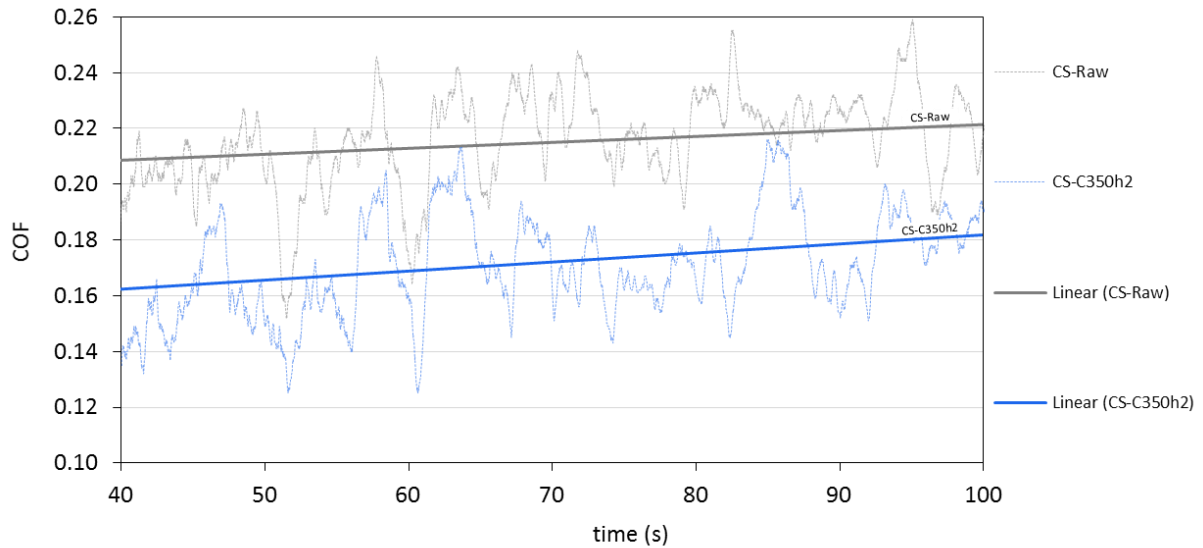


Figure 162: Apparent COF of the textured surface. Combined chart: CS-Raw and CS-C350h2, including the respective linear regression line. As-honed surface specimen.

4.2.6. Summary of the Case-Study

The SPN treatment promoted N-enrichment at shallow depths from the surface. The X-Ray diffraction analysis confirmed that ϵ -nitride (Fe_3N) was formed. As a result, the microhardness of the sample surface was enhanced.

The peak roughness (S_{pk}) number somewhat increased after the SPN treatment, whereas S_k and S_{vk} either increased or decreased. Whatever the sample area, the maximum roughness increment observed was lower than $0.08 \mu\text{m}$.

Using XRD analysis, ϵ -nitride (Fe_3N) was identified in the condition after shallow plasma nitriding process, matching with both results of microhardness and WDS microanalysis of nitrogen enrichment at shallow depths of the surface.

The apparent COF has decreased after shallow plasma nitriding (SPN) treatment. Consequently, friction force under the tested condition has also decreased.

The groove area, as well as the pile-up area, decreased after SPN. First microcracks were identified at distance approximately equal to 1 mm, with corresponding critical load of 2.8 N and scratch depth of about $0.7 \mu\text{m}$.

Although the tensile microcracks found in material matrix as a result of the progressive testing load, no spallation feature was observed. This is an indication that honed surface had enough toughness to support the abusive load case of the sclerometry test applied with no material detachment (delamination). This approach suggests that such treatment is proper for smooth honing finishing applications, e.g., plateau honing cylinder bores.

There were minimal differences of roughness texture before and after SPN treatment. The results obtained from the researched application suggest feasibility for SPN employment in pre-textured pearlitic cast iron components.

The effects of the shallow plasma nitriding process applied in a pre-textured pearlitic GCI specimen extracted from ICE cylinder were assessed by virtue of well-established analysis methods. Results demonstrated that the roughness texture pattern was satisfactorily preserved after N-enrichment and consequent formation of ϵ -nitride (Fe_3N).

4.3. Synthesis

In general, the height of peaks above the core surface – “peak roughness” (S_{pk}) - tended to increase after SPN treatment. As the SPN temperature increased from 350 °C to 400 °C, the final peak roughness (S_{pk}) also tended to increase. Changes on the other roughness parameters assessed were negligible.

Previous works, e.g., [62], performed in GCI at higher temperature-time levels resulted in expressive surface roughness increase after treatment. The relative low temperature-time adopted in the present work represented a key factor to control the peak roughness response after plasma nitriding treatments. In the case-study, which has been performed at 350 °C during 2h, the marginal growing of final peak roughness (S_{pk}) reproduced the tendencies verified with in-lab textured flat specimens.

The surface texture at final state tended to follow the topography pattern at initial state, as demonstrated by the statistical analysis. Surface aspects assessed via Scanning Electronic Microscopy confirmed that texture remained preserved after SPN treatments. Similar behavior has been verified in case-study of industrially honed samples extracted from engine cylinder block. After shallow plasma nitriding treatment, the honing texture remained preserved. Supplementary data specifically from cylinder block honed samples treated in plasma nitriding conditions were not identified in available literature, although there are clear indications that texture pattern is sensitive to temperature-time conditions of the plasma nitriding [62].

Influence of temperature and time on the nitrogen concentration as a function of distance from surface has been assessed via Wavelength-Dispersive X-Ray Spectroscopy (WDS). As expected, concentration of nitrogen decreased with distance from surface, with shallow depth of penetration. Previous work [67], also using WDS microanalysis, performed quantitative characterization of nitrogen concentration gradient as a function of distance of penetration after plasma nitriding.

Confirmation of shallow depth nitrogen enrichment in cast iron was also assessed considering a potential application - engine cylinder bore honed sample. Here, the N-content was assessed both through quantitative (WDS) and qualitative (EDS) technics. Therefore, the adherence of in-lab textured flat specimens results with respect to as-honed textured specimen has been documented accordingly.

As the SPN temperature-time increased, the intensity of ϵ -nitride peaks characterized through X-ray diffraction technics have also increased. Previous works, e.g., [64], also characterized ϵ -nitride peaks in pearlite matrix via XRD technics. The samples had also been treated in N_2-H_2 plasma atmosphere. Accordingly, here ϵ -nitride peaks were identified in a comparative basis to a raw sample in the case-study section. The findings confirmed the SPN treatment feasibility to form ϵ -nitride in a potential application with minimum level of temperature and time.

On the effect of SPN treatment on microhardness, results demonstrated that hardness increased significantly with SPN treatment. As the treatment temperature increased from 350 °C to 400 °C, the final surface hardness also tended to increase, showing some degree of correlation between SPN temperature and final hardness.

Surface hardness increasing of GCI samples treated in N_2-H_2 plasma atmosphere has also been documented in previous work [60]. Similar behavior verified through the study of in-lab textured flat specimens has also been confirmed in case-study of industrially honed sample extracted from cylinder block.

On the sclerometry test response, at shallow depths, “groove area” (S_s) and scratch depth (dh) clearly decreased after SPN treatment, as an effect attributed to the increase of surface strength due to plasma nitriding. In the flat specimens, it was not possible to detect any substantial contrast of “pile-up area” (S_p) after SPN. Previous work [76] also characterized the groove profile resulting from the sclerometry test of GCI samples through 3-D interference measurements. As highlighted in [76], the material close the indenter is in fact compressed plastically so that some fraction of the ‘lost’ material is not actually removed from the solid.

In addition, the deformation energy implied by the indenter - at least partially - are

somewhat consumed during damage events, such as the tensile cracks nucleation and growth, that has been evidenced herein during post-test characterization of both in-lab textured flat specimens and as-honed textured specimens.

Tensile microcracks damage mode characterized for both in-lab textured flat specimens and case-study. Based on a qualitative assessment, the critical load [70] for tensile microcracks feature in material matrix was deemed from 2.8 N to 4.6N depending on the experimental condition. As the SPN temperature increased from 350 °C to 400 °C, the estimated critical damage load also tended to increase from 2.8N to 4.6N. Previous work [101] applying similar instrumented linear sclerometry test procedure in plasma nitriding specimens had also indicated damage mode of tensile microcracks.

In spite of the resulting tensile microcracks found in material matrix in all experimental conditions, no spallation feature [70] has been observed. Therefore, critical load for spallation feature was deemed as higher than 10 N, which indicated surface toughness enough to support the abusive load case of the sclerometry test applied with no material detachment.

Similar sclerometry test response has been confirmed in the industrially honed samples extracted from engine cylinder block, with critical damage load estimated in 2.8N.

In general, the apparent COF measured through instrument linear sclerometry test approach tended to decrease after shallow plasma nitriding (SPN) treatment. Such behavior was attributed to the iron nitride formation [69], whose morphology [69] and superior hardness would play a role to reduce the friction of the matrix in contact with the indenter. In addition, previous works, e.g., [75], had also successfully applied linear sclerometry in GCI, in order to analyze the aspects related to friction, scratch geometry and the graphite.

Similar behavior with respect to friction response before/after SPN treatment was confirmed in honed samples extracted from engine cylinder block.

4.3.1. Synthesis board

A synthesis board consolidating the main findings of the present study is shown in Table 30. The board comprises the aspects approached through the research of plasma-assisted modifications of pre-textured surfaces applying shallow depth nitriding in cast iron.

Topography and instrumented sclerometry test response along with characterization outcomes are briefly commented. In addition, associated case-study response and an example of previous work reference are commented next to each main finding of a listed aspect.

Table 30: Synthesis Board

Aspect	Main Findings	Case-study response	Previous work info
Effect of SPN treatment on topography (I)	<p>On the influence of temperature-time:</p> <p>The peak roughness (Spk) tended to increase after SPN treatment.</p> <p>As the SPN temperature increased from 350 °C to 400 °C, the final peak roughness (Spk) also tended to increase.</p> <p>Experiment at 350 °C 2h did not produce significant statistical changes of peak height data average. In such condition, increase of Spk was marginal.</p>	<p>The case-study was performed at 350 °C 2h temperature-time level.</p> <p>Marginal growth of peak roughness (Spk) reproduced the tendency previously verified with in-lab textured flat specimens.</p>	<p>Previous work [62] performed in GCI at higher temperature-time levels resulted in expressive surface roughness increasing after treatment.</p>
Effect of SPN treatment on topography (II)	<p>On the topography state:</p> <p>The final texturing state tended to follow the initial topography pattern.</p> <p>Surface aspects assessed via SEM confirmed that texture remained preserved after SPN treatments.</p>	<p>Similar behavior verified in case-study of industrially honed samples extracted from cylinder block.</p> <p>After SPN, the honing texture remained preserved.</p>	<p>Comparable data of engine cylinder block (as-honed samples) treated in similar conditions of present study, have not been identified in available literature.</p>

Aspect	Main Findings	Case-study response	Previous work info
Nitrogen content as a function of depth from surface	<p>Influence of temperature and time on the nitrogen concentration as a function of distance from surface was assessed via WDS microanalysis.</p> <p>Nitrogen concentration decreased with distance from surface, with shallow depth of penetration.</p>	<p>Confirmation of shallow depth nitrogen enrichment in cast iron.</p> <p>A potential application - engine cylinder bore honed sample - was assessed via both WDS and EDS technics.</p>	<p>Previous work [67] using WDS reported gradient of nitrogen concentration as a function of distance of penetration after plasma nitriding.</p>
Nitride peaks identified through XRD analysis	<p>As the SPN temperature-time increased, the intensity of XRD ϵ-nitride peaks also tended to increase.</p>	<p>Confirmation in a potential application with minimum level of temperature and time, where ϵ-nitride peaks were identified in a comparative basis.</p>	<p>Previous work [64] characterized ϵ-nitride peaks via XRD technics. The samples had also been treated in N_2-H_2 plasma atmosphere.</p>
Effect of SPN treatment on microhardness	<p>The hardness increased significantly with SPN treatment.</p> <p>As the SPN temperature increased from 350 °C to 400 °C, the final surface hardness also tended to increase.</p>	<p>Similar behavior verified in case-study of industrially honed sample extracted from cylinder block.</p> <p>After SPN, the final surface hardness increased substantially.</p>	<p>Previous work [60] documented surface hardness increasing of GCI samples treated in N_2-H_2 plasma atmosphere.</p>

Aspect	Main Findings	Case-study response	Previous work info
Sclerometry test response (I)	<p>On the “Pile-up area” (Sp), “groove area” (Ss) and scratch depth (dh):</p> <p>At shallow depths, Ss and dh decreased after SPN treatment, as an effect attributed to the increase of surface strength due to plasma nitriding.</p> <p>In the flat specimens, it was not possible to detect any substantial contrast of Sp after SPN.</p>	<p>With regard to Ss and dh, similar behavior was verified in industrially honed samples, with Ss and dh decreasing at shallow depths after SPN treatment.</p> <p>Resulting “pile-up area” (Sp) decreased after SPN treatment across the first range of scratch distance, evidencing lower level of micro-ploughing zone.</p>	<p>Previous work [76] characterized the groove profile resulting from the sclerometry test of GCI samples through 3-D interference measurements.</p>
Sclerometry test response (II)	<p>On the SEM analysis of the scratch and critical load approach:</p> <p>As the SPN temperature increased from 350 °C to 400 °C, the estimated critical damage load also tended to increase from 2.8N to 4.6N.</p>	<p>Tensile cracks damage mode.</p> <p>Similar type of damage mode verified in industrially honed samples extracted from cylinder block, with critical damage load estimated in 2.8N.</p>	<p>Previous work [72,101] also reported tensile cracks damage mode, assessed via linear sclerometry test.</p>
Sclerometry test response (III)	<p>On the friction response based on sclerometry test:</p> <p>The apparent COF tended to decrease after shallow plasma nitriding (SPN) treatment.</p>	<p>Similar behavior with respect to friction in honed samples extracted from cylinder block.</p>	<p>Previous work [72,75] applied linear sclerometry in GCI, in order to analyze aspects related to friction, scratch geometry and the graphite.</p>

5. Conclusions

An alternative of plasma-assisted treatment to enhance pre-textured surfaces made of gray cast iron was studied. The treatment – termed shallow plasma nitriding (SPN) - was performed in the laboratorial installations of the University of São Paulo (USP). The specimens were produced from engine cylinder blocks of the automotive industry (GM).

In-lab textured specimens were treated at relative low temperature and short time conditions. Testing and characterization were performed in the laboratories of USP and GM. Assessment of responses included 3-D topography and instrumented linear sclerometry test.

In addition, the potential for extensive usage of SPN was approached by applying one of the experimental conditions in an industrial component. The sample had its surface textured by plateau honing process, and was considered as an example of surface to be enhanced.

Within the scope of test and analysis of this work, the following conclusions were drawn:

- The height of peaks above the core surface (Spk) tends to increase after SPN. The intensity of growth of pre-existent peaks is related to temperature-time of plasma treatment. Changes of peaks material ratio (Sr1) follows similar trends as Spk, but with lower intensity. Therefore, the development of new peaks is less frequent than the growth of existent ones.
- The treatment performed at 350 °C for 2h does not produce significant changes of statistical distribution average (mean) of peak height data (Spk). In such condition, the increase of Spk is marginal, whereas increase of data variability is a general tendency.
- SEM observations of surface appearance demonstrate that texture pattern is satisfactorily preserved after SPN. The sequence of well-marked parallel grooves reflects the 3-D interferometry results. Graphite pockets are still visible after experiments, and there are no significant differences between results at different temperature-time conditions.
- WDS microanalysis demonstrated that N-content decreases monotonically from high values at top of surfaces ($N > 9$ wt%) until it tends to zero wt% at 5 μm of distance, therefore constituting nitrogen enrichment at shallow depths. Beyond 3 μm of depth, the change of curve slope shows that gradient of nitrogen is reduced beyond such distance, indicating transition between diffusion zone and core material.
- XRD analysis evidenced a progressive increase of ϵ -nitride phase as a function of the experimental temperature-time condition. This result is consistent with the WDS data of N-content, hence confirming the modification of the pre-textured surfaces via shallow plasma

nitriding, with the N-enrichment with consequent formation of ϵ -nitride (Fe_3N) phase.

- Surface microhardness increases significantly with SPN treatment. As the SPN temperature increased from 350 °C to 400 °C, the final surface hardness tended to increase. SPN time does not appear to affect significantly the range of hardness response values.
- Microhardness results are consistent with both XRD patterns and WDS microanalysis results. Based on the nitrogen concentration profile, the hardness indentation depth is located within the N-enriched zone.
- At shallow depths of all assessed conditions, the “groove area” (S_s) and depth (dh) of scratch produced during instrumented sclerometry test, decrease after SPN treatment. Such effect was attributed to the increase of surface strength due to plasma nitriding. In the flat specimens, it was not possible to detect any substantial contrast of S_p after SPN.
- SEM analysis of the scratch produced by sclerometry test indicates that, as the SPN temperature increases from 350 °C to 400 °C, the estimated critical damage load also tends to increase from 2.8N to 4.6N.
- Tensile microcracks is the predominant damage mode revealed during examination of scratch track via SEM. The density of cracks increases with indenter load and test distance. The absence of spallation feature indicates surface toughness enough to support the load case of the sclerometry test with no material detachment.
- The apparent COF measured through sclerometry decreased after SPN. Such response indicates lower energy consumption during the test, and is attributed to the iron nitride formation, that plays a role to reduce the friction between material matrix and indenter.
- The case-study performed at 350 °C 2h satisfactorily reproduced the behaviors previously verified with in-lab textured flat specimens, in terms of testing and analysis outcome.

Microhardness measurements and instrumented linear sclerometry test (‘scratch test’) results indicated that ϵ -iron nitride formation and solid solution hardening could provide enhanced properties to the surface of general pearlitic cast iron components, such as increase of wear resistance, and decrease of apparent coefficient of friction, in the assessed conditions.

Nitrogen profile characterized by consistent microanalysis methodology - wavelength dispersive X-Ray spectroscopy - confirmed N-enrichment occurring at shallow depth, whereas the formation of ϵ -nitride was evidenced by X-Ray diffraction patterns.

The effects of the SPN process applied in pre-textured GCI specimens were assessed by well-established analysis methods. Under the conditions studied, it was demonstrated that texture pattern was preserved after N-enrichment and consequent formation of ϵ -nitride (Fe_3N). Therefore, the treatment was considered suitable for micrometric scale topography surfaces.

6. Suggestions for future research

The thesis results point out opportunities for future research:

- (1) Investigate the effect of SPN on friction and wear behaviors of GCI pre-textured specimens, assessed in a ring-on-cylinder test [112] under boundary, mixed, and hydrodynamic lubrication regimes. The tests will be performed using in-lab textured flat specimens, and as-honed cylindrical surface of an internal combustion engine cylinder.

- (2) Assess one or more conditions of SPN described herein on internal combustion engine cylinders submitted to dynamometer durability tests [58]. Verify gains in performance due to lower friction, and quantify the complete bore wear applying novel measurement techniques [113], via comparative computational analysis of material ratio curves.

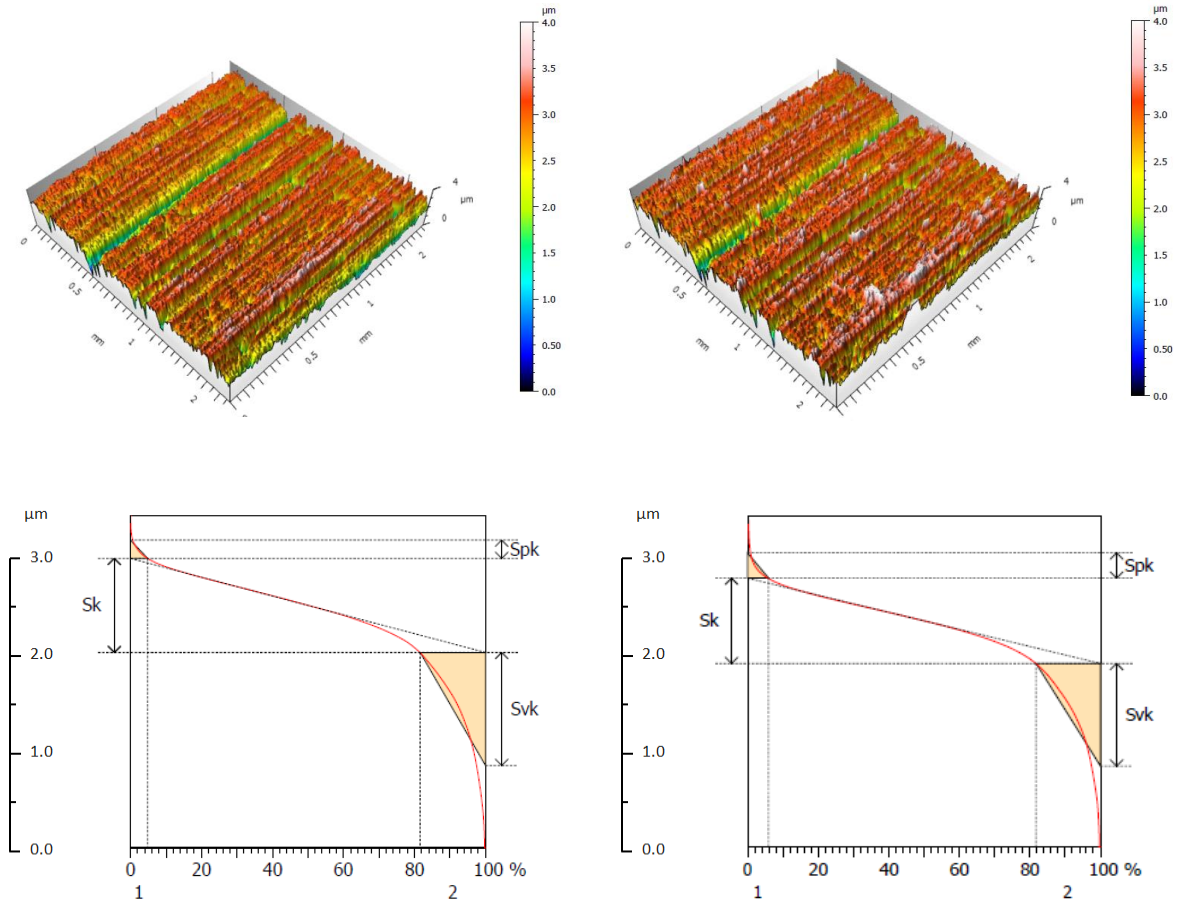
Appendix A - 3-D roughness results: Supplement of Chapter 4

Experiment E1 (400 °C 4 h)

Sample 02 (s2)

(a) Before SPN

(b) After SPN



Parameters	Value	Unit
Sk	1.074	μm
Spk	0.2094	μm
Svk	1.291	μm
Sr1	4.814	%
Sr2	81.56	%

Parameters	Value	Unit
Sk	1.080	μm
Spk	0.3195	μm
Svk	1.299	μm
Sr1	5.886	%
Sr2	81.74	%

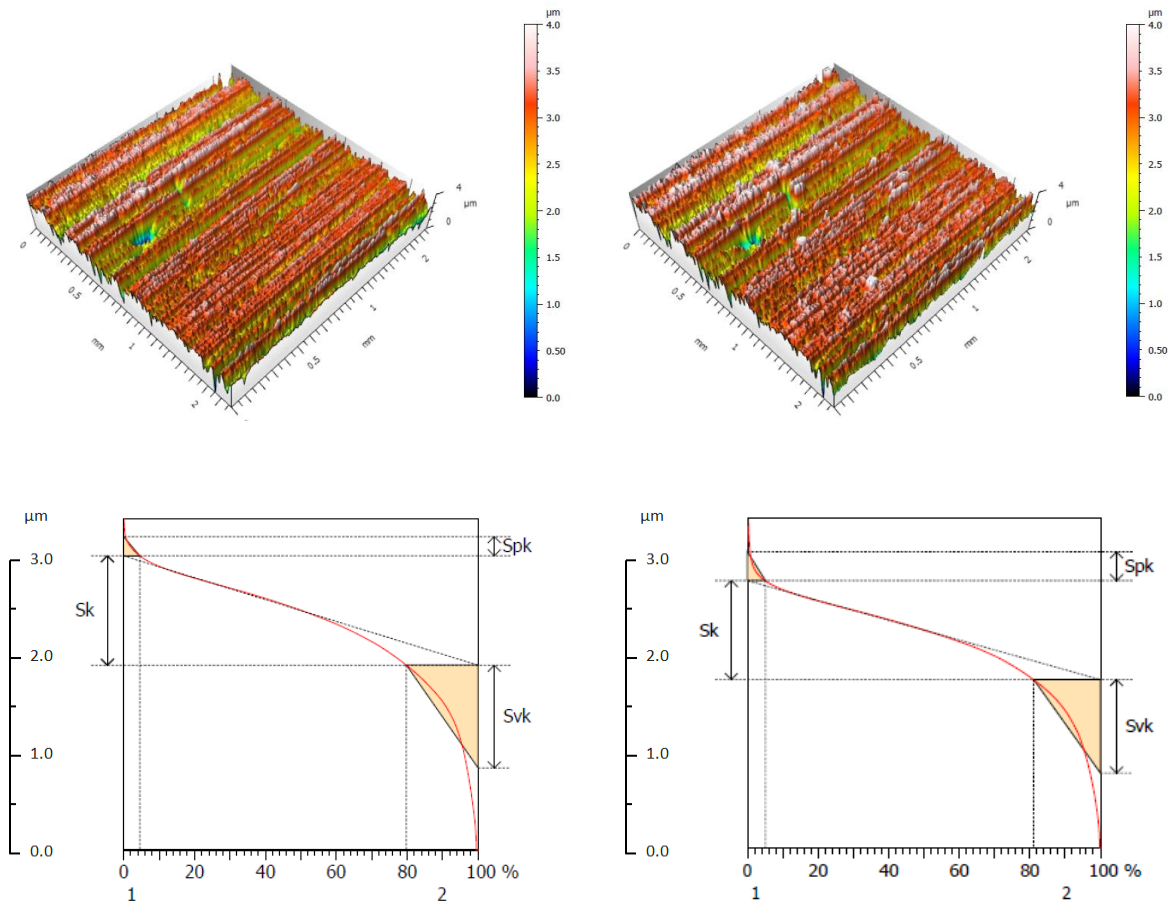
Figure A1: Experiment E1 (400 °C 4 h). Sample 02 (s2) - coordinates x, y = 7.0, 5.0 mm, sampling area = 1.6 x 1.6 μm. 3-D surface profile and material ratio curve. Conditions before (a) and after treatment (b).

Experiment E1 (400 °C 4 h)

Sample 03 (s3)

(a) Before SPN

(b) After SPN



Parameters	Value	Unit
Sk	1.315	µm
Spk	0.2316	µm
Svk	1.236	µm
Sr1	4.567	%
Sr2	79.77	%

Parameters	Value	Unit
Sk	1.345	µm
Spk	0.3919	µm
Svk	1.271	µm
Sr1	5.080	%
Sr2	81.08	%

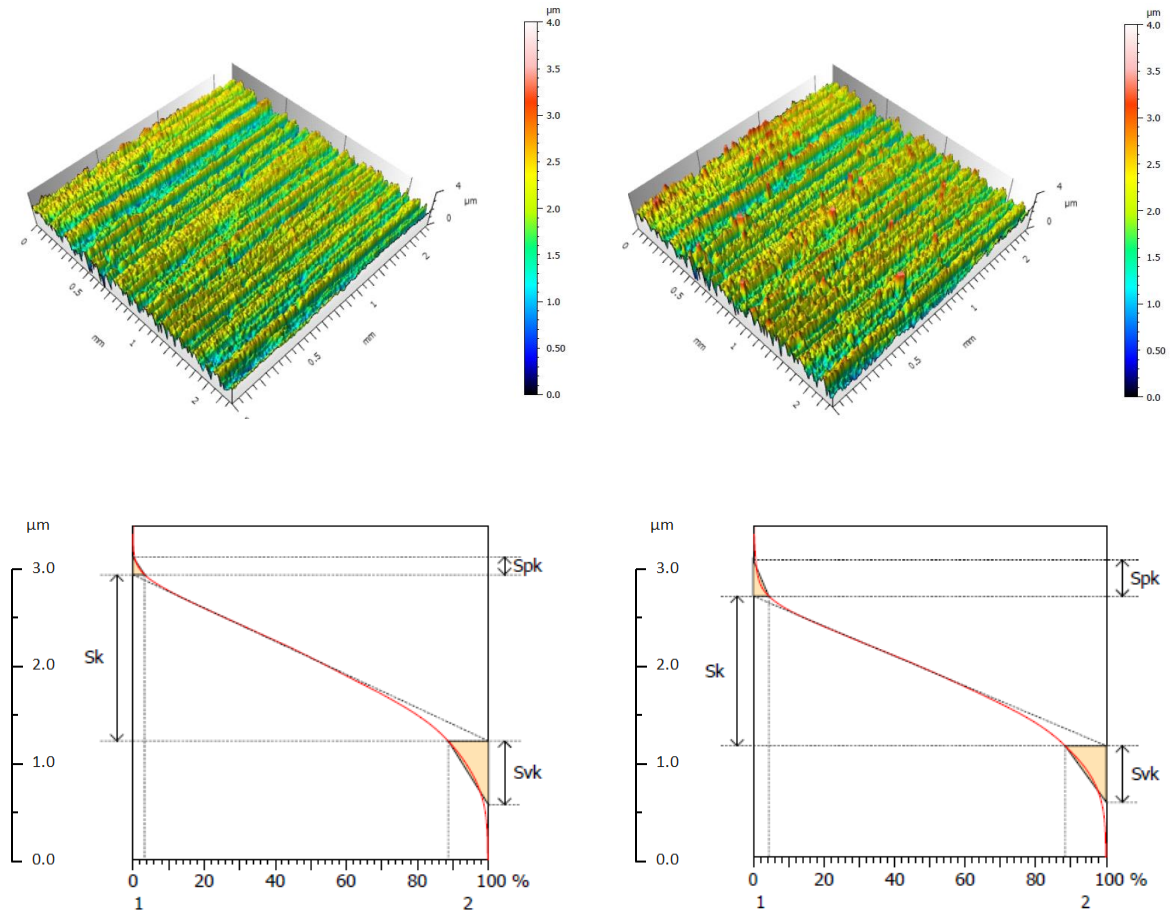
Figure A2: Experiment E1 (400 °C 4 h). Sample 03 (s3) - coordinates x, y = 9.0, 5.0 mm, sampling area = 1.6 x 1.6 µm. 3-D surface profile and material ratio curve. Conditions before (a) and after treatment (b).

Experiment E1 (400 °C 4 h)

Sample 04 (s4)

(a) Before SPN

(b) After SPN



Parameters	Value	Unit
S_k	1.474	μm
S_{pk}	0.1563	μm
S_{vk}	0.5650	μm
Sr_1	3.250	%
Sr_2	88.75	%

Parameters	Value	Unit
S_k	1.505	μm
S_{pk}	0.3633	μm
S_{vk}	0.5676	μm
Sr_1	4.408	%
Sr_2	88.36	%

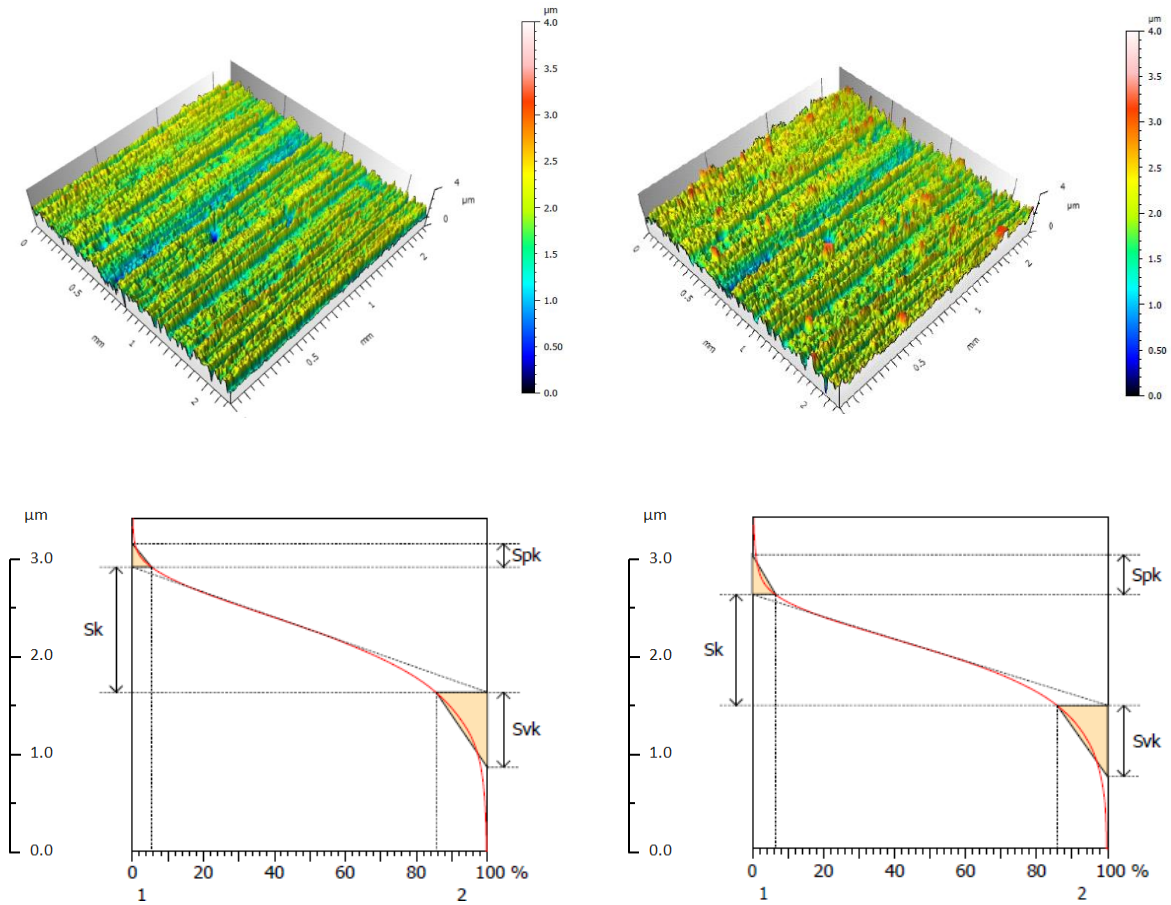
Figure A3: Experiment E1 (400 °C 4 h). Sample 04 (s4) - coordinates $x, y = 11.0, 5.0$ mm, sampling area = 1.6×1.6 μm . 3-D surface profile and material ratio curve. Conditions before (a) and after treatment (b).

Experiment E1 (400 °C 4 h)

Sample 05 (s5)

(a) Before SPN

(b) After SPN



Parameters	Value	Unit
Sk	1.018	μm
Spk	0.1894	μm
Svk	0.6110	μm
Sr1	5.398	%
Sr2	85.65	%

Parameters	Value	Unit
Sk	1.050	μm
Spk	0.3751	μm
Svk	0.6749	μm
Sr1	6.538	%
Sr2	85.84	%

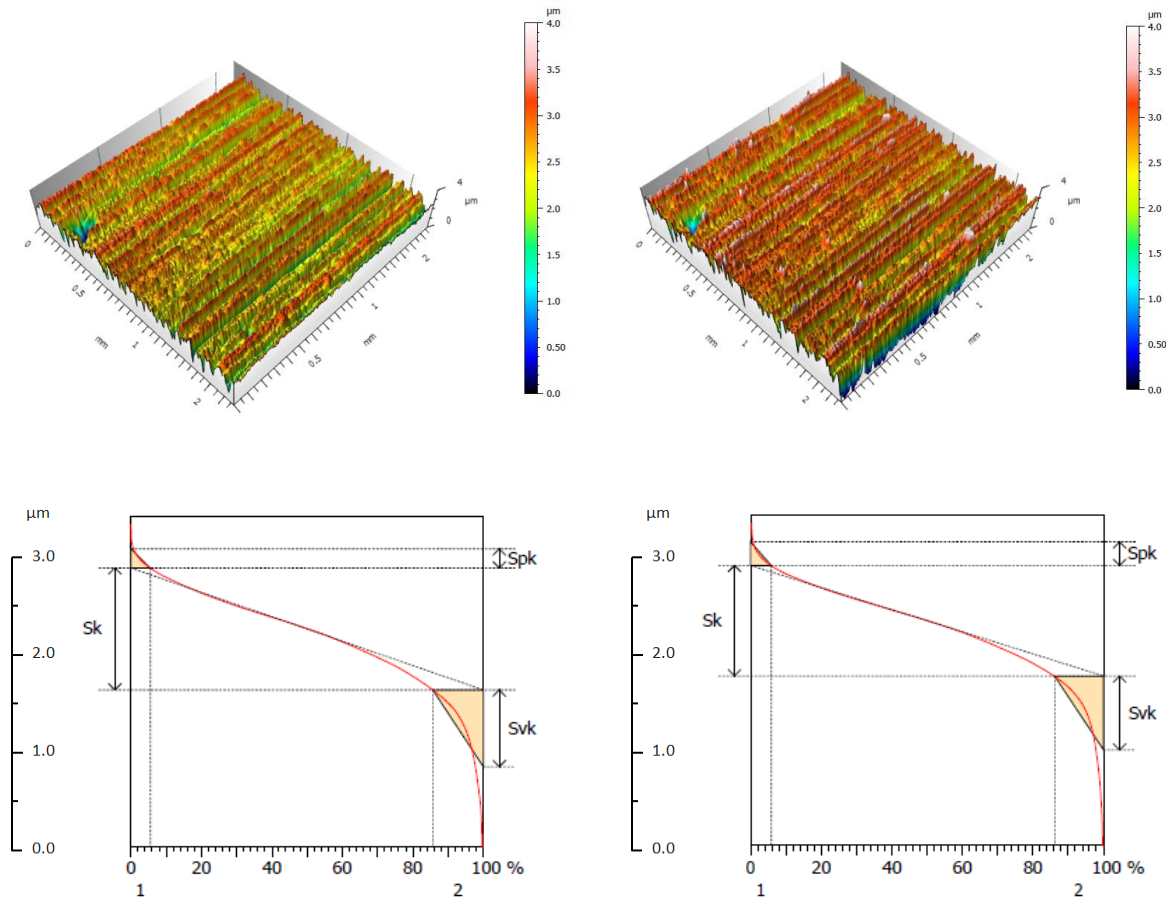
Figure A4: Experiment E1 (400 °C 4 h). Sample 05 (s5) - coordinates x, y = 13.0, 5.0 mm, sampling area = 1.6 x 1.6 μm. 3-D surface profile and material ratio curve. Conditions before (a) and after treatment (b).

Experiment E2 (400 °C 2 h)

Sample 02 (s2)

(a) Before SPN

(b) After SPN



Parameters	Value	Unit
Sk	1.337	μm
Spk	0.2087	μm
Svk	0.8412	μm
Sr1	5.506	%
Sr2	85.71	%

Parameters	Value	Unit
Sk	1.299	μm
Spk	0.2770	μm
Svk	0.8704	μm
Sr1	5.837	%
Sr2	86.14	%

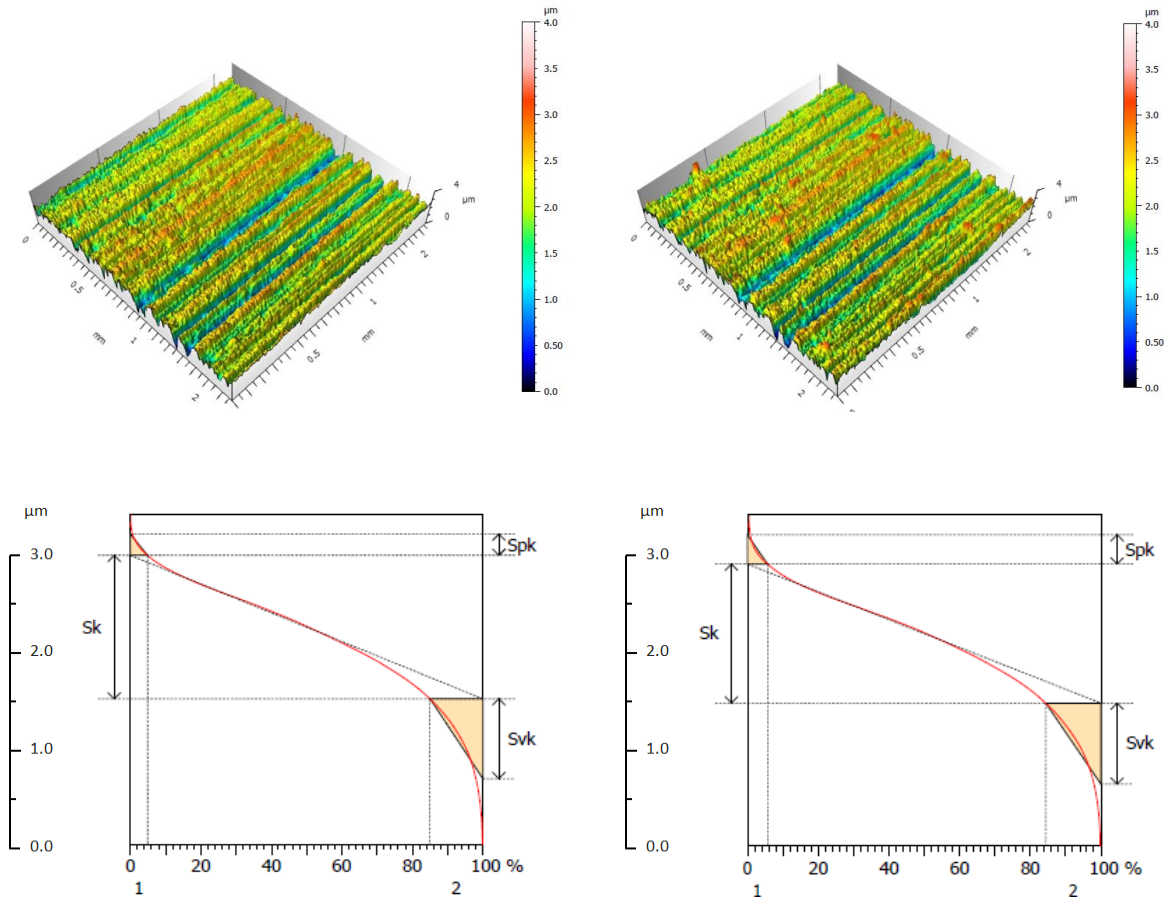
Figure A5: Experiment E2 (400 °C 2 h). Sample 02 (s2) - coordinates x, y = 7.0, 5.0 mm, sampling area = 1.6 x 1.6 μm. 3-D surface profile and material ratio curve. Conditions before (a) and after treatment (b).

Experiment E2 (400 °C 2 h)

Sample 03 (s3)

(a) Before SPN

(b) After SPN



Parameters	Value	Unit
Sk	1.301	µm
Spk	0.1926	µm
Svk	0.7232	µm
Sr1	4.897	%
Sr2	85.00	%

Parameters	Value	Unit
Sk	1.282	µm
Spk	0.2697	µm
Svk	0.7478	µm
Sr1	5.694	%
Sr2	84.39	%

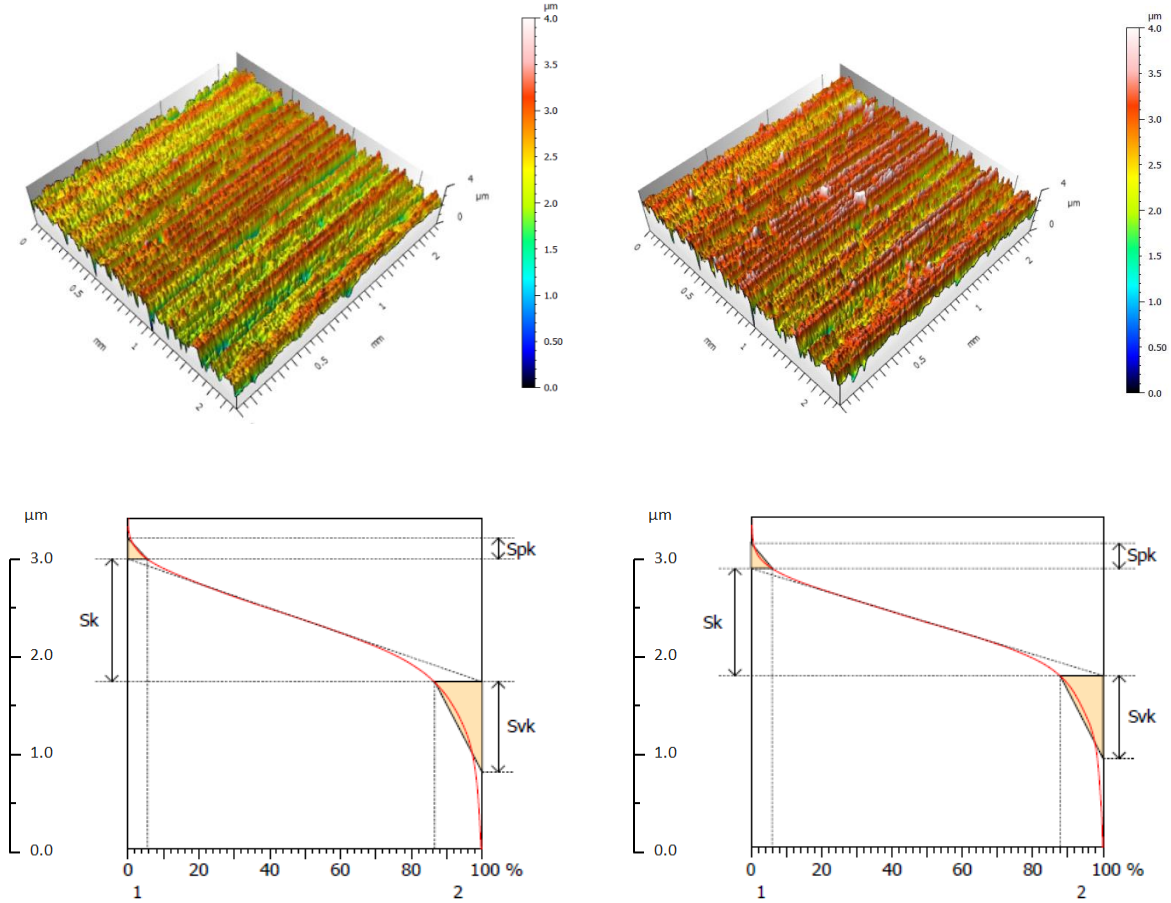
Figure A6: Experiment E2 (400 °C 2 h). Sample 03 (s3) - coordinates x, y = 9.0, 5.0 mm, sampling area = 1.6 x 1.6 µm. 3-D surface profile and material ratio curve. Conditions before (a) and after treatment (b).

Experiment E2 (400 °C 2 h)

Sample 04 (s4)

(a) Before SPN

(b) After SPN



Parameters	Value	Unit
Sk	1.294	μm
Spk	0.2196	μm
Svk	0.9527	μm
Sr1	5.473	%
Sr2	86.62	%

Parameters	Value	Unit
Sk	1.283	μm
Spk	0.3028	μm
Svk	0.9926	μm
Sr1	6.025	%
Sr2	87.83	%

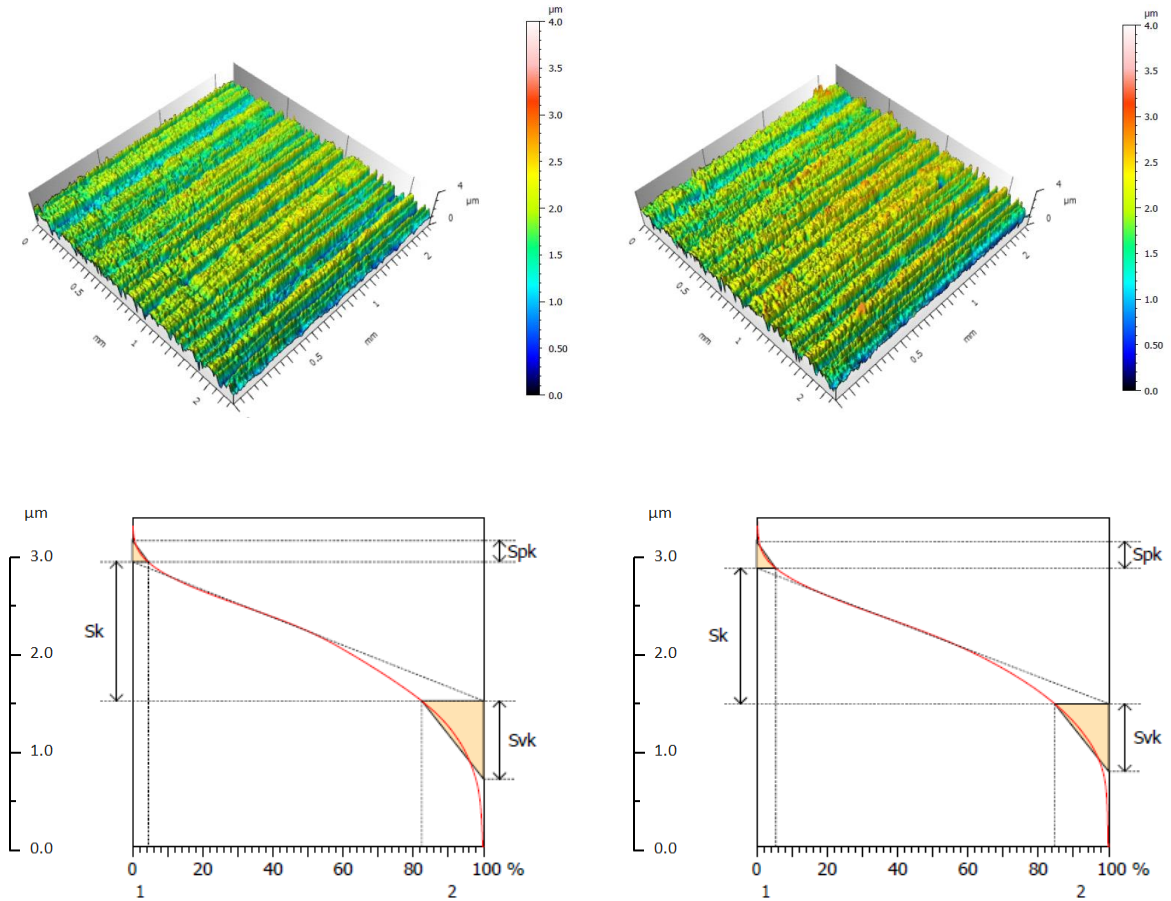
Figure A7: Experiment E2 (400 °C 2 h). Sample 04 (s4) - coordinates x, y = 11.0, 5.0 mm, sampling area = 1.6 x 1.6 μm. 3-D surface profile and material ratio curve. Conditions before (a) and after treatment (b).

Experiment E2 (400 °C 2 h)

Sample 05 (s5)

(a) Before SPN

(b) After SPN



Parameters	Value	Unit
Sk	1.098	μm
Spk	0.1682	μm
Svk	0.6183	μm
Sr1	4.522	%
Sr2	82.37	%

Parameters	Value	Unit
Sk	1.183	μm
Spk	0.2326	μm
Svk	0.5906	μm
Sr1	5.400	%
Sr2	84.65	%

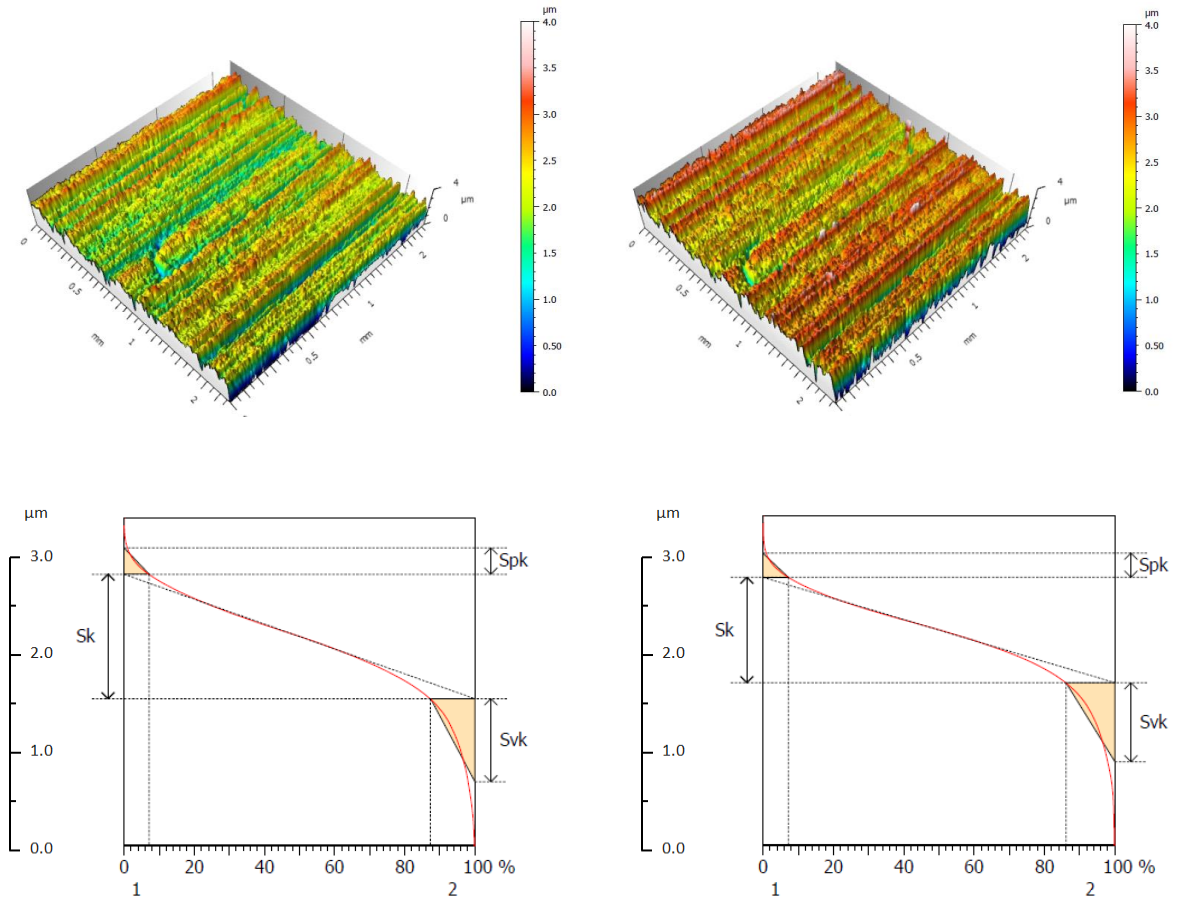
Figure A8: Experiment E2 (400 °C 2 h). Sample 05 (s5) - coordinates x, y = 13.0, 5.0 mm, sampling area = 1.6 x 1.6 μm. 3-D surface profile and material ratio curve. Conditions before (a) and after treatment (b).

Experiment E3 (350 °C 4 h)

Sample 02 (s2)

(a) Before SPN

(b) After SPN



Parameters	Value	Unit
Sk	1.229	µm
Spk	0.2603	µm
Svk	0.8197	µm
Sr1	7.136	%
Sr2	87.34	%

Parameters	Value	Unit
Sk	1.241	µm
Spk	0.2852	µm
Svk	0.9303	µm
Sr1	7.204	%
Sr2	86.10	%

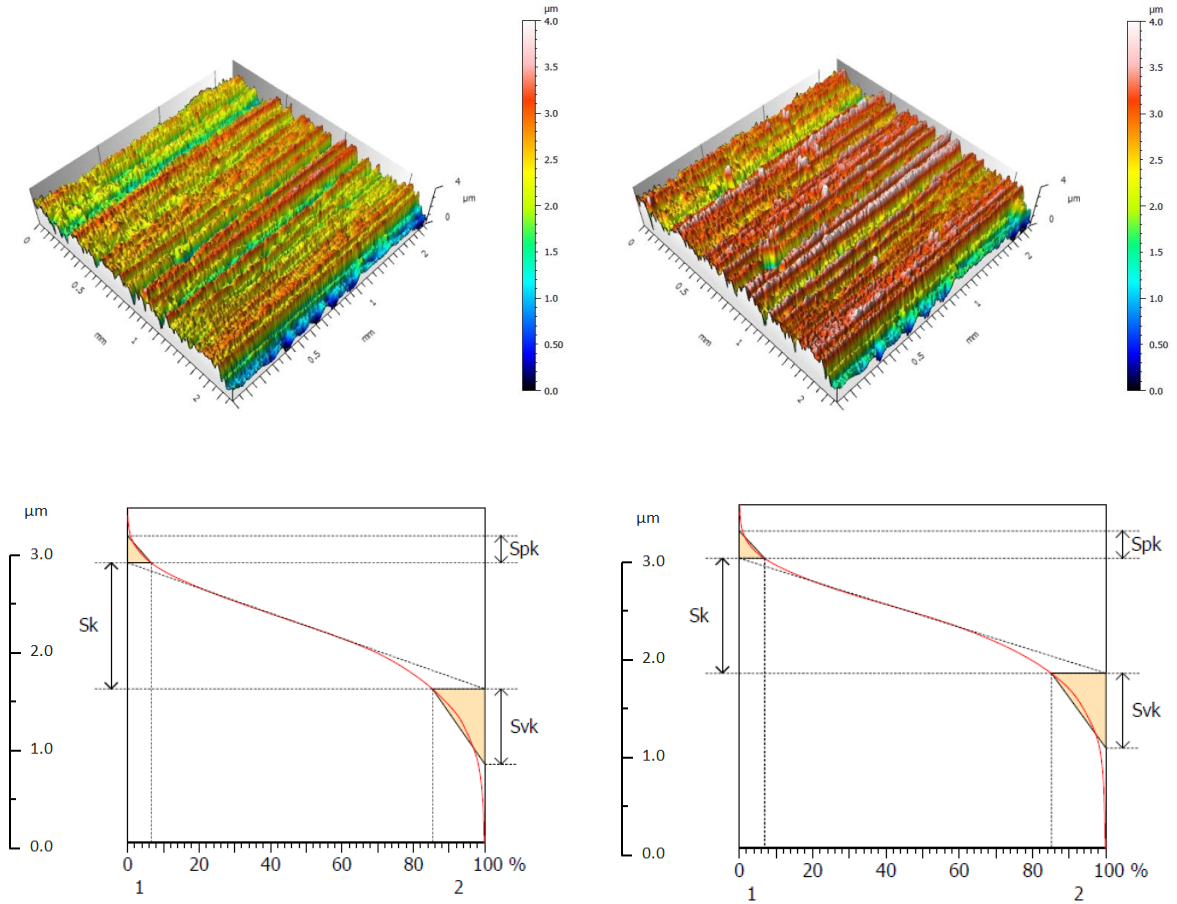
Figure A9: Experiment E3 (350 °C 4 h). Sample 02 (s2) - coordinates x, y = 7.0, 5.0 mm, sampling area = 1.6 x 1.6 µm. 3-D surface profile and material ratio curve. Conditions before (a) and after treatment (b).

Experiment E3 (350 °C 4 h)

Sample 03 (s3)

(a) Before SPN

(b) After SPN



Parameters	Value	Unit
Sk	1.339	μm
Spk	0.2858	μm
Svk	0.8005	μm
Sr1	6.586	%
Sr2	85.34	%

Parameters	Value	Unit
Sk	1.378	μm
Spk	0.3264	μm
Svk	0.8986	μm
Sr1	6.933	%
Sr2	85.13	%

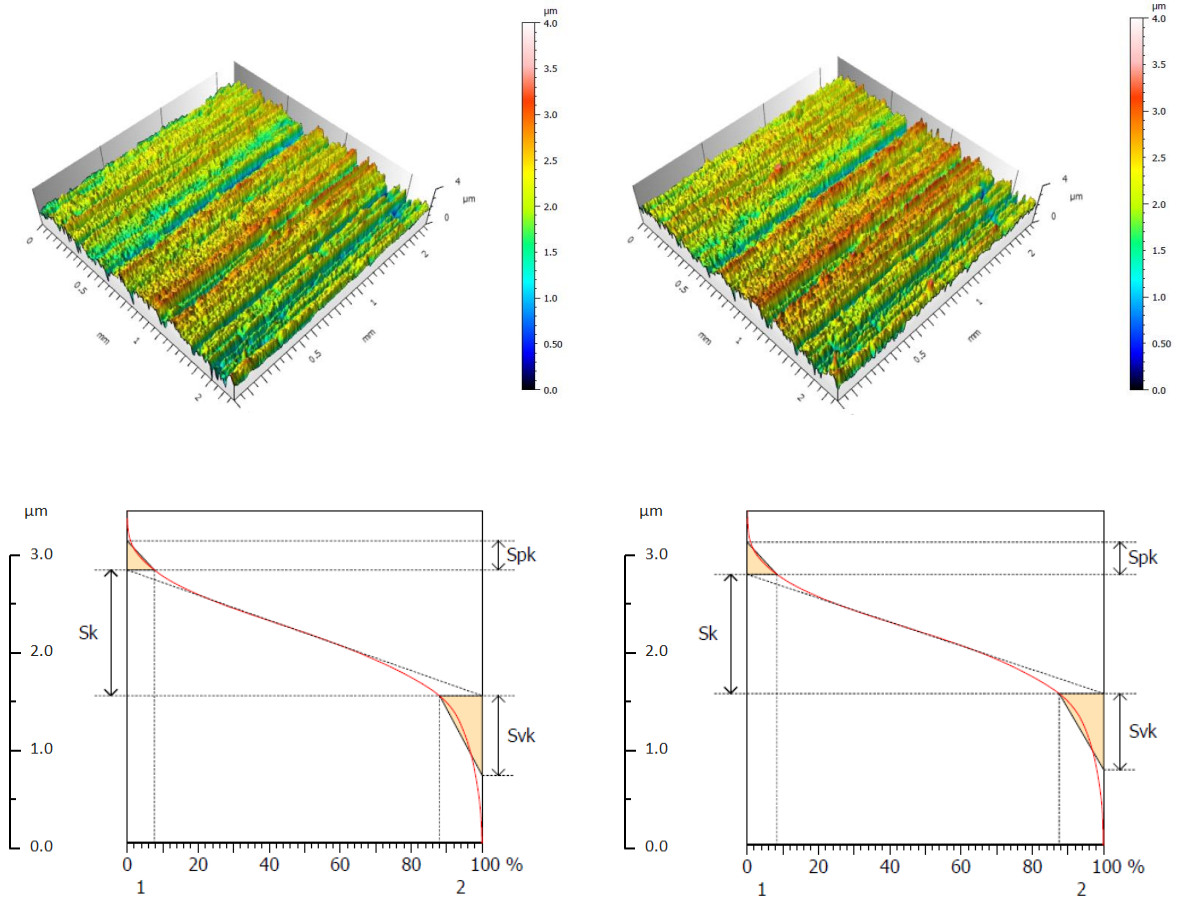
Figure A10: Experiment E3 (350 °C 4 h). Sample 03 (s3) - coordinates x, y = 9.0, 5.0 mm, sampling area = 1.6 x 1.6 μm. 3-D surface profile and material ratio curve. Conditions before (a) and after treatment (b).

Experiment E3 (350 °C 4 h)

Sample 04 (s4)

(a) Before SPN

(b) After SPN



Parameters	Value	Unit
Sk	1.186	µm
Spk	0.2740	µm
Svk	0.7528	µm
Sr1	7.692	%
Sr2	87.99	%

Parameters	Value	Unit
Sk	1.182	µm
Spk	0.3194	µm
Svk	0.7573	µm
Sr1	8.363	%
Sr2	87.51	%

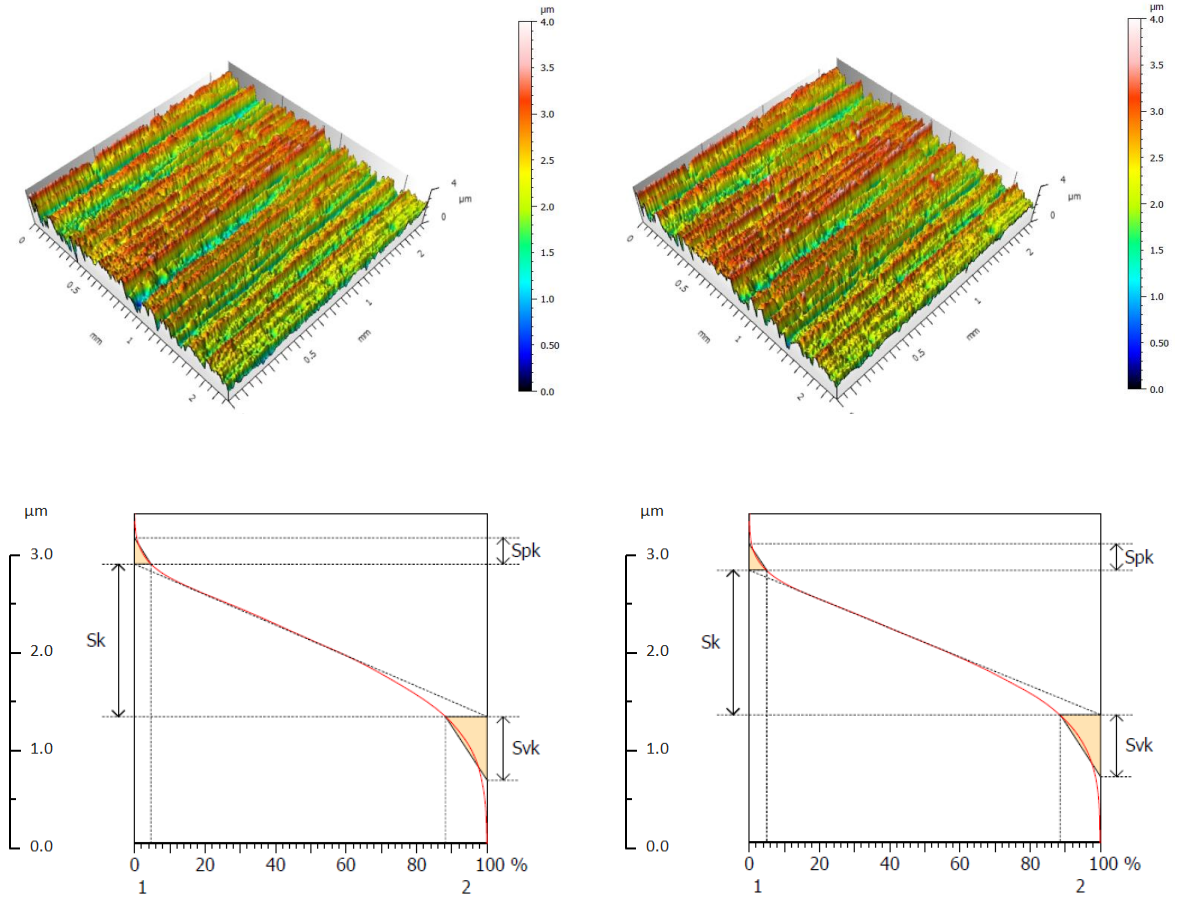
Figure A11: Experiment E3 (350 °C 4 h). Sample 04 (s4) - coordinates x, y = 11.0, 5.0 mm, sampling area = 1.6 x 1.6 µm. 3-D surface profile and material ratio curve. Conditions before (a) and after treatment (b).

Experiment E3 (350 °C 4 h)

Sample 05 (s5)

(a) Before SPN

(b) After SPN



Parameters	Value	Unit
Sk	1.664	µm
Spk	0.2860	µm
Svk	0.6935	µm
Sr1	4.653	%
Sr2	88.15	%

Parameters	Value	Unit
Sk	1.666	µm
Spk	0.3033	µm
Svk	0.7147	µm
Sr1	5.032	%
Sr2	88.53	%

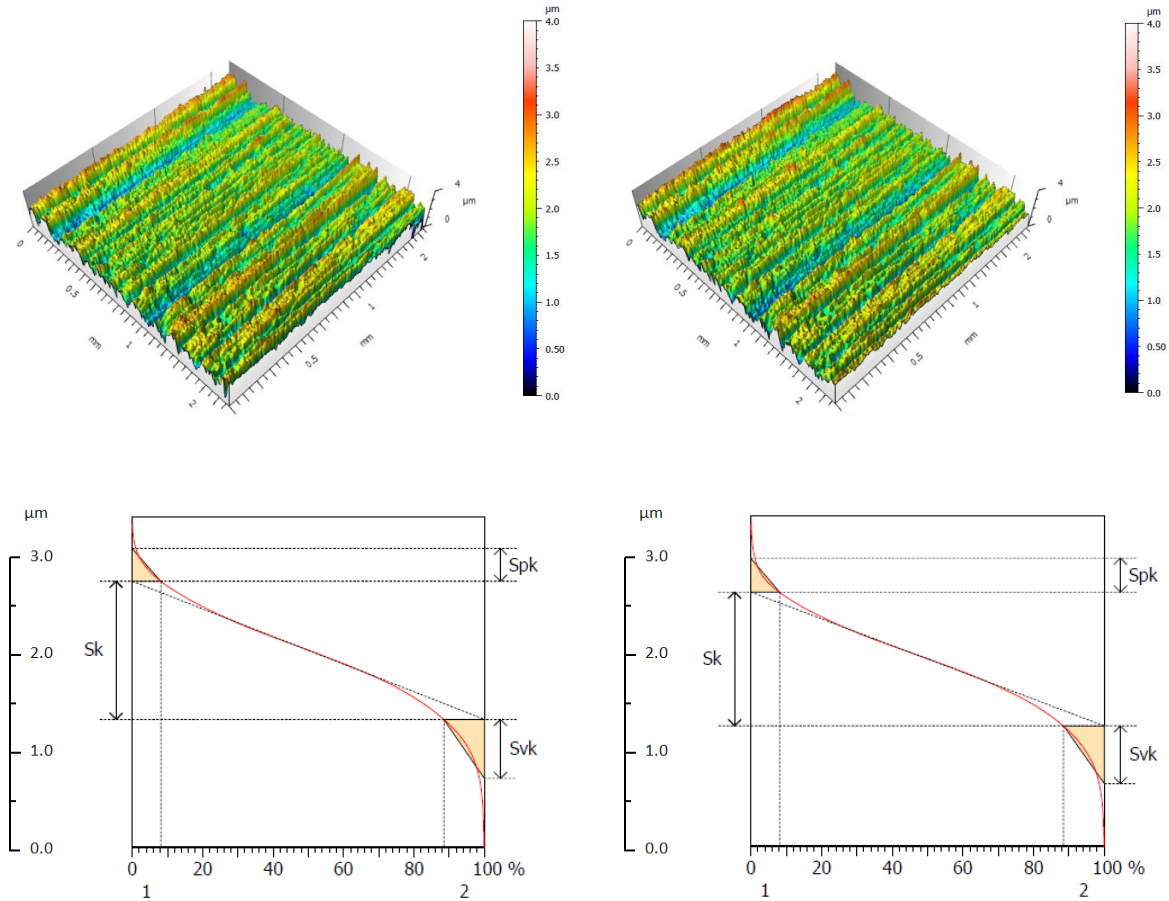
Figure A12: Experiment E3 (350 °C 4 h). Sample 05 (s5) - coordinates x, y = 13.0, 5.0 mm, sampling area = 1.6 x 1.6 µm. 3-D surface profile and material ratio curve. Conditions before (a) and after treatment (b).

Experiment E4 (350 °C 2 h)

Sample 02 (s2)

(a) Before SPN

(b) After SPN



Parameters	Value	Unit
S_k	1.255	μm
S_{pk}	0.2988	μm
S_{vk}	0.5370	μm
Sr_1	8.136	%
Sr_2	88.49	%

Parameters	Value	Unit
S_k	1.256	μm
S_{pk}	0.3184	μm
S_{vk}	0.5422	μm
Sr_1	8.130	%
Sr_2	88.43	%

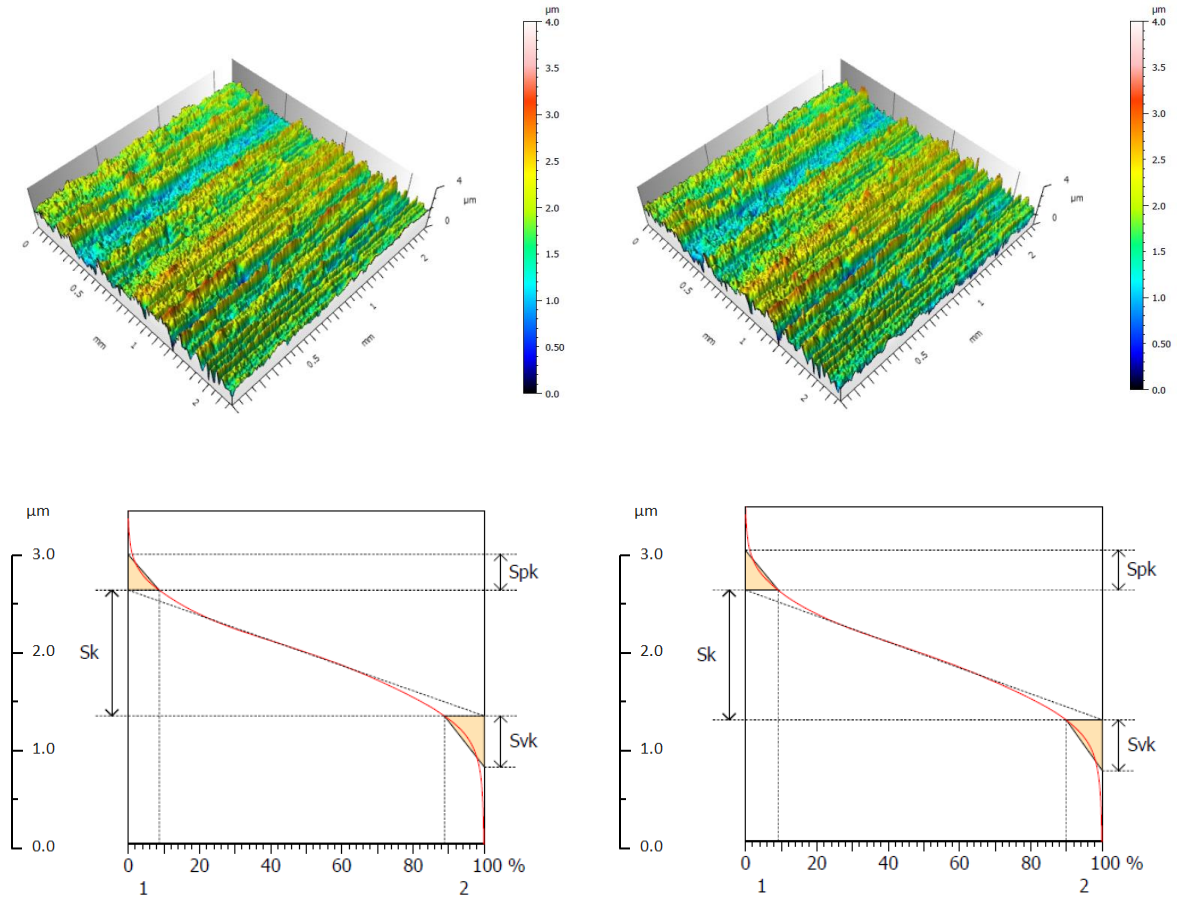
Figure A13: Experiment E4 (350 °C 2 h). Sample 02 (s2) - coordinates x, y = 7.0, 5.0 mm, sampling area = 1.6 x 1.6 μm . 3-D surface profile and material ratio curve. Conditions before (a) and after treatment (b).

Experiment E4 (350 °C 2 h)

Sample 03 (s3)

(a) Before SPN

(b) After SPN



Parameters	Value	Unit
S_k	1.150	μm
S_{pk}	0.3262	μm
S_{vk}	0.4680	μm
Sr_1	8.720	%
Sr_2	88.77	%

Parameters	Value	Unit
S_k	1.173	μm
S_{pk}	0.3601	μm
S_{vk}	0.4604	μm
Sr_1	9.213	%
Sr_2	89.86	%

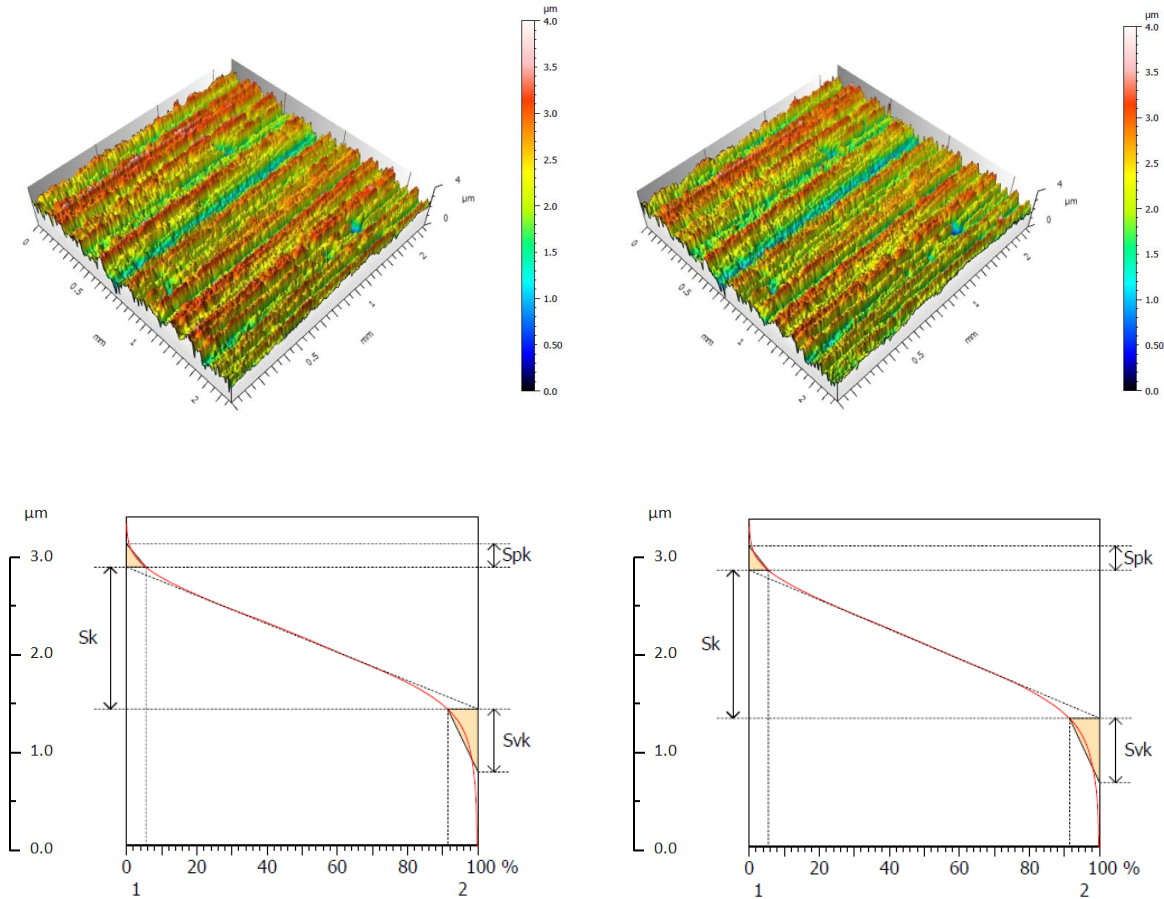
Figure A14: Experiment E4 (350 °C 2 h). Sample 03 (s3) - coordinates x, y = 9.0, 5.0 mm, sampling area = 1.6 x 1.6 μm . 3-D surface profile and material ratio curve. Conditions before (a) and after treatment (b).

Experiment E4 (350 °C 2 h)

Sample 04 (s4)

(a) Before SPN

(b) After SPN



Parameters	Value	Unit
Sk	1.564	μm
Spk	0.2583	μm
Svk	0.6938	μm
Sr1	5.566	%
Sr2	91.42	%

Parameters	Value	Unit
Sk	1.586	μm
Spk	0.2588	μm
Svk	0.6925	μm
Sr1	5.469	%
Sr2	91.42	%

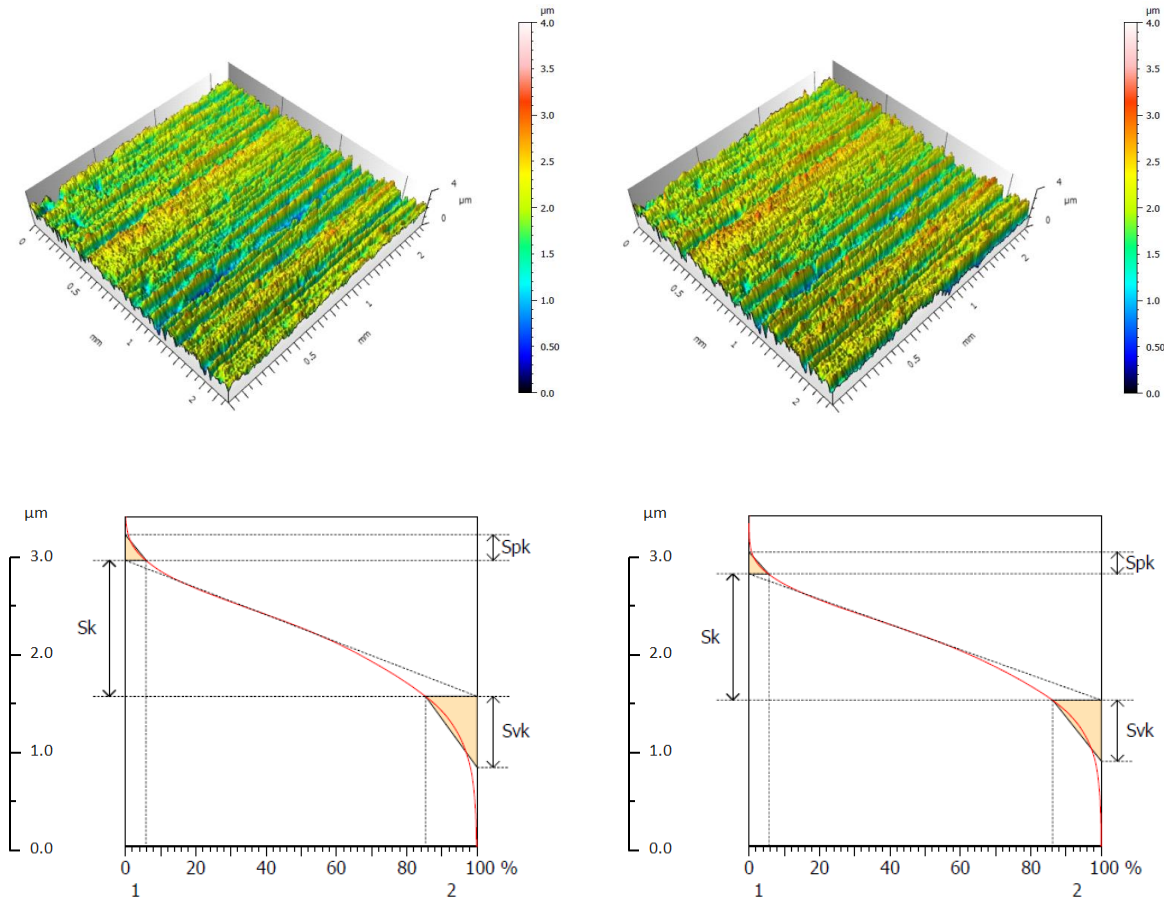
Figure A15: Experiment E4 (350 °C 2 h). Sample 04 (s4) - coordinates x, y = 11.0, 5.0 mm, sampling area = 1.6 x 1.6 μm. 3-D surface profile and material ratio curve. Conditions before (a) and after treatment (b).

Experiment E4 (350 °C 2 h)

Sample 05 (s5)

(a) Before SPN

(b) After SPN



Parameters	Value	Unit
Sk	1.150	μm
Spk	0.2164	μm
Svk	0.6013	μm
Sr1	5.874	%
Sr2	85.30	%

Parameters	Value	Unit
Sk	1.182	μm
Spk	0.2043	μm
Svk	0.5733	μm
Sr1	5.624	%
Sr2	86.17	%

Figure A16: Experiment E4 (350 °C 2 h). Sample 05 (s5) - coordinates x, y = 13.0, 5.0 mm, sampling area = 1.6 x 1.6 μm. 3-D surface profile and material ratio curve. Conditions before (a) and after treatment (b).

References

- [1] "D. dos Santos Filho, Alterações metalúrgicas e topográficas do cilindro de bloco de motor de combustão interna flex-fuel, Dissertação (Mestrado) - Escola Politécnica da Universidade de São Paulo, São Paulo-BR: USP, 2013".
- [2] "F. Cabanettes, Z. Dimkovski, B.-G. Rosén, Roughness variations in cylinder liners induced by honing tools wear, *Precision engineering* 41 (2015) 40-46".
- [3] "J. Vatauvuk, V. Demarchi, The effect of the addition of hard particles on the wear of liner and ring materials running with high sulfur fuel, SAE paper 950527, SAE Int., 1995".
- [4] "P. Kodali, P. How, W. D McNulty, Methods of improving cylinder liner wear, SAE paper 2000-01-0926, SAE Int., 2000".
- [5] "E. Rejowski, E.D. Rejowski, P. Mordente Sr, M.F. Pillis, T. Casserly, Application of DLC coating in cylinder liners for friction reduction, SAE paper 2012-01-1329, SAE Int., 2012".
- [6] "D.B. Salvaro, R.O. Giacomelli, R. Binder, C. Binder, A.N. Klein, J.D. Biasoli de Mello, Assessment of a multifunctional tribological coating (nitride+DLC) deposited on grey cast iron in a mixed lubrication regime, *Wear* 376 (2017) 803-812".
- [7] "R.O. Giacomelli, D.B. Salvaro, T. Bendo, C. Binder, A.N. Klein, J.D. Biasoli de Mello, Topography evolution and friction coefficient of gray and nodular cast irons with duplex plasma nitrided+DLC coating, *Surface and Coatings Technology* 314 (2017) 18-27".
- [8] "J. Paulo Davim (Ed.), *Machining of hard materials*, London-UK: Springer-Verlag, 2011".
- [9] "E. Nakamura, H. Uchida, S. Koyama, The improvement of distortion by high-temperature oil quenching, 2nd International conference, Quenching and the control of distortion, ASM Int., 1996".
- [10] "D. Pye, *Practical nitriding and ferritic nitrocarburizing*, Materials Park-US: ASM Int., 2003".
- [11] "C.A. dos Santos, *Composição superficial e propriedades mecânicas e tribológicas de aços carbono implantados com nitrogênio*, Tese (Doutorado) - Instituto de Física da UFRGS, Porto Alegre-BR: UFRGS, 1984".

- [12] "G.F. Bason, A new method of nitrogen case hardening, Transactions of the American society for steel treating 14 (1928) 33-41".
- [13] "A.R. Franco Júnior, Obtenção de revestimentos dúplex por nitretação a plasma e PVD-TiN em aços ferramenta AISI D2 e AISI H13, Tese (Doutorado) - Escola Politécnica da Universidade de São Paulo, São Paulo-BR: USP, 2003".
- [14] "C.E. Pinedo, Tratamentos superficiais para aplicações tribológicas, Metalurgia e materiais, Caderno técnico (2004) 162-169".
- [15] "C. Alves Júnior, Nitretação a plasma, fundamentos e aplicações, LabPlasma Universidade Federal do Rio Grande do Norte, Natal-BR: UFRN, 2001".
- [16] "R.C. Cordeiro, Nitretação iônica por plasma pulsado de aços inoxidáveis duplex, Dissertação (Mestrado) - Universidade Federal do Rio de Janeiro, Rio de Janeiro-BR: UFRJ/COPPE, 2010".
- [17] "C.S. Gonçalves, Efeito do processo de nitretação sob plasma no comportamento em fadiga térmica dos aços ferramenta para moldes para injeção de alumínio sob pressão, Dissertação (Mestrado) - Escola Politécnica da Universidade de São Paulo, São Paulo-BR: USP, 2012".
- [18] "K. Holmberg, P. Andersson, A. Erdemir, Global energy consumption due to friction in passenger cars, Tribology International 47 (2012) 221-234".
- [19] "J.B. Heywood, Motor vehicle emissions control: past achievements, future prospects, Handbook of air pollution from internal combustion engines, Eran Sher (Ed.), San Diego-US: Academic Press, 1998".
- [20] "A.M.K.P. Taylor, Science review of internal combustion engines, Energy Policy 36 (2008) 4657-4667".
- [21] "T.S. Sudarshan, S.B. Bhaduri, Wear in cylinder liners, Wear 91 (1983) 269-279".
- [22] "L.L. Ting, J.E. Mayer Jr., Piston ring lubrication and cylinder bore wear analysis, part I – theory, Journal of Lubrication Technology, Transactions of the ASME 96 (1974) 305-313".
- [23] "L.L. Ting, J.E. Mayer Jr., Piston ring lubrication and cylinder bore wear analysis, part II – theory verification, Journal of Lubrication Technology, Transactions of the ASME 96 (1974) 258-266".
- [24] "A.V. Sreenath, N. Raman, Running-in wear of a compression ignition engine: factors influencing the conformance between cylinder liner and piston rings, Wear 38 (1976) 271-289".

- [25] "J. Nadel, T.S. Eyre, Cylinder liner wear in low speed diesel engines, *Tribology International* 11 (1978) 267–271".
- [26] "R.A. Daskivich, Bearing length ratio applied to the measurement of engine cylinder-bore wear, *Precision Engineering* 6 (1984) 31-33".
- [27] "G.C. Barber, K.C. Ludema, The break-in stage of cylinder-ring wear: A correlation between fired engines and a laboratory simulator, *Wear* 118 (1987) 57-75".
- [28] "T.S. Eyre, K.K. Dutta, F.A. Davis, Characterization and simulation of wear occurring in the cylinder bore of the internal combustion engine, *Tribology International* 23 (1990) 11-16".
- [29] "E.A. Khorshid, A.M. Nawwar, A review of the effect of sand dust and filtration on automobile engine wear, *Wear* 141 (1991) 349–371".
- [30] "B.-G. Rosén, R. Ohlsson, T.R. Thomas, Wear of cylinder bore microtopography, *Wear* 198 (1996) 271–279".
- [31] "Y. Wang, S.C. Tung, Scuffing and wear behavior of aluminum piston skirt coatings against aluminum cylinder bore, *Wear* 225-229 (1999) 1100-1108".
- [32] "M. Priest, C.M. Taylor, Automobile engine tribology - approaching the surface, *Wear* 241 (2000) 193–203".
- [33] "A. Gangopadhyay, Development of a piston ring-cylinder bore wear model, SAE paper 2000-01-1788, SAE Int., 2000".
- [34] "E. Decencière, D. Jeulin, Morphological decomposition of the surface topography of an internal combustion engine cylinder to characterize wear, *Wear* 249 (2001) 482-488".
- [35] "M.F. Jensen, J. Bottiger, H.H. Reitz, M.E. Benzon, Simulation of wear characteristics of engine cylinders, *Wear* 253 (2002) 1044–1056".
- [36] "E.W. Schneider, D.H. Blossfeld, Effect of break-in and operating conditions on piston ring and cylinder bore wear in spark-ignition engines, SAE paper 2004-01-2917, SAE Int., 2004".
- [37] "A. Edrisy, T. Perry, A.T. Alpas, Investigation of scuffing damage in aluminum engines with thermal spray coatings, *Wear* 259 (2005) 1056-1062".
- [38] "J.J. Truhan, J. Qu, P.J. Blau, A rig test to measure friction and wear of heavy duty diesel engine piston rings and cylinder liners using realistic lubricants, *Tribology International* 38 (2005) 211-218".

- [39] "J.J. Truhan, J. Qu, P.J. Blau, The effect of lubricating oil condition on the friction and wear of piston ring and cylinder liner materials in a reciprocating bench test, *Wear* 259 (2005) 1048-1055".
- [40] "M. Dienwiebel, K. Pohlmann, M. Scherge, Origins of the wear resistance of AlSi cylinder bore surfaces studies by surface analytical tools, *Tribology International* 40 (2007) 1597-1602".
- [41] "J. Keller, V. Fridrici, Ph. Kapsa, S. Vidaller, J.F. Huard, Influence of chemical composition and microstructure of gray cast iron on wear of heavy duty diesel engines cylinder liners, *Wear* 263 (2007) 1158-1164".
- [42] "E. Tomanik, Friction and wear bench tests of different engine liner surface finishes, *Tribology International* 41 (2008) 1032-1038".
- [43] "B.E. Slattery, T. Perry, A. Edrisy, Microstructural evolution of a eutectic Al-Si engine subjected to severe running conditions, *Materials Science and Engineering A* 512 (2009) 76-81".
- [44] "Z. Dimkovski, C. Anderberg, B.-G. Rosén, R. Ohlsson, T.R. Thomas, Quantification of the cold worked material inside the deep honing grooves on cylinder liner surfaces and its effect on wear, *Wear* 267 (2009) 2235-2242".
- [45] "B.E. Slattery, A. Edrisy, T. Perry, Investigation of wear induced surface and subsurface deformation in a linerless Al-Si engine, *Wear* 269 (2010) 298-309".
- [46] "W. Grabon, P. Pawlus, J. Sep, Tribological characteristics of one-process and two-process cylinder liner honed surfaces under reciprocating sliding conditions, *Tribology International* 43 (2010) 1882–1892".
- [47] "L. Gara, Q. Zou, B.P. Sangeorzan, G.C. Barber, H.E. McCormick, M.H. Mekari, Wear measurement of the cylinder liner of a single cylinder diesel engine using a replication method, *Wear* 268 (2010) 558-564".
- [48] "Z. Dimkovski, L. Baath, S. Rosén, R. Ohlsson, B.-G. Rosén, Interference measurements of deposits on cylinder liner surfaces, *Wear* 270 (2011) 247-251".
- [49] "X. Meng-Burany, T.A. Perry, A.K. Sachdev, A.T. Alpas, Subsurface sliding wear damage characterization in Al-Si alloys using focused ion beam and cross-sectional TEM techniques, *Wear* 270 (2011) 152-162".
- [50] "J. Michalski, P. Woś, The effect of cylinder liner surface topography on abrasive wear of piston–cylinder assembly in combustion engine, *Wear* 271 (2011) 582-589".

- [51] "Z. Dimkovski, C. Anderberg, R. Ohlsson, B.-G. Rosén, Characterisation of worn cylinder liner surfaces by segmentation of honing and wear scratches, *Wear* 271 (2011) 548-552".
- [52] "P.R. De Silva, M. Priest, P.M. Lee, R.C. Coy, R.I. Taylor, Tribometer investigation of frictional response of piston rings lubricated with separated phases of lubricant contaminated with biofuel ethanol and water, *Tribology Letters* 43 (2011) 107-120".
- [53] "A.R. Riahi, A.T. Alpas, Wear map for grey cast iron, *Wear* 255 (2003) 401-409".
- [54] "J.M. Han, R. Zhang, O.O. Ajayi, G.C. Barber, Q. Zou, L. Guessous, D. Schall, S. Alnabulsi, Scuffing behavior of gray iron and 1080 steel in reciprocating and rotational sliding, *Wear* 271 (2011) 1854–1861".
- [55] "D. dos Santos Filho, H. Goldenstein, Cast iron graphite effects on the local wear of a flex-fuel engine cylinder, SAE paper 2015-36-0469, SAE Int., 2015".
- [56] "Y. Esaki, T. Ishiguro, N. Suzuki, Mechanism of intake-valve deposit formation part 1: characterization of deposits, SAE paper 900151, 1990".
- [57] "G. Kalghatgi, Deposits in gasoline engines - A literature review, SAE paper 902105, SAE Int., 1990".
- [58] "D. dos Santos Filho, A.P. Tschiptschin, H. Goldenstein, Effects of ethanol content on cast iron cylinder wear in a flex-fuel internal combustion engine—A case study, *Wear* 406–407 (2018) 105-117".
- [59] "M. Roensch, Observations on cylinder-bore wear, SAE paper 370134, SAE Int., 1937".
- [60] "G. Nicoletto, A. Tucci, L. Esposito, Sliding wear behavior of nitrided and nitrocarburized cast irons, *Wear* 197 (1996) 38-44".
- [61] "R. Zenker, A. Buchwalder, K. Rüttrich, W. Griesbach, K. Nagel, First results of a new duplex surface treatment for cast iron: Electron beam remelting and plasma nitriding, *Surface and Coatings Technology* 236 (2013) 58-62".
- [62] "E. Rolinski, A. Konieczny, G. Sharp, Influence of nitriding mechanisms on surface roughness of plasma and gas nitrided/nitrocarburized gray cast iron, *Heat Treating Progress* 3 (2007) 39-46".
- [63] "J. Baranowska, Surface quality of grey cast irons in the context of nitriding and oxygen-sulphur nitriding, *Surface and Coatings Technology* 100 (1998) 271-275".

- [64] "E.J. Mittemeijer, W.T.M. Straver, P.F. Colijn, P.J. van der Schaaf, J.A. van der Hoeven, The conversion cementite \rightarrow ϵ -nitride during the nitriding of FeC-alloys, *Scripta Metallurgica* 14 (1980) 1189-1192".
- [65] "N. Nayeypashae, M. Soltanieh, Sh. Kheirandish, A study on formation and growth mechanism of nitride layers during plasma nitriding process of plastic injection mold steel, *Materials and Manufacturing Processes* 31 (2016) 1192-1200".
- [66] "M.A.J. Somers, Development of compound layer and diffusion zone during nitriding and nitrocarburizing of iron and steels, *Comprehensive Matls. Proc.* 12 (2014) 413-437, S. Hashmi, C.J. Van Tyne, G.F. Batalha, B. Yilbas (Eds.), Amsterdam-NL: Elsevier, 2014".
- [67] "C.M Garzón, A.R. Franco, A.P. Tschiptschin, Thermodynamic analysis of M7C3 carbide dissolution during plasma nitriding of an AISI D2 tool steel, *ISIJ International* 57 (2017) 737-745".
- [68] "A. Toro, A.P. Tschiptschin, Chemical characterization of a high nitrogen stainless steel by optimized electron probe microanalysis, *Scripta Materialia* 63 (2010) 803–806".
- [69] "Y. Inokuti, N. Nishida, N. Ohashi, Formation of Fe₃N, Fe₄N and Fe₁₆N₂ on the surface of iron, *Metallurgical Transactions A* 6 (1975) 773-784".
- [70] "ASTM C1624-05, Standard test method for adhesion strength and mechanical failure modes of ceramic coatings by quantitative single point scratch testing, ASTM Int., 2010".
- [71] "R. Nakamura, A. Iwabuchi, Role of graphite in cast iron on tribological behaviour in nano-scratch test, *J Adv Mech Des Syst Manuf* 6 (2012) 1046-1056".
- [72] "M. Mendas, S. Benayoun, Investigating the effects of microstructure on the wear mechanisms in lamellar cast irons via microscratch tests, *Tribology International* 67 (2013) 124-131".
- [73] "R. Ghasemi, L. Elmquist, A study on graphite extrusion phenomenon under the sliding wear response of cast iron using microindentation and microscratch techniques, *Wear* 320 (2014) 120-126".
- [74] "R. Ghasemi, L. Elmquist, The relationship between flake graphite orientation, smearing effect, and closing tendency under abrasive wear conditions, *Wear* 317 (2014) 153-162".
- [75] "J.L. do Vale, M. Cortz, V.M.S. Bertolini, C.H. da Silva, G. Pintaude, Comparison of scratch resistance of lamellar and compacted graphite irons used in cylinder liners, *J Braz. Soc. Mech. Sci. Eng.* 39 (2017) 3981–3988".

- [76] "L.A. Franco, A. Sinatora, Material removal factor (fab): A critical assessment of its role in theoretical and practical approaches to abrasive wear of ductile materials, *Wear* 382-383 (2017) 51-61".
- [77] "W. Crookes, On Radiant Matter, A lecture delivered to the British Association for the Advancement of Science, at Sheffield, Friday, August 22, 1879, *The Popular Science Monthly* (1879) 13-24".
- [78] "B. Jones, *Life and Letters of Faraday*, London-UK: Longmans, Green and Co., 1870".
- [79] "G.P. Thomson, *The electron*, Oak Ridge-US: United States Atomic Energy Commission, Office of Information Services, 1972".
- [80] "I. Langmuir, Oscillations in ionized gases, *Proceedings of the National Academy of Sciences of the United States of America* 14 (1928) 627-637".
- [81] "S.C. Brown, *Gaseous Electronics, A Short History of Gaseous Electronics*, San Diego-US: Academic Press, 1978".
- [82] "M. I. Boulos, P. Fauchais, E. Pfender, *Thermal Plasmas - Fundamentals and Applications - Vol. 1*, London-UK: Springer Science & Business Media, 1994".
- [83] "D. Gurnett, A. Bhattacharjee, *Introduction to plasma physics: with space and laboratory applications*, New York-US: Cambridge University Press, 2005".
- [84] "ISO 945-1, *Microstructure of cast irons - Part 1: Graphite classification by visual analysis*, International Organization for Standardization, 2008".
- [85] "W. Kaplonek, C. Lukianowicz, Coherence correlation interferometry in surface topography measurements, *Recent Interferometry Applications in Topography and Astronomy*, I. Padron (Ed.), London-UK: Intech, 2012".
- [86] "P. Dobrzański, P. Pawlus, A study of filtering techniques for areal surface topography assessment, *Proc. of the Inst. of Mech. Eng., Part B: Journal of Eng. Manuf.* 225 (2011) 2096 - 2107".
- [87] "ISO 4287, *Geometrical product specifications - Surface texture: Profile method - Terms, definitions and surface texture parameters*, International Organization for Standardization, 1997".
- [88] "Minitab 18 Statistical software version 18.1 (Computer software), Minitab, Inc., 2017".
- [89] "R.A. Fisher, *Statistical methods for research workers*, 5th edition, London-UK: Oliver and Boyd, 1934".

- [90] "J.W. Tukey, Comparing individual means in the analysis of variance, *Biometrics* 5 no. 2 (1949) 99-114".
- [91] "I.M. Hutchings, *Tribology: Friction and Wear of Engineering Materials*, London-UK: Edward Arnold, 1992".
- [92] "R. Leach, L. Brown, X. Jiang, R. Blunt, M. Conroy, D. Mauger, Measurement good practice guide no. 108, Guide to the measurement of smooth surface topography using coherence scanning interferometry, Teddington-UK: National Physical Laboratory, 2008".
- [93] "H. Zahouani, M. EL Mansori, Multi-scale and multi-fractal analysis of abrasive wear signature of honing process, *Wear* 376–377A (2017) 178-187".
- [94] "Wavelength-dispersive (X-ray) Spectroscopy, Essential knowledge briefings, Microscopy EKB Series, J. Heat (Ed.), Spectroscopy and Separations EKB Series, N. Taylor (Ed.), First Edition, West Sussex-UK: John Wiley & Sons Ltd, 2016".
- [95] "T.C. Buttery, J.F. Archard, Grinding and abrasive wear, *Proc. Inst. Mech. Eng.* 185 (1970) 537–551".
- [96] "S.J.B. Reed, Optimization of wavelength dispersive x-ray spectrometry analysis conditions, *J. Res. Natl. Inst. Stand. Technol.* 107 (2002) 497–502".
- [97] "B. Cullity, S. Stock, *Elements of x-ray diffraction*, 3rd edition, Upper Saddle River-US: Prentice Hall, 2001".
- [98] "C. Borchers, R. Kirchheim, Cold-drawn pearlitic steel wires, *Progress in Materials Science* 82 (2016) 405-444".
- [99] "J.D. Embury, R.M. Fisher, Structure and properties of drawn pearlite, *Acta Metall.* 14 (1966) 147-159".
- [100] "J. Toribio, V. Kharin, M. Lorenzo, D. Vergara, Role of drawing-induced residual stresses and strains in the hydrogen embrittlement susceptibility of prestressing steels, *Corrosion Science* 53 (2011) 3346-3355".
- [101] "M.T. Umemura, L.B. Varela, C.E. Pinedo, R.C. Cozza, A.P. Tschiptschin, Assessment of tribological properties of plasma nitrided 410S ferritic-martensitic stainless steels, *Wear* 426–427 A (2019) 49-58".
- [102] "P. Pawlus, T. Cieslak, T. Mathia, The study of cylinder liner plateau honing process, *Journal of Materials Processing Technology* 209 (2009) 6078-6086".

- [103] "ISO 25178-2, Geometrical product specifications - Surface texture: Areal - Terms, definitions and surface texture parameters, International Organization for Standardization, 2012".
- [104] "W.F. Sales, A.R. Machado, J. Bonney, E.O. Ezugwu, Evaluation of cutting fluids using scratch tests and turning process, J Braz. Soc. Mech. Sci. Eng. 4 (2007) 372-378"
- [105] "E. Tomanik, E. Nocera, J. Vatauvuk, Ion nitrided piston rings, III Workshop RECOPE - Redes Cooperativas de Pesquisa, Melhoria das Propriedades Superficiais de Metais, Escola Politécnica da Universidade de São Paulo (1999) 62-69".
- [106] "J. Vatauvuk, J.C. Vendramim, L.A. Bloem S. Jr., Breve discussão do componente 'rugosidade' em aço carbono SAE 1045 e SAE 1035 nitretados pelos processos: sal, gás e plasma, III Workshop RECOPE - Redes Cooperativas de Pesquisa, Melhoria das Propriedades Superficiais de Metais, Escola Politécnica da Universidade de São Paulo (1999) 70-81".
- [107] "J. Vatauvuk, Mecanismos de desgaste em anéis de pistão e cilindros de motores de combustão interna, Tese (Doutorado) - Escola Politécnica da Universidade de São Paulo, São Paulo-BR: USP, 1994".
- [108] "R.B. Obara, Avaliação do desgaste em cilindros de motores de combustão interna – Mapeamento de mecanismos e quantificação do desgaste, Tese (Doutorado) - Escola Politécnica da Universidade de São Paulo, São Paulo-BR: USP, 2018".
- [109] "L.A. Franco, Abrasão de ferro fundido cinzento: aplicação a motores automotivos, Tese (Doutorado) - Escola Politécnica da Universidade de São Paulo, São Paulo-BR: USP, 2015".
- [110] "V.H. Bulsara, S. Chandrasekar, T.N. Farris, Scratch testing, Materials Park-US: ASM Int., 2003"
- [111] "J. Vatauvuk, S.A.L. Pereira, W.A. Monteiro, Efeito do encruamento no processo de nitretação de aços inoxidáveis austeníticos AISI 304 e 316, TTT 2012 – VI Conferência Brasileira sobre Temas de Tratamento Térmico (2012) 245-256".
- [112] "J.L. do Vale, C. Silva, G. Pintaude, Tribological performance assessment of lamellar and compacted graphite irons in lubricated ring-on-cylinder test, Wear 426-427 A (2019) 471-480".
- [113] "R.B. Obara, A. Sinatora, Quantification of cylinder bores almost 'zero-wear', Wear 364-365 (2016) 224-232".